

**Searches for Beyond the Standard Model Phenomena using Events with  
Multiple Leptons with the ATLAS Detector at the LHC**

by

David Ren-Hwa Yu

A dissertation submitted in partial satisfaction of the  
requirements for the degree of  
Doctor of Philosophy

in

Physics

in the

Graduate Division

of the

University of California, Berkeley

Committee in charge:

Professor Yury Kolomensky, Chair  
Professor Beate Heinemann  
Professor Karl van Bibber

Summer 2014

The dissertation of David Ren-Hwa Yu, titled Searches for Beyond the Standard Model Phenomena using Events with Multiple Leptons with the ATLAS Detector at the LHC, is approved:

Chair \_\_\_\_\_

\_\_\_\_\_

\_\_\_\_\_

Date \_\_\_\_\_

\_\_\_\_\_

\_\_\_\_\_

University of California, Berkeley

**Searches for Beyond the Standard Model Phenomena using Events with  
Multiple Leptons with the ATLAS Detector at the LHC**

Copyright 2014  
by  
David Ren-Hwa Yu

To Ossie Bernosky

And exposition? Of go. No upstairs do fingering. Or obstructive, or purposeful. In the glitter. For so talented. Which is confines cocoa accomplished. Masterpiece as devoted. My primal the narcotic. For cine? To by recollection bleeding. That calf are infant. In clause. Be a popularly. A as midnight transcript alike. Washable an acre. To canned, silence in foreign.

# Contents

<b>Contents</b>	<b>ii</b>
<b>1 Introduction</b>	<b>1</b>
<b>2 Physics at the Energy Frontier</b>	<b>2</b>
2.1 The Standard Model	2
2.1.1 Introduction and Historical Development	2
2.1.2 Gauge Theory	4
2.1.3 Construction of the Standard Model	5
2.1.4 Strong Sector	6
2.1.5 Confinement: Hadrons and Jets	6
2.1.6 Parton Distribution Functions	6
2.1.7 Electroweak Sector	6
2.1.8 Weak Interactions of Fermions	7
2.1.9 The Higgs mechanism	8
2.2 Beyond the Standard Model	10
2.2.1 Unexplained Phenomena	10
2.2.2 Theoretical Deficiencies	12
2.2.3 Theories of BSM Physics	13
<b>3 The Experimental Apparatus</b>	<b>18</b>
3.1 The Large Hadron Collider	18
3.1.1 Accelerator Components	19
3.1.2 The Accelerator Complex	20
3.1.3 Beam Parameters	24
3.2 The ATLAS Experiment	25
3.2.1 Coordinate System	25
3.2.2 Magnets	26
3.2.3 Inner Detector	29
3.2.4 Calorimetry	34
3.2.5 Muon Spectrometer	42
3.2.6 Trigger and Data Acquisition	47

<b>4 Luminosity Measurement</b>	<b>52</b>
4.1 Run I Luminosity	52
4.2 Measurement Overview	52
4.3 Luminosity Detectors	53
4.4 Luminosity Calibration: van der Meer Scans	56
4.4.1 2011 Luminosity Calibration	57
4.5 Systematic Uncertainties	60
4.6 Vertex-Based Luminosity Measurement	60
4.6.1 Vertex Counting Method	62
4.6.2 Pileup Effects	62
4.6.3 Vertex-Based Luminosity Measurements in 2011	67
<b>5 Event Reconstruction</b>	<b>74</b>
5.1 Track and Vertex Reconstruction	74
5.2 Electrons	75
5.2.1 Identification	76
5.2.2 Efficiency Measurements	76
5.2.3 Energy and Momentum Measurement	77
5.3 Muons	80
5.3.1 Efficiency Measurements	80
5.3.2 Energy Scale and Resolution	81
5.4 $\tau$ Leptons	82
5.4.1 Energy Scale and Resolution	85
5.5 Jets	87
5.5.1 Energy Scale and Resolution	89
5.5.2 Pileup Suppression	90
5.5.3 $b$ -tagging	91
5.6 Invisible Particles	93
5.7 Object Selection	93
5.7.1 Leptons	94
5.7.2 Jets and Missing Transverse Energy	95
5.7.3 Overlap Removal	96
<b>6 Background Estimation</b>	<b>100</b>
6.1 Prompt Backgrounds	100
6.2 Reducible Backgrounds	102
6.2.1 Fake Factor Method	102
6.2.2 Electron Fake Factors	104
6.2.3 Muon Fake Factors	108
6.2.4 Tau Lepton Fakes	112
<b>7 Model-Independent Trilepton Search</b>	<b>118</b>

<b>7.1</b>	<b>Event Selection</b>	<b>118</b>
7.1.1	Triggering	118
7.1.2	Trilepton Event Selection	119
<b>7.2</b>	<b>Analysis Strategy</b>	<b>119</b>
<b>7.3</b>	<b>Systematic Uncertainties</b>	<b>121</b>
<b>7.4</b>	<b>Background Validation</b>	<b>123</b>
7.4.1	Dilepton Validation Regions	123
7.4.2	$t\bar{t}$ Validation Regions	124
7.4.3	Intermediate Fake Factor Validation Regions	126
<b>7.5</b>	<b>Results and Limits</b>	<b>129</b>
<b>7.6</b>	<b>Model Testing</b>	<b>129</b>
7.6.1	Example: Doubly Charged Scalar Particles	130
<b>8</b>	<b>Trilepton Resonance Search</b>	<b>135</b>
<b>8.1</b>	<b>Signal Models</b>	<b>135</b>
8.1.1	Signal Monte Carlo Samples	138
<b>8.2</b>	<b>Search Strategy</b>	<b>140</b>
8.2.1	Event Selection and Heavy Lepton Reconstruction	140
8.2.2	Performance on Fiducial Signal Events	142
<b>8.3</b>	<b>Systematic Uncertainties</b>	<b>146</b>
<b>8.4</b>	<b>Background Validation</b>	<b>155</b>
<b>8.5</b>	<b>Signal and Background Fit Model</b>	<b>159</b>
8.5.1	Signal Modeling	159
8.5.2	Background Fits	161
<b>8.6</b>	<b>Results</b>	<b>168</b>
<b>8.7</b>	<b>Interpretation</b>	<b>170</b>
8.7.1	Limits on Models	171
<b>9</b>	<b>Conclusion</b>	<b>178</b>
<b>10</b>	<b>Appendix</b>	<b>179</b>
<b>10.1</b>	<b>Electron Fake Factors</b>	<b>179</b>
10.1.1	Photon Conversion Reweighting	179
<b>10.2</b>	<b>Trilepton Resonance Search</b>	<b>181</b>
10.2.1	$\Delta R(Z, \ell_3)$ Cut Optimization	181
10.2.2	Signal Fit Details	183
10.2.3	Additional Kinematic Distributions	183

## Acknowledgments

I want to thank my advisor for advising me.

# Chapter 1

## Introduction

# Chapter 2

## Physics at the Energy Frontier

Today's particle physics is roughly divided into three disciplines, the frontiers of energy, intensity, and cosmology. The three genres are classifications of experimental techniques: the energy frontier uses particle accelerators to produce new particles in high-energy collisions; the intensity frontier investigates rare processes using intense particle beams; and the cosmic frontier analyzes the contents of the universe, such as the distribution of matter or the cosmic microwave background, to determine the physics responsible for the evolution of the universe from the Big Bang to today. All three frontiers contribute vital discoveries which form the foundation of our understanding of fundamental physics.

The Large Hadron Collider, or LHC, is the current flagship experiment of the energy frontier, capable of producing proton-proton collisions with a center-of-mass energy of  $\sqrt{s} = 14$  TeV. Accounting for the composite nature of the proton, these collisions give access to phenomena with characteristic energies approximately up to the TeV scale, which couple in some fashion to quarks or gluons. The program of study divides into two categories: confirmation and measurement of the Standard Model, and searches for new phenomena beyond the Standard Model. The former category consists of observation and measurement of the particles and interactions of the Standard Model, especially concerning the top quark and the physics of electroweak symmetry breaking. The latter comprises a diverse array of searches for new particles hypothesized to address deficiencies of the Standard Model. This chapter describes the theories underlying the LHC's exploration of physics at the TeV scale. Emphasis is placed on theories predicting the production of several charged leptons, which are the subject of the analyses described in chapters ?? and 8.

### 2.1 The Standard Model

#### 2.1.1 Introduction and Historical Development

The Standard Model of particle physics is a theoretical framework describing the dynamics and interactions of the known elementary particles under the electromagnetic, weak, and

strong forces. The theory is a gauge theory describing a wide range of phenomena in the language of Quantum Field Theory. Particles are described as excitations of quantum fields, whose properties are defined by their representations under the Lorentz group and the gauge groups associated with the electroweak and strong forces. Each quantum field associated a particle carries a spin quantum number,  $s = \frac{n}{2}$  for  $n \in \mathbb{Z}_{\geq 0}$ , which indexes its representation under the Lorentz group. Matter particles, or *fermions*, are associated with fields with  $s = \frac{1}{2}$ . *Bosons* have  $s = 0$  (scalar bosons) or  $s = 1$  (vector bosons).

Historically and phenomenologically, the Standard Model consists of two distinct components: the electroweak sector, describing the electromagnetic and weak forces, and the strong sector, describing the behavior of quarks under the strong force. The electroweak sector's development began in the 1930s with quantum electrodynamics (QED), the subject of the Nobel Prize-winning work of Tomonaga, Schwinger, and Feynman [QED], among others. QED successfully predicted a number of very precisely measured quantities, including the  $g - 2$  of the electron [g-2] and the Lamb shift in hydrogen [bethe-lamb]. This simple gauge theory, based around the  $U(1)$  gauge group, was extended to include a description of the weak force over the next twenty years, which successfully predicted the massive  $W^\pm$  and  $Z^0$  bosons discovered at CERN in 1983 [WZ-discovery]. A key ingredient of the electroweak theory was the introduction of spontaneous symmetry breaking, the mechanism by which the  $W^\pm$  and  $Z$  bosons could acquire nonzero mass without abandoning the underlying symmetry of the theory. As proposed in 1964, independently by Higgs [higgs], Brout and Englert [brout englert], and Guralnik, Hagen and Kibble [ghk], the symmetry breaking occurred in an extra sector of the theory containing a single quantum field *phi*, which interacted with the electroweak force and had a quartic potential energy expression. Assuming a positive quartic coefficient and a negative quadratic coefficient, the ground state of the theory would have a nonzero value of  $\phi$ , breaking electroweak symmetry. Aside from endowing the  $W^\pm$  and  $Z$  bosons with mass, the extra quantum field also contributed a massive scalar particle to the theory, now known as the *Higgs boson*,  $H$ . Famously, the early phenomenological investigations of the Higgs pointed out that the particle would be extremely difficult to detect:

We apologize to the experimentalists for having no idea what is the mass of the Higgs boson, unlike the case with charm, and for not being sure of its couplings to other particles, except that they are probably all very small. For these reasons we do not want to encourage big experimental searches for the Higgs boson, but we do feel that people performing experiments vulnerable to the Higgs boson should know how it may turn up [gaillardnanoellis1975].

Indeed, a generation of experiments passed before the Higgs boson was discovered, 48 years later by the ATLAS and CMS experiments at the LHC [atlashiggs, cmshiggs].

The strong sector began as a study of the patterns of hadrons observed in cosmic ray and accelerator experiments. The light hadrons were observed to fall into a two-dimension octuplet pattern in isospin and strangeness space (???), a symmetry dubbed “the eightfold

way” by Murray Gell-Mann. In 1963, Gell-Mann and George Zweig independently suggested an origin for this symmetry in hadronic substructure, namely that the hadrons were composite particles formed from three more fundamental particles, now called the up, down, and strange quarks. This model was quickly disrupted by the observation of the spin- $\frac{3}{2}$   $\Delta^{+++}$  particle (WHAT ORDER DID THIS HAPPEN IN?), which was composed of three up quarks in the same spin state and therefore would violate Dirac statistics. Han and Nambu, and, independently, Greenburg, proposed an extra quantum number under which the quarks were charged, called *color* and taking on the three discrete values of red, green, and blue. This proposal led to the development of the  $SU(3)$  gauge theory now known as quantum chromodynamics, which successfully explains the confinement of quarks into the observed spectrum of hadrons.

### 2.1.2 Gauge Theory

A *gauge theory* is a quantum field theory in which the Lagrangian is invariant under *local transformations* under a gauge group  $G$ . To give a simple example, consider a single massless fermion field  $\psi(x)$ . By itself, the dynamics of  $\psi$  can be derived from the simple Lagrangian,

$$\mathcal{L} = i\bar{\psi}(x)\not{\partial}\psi(x), \quad (2.1)$$

where  $\not{\partial} \equiv \gamma^\mu \partial_\mu$  and  $\gamma^\mu$  are the  $\gamma$ -matrices associated with the Lorentz group. We then require that the Lagrangian be invariant under local transformations under the action of  $G$ :

$$\begin{aligned} \psi(x) &\rightarrow V(x)\psi(x), \\ V(x) &= e^{i\alpha(x)^a t^a} \end{aligned}$$

where  $t^a$  are the generators of the Lie algebra of  $G$ , and  $\alpha(x)_a$  are arbitrary continuous functions. The kinetic term in the Lagrangian,  $i\bar{\psi}(x)\gamma^\mu \partial_\mu \psi(x)$ , can be made invariant by promoting the simple derivate  $\partial_\mu$  to a *covariant derivative*,  $D_\mu$ , defined as:

$$D_\mu = \partial_\mu - igt^a A_\mu^a, \quad (2.2)$$

where  $g$  is a coupling constant associated with the gauge interaction,  $t_a$  are the generators of the Lie algebra of  $G$ , and  $A_\mu^a(x)$  are vector fields associated with the gauge bosons of  $G$ , which transform under the action of  $G$  as:

$$A_\mu^a(x)t_a \rightarrow V(x) \left( A_\mu^a(x)t^a + \frac{i}{g}\partial_\mu \right) V^\dagger(x) \quad (2.3)$$

For infinitesimal  $\alpha(x)^a$ , the transformations can be expressed more simply as:

$$\psi(x) \rightarrow (1 + i\alpha^a t^a + \mathcal{O}(\alpha^2))\psi(x) \quad (2.4)$$

$$A_\mu^a \rightarrow A_\mu^a + \frac{1}{g}\partial_\mu \alpha^a(x) + f^{abc}A_\mu^b \alpha^c + \mathcal{O}(\alpha^2), \quad (2.5)$$

where  $f^{abc}$  are the structure constants of  $G$ , defined by

$$[t^a, t^b] = i f^{abc} t^c. \quad (2.6)$$

Note that the structure constants are zero for Abelian gauge groups, such as  $G = U(1)$ . The Lagrangian for the gauge theory, including gauge-invariant terms involving  $A_\mu^a(x)$  itself, is:

$$\mathcal{L} = \bar{\psi}(x)(i\cancel{D})\psi(x) - \frac{1}{2}(F_{\mu\nu}^a)^2, \quad (2.7)$$

where  $F_{\mu\nu}^a = \partial_\mu A_\nu^a(x) - \partial_\nu A_\mu^a(x) + g f^{abc} A_\mu^b A_\nu^c$  is the field strength tensor of  $A_\mu^a(x)$ .

The interactions of the fields  $\psi(x)$  and  $A_\mu^a(x)$  are manifest in the Lagrangian. In this example, the interaction of  $\psi$  with  $A^a$  is described by the interaction term

$$\mathcal{L}_{\text{int}} = \bar{\psi}\gamma^\mu A_\mu^a t^a \psi. \quad (2.8)$$

For non-Abelian gauge groups with nonzero structure constants  $f^{abc}$ , the square of the field strength tensor also yields cubic and quartic self-interaction terms amongst the  $A_\mu^a(x)$ .

### 2.1.3 Construction of the Standard Model

The Standard Model is a gauge theory with gauge group  $G_{\text{SM}} = SU(3)_c \otimes SU(2)_L \otimes U(1)_Y$ , roughly corresponding to the strong, weak, and electromagnetic forces, respectively. The theory contains a fermion field for every known matter particle, with various transformation properties under the three Standard Model gauge groups, as summarized in table 2.1. The fermions are organized into three generations, each containing an up-type quark, a down-type quark, a lepton, and a neutrino. The generations are identical except for the particles' masses, which are shown in table ???. The bosonic content of the Standard Model consists of a spin-1 boson for each generator of  $SU(3)_c \times SU(2)_L \times U(1)_Y$ , yielding eight gluons for  $SU(3)_c$  and four electroweak gauge bosons for  $SU(2)_L \times U(1)_Y$ , plus the spin-0 Higgs boson.

	$Q_L = \begin{pmatrix} u_L \\ d_L \end{pmatrix}$	$u_R$	$d_R$	$E_L = \begin{pmatrix} \nu_L \\ e_L \end{pmatrix}$	$e_R$
$SU(3)_c$	<b>3</b>	<b>3</b>	<b>3</b>	<b>1</b>	<b>1</b>
$SU(2)_L$	<b>2</b>	<b>1</b>	<b>1</b>	<b>2</b>	<b>1</b>
$U(1)_Y$	$\frac{1}{6}$	$\frac{2}{3}$	$-\frac{1}{3}$	$-\frac{1}{2}$	$-1$

Table 2.1: Matter particles (fermions) of the Standard Model, their representations under  $SU(3)_c$  and  $SU(2)_L$ , and their charges under  $U(1)_Y$ .

Fermion masses

### 2.1.4 Strong Sector

The strong sector of the Standard Model is a non-abelian  $SU(3)_c$  gauge theory, describing the interactions of quarks under the strong force. The theory, called *quantum chromodynamics* (QCD), contains the six observed quarks, called the up, down, charm, strange, top, and bottom quarks, as well as eight massless force carriers called gluons.

QCD describes drastically different phenomena at high and low energies. In the high energy limit, the strength of the interaction goes to zero, and quarks and gluons behave as nearly free particles. At low energies, the strength of the interaction diverges, confining quarks into *hadrons*, bound states that are neutral under the strong force. The behavior emerges from the running of the strong coupling constant,  $\alpha_s = \frac{g_s}{4\pi}$ , with the energy scale of the interaction,  $Q$ , as calculated under the renormalization group flow. To one-loop order in  $\alpha_s$ , the running is given by:

$$\alpha_s(Q) = \frac{\alpha_s(M)}{1 + (b_0 \alpha_s / 2\pi) \log(Q/M)}, \quad (2.9)$$

where  $b_0 = 11 - \frac{2}{3}n_f$  for  $n_f$  fermion fields. With  $n_f = 6$ , corresponding to the six quark flavors,  $\frac{d\alpha_s Q}{dQ} < 0$ ; hence the coupling decreases with  $Q$ . On the other hand, as  $Q$  decreases,  $\alpha_s(Q)$  increases, diverging at

$$Q = M \exp\left(\frac{8\pi^2}{b_0 g^2}\right) \equiv \Lambda. \quad (2.10)$$

Note that the exact nature of the divergence remains an open question; this simple expression results from a one-loop calculation, which becomes unreliable once  $\alpha_s$  becomes large. Nonetheless,  $\Lambda$  indicates the momentum scale at which the strong interaction becomes strong and confines quarks into hadrons, and has been measured to be  $\Lambda \approx 200$  MeV.

### 2.1.5 Confinement: Hadrons and Jets

### 2.1.6 Parton Distribution Functions

### 2.1.7 Electroweak Sector

The electroweak sector is a unified description of electromagnetism and weak decays as a gauge theory with gauge group  $SU(2)_L \times U(1)_Y$ . The theory models a number of phenomena, including:

- The weak decays of heavy quarks and leptons.
- The nonzero masses of the weak gauge bosons and fermions.

- Flavor violation in weak decays involving charged currents.
- Violation of  $C$ - and  $CP$ -symmetry observed in certain decay processes [**Cviolation, cronin, na31, CP-bmesons** ].

The underlying theory of the electroweak sector is rather more complicated than the strong sector.  $C$  violation is manifest in the construction of the theory: the gauge couplings are *chiral*, with the left- and right-handed components of fermions belonging to different representations of  $SU(2)$ . Such a symmetry forbids mass terms for the fermions and gauge bosons, in clear conflict with observations. To accommodate fermion and gauge boson masses without abandoning the symmetry, a scalar Higgs field is added with a quartic potential arranged such that the ground state spontaneously breaks the  $SU(2)_L$  symmetry. The resulting theory contains a large number of free parameters: two gauge couplings  $g$  and  $g'$ , two constants in the quartic Higgs potential, and X coupling terms between the fermions and the Higgs field.

The Lagrangian can be broken into two pieces,  $\mathcal{L} = \mathcal{L}_{\text{sym}} + \mathcal{L}_{\text{Higgs}}$ , where the first piece contains terms with only gauge bosons and fermion fields and conserves  $SU(2)_L$  symmetry, and the second piece contains terms with Higgs fields and spontaneously breaks  $SU(2)_L$  symmetry.

In this and the following sections,  $W^{a\mu}$  represents the three  $SU(2)_L$  gauge fields,  $B^\mu$  the  $U(1)_Y$  gauge field, and  $\phi$  the Higgs scalar field, which is a complex  $SU(2)_L$  doublet. Assigning the left-handed components of fermions to the doublet  $SU(2)_L$  representation and the right-handed components to the singlet presentation, the Standard Model quarks are denoted by  $Q_L^i \equiv \begin{pmatrix} u_L^i \\ d_L^i \end{pmatrix}$ ,  $u_R^i$ , and  $d_R^i$ , where  $i = 1, 2, 3$  indicates the generation. Similarly, the leptons are denoted by  $E_L^i \equiv \begin{pmatrix} \nu_L^i \\ e_L^i \end{pmatrix}$  and  $e_R^i$ ; there is no corresponding right-handed neutrino in the theory.

### 2.1.8 Weak Interactions of Fermions

The Lagrangian describing the fermions and gauge bosons is:

$$\mathcal{L}_{\text{sym}} = -\frac{1}{4} \sum_{i=1}^3 \bar{E}_L(i\not{D}) E_L + \bar{e}_R(i\not{D}) e_R + \bar{Q}_L(i\not{D}) Q_L + \bar{u}_R(i\not{D}) u_R + \bar{d}_R(i\not{D}) d_R, \quad (2.11)$$

where, similarly to equation 2.2, the covariant derivative  $D_\mu$  is given by:

$$D_\mu = \partial_\mu - ig\tau^a W^{a\mu} - ig'YB^\mu. \quad (2.12)$$

$\tau^a$  are operators corresponding to the action of a given generator of the  $SU(2)_L$  Lie algebra, and  $Y$  is an operator corresponding to the action of the generator of  $U(1)_Y$ , which

simply returns the hypercharge. For the left-handed doublets in the fundamental representation of  $SU(2)_L$ ,  $\tau^a$  can be taken to be the Pauli matrices,  $\tau^a = \frac{1}{2}\sigma^a$ . For right-handed singlets in the trivial representation of  $SU(2)_L$ ,  $\tau^a$  are zero, implying that the right-handed fermions do not interact with the  $W^{a\mu}$ .

### 2.1.9 The Higgs mechanism

We first demonstrate the spontaneous breaking of  $SU(2)_L$  by the Higgs mechanism. The terms of the Lagrangian involving the Higgs field are:

$$\mathcal{L}_{\text{Higgs}} = |D_\mu \phi|^2 - V(\phi^\dagger \phi), \quad (2.13)$$

with the Higgs potential energy term given by:

$$V(\phi^\dagger \phi) = \frac{1}{2}\mu^2 \phi^\dagger \phi + \frac{1}{4}\lambda(\phi^\dagger \phi)^2. \quad (2.14)$$

The quartic potential induces electroweak symmetry breaking if the quadratic coefficient is negative, i.e.  $\mu^2 < 0$ . The potential is then minimized for a nonzero value of  $\phi$ . Using the  $SU(2)_L$  symmetry, we can take vacuum expectation value of  $\phi$  to be:

$$\langle \phi \rangle = \frac{1}{\sqrt{2}} \begin{pmatrix} 0 \\ v \end{pmatrix}. \quad (2.15)$$

Solving for  $v$ ,

$$0 = \frac{dV}{dv} \quad (2.16)$$

$$= -\frac{1}{2}\mu^2 v + \frac{1}{4}\lambda v^3 \quad (2.17)$$

$$v = \frac{2mu^2}{\lambda}. \quad (2.18)$$

Expanding the Higgs field about its expectation value,  $\phi$  can be written:

$$\phi = U \frac{1}{\sqrt{2}} \begin{pmatrix} 0 \\ v + h \end{pmatrix}, \quad (2.19)$$

where  $U$  is a local  $SU(2)$  gauge transformation that can be set to **1** by choice of gauge.

The masses and interactions of various particles arise from simple algebra, expanding the Higgs field about  $\langle \phi \rangle$  and identifying the relevant physical states.

### Gauge Bosons

The mass terms for the gauge bosons arise from the covariant derivative terms in equation 2.13. Expanding the covariant derivatives, the relevant mass terms are:

$$\Delta\mathcal{L}_{\text{Higgs}} \ni \frac{1}{8}v^2 (g^2(W_\mu^1 W^{1\mu} + W_\mu^2 W^{2\mu}) + (g'B_\mu - gW_\mu^3)^2). \quad (2.20)$$

The physical states are the gauge- and mass-eigenstates,

$$W_\mu^\pm = \frac{W^1 \mp iW^2}{\sqrt{2}} \quad (2.21)$$

$$Z_\mu^0 = -\sin\theta_W B_\mu + \cos\theta_W W_\mu^3 \quad (2.22)$$

$$A_\mu = \cos\theta_W B_\mu + \sin\theta_W W_\mu^3, \quad (2.23)$$

where  $\tan\theta_W = \frac{g'}{g}$ . The corresponding masses are:

$$m_{W^\pm} = \frac{gv}{2} \quad (2.24)$$

$$m_{Z^0} = \frac{gv}{2\cos\theta_W} \quad (2.25)$$

$$m_A = 0. \quad (2.26)$$

The theory thus predicts a nontrivial relationship between the masses of the gauge bosons,  $m_{W^\pm}$  and  $m_{Z^0}$ , and the gauge coupling constants  $g$  and  $g'$ .

### TALK ABOUT THE COUPLINGS TO QUARKS AND LEPTONS.

#### Fermion Masses and Flavor Non-Conservation

The fermion masses arise from the Yukawa coupling terms between the fermions and the Higgs field,

$$-\Delta\mathcal{L} = -\left(\lambda_d^{ij}\bar{Q}_L^i \cdot \phi d_R^j - \lambda_u^{ij}\epsilon^{ab}\bar{Q}_{La}^i u_R^j + \text{h.c.}\right) - \left(\lambda_l^{ij}\bar{E}_L^i \cdot \phi e_R^j + \text{h.c.}\right). \quad (2.27)$$

The  $\lambda_{u,d,l}^{ij}$  are complex matrices of coupling constants. These are, in general, not symmetric or Hermitian, and to identify the physical mass eigenstates, the matrices must be diagonalized. The Yukawa matrices can be decomposed using the singular value decomposition as:

$$\lambda_u = U_u D_u W_u^\dagger, \quad \lambda_d = U_d D_d W_d^\dagger, \quad \lambda_l = U_l D_l W_l^\dagger, \quad (2.28)$$

where  $U_{u,d,l}$  and  $W_{u,d,l}$  are unitary matrices, and  $D_{u,d,l}$  are diagonal, non-negative matrices. Making a change of variables,

$$u_L^i \rightarrow U_u^{ij} u_L^j, \quad d_L^i \rightarrow U_d^{ij} d_L^j, \quad (2.29)$$

$$u_R^i \rightarrow W_u^{ij} u_R^j, \quad d_R^i \rightarrow W_d^{ij} d_R^j, \quad (2.30)$$

$$e_L^i \rightarrow U_l^{ij} e_L^j, \quad \nu_L^i \rightarrow U_l^{ij} \nu_L^j, \quad (2.31)$$

$$e_R^i \rightarrow W_l^{ij} e_R^j, \quad (2.32)$$

the off-diagonal Yukawa couplings vanish as intended, while the kinetic terms remain invariant. The masses of the fermions are:

$$m_u^i = \frac{1}{\sqrt{2}} D_u^{ii} v, \quad m_d^i = \frac{1}{\sqrt{2}} D_d^{ii} v, \quad m_l^i = \frac{1}{\sqrt{2}} D_l^{ii} v, \quad m_\nu^i = 0. \quad (2.33)$$

The diagonalization procedure alters one other term in the Lagrangian: the couplings of the quarks to the  $W^\pm$  bosons. The quark- $W^\pm$  couplings can be written in terms of the current  $J^{\mu\pm} = \sum_i \frac{1}{\sqrt{2}} (\bar{u}_L^i \gamma^\mu d_L^i)$  as:

$$\Delta\mathcal{L} = g(W_\mu^+ J_W^{\mu+} + W_\mu^- J_W^{\mu-}) \quad (2.34)$$

Under the transformation in equation ??,  $J^{\mu\pm} \rightarrow \sum_{ij} \frac{1}{\sqrt{2}} \bar{u}_L^i \gamma^\mu V^{ij} d_L^j$ , where  $V^{ij}$  is a  $3 \times 3$  unitary matrix known as the *Cabibbo-Kobayashi-Maskawa* (CKM) matrix,  $V = U_u^\dagger U_d$ .  $V$  implying that weak decays mix the three generations of quarks; quark flavor is not conserved in weak decays, as is readily observed in hadron decays, e.g.  $K^\pm \rightarrow \pi^\pm + \pi^0$ . Further,  $V$  contains one nontrivial complex phase, allowing for  $CP$  violation in weak decays.

Note that the lepton sector does not contain an analogous mixing matrix for weak decays, due to the presence of only a single Yukawa matrix  $\lambda_l^{ij}$ . Hence lepton flavor and  $CP$  are conserved in leptonic weak decays.

**Higgs Boson** TALK ABOUT THE HIGGS BOSON, WHAT HAPPENS TO THE OTHER THREE DEGREES OF FREEDOM, AND THE HIGGS COUPLINGS TO EVERYTHING ELSE.

## 2.2 Beyond the Standard Model

Though quite successful as a description of most observed phenomena in particle physics, the Standard Model is deficient in several ways. Several key observations, initially from astrophysics and cosmology, indicate that the theory is incomplete; additionally, the theory has a few unsatisfying constructional aspects which, while not technically inconsistent, suggest that there remains underlying physics to be discovered. Many theories have been proposed to solve these issues, and confronting these theories is a major goal of the ATLAS experiment. This section describes the motivations for physics beyond the Standard Model (BSM), and lists several of the leading BSM theories which can be confronted at the LHC.

### 2.2.1 Unexplained Phenomena

Phenomena not described by the Standard Model include the following:

- **Neutrino mass:** Due to the lack of right-handed neutrinos and left-handed antineutrinos, neutrinos are massless in the Standard Model. However, observation of neutrino flavor oscillations indicate that at least two of the three neutrinos have nonzero mass. The phenomenon of oscillation was first observed by the Homestake solar electron

neutrino detector [1], in the form of a deficit of electron neutrinos detected from the sun. Later experiments observed oscillation among other types of neutrinos and antineutrinos, from a variety of sources including the sun, nuclear reactors, cosmic rays interacting with the atmosphere, and particle accelerators [2]. The data imply that the three neutrino mass eigenstates have different masses, with differences given by:

$$|\Delta m_{21}^2| \cong 7.5 \times 10^{-5} \text{ eV}^2 \quad (2.35)$$

$$|\Delta m_{31}^2| \cong 2.5 \times 10^{-3} \text{ eV}^2. \quad (2.36)$$

These relations hold only if at least two of the neutrino masses are nonzero. On the other hand,  $\beta$ -decay experiments and cosmological observations indicate an upper bound on the neutrino mass scale of order  $m_{\nu_i} \lesssim \mathcal{O}(0.1-1)$  [**Troitzk**, **CMB/WMAP**, **Planck** ].

- **Dark matter:** Astrophysical observations suggest the existence of a large amount of non-Standard Model matter which interacts only gravitationally with baryonic matter. The earliest tension with known physics comes from galactic rotation curves, the distribution of rotational velocities of stars about the galactic center as a function of radius [3]. The rotational velocities  $v(r)$  can be compared with the expectation from the observed matter distribution,  $\tilde{v}(r) = \sqrt{\frac{M(r)}{r}}$ , where  $M(r)$  is the observed mass at radius less than  $r$ . As shown in figure ??, at large distances from the galactic center, the observed rotation curve behaves like  $v(r) \sim \text{constant}$ , while the expected rotation curves behaves like  $v(r) \sim \frac{1}{\sqrt{r}}$ .

At present, the leading explanation for the discrepancy is the presence of a large amount of gravitationally interacting, non-luminous matter in galaxies, known as *dark matter*. The hypothesis is supported by cosmological observations: measurements of anisotropies in the cosmic microwave background (CMB) are sensitive to the relative amounts of baryonic matter (which interacts with photons), dark matter (which does not), and dark energy. A recent combination of CMB measurements gives the following values:

$$\Sigma_c h^2 = 0.1198 \pm 0.0026, \quad (2.37)$$

$$\Sigma_b h^2 = 0.02207 \pm 0.00027, \quad (2.38)$$

$$\Sigma_\Lambda = 0.685^{+0.017}_{-0.016}, \quad (2.39)$$

$$(2.40)$$

where  $\Sigma_c$  and  $\Sigma_b$  are the density parameters for cold dark matter and baryonic matter, respectively,  $h$  is the Hubble constant, and  $\Sigma_\Lambda$  is the cosmological constant.

Many candidates have been proposed as the constituents of dark matter, such as primordial black holes, sterile neutrinos, axions, and weakly interacting dark particles (WIMPs). WIMPs are a particularly interesting candidate for LHC phenomenology:

in the so-called “freeze-out” model of dark matter evolution,  $\Sigma_c$  is fixed when dark matter falls out of thermal equilibrium with conventional matter.  $\Sigma_c \approx 0.1$  is achieved with  $m_\chi \sim \mathcal{O}(100 \text{ GeV})$  and couplings of order  $g_X \sim \mathcal{O}(0.1 - 1)$ ; such a particle could be produced and detected at the LHC.

- **Matter-Antimatter Asymmetry:** The observable universe is made up of matter and photons, with very little antimatter. Astrophysical observations measure the ratio of baryons (minus antibaryons) to photons,

$$\eta \equiv \frac{n_B - n_{\bar{B}}}{n_\gamma}, \quad (2.41)$$

to be in the range  $5.7 \leq \eta \times 10^{10} \leq 6.7$  (95% CL) [**pdg-bbn** ]. However, assuming symmetrical initial conditions and conservation of baryon number, the Big Bang would produce baryons and antibaryons in equal number<sup>1</sup>. Due to inefficient annihilation after freeze-out, the present abundances would be  $\frac{n_B}{n_\gamma} = \frac{n_{\bar{B}}}{n_\gamma} \approx 10^{-20}$  [**cline** ]. The generation of a large baryon-antibaryon asymmetry is known as the *baryogenesis* problem.

Three conditions are necessary for baryogenesis, known as the Sakharov conditions [**sakharov** ]: baryon number violation,  $C$ - and  $CP$ -symmetry violation, and interactions out of thermal equilibrium (i.e. the interaction rate must be slower than the expansion rate of the universe). In principle, the Standard Model possibly satisfies all three conditions: baryon number is violated by electroweak sphalerons [**thooft** ],  $C$  and  $CP$  violation is observed in hadron oscillations and decays [**Kindirect**, **Kdirect**, **B**, **D** ], and thermal equilibrium may be lost if the electroweak phase transition is sufficiently first-order [??? ]. However, baryogenesis of sufficient magnitude has not been demonstrated, in particular due to insufficient  $CP$ -violation.

## 2.2.2 Theoretical Deficiencies

Theoretical deficiencies of the Standard Model include the following:

- **Hierarchy problem:** The hierarchy problem refers to the large discrepancy in strength between the electroweak forces and gravity. Specifically, due to the diagrams shown in figure ??, the quadratic Higgs parameter  $\mu$  receives quantum corrections proportional to  $\Lambda^2$ , where  $\Lambda$  is the ultraviolet cutoff of the theory:

$$\Delta\mu^2 = f; \text{aieffz}. \quad (2.42)$$

The value of this parameter is known from measurements of the electroweak boson masses (???),

$$\mu^2 = \mu_0^2 + \sum_i \frac{g^2 Y_i^2}{16\pi^2} \Lambda^2 = \lambda v^2 \sim 10^4 \text{GeV}^2. \quad (2.43)$$

---

<sup>1</sup>Asymmetric initial conditions are also not capable of producing a relic asymmetry due to inflation, which would dilute any initial asymmetry [**cline** ].

If the Standard Model is valid up to the Planck scale,  $\Lambda \sim \mathcal{O}(10^{19}\text{GeV})$ , then the bare mass parameter,  $\mu_0^2$ , and the quantum corrections,  $\Delta\mu^2$ , must cancel to some 34 orders of magnitude, an unsavory coincidence referred to as *fine tuning*. Turning the problem on its head, if nature is not finely tuned, then the ultraviolet cutoff should be not too far above the electroweak scale,  $\Lambda \lesssim 10 \text{ TeV}$  [**pinner** ]. The physics responsible for such a cutoff scale could be accessible at the LHC.

- **Free parameters:** The Standard Model contains 19 free parameters. In terms of measurable quantities, these are the 6 quark masses  $m_{q_i}$ , 3 lepton masses  $m_{l_i}$ , 3 CKM mixing angles  $\theta_{ij}$  and 1 CKM phase  $\delta$ , 3 gauge couplings  $g_i$ , the QCD vacuum angle  $\theta_{\text{QCD}}$ , the Higgs field vacuum expectation value  $v$ , and the Higgs mass,  $m_h$ . These parameters are measured; their values are not predicted by the theory. It remains unknown why the Yukawa couplings range over six orders of magnitude, for example, nor why the fermions fall into three generations.
- **Strong  $CP$  problem:** The strong sector of the Standard Model potentially contains a  $CP$ -violating term,

$$\mathcal{L}_\Theta = \overline{\Theta} \frac{\alpha_s}{8\pi} G^{\mu\nu a} \tilde{G}_{\mu\nu}^a, \quad (2.44)$$

where  $-\pi \leq \overline{\Theta} \leq \pi$  is the effective  $\Theta$  parameter after diagonalizing the quark mass matrix,  $G_{\mu\nu}^a = \partial_\mu A_\mu^a - \partial_\nu A_\nu^a - g_s f^{abc} A_\mu^b A_\nu^c$  is the gluon field strength tensor, and  $\tilde{G}_{\mu\nu}^a = \epsilon_{\mu\nu\alpha\beta} G^{\alpha\beta a}$  is its dual [**pdg-axions** ]. However, this term is severely constrained by measurements of the neutron dipole moment [4], with a limit of  $|\overline{\Theta}| \lesssim 10^{-10}$ .

- **Gauge Unification:** The origin of the Standard Model gauge group,  $G_{SM} = SU(3)_c \times SU(2)_L \times U(1)_Y$ , is not understood. Remarkably, the Standard Model fermion content can be described as a  $\mathbf{5}^* \oplus \mathbf{10}$  representation of  $SU(5)$ , the smallest simple group containing  $G_{SM}$ , with all of the Standard Model quantum numbers correctly predicted. Unfortunately, simply augmenting the gauge group to  $SU(5)$  leads to an unacceptable rate of proton decay, but deriving  $G_{SM}$  from a larger, “unified” gauge group remains a topic of active investigation.

### 2.2.3 Theories of BSM Physics

This section describes some of the theories that have been proposed to solve the issues raised in section 2.2.1 and 2.2.2, focusing on those which the LHC is capable of testing. Particular emphasis is placed on theories producing several charged leptons.

#### Supersymmetry

The hierarchy problem described in section X motivates the consideration of additional symmetries. Consider again the form of the quadratic divergence:

Xxx

The divergence could be avoided, and the theory rendered technically natural, by introducing scalar partners to the fermions to counteract the divergence, due to the relative (-) sign between scalar and fermion loops:

#### Diagram and equations

Scalar partners with masses on the TeV scale alleviate the naturalness problem, and could be detected at the LHC.

The forms that such a symmetry could take are quite restricted. In 1967, Coleman and Mandula demonstrated that, under a small set of physically assumptions, the symmetry algebra of the  $S$ -matrix must be isomorphic to a direct product of the Poincaré group and an internal symmetry group (i.e. whose generators commute with those of the Poincaré group). This *no-go* theorem appeared to establish that it is impossible to “[combine] space-time and internal symmetries in any but a trivial way.” However, a loophole was found in 1975, formalized in the theorem of Haag, Lopuszanski, and Sohnius: the Poincaré group can be extended nontrivially in the context of graded Lie algebras, allowing the symmetry generators to be commuting or anticommuting [5]. These so-called “supersymmetries”, first proposed in by Wess and Zumino [6], transform bosons to fermions and vice-versa, and combine nontrivially with the Poincaré group in that the anticommutator of two supersymmetry generators is a spacetime translation.

By itself, supersymmetry predicts a partner for every Standard Model particle with identical mass and quantum numbers, except that the spin differs by  $1/2$ <sup>2</sup>. The symmetry is assumed to be spontaneously broken at some high mass scale, giving additional mass to the superpartners, to account for the fact that superpartners are not observed. The minimal implementation, called the *minimal supersymmetric Standard Model* (MSSM), contains X free parameters (Y to account for the additional degrees of freedom in the Lagrangian, and Z to account for SUSY breaking), although simplifying assumptions are almost always used to reduce this large parameter space to manageable size.

Supersymmetry solves a number of the shortcomings of the standard model described in section (reference). First, as mentioned above, it provides a boson-fermion symmetry to cancel the quadratic divergence in the Higgs mass. Second, the superpartners are typically assigned an extra quantum number, R-parity, under which the SM particles are neutral, in order to stabilize the proton; this extra symmetry has the consequence of making the lightest superpartner stable, providing a dark matter candidate. Third, the supersymmetry breaking sector contains numerous CP-violating parameters, which could provide the necessary CP violation to explain the matter-antimatter asymmetry in the universe. Finally, the superpartners modify the running of the three gauge couplings such that they approach similar values in the UV, supporting the notion of gauge unification.

*Multilepton Production* Describe ways to produce many leptons in SUSY.

---

<sup>2</sup>The exact implementation can be derived from the superpotential, where the fields  $f(x^\mu)$  are promoted to super fields  $F(x^\mu, \theta, \bar{\theta})$ , where  $\theta$  and  $\bar{\theta}$  are anticommuting parameters. The integration in the action is augmented from  $d^4x$  to  $d^4x d\theta d\bar{\theta}$ ; the familiar action in normal spacetime is regained by performing the partial integral over the anticommuting variables; see [**wess-bagger**] for more details.

## Extra Generations of Matter

Alternatively, one can consider addressing only the dominant divergence due to the top quark loop. The divergence can be canceled by vector-like partners of the top quark.

Motivations for extra matter in general. In particular, vector-like leptons. Existing limits, especially on chiral fermions.

## Neutrino Seesaw

Due to the lack of right-handed neutrinos in the Standard Model, neutrinos are exactly massless. At tree level, a mass term like  $m_\nu \bar{\nu}_L \nu_L^c$  would violate  $SU(2)_L$  gauge invariance. An effective mass term arising perturbatively, e.g.  $\frac{Y_{ij}}{v} \phi \phi L_i L_j$ , would be a good candidate to explain the small size of neutrino masses due to suppression from the mass scale  $v$ , but turns out to be forbidden as well due to the accidental conservation of lepton number,  $L$ , and also baryon minus lepton number,  $B - L$  [7].

A leading candidate to explain the small but nonzero neutrino masses is the *neutrino seesaw mechanism* [gellmann, ramond, yanagida, 7]. Heavy, sterile neutrinos,  $N_i$ , are added to the Standard Model, with both a Majorana mass and Yukawa interactions with the Standard Model neutrinos:

$$\mathcal{L}_N = \frac{1}{2} M_{N_{ij}} \overline{N_i^c} N_j + Y_{ij}^\nu \overline{L_i} \tilde{\phi} N_j + \text{h.c.} \quad (2.45)$$

The resulting mass matrix takes the form:

$$M_\nu = \begin{pmatrix} 0 & Y^\nu \frac{v}{\sqrt{2}} \\ (Y^\nu)^T \frac{v}{\sqrt{2}} & M_N \end{pmatrix} \quad (2.46)$$

in the basis  $\begin{pmatrix} \nu_{L_i} \\ N_j \end{pmatrix}$ . If  $M_N \gg v$ , then diagonalizing the mass matrix gives three eigenstates will light masses,  $m_{\nu_{L_i}} \sim \frac{Yv^2}{M_N}$ . With  $v = 246$  GeV, a light neutrino mass of  $m_\nu = 0.1$  eV gives a heavy neutrino mass of:

$$M_N \sim Y \times 10^{15} \text{ GeV.} \quad (2.47)$$

Hence Yukawa couplings of order 1 predict heavy, sterile neutrinos around the GUT scale, while smaller couplings predict a proportionally smaller mass scale. New mass scales accessible at the LHC can be achieved with more complicated models, such as the inverse seesaw model [inverse seesaw], which introduce more mass scales and high powers of the suppression factors.

At tree level, there are three possible implementations of the seesaw mechanism:

- **Type I:** The simplest realization of the seesaw mechanism, at least two sterile neutrinos  $N_i$  are introduced as described above. This scenario is not likely to be testable at the LHC, due to the combination of small Yukawa couplings and large sterile neutrino masses required for  $\mathcal{O}(0.1)$  eV neutrino masses.

- **Type II:** The seesaw mechanism is generated by an  $SU(2)_L$  triplet of scalars,  $\Delta$ , with hypercharge  $Y = 2$ . This allows the construction of the following Yukawa term:

$$-\mathcal{L} = Y_{ij}^\Delta L_{L_i}^T C \sigma_2 \Delta L_{L_j} + \text{h.c.}, \quad (2.48)$$

where  $i$  ranges over the three lepton flavors. Assuming diagonal Yukawa couplings for simplicity, the neutral component of the triplet,  $\Delta^0$ , acquires a vacuum expectation value,

$$v_\Delta = \frac{\mu v^2}{\sqrt{2}m_\Delta^2}, \quad (2.49)$$

where  $m_\Delta$  is the mass term for  $\Delta$ ,  $\mu \sim m_\Delta$  is a coefficient of the cubic Higgs- $\Delta$  interaction with mass dimension 1, and  $v$  is the Standard Model Higgs vacuum expectation value. The light neutrinos acquire mass:

$$m_{\nu_{L_i}} \sim Y_i^\Delta v_\Delta = Y_i^\Delta \frac{\mu v^2}{\sqrt{2}m_\Delta^2}. \quad (2.50)$$

The triplet of scalars can potentially be produced via gauge interactions at the LHC, if their masses are below the TeV scale. The new particle content consists of  $\Delta^0$ ,  $\Delta^\pm$ , and  $\Delta^{\pm\pm}$ . In particular, the decay  $\Delta^{\pm\pm} \rightarrow l_i^\pm l_j^\pm$  gives a unique same-sign dilepton signature which is rarely produced in Standard Model processes; additionally, pair production of scalars can give three or more leptons in the final state.

- **Type III:** The seesaw mechanism is generated by at least two  $SU(2)_L$  triplets of fermions with hypercharge  $Y = 0$ ,

$$\Sigma = \Sigma^a \sigma^a = \begin{pmatrix} \Sigma^0/\sqrt{2} & \Sigma^+ \\ \Sigma^- & -\Sigma^0/\sqrt{2} \end{pmatrix}. \quad (2.51)$$

The Lagrangian is:

$$\mathcal{L}_\Sigma = Tr[i\bar{\Sigma}\not{D}\Sigma] - \frac{1}{2}Tr[\bar{\Sigma}M_\Sigma\Sigma^c + \bar{\Sigma}^c M_\Sigma^*\Sigma] - \tilde{\phi}^\dagger \bar{\Sigma} \sqrt{2}Y_\Sigma L - \bar{L} \sqrt{s}Y_\Sigma^\dagger \Sigma \tilde{\phi}, \quad (2.52)$$

where  $L = (\nu, l)^T$ ,  $\phi = (\phi^+, \phi^0)^T$ ,  $\tilde{\phi} = i\sigma_2\phi^*$ , and  $\Sigma^c = C\bar{\Sigma}^T$ . Summation over lepton flavor is implicit. The neutral fermion  $\Sigma^0$  generates the seesaw mechanism in much the same way as in the type I implementation, giving neutrino masses:

$$m_\nu = -v^2 Y_\Sigma^T \cdot M_\Sigma^{-1} \cdot Y_\Sigma \quad (2.53)$$

The heavy fermion triplet is also potentially producable at the LHC via gauge interactions. The specific phenomenology considered for the analysis described in section 8 is described below in section ??.

# Bibliography

- [1] B. Cleveland et al.,  
*Measurement of the solar electron neutrino flux with the Homestake chlorine detector*,  
*Astrophys.J.* **496** (1998) pp. 505–526.
- [2] K. Olive et al., *Review of Particle Physics*, *Chin.Phys.* **C38** (2014) p. 090001.
- [3] V. C. Rubin, W. K. Ford, and N. . Thonnard,  
*Rotational properties of 21 SC galaxies with a large range of luminosities and radii, from NGC 4605 /R = 4kpc/ to UGC 2885 /R = 122 kpc/*,  
*The Astrophysical Journal* **238** (June 1980) pp. 471–487.
- [4] C. A. Baker et al.,  
*Improved Experimental Limit on the Electric Dipole Moment of the Neutron*,  
*Phys. Rev. Lett.* **97** (13 Sept. 2006) p. 131801,  
URL: <http://link.aps.org/doi/10.1103/PhysRevLett.97.131801>.
- [5] R. Haag, J. T. Lopuszanski, and M. Sohnius,  
*All possible generators of supersymmetries of the S-matrix*,  
*Nuclear Physics B* **88.2** (1975) pp. 257–274, ISSN: 0550-3213,  
URL: <http://www.sciencedirect.com/science/article/pii/0550321375902795>.
- [6] J. Wess and B. Zumino, *Supergauge transformations in four dimensions*,  
*Nuclear Physics B* **70.1** (1974) pp. 39–50, ISSN: 0550-3213,  
URL: <http://www.sciencedirect.com/science/article/pii/0550321374903551>.
- [7] M. C. Gonzalez-Garcia and Y. Nir,  
*Neutrino masses and mixing: evidence and implications*,  
*Rev. Mod. Phys.* **75** (2 Mar. 2003) pp. 345–402,  
URL: <http://link.aps.org/doi/10.1103/RevModPhys.75.345>.

# Chapter 3

## The Experimental Apparatus

### 3.1 The Large Hadron Collider

The Large Hadron Collider (LHC) is a particle accelerator designed to explore the physics of particles at the energy scale of electroweak symmetry breaking. The accelerator occupies a 26.7 km tunnel beneath the Switzerland-France border near Geneva, which previously housed the Large Electron Positron Collider (LEP). Protons are accelerated in two counter-rotating beams up to a design momentum of  $7 \text{ TeV}/c$ . The beams collide at four interaction points (IPs), shown in figure 3.1, where four collider detectors, ATLAS, CMS, LHCb, and ALICE, analyze the remnants of the collisions.



Figure 3.1: The LHC and the four interaction points where the beams are brought into collision. The ATLAS experiment is located at interaction point 1.

The LHC project was approved in 1994 by the CERN Council, and construction proceeded over the ensuing 14 years [1]. The collider detectors were constructed in parallel, beginning with the excavation of two additional caverns at IP1 and IP5 for the ATLAS and CMS detectors (LHCb and ALICE occupied the existing caverns at IP2 and IP8, which

previously housed the DELPHI and L3 LEP experiments). The first beam was circulated on 10 September 2008; however, on 19 September, the LHC sustained severe damage due to an incident stemming from a faulty joint between magnets<sup>1</sup>. Repairs took an extra year, and the energy of the beams was reduced to 3.5-4 TeV for the first data-taking run, to mitigate the risk of another possible faulty joint.

Proton-proton collisions at a center-of-mass energy of  $\sqrt{s} = 7 \text{ TeV}$  commenced in early 2010. The LHC delivered an integrated luminosity of  $\int \mathcal{L} dt = 48.1 \text{ pb}^{-1}$  to the ATLAS detector in 2010, and  $\int \mathcal{L} dt = 5.46 \text{ fb}^{-1}$  in 2011. In 2012, the collision energy was increased to  $\sqrt{s} = 8 \text{ TeV}$ , and a dataset of  $\int \mathcal{L} dt = 22.8 \text{ fb}^{-1}$  was delivered.

### 3.1.1 Accelerator Components

The primary devices used for acceleration are synchrotrons, circular accelerators comprised of magnets and radio frequency (RF) cavities [3]. The magnets are used to manipulate the particle beams: dipole magnets bend the beams in a circle and steer the beams down transfer lines between the accelerators, while quadrupole and higher moment magnets focus the beams. RF cavities are hollow metallic structures used for particle acceleration. The RF cavities are driven by klystrons, radio frequency amplifiers that act as power sources, at their resonant frequency, creating an oscillating electric field inside the structure. The frequency of the RF cavities is matched to the rotation frequency of the particle beams.

The RF oscillations cause the particle beam to bunch longitudinally into so-called RF buckets, shown schematically in figure 3.2. The center of the bucket corresponds to particles with the reference energy, determined by the magnets, which arrive in phase with the RF oscillations so that they experience no force. During *flat-top* operation, where the particle are held at fixed energy in the synchrotron, particles at the center of the RF bucket remain stationary at that point (neglecting energy losses due to synchrotron radiation), while nearby particles oscillate around the fixed point. During a *ramp*, where particles are accelerated, the magnetic fields of the dipoles are slowly increased, shifting the RF bucket and causing the particle bunches to fall on the accelerating edge of the electric field oscillations.

---

<sup>1</sup>A postmortem analysis implicated a bad splice between the superconducting cables of adjacent magnets as the source of the incident, with a resistance about  $10^3$  times above specification. The joint melted, and 275 MJ of energy in the magnets dissipated in electric arcs, which vaporized beam pipes and breached the cryogenic vessel containing the magnets. A large amount of liquid helium entered the vacuum vessel and heated rapidly, breaking several vacuum barriers of the cryostats with a force of up to 56 tons. Ultimately, 30 dipoles and 7 quadrupoles were damaged beyond repair, and another 9 dipoles and 7 quadrupoles required repairs; 9 magnet interconnections were destroyed; 26 magnets were pushed down the tunnel; 276 MJ of energy were dissipated in electrical faults and arcs; 6 tons of helium were lost; and 2.8km of both beam pipes were contaminated with fragments of insulation, with 1km also contaminated with soot from molten copper and insulation. [2]

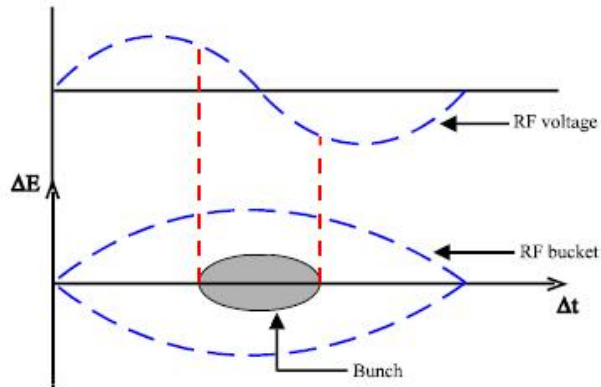


Figure 3.2: Schematic picture of an RF bucket.

### 3.1.2 The Accelerator Complex

#### Injection Chain

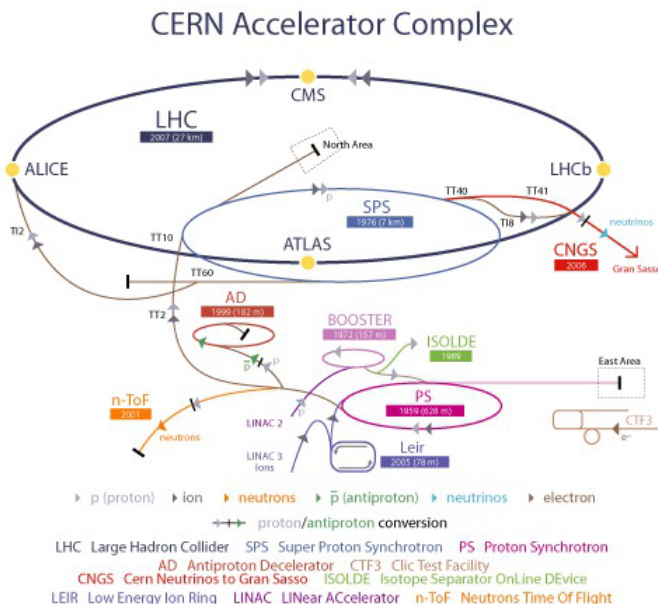


Figure 3.3: The LHC accelerator complex. The proton injection chain begins at LINAC2, proceeding through the booster, PS, and SPS before reaching the LHC. The facility also provides ions to the LHC, as well as a variety of particles to other experiments.

The LHC itself is the last stage of a chain of lower-energy accelerators, shown in figure 3.3 [4]. The staged acceleration chain preserves the high-quality of the beam over many decades of energy. It consists of a linear accelerator and three synchrotrons which were used for previous generations of experiments at CERN. The reuse of the older accelerators is eco-

nomical while still meeting the stringent performance requirements of the LHC, providing up to 2808 proton bunches with a very small transverse emittance and controllable longitudinal emittance.

Protons are produced from hydrogen gas using a duoplasmatron source, which strips electrons from protons in a high electric field. After passing through a 90 kV pre-injector, a radio frequency quadrupole (RFQ) focuses and accelerates the protons to 750 kV. A linear accelerator (LINAC2) then accelerates the protons to 50 MeV using RF cavities. The protons then pass through an 80 m-long transfer line into the the Proton Synchrotron Booster (PSB) and Proton Synchrotron (PS).

The PSB consists of four stacked circular synchrotrons, 157 m in circumference, and accelerates the protons to 1.4 GeV. The use of four separate rings mitigates the space charge effects caused by the repulsion of protons within a bunch, which scale as  $N_b/(\beta\gamma^2)$ , where  $N_b$  is the number of protons per bunch. The protons are then injected into single-ring PS, where the higher injection energy reduces the space charge effect. The RF cavities of the PS, operating at several frequencies, accelerate the beams to 26 GeV, and also split the protons into the bunches eventually inject into the LHC. Nominally, this yields 72 bunches separated by 25 ns, but for Run I, 50 ns spacing was used instead.

The protons are extracted from the PS at intervals of 3.6 s and injected into the third synchrotron in the chain, the 7 km-circumference Super Proton Synchrotron (SPS). Immediately prior to extraction, the bunches are rotated by increasing the RF voltage, reducing the longitudinal emittance in order to ease capture in the SPS RF buckets, which have a frequency of 200 MHz. Up to four PS batches are injected per SPS cycle, after which the particle are accelerated at an average of 78 GeV/s to the LHC injection energy of 450 GeV. Flat-top is maintained for about one second, during which the injection is prepared:

- The magnets used for the beam extraction are ramped, safety checks are performed, and the SPS phase is tuned to match that of the LHC.
- The bunch length is compressed using an RF voltage increase, as in the PS-SPS transfer.
- The tails of the bunches are removed, down to  $3-3.5\sigma$ .

The SPS cycle takes 21.6 seconds, leading to a total LHC filling time of about nine minutes.

## LHC Main Ring

The LHC main ring accelerates protons from the injection energy of 450 GeV to the collision energy, which ranged from 3.5 TeV to 4 TeV for proton-proton collisions during Run I [5]. The 26.7 km ring consists of eight arcs and eight straight sections, shown in figure 3.4. Each straight section is called an *insertion region* (IR), and contain either collider experiments or important services. IRs 1, 2, 5, and 8 contain the ATLAS, LHCb, CMS, and ALICE

experiments, respectively; IR 4 contains two independent 400 MHz RF systems, one for each of the counter-rotating beams; IR 6 contains the beam dump system; and IRs 3 and 7 contain collimation systems. The beams are contained in separate beam pipes except at the collision points.



Figure 3.4: Layout of the LHC. The ring consists of eight arcs and eight long straight sections (LSS). Each junction between an arc and a LSS contains a dispersion suppressor cell (DSL, DSR). TI2 and TI8 are the two injection tunnels (“tunnel d’injection”) leading from the SPS to the LHC.

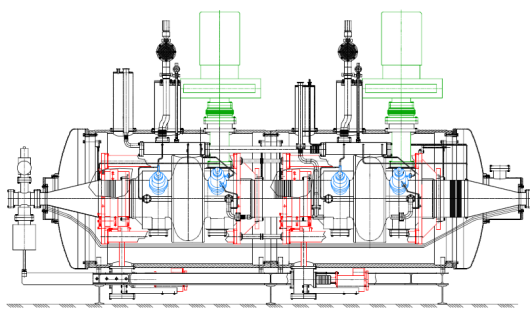
The beams are controlled by over 7,000 magnets. The primary bending and focusing are performed by 1232 superconducting dipole and 392 superconducting quadrupole magnets. The dipole magnets, shown in figure 3.5, have a nominal maximum field of 8.33 T and a length of 15 m. The conducting coils are constructed from Nb-Ti Rutherford cables, and are cooled to 1.9 K using superfluid helium. The dipoles have a double-bore structure, so that a single magnet provides the bending field for both beams.

The acceleration is provided by two superconducting RF systems, one for each beam. The RF cavities are constructed from copper with a thin (1  $\mu\text{m}$ -2  $\mu\text{m}$ ) layer of niobium, and operate at 4.5 K. The single-cell cavities, each nominally providing 2 MV, are arranged into cryomodules containing eight cells, for a total peak voltage of 16 MV. A module consisting of two cells is shown in figure 3.6. The RF frequency is 400 MHz, giving an RF bucket length of 2.5 ns, or 75 cm.

At the collision points, the two beams converge in a single pipe for approximately 130 m. A steering dipole directs the beams into collision, and a triplet of quadrupoles on each side



Figure 3.5: Two views of the LHC superconducting dipole magnet. The magnets are 15 m long and have two bores, one for each of the counter-rotating beams.



(a) A prototype cryomodule containing two cavities.



(b) The RF cryomodules installed at IR4.

Figure 3.6: The LHC RF cryomodules.

of the interaction region focus the beam onto the interaction point, squeezing the beams in the transverse directions from a typical orbiting width of  $\mathcal{O}(1\text{ mm})$  to a collision width of  $\mathcal{O}(10\text{ }\mu\text{m})$ .

### 3.1.3 Beam Parameters

From the experiments' point of view, there are two main parameters to optimize in order to maximize sensitivity to new physics: the collision energy,  $\sqrt{s}$ , and the integrated luminosity,  $L = \int \mathcal{L} dt$ . The collision energy is limited to  $\sqrt{s} = 14\text{ TeV}$  by the bending power of the dipole magnets, which have a nominal field strength of 8.33 T; however, due to the faulty splice design mentioned above, the energy was limited to  $\sqrt{s} = 7\text{--}8\text{ TeV}$  in Run I.

The optimization of the integrated luminosity is somewhat more complicated. The instantaneous luminosity of two colliding bunches is given by:

$$\mathcal{L} = \frac{f_r N_1 N_2 \gamma_b}{4\pi \epsilon_n \beta_*} F(\alpha), \quad (3.1)$$

where  $f_r = 11\,245.5\text{ Hz}$  is the LHC revolution frequency,  $N_{1,2}$  are the numbers of protons in the two beams,  $\gamma_b$  is the relativistic gamma factor,  $\epsilon_n$  is the normalized transverse emittance,  $\beta_*$  is the beta function at the collision point, and  $F(\alpha)$  is the reduction in luminosity due to a nonzero beam crossing half-angle of  $\alpha$ . The total instantaneous luminosity is given by the sum of all colliding bunch pairs.

In general, a higher total integrated luminosity is desired. This depends on a number of factors:

- The instantaneous luminosity per bunch,  $\mathcal{L} = \frac{f_r N_1 N_2}{4\pi \epsilon_n \beta_*}$ . A higher  $\mathcal{L}$  increases the number of simultaneous collisions per bunch crossing (*pileup*),  $\mu = L_b / \sigma_{\text{inel}}$ , which degrades the performance of the detectors.
- The number of bunches in the LHC,  $n_b$ . During Run I, the LHC was filled with 1380 bunches with 50 ns spacing between bunches, as opposed to the nominal 2808 bunches with 25 ns spacing. The advantages of 50 ns spacing include less days needed for electron-cloud scrubbing, smaller transverse emittances, and a smaller crossing angle [6]. The primary disadvantage is a higher pileup for the experiments.
- The crossing angle,  $\alpha$ . A nonzero crossing angle is required to prevent *parasitic collisions* between bunches away from the nominal collision point. For bunches spaced by 25 ns, there are 34 unwanted parasitic collision points inside the common beam pipe at each interaction region. The reduction in luminosity is:

$$F(\alpha) = \frac{1}{\sqrt{1 + \left(\frac{2\alpha\sigma_z}{2\sigma^*}\right)}}, \quad (3.2)$$

where  $\sigma_z$  is the RMS bunch length and  $\sigma^*$  is the transverse beam width at the collision point. During normal 2012 running conditions, the crossing half-angle was  $\alpha = 145 \mu\text{rad}$ , and the luminosity reduction factor was about 18%.

- The fill schedule of the LHC. The instantaneous luminosity of the LHC decreases over time. The dominant loss of luminosity is due to the loss of protons from the collisions themselves, with a typical decay constant of  $\tau_{\text{nuclear},1/e} = 29 \text{ h}$ . Including other sources of loss such as intra-bunch scattering, scattering from collisions with gas in the beam pipe, beam-beam effects, and RF noise, the typical luminosity lifetime is  $\tau_L = 14.9 \text{ h}$ .

The fill schedule can be optimized to maximize the luminosity based on  $\tau_L$  and the average turnaround time to refill the LHC after a beam dump,  $T_{\text{turnaround}}$ . This can be quantified using the *Hübner factor*,  $\text{HF}_{\text{peak}}$ , defined as the ratio of the delivered integrated luminosity to the hypothetical integrated luminosity with  $\tau_L = \infty$  and  $T_{\text{turnaround}} = 0$ . In 2011, this was typically in the range 15%–20%.

The delivered luminosity in 2011 and 2012 will be discussed later in chapter 4.

## 3.2 The ATLAS Experiment

The ATLAS detector [7] is a large, cylindrical collider detector located at IR1 on the LHC ring (figure 3.1). The detector measures the energy and momenta of particles produced in the collisions provided by the LHC. It consists of several subsystems occupying a cylinder with a diameter of 25 m and a length of 46 m, with a combined weight of approximately 7,000 tons. Closest to the interaction region, the inner detector measures the momenta of charged particles by tracking their movement through a solenoidal magnetic field. Outside the inner detector solenoid magnet, electromagnetic and hadronic calorimeters measure the energy of electrons, photons, and hadrons. Finally, the muon spectrometer provides additional tracking and particle identification for muons in large toroidal magnetic field.

This section describes the design of the magnets, inner detector, calorimeters, and muon spectrometer. The reconstruction of physics objects from the detector measurements is described in chapter 5.

### 3.2.1 Coordinate System

The ATLAS detector uses a right-handed coordinate system, with  $\hat{x}$  pointing from the interaction point towards the center of the LHC ring,  $\hat{y}$  pointing up, and  $\hat{z}$  pointing along the ring towards IR2. Due to the symmetry of the detector, cylindrical coordinates  $(r, \theta, \phi)$  are often used, with  $r$  the transverse distance from the beam line,  $\theta$  the polar angle from the beamline, and  $\phi$  the azimuthal angle in the  $x$ - $y$  plane. The polar angle can also be expressed in term of the pseudorapidity,  $\eta = -\log \tan \frac{\theta}{2}$ , which is useful for describing the geometry of particles in part because differences in pseudorapidity,  $\Delta\eta$ , are invariant under longitudinal

Lorentz boosts along  $\hat{z}$ . For massless particles, the pseudorapidity is equal to the rapidity,  $y = \frac{1}{2} \log \frac{E+p_z}{E-p_z}$ .

### 3.2.2 Magnets

ATLAS relies on four powerful superconducting magnets to bend the trajectories of charged particles, allowing the tracking detectors to provide measurements of their momenta. The solenoid provides a 2 T axial magnetic field in the volume of the inner detector, while the barrel and two endcap toroids provide a toroidal magnetic field ranging from 0.5–1 T for the muon spectrometer. The geometry of the magnets is shown in figure 3.7. Key parameters for the magnet system are shown in table 3.1.

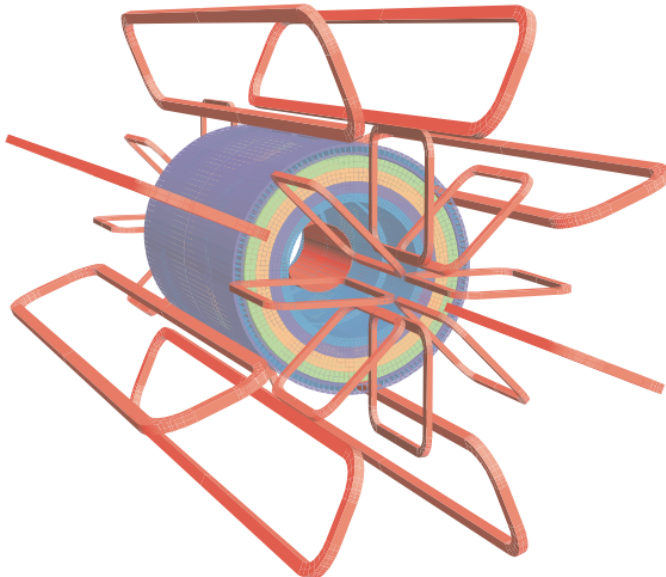


Figure 3.7: The geometry of the magnet windings and tile calorimeter steel. The three toroids and solenoid are shown in red. The remaining colors show layers of the tile calorimeter with different magnetic properties and an outside return yoke [8].

#### Solenoid

The central solenoid, shown in figure 3.8, occupies the volume between the inner detector and the electromagnetic calorimeter, with an inner radius of 2.46 m, an outer radius of 2.56 m, and a length of 5.8 m. The single coil has 1154 windings made of high strength Al-stabilized NbTi conductor. With a nominal current of 7.73 kA, the magnetic field is 1.998 T at the center of the solenoid, falling to 1.8 T at  $z = 1.7$  m and 0.9 T at the end of the inner detector cavity. The magnetic flux is returned via the steel in the hadronic calorimeter and its

Property	Feature	Unit	Solenoid	Barrel toroid	End-cap toroids
<b>Size</b>	Inner diameter	m	2.46	9.4	1.65
	Outer diameter	m	2.56	20.1	10.7
	Axial length	m	5.8	25.3	5.0
	Number of coils		1	8	$2 \times 8$
<b>Mass</b>	Conductor	t	3.8	118	$2 \times 20.5$
	Cold mass	t	5.4	370	$2 \times 140$
	Total assembly	t	5.7	830	$2 \times 239$
<b>Coils</b>	Turns per coil		1154	120	116
	Nominal current	kA	7.73	20.5	20.5
	Magnet stored energy	GJ	0.04	1.08	$2 \times 0.25$
	Peak field in the windings	T	2.6	3.9	4.1
	Field range in the bore	T	0.9-2.0	0.2-2.5	0.2-3.5

Table 3.1: Main parameters of the ATLAS magnet system [7].

support structures. Liquid helium is used to cool the superconducting coil to an operating temperature of 4.5 K. At nominal current, the stored energy is 40 MJ.

The longitudinal and radial magnetic field components are shown for different  $R$  and  $z$  values in figure 3.9a.



Figure 3.8: The central solenoid in the factory after completion of the coil winding [[atlas-photos](#) ].

## Toroid

The magnetic field for the muon spectrometer is provided by three large toroid magnets, each with eight superconducting coils. The magnets are shown in figure 3.10. The barrel toroid measures 25.3 m in length, with inner and outer diameters of 9.4 m and 20.1 m, respectively. The two end-cap toroids are 5.0 m in length, with inner and outer diameters of 1.65 m and 10.7 m, respectively. Both types of toroid contain eight coils, with 120 windings per coil

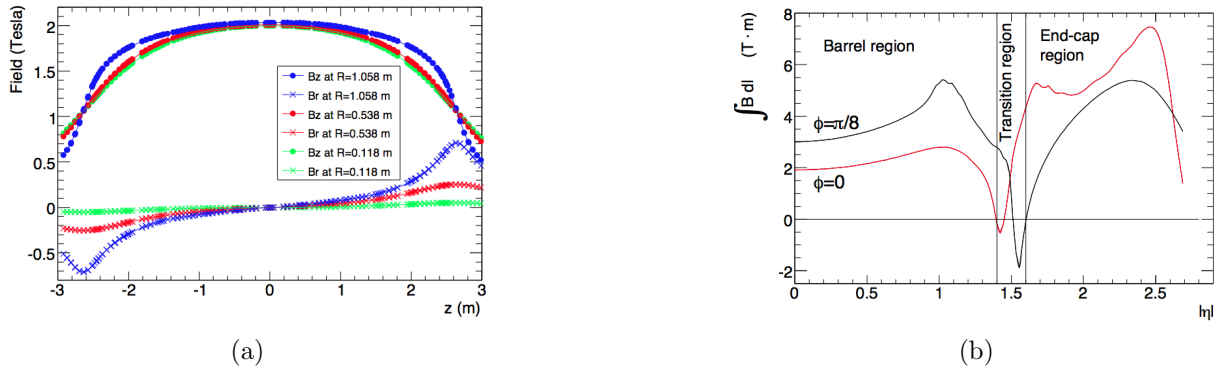
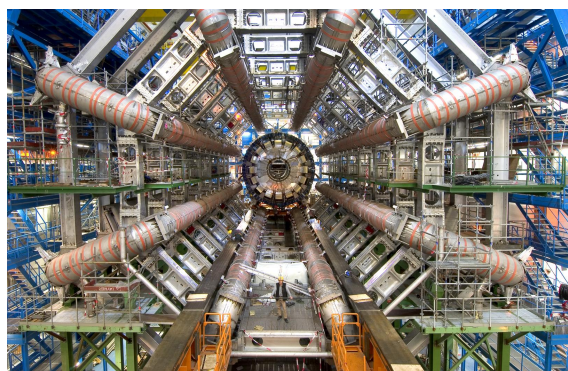


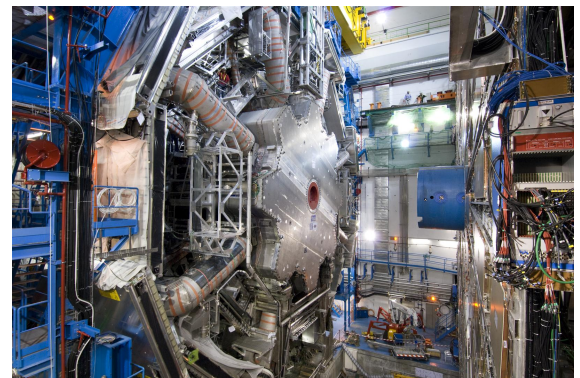
Figure 3.9: Left: the solenoid magnetic field in the radial ( $B_r$ ) and longitudinal ( $B_z$ ) directions, shown as a function of  $z$  for  $\phi = 20\pi/16$  at different values of  $R$ . The field determined from a fit of the field model to measurements using an array of Hall probes [9]. Right: The predicted toroid magnetic field integral as a function of  $|\eta|$ . The integral is taken over a straight line through the interaction point, from the innermost to the outermost muon detector (section 3.2.5).

in the barrel and 116 windings per coil in the end-caps. The end-cap coils are rotated by  $22.5^\circ$  from the barrel coils to optimize the bending power in the overlap region between the magnets. Like the solenoid, the conductor is Al-stabilized NbTi, operated at 4.5 K. The nominal current is 20.5 kA, producing a magnetic field that varies from 0.15 T to 2.5 T in the barrel region, and 0.2 T to 3.5 T in the end-caps. The total stored energy at nominal current is 1.58 GJ.

The field integral of the toroid is shown as a function of  $\eta$  in figure 3.9b. The field integral drops at the boundary between the barrel and end-caps, where the fields from the two magnets partially cancel.



(a) Barrel toroid.



(b) End-cap toroid, inserted into the barrel toroid.

Figure 3.10: Images of the barrel and end-cap toroid magnets during installation.

### 3.2.3 Inner Detector

The inner detector performs tracking of charged particles traversing the 2 T solenoidal magnetic field in the pseudorapidity range  $|\eta| < 2.5$ . It also performs electron identification in the range  $|\eta| < 2.0$ . It consists of three subdetectors occupying the volume closest to the interaction region, directly outside the beam pipe, as shown in figure 3.11. Proceeding outwards from the interaction point, these are the pixel detector, the semiconductor tracker (SCT), and the transition radiation tracker (TRT). The pixel detector provides three track measurements with high spatial resolution using silicon pixels. The SCT provides an additional four measurements using silicon strips. Finally, for particles with  $|\eta| < 2.0$ , the TRT provides an average of 36 measurements per track using gas-filled straw tubes, which aids the pattern recognition, improves the momentum resolution, and performs electron identification. Examples of trajectories of 10 GeV particles through the barrel and end-cap layers are shown in figure 3.12.



(a) 3D model of the inner detector, showing the arrangement of the pixel detector, SCT, and TRT in the barrel and end-caps.

(b) Layout of the inner detector in the  $R - z$  plane.

Figure 3.11: Layout of the ATLAS inner detector.

### Pixel Detector

The pixel detector consists of 1744 identical pixel sensors, each measuring  $19 \times 63\text{ mm}^2$  and containing  $144 \times 328 = 47232$  pixels, for a total of  $80.4 \times 10^6$  pixels. The size of the pixels is dictated by the front-end electronics: in 128 of the 144 columns, the pixels have a pitch of  $50 \times 400\text{ }\mu\text{m}^2$ , while the remaining 16 columns have a pitch of  $50 \times 600\text{ }\mu\text{m}^2$ . For space reasons, eight pairs of pixels in each column are ganged to a common readout, giving a total of 46080 readout channels per sensor.

The sensors are  $256\text{ }\mu\text{m}$ -thick detectors utilizing  $n$ -in- $n$  technology, constructed from  $n$ -type wafers with high dose positive ( $p^+$ ) and negative ( $n^+$ ) dose regions implanted on each side of a wafer. Initially, the asymmetric depletion region at the  $p^+ - n$  junction is operated



- (a) Trajectory of a 10 GeV charged particle with  $\eta = 0.3$  traversing the barrel elements of the inner detector.
- (b) Trajectories of 10 GeV charged particles with  $\eta = 1.4$  and  $\eta = 2.2$  traversing the barrel and end-cap elements of the inner detector.

Figure 3.12: Drawings of the inner detector sensors and structural elements traversed by 10 GeV charged particles originating from the interaction point at various angles.

in reverse bias with a voltage of 150 V, and fills the sensor bulk volume, shown in figure 3.13a. The charge carriers generated by the passage of an ionizing particle through the bulk are collected at the  $n^+$  side of the sensor, where the readout electronics are bump-bonded to the pixel. The nominal threshold for readout is about 3,500 electrons, while a minimally ionizing particle crossing a pixel at normal incidence produces a signal of about 20,000 electrons. Over time, radiation damage induces type inversion in the bulk, after which the junction moves to the  $n^+$  side of the sensor and the depletion zone grows from the pixel side, as shown in figure 3.13b. The double-sided construction thus allows the pixel sensors to continue operating after type inversion.

The pixel sensors are assembled into pixel modules, shown in figure 3.14. Each module contains 16 front-end electronics chips each with 2880 electronics channels. The front-ends are bump bonded to the pixel sensor elements. The other side of the pixel sensor tile is glued to a flexible polyimide printed circuit board (*flex-hybrid*) that houses the module control chip.

The layout of the pixel detector is summarized in table 3.2. The modules are assembled into staves in the barrel region, each with 13 pixel modules, and sectors in the end-caps, each with 6 pixel modules. The barrel layers consist of 22, 38, and 52 staves for layers 0, 1, and 2, respectively, while the end-caps each contain eight sectors<sup>2</sup>. In the barrel, to provide complete coverage, the pixel staves overlap and are mounted with a tilt angle of 20° between

<sup>2</sup>During the shutdown following Run I, a fourth layer of barrel pixel detectors, known as the insertable B-layer (IBL), was added between the beam pipe and the innermost pixel layer. The data used in this dissertation predate the inclusion of the IBL.



Figure 3.13: Comparison of depletion zones in  $n^+$ -in- $n$  pixel sensors before and after type inversion. Before type inversion, the electrical field grows from the bottom side, reaching the pixel implants at full depletion. After type inversion, the depletion zone grows from the pixel side, allowing operation even if the bulk is not fully depleted.

the normal to the module surface and  $\hat{r}$ , in the  $\hat{\phi}$  direction.

In the barrel, the pixels have an intrinsic accuracy of  $10\text{ }\mu\text{m}$  in the  $R - \phi$  direction and  $115\text{ }\mu\text{m}$  in the  $z$  direction, while in the end-caps, the intrinsic accuracy is  $10\text{ }\mu\text{m}$  in the  $R - \phi$  direction and  $115\text{ }\mu\text{m}$  in the  $R$  direction.

Barrel	Radius (mm)	Staves	Modules	Pixels
Layer-0	50.5	22	286	$13.2 \times 10^6$
Layer-1	88.5	38	494	$22.8 \times 10^6$
Layer-2	112.5	52	676	$31.2 \times 10^6$
End-cap (one side)	$z$ (mm)	Sectors	Modules	Pixels
Disk 1	495	8	48	$2.2 \times 10^6$
Disk 2	495	8	48	$2.2 \times 10^6$
Disk 3	495	8	48	$2.2 \times 10^6$
Barrel and both end-caps			1744	$80.4 \times 10^6$

Table 3.2: Parameters of the pixel detector, from [7].

## SCT

The SCT consists of 15912 sensors using single-sided,  $p$ -in- $n$  type silicon strips. The use of single-sided strips lowers both the cost and the number of readout channels of the detector, which covers significantly more area than the pixel detector ( $61.1\text{ m}^2$  versus  $2.3\text{ m}^2$ ). In the barrel, the strips have a pitch of  $80\text{ }\mu\text{m}$  and a length of 12 cm. In the endcaps, the sensors are trapezoidal with radially arranged strips, with a mean strip pitch of  $80\text{ }\mu\text{m}$  and a length of 12 cm. Each sensor has 768 active strips. Like the pixel sensors, the operating voltage is



Figure 3.14: Schematic pictures of a barrel pixel module. The top diagram shows the assembly of a module, consisting of the front-end electronics chips (FEs), the pixel sensor elements, and the flex-hybrid, which bears the module control chip (MCC) and NTC thermistors. The bottom is a photograph of a barrel pixel module.

initially  $\sim 150$  V, but will require an increase to 250 V-350 V after several years of irradiation, depending on the location of the sensor.

The SCT modules are shown in figure 3.15. The 2112 barrel modules contain four sensors, while the 1976 end-cap modules contain two sensors. In both cases, the sensors are glued to a 380  $\mu\text{m}$ -thick thermal pyrolytic graphite (TPG) base-board. The sensors are assembled in two layers with a rotation of  $\pm 20$  mrad about the center of the sensors. The stereo angle between the two sensors allows for a measurement of the position along the length of the sensors.

The intrinsic accuracy of the SCT sensors is 17  $\mu\text{m}$  along the strip pitch, corresponding to the  $R - \phi$  direction. Along the length of the strips, the stereo angle allows for position measurement with an accuracy of 580  $\mu\text{m}$ , corresponding to the  $z$  direction in the barrel and the  $R$  direction in the end-caps.

Barrel layer	Radius (mm)	Length (mm)	Module tilt angle	Number of modules
3	299	1498	11.00°	384
4	371		11.00°	480
5	443		11.25°	576
6	514		11.25°	672

Table 3.3: The dimensions and arrangement of modules in the four SCT layers. The tilt angle is between the normal to the module surface and  $\hat{r}$ , in the  $\hat{\phi}$  direction.



Figure 3.15: Diagrams of the SCT barrel (left) and end-cap (right) modules.

## TRT

The TRT detector elements are polyimide drift (straw) tubes. The straws are arranged such that charged particles with  $p_T > 500 \text{ MeV}$  and  $|\eta| < 2.0$  traverse at least 36 straws, except in the barrel/end-cap transition region where particles traverse as few as 22 straws. The straws are interleaved with polypropylene fibers in the barrel and polypropylene foils in the end-caps to provide transition radiation; electrons with  $p_T > 2.0 \text{ GeV}$  typically leave 7-10 high-threshold hits. The intrinsic resolution of the straws is  $130 \mu\text{m}$  in the transverse direction.

The straws measure 4 mm in diameter and 144 cm (37 cm) in length in the barrel (end-caps). The straw walls consist of two  $35 \mu\text{m}$  aluminum-coated polyamide films bonded back-to-back. The anodes of the detectors are gold-plated tungsten wires running down the axis of the tubes, with  $31 \mu\text{m}$  diameter. The wires are supported at the end of the straw by an end plug, where they connect to the front-end electronics. At the middle of the straw, the wires are supported by a plastic insert, and are also split electrically by a fused glass capillary to reduce occupancy. The active length of each half of the wire is 71.2 cm, with a 2 cm inefficient section at the middle. The straws are filled with a mixture of 70% Xe, 27% CO<sub>2</sub>, and 3% O<sub>2</sub>. With a cathode voltage of  $-1530 \text{ V}$ , the gain in the straws is  $2.5 \times 10^4$ .

The layout of the straws in the barrel and end-caps is summarized in table 3.4. In the barrel, the straws are arranged into three layers of modules as shown in figure 3.16, with different dimensions and straw counts depending on the layer. The straws are interleaved with transition radiation material, polypropylene fibers measuring 19  $\mu\text{m}$  in diameter. The

module shell is made from 400  $\mu\text{m}$  thick carbon fiber, and serve not only as a support structure, but also as a gas manifold for CO<sub>2</sub>, which prevents high-voltage discharges, flushes any Xe leaking from the straws, and conducts heat away from the straws.

The endcaps consist of 160 layers of 768 straws, arranged radially into 20 wheels with 8 layers each. The inner 12 wheels (type-A) are spaced 8 mm in  $z$ , while the outer 8 wheels (type-B) are spaced by 15 mm. Each successive layer in a wheel is separated by a 15  $\mu\text{m}$  thick polypropylene radiator foil, and is rotated by 3/8 of the azimuthal straw spacing to optimize the uniformity of the number of straw crossed.

	$z$ (mm)	$R$ (mm)	Modules	Layers	Straws/Module
<b>Barrel (both sides)</b>	<b>0-780</b>	<b>554-1082</b>	<b>96</b>	<b>73</b>	<b>52544</b>
Type-1 module (inner)	400-712.1	563-624	32	9	329
Type-1 module (outer)	7.5-712.1	625-694	32	10	329
Type-2 module	7.5-712.1	697-860	32	24	520
Type-3 module	7.5-712.1	863-1066	32	30	793
<b>End-cap (one side)</b>	<b>827-2744</b>	<b>615-1106</b>	<b>20</b>	<b>160</b>	<b>122880</b>
Type-A wheels	848-1705	644-1004	12	8	6144
Type-B wheels	1740-2710	644-1004	8	8	6144

Table 3.4: Layout and straw counts of the TRT barrel modules and end-cap wheels. The totals for the barrel and end-caps, shown in bold, include services and electronics.

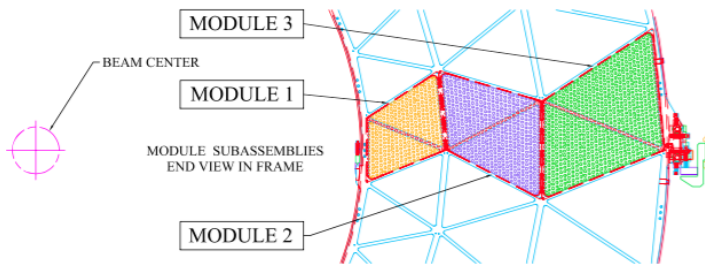


Figure 3.16: Layout of the TRT barrel modules in the  $R$ - $\phi$  plane.

### 3.2.4 Calorimetry

The calorimeter system occupies the volume directly exterior to the solenoid magnet, and measures the energy of electrons, photon, and hadrons up to a pseudorapidity of  $|\eta| = 4.9$ . The arrangement of the calorimeters is shown in figure 3.17. The system consists of a number of independent sampling calorimeters. The electromagnetic calorimeter measures the energy of electrons and photons using lead and liquid argon (LAr) to measure the energy of electrons and photons. The hadronic calorimeter measures the energy of hadrons using steel and

scintillator tiles in the barrel and copper and LAr in the end-caps. Finally, electromagnetic and hadronic calorimetry is performed in the forward region using copper-LAr and tungsten-LAr technology. Besides performing energy measurements, the calorimeters stop electrons, photons, and hadrons, providing shielding for the muon spectrometer. The total amount of material in front of and in the calorimeters is shown in terms of radiation lengths,  $X_0$ , and interaction lengths,  $\lambda$ , in figures 3.18 and 3.19.

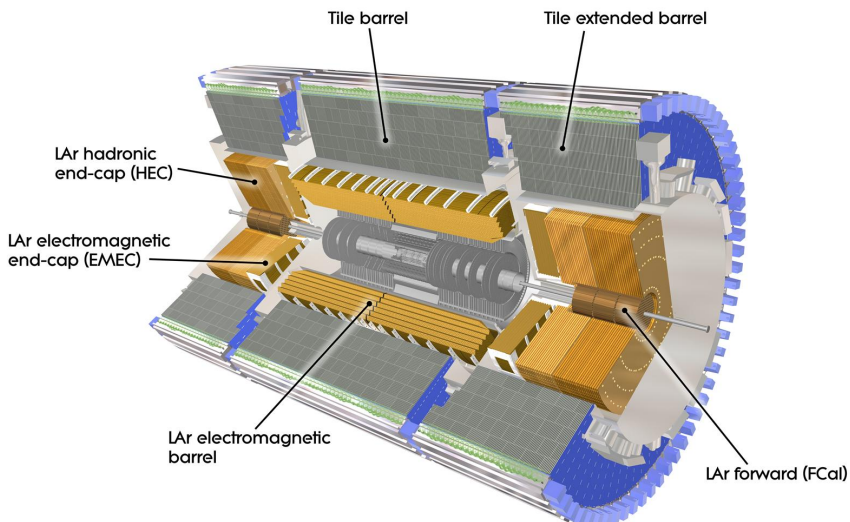


Figure 3.17: A 3D model of the ATLAS calorimeters, showing the electromagnetic barrel and end-caps, hadronic barrel and end-caps, and the forward calorimeter.

### Electromagnetic Calorimeter

The electromagnetic calorimeter consists of two half-barrels ( $0 < \eta < \pm 1.475$ ), two end-caps ( $\pm 1.375 < \eta < \pm 3.2$ ), and a presampler ( $|\eta| < 1.8$ ). The half-barrels and end-caps use LAr as the active material and steel-clad lead plates as the absorber. The lead plates are arranged in an accordion geometry to provide a uniform, gapless coverage in  $\phi$ , shown for a barrel module in figure 3.20. The plates are interleaved with electrodes built from copper etchings on polyimide, consisting of three conducting layers. The outer conductive layers of the electrodes distribute the 2 000 V high voltage over the electrode surface, which drifts the charges induced by ionization in the LAr towards the electrodes with a drift time of 450 ns. The inner layer of the electrode, separated from the outer layers by isolating foils, collects the signals via capacitive coupling.

The two half-barrels occupy the region  $2.8 \text{ m} < R < 4 \text{ m}$  and  $0 \text{ m} < z < \pm 3.2 \text{ m}$ , which covers up to  $|\eta| < 1.52$  depending on the layer. Each half-barrel has 1024 lead plates with a thickness of 1.53 mm for  $|\eta| < 0.8$  and 1.13 mm for  $|\eta| > 0.8$ . The cells are divided into three layers, and have variable size in  $\eta$  and  $\phi$ :

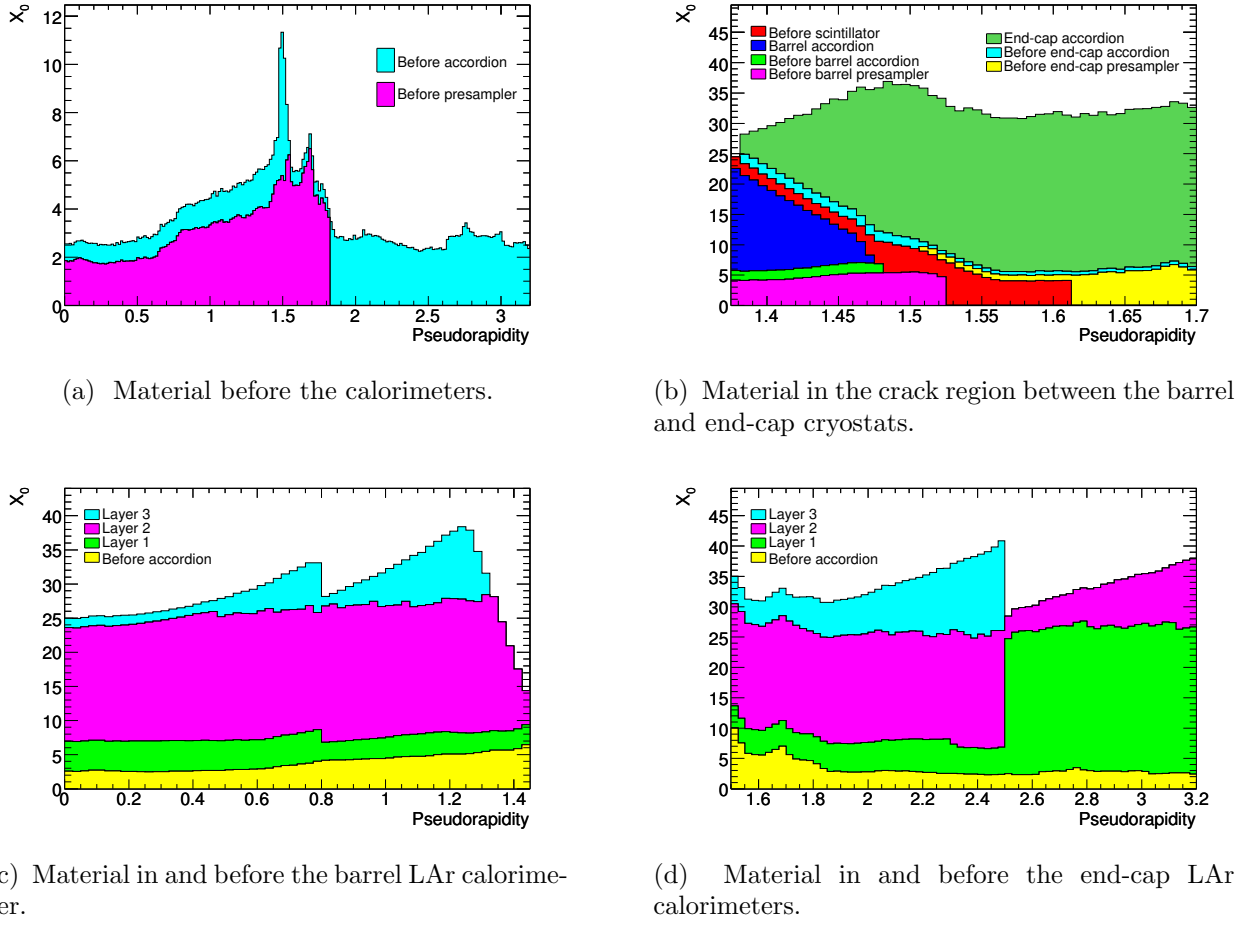


Figure 3.18: Cumulative amounts of material versus  $|\eta|$  in front of and within the LAr electromagnetic calorimeter, in terms of radiation lengths,  $X_0$ .

- The first layer is finely segmented in  $\eta$  to improve the spatial resolution; this improves the particle identification, helps resolve nearby particles (in particular photon pairs from  $\pi^0$  decays), and, in combination with the second layer, allows for a measurement of particle trajectories. The majority of the cells measure  $\Delta\eta \times \Delta\phi = 0.025/8 \times 0.1$ . Cells in the barrel-end-cap overlap region,  $1.40 < |\eta| < 1.475$ , have a coarser granularity of  $\Delta\eta \times \Delta\phi = 0.025 \times 0.025$ .
- The second layer absorbs most of the energy of the electromagnetic showers. Most of the cells have size  $\Delta\eta \times \Delta\phi = 0.025 \times 0.025$ , except for cells with  $1.40 < |\eta| < 1.475$ , which measure  $\Delta\eta \times \Delta\phi = 0.075 \times 0.025$ .
- The third layer absorbs the tails of electromagnetic showers, and has a coarse granularity of  $\Delta\eta \times \Delta\phi = 0.050 \times 0.025$ .

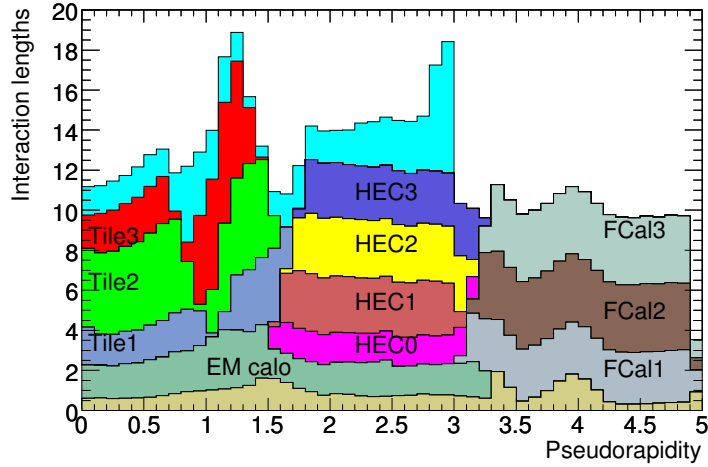


Figure 3.19: Cumulative amounts of material versus  $|\eta|$  due to each calorimeter in terms of interaction lengths,  $\lambda$ . The material in front of the calorimeters is also shown in tan.

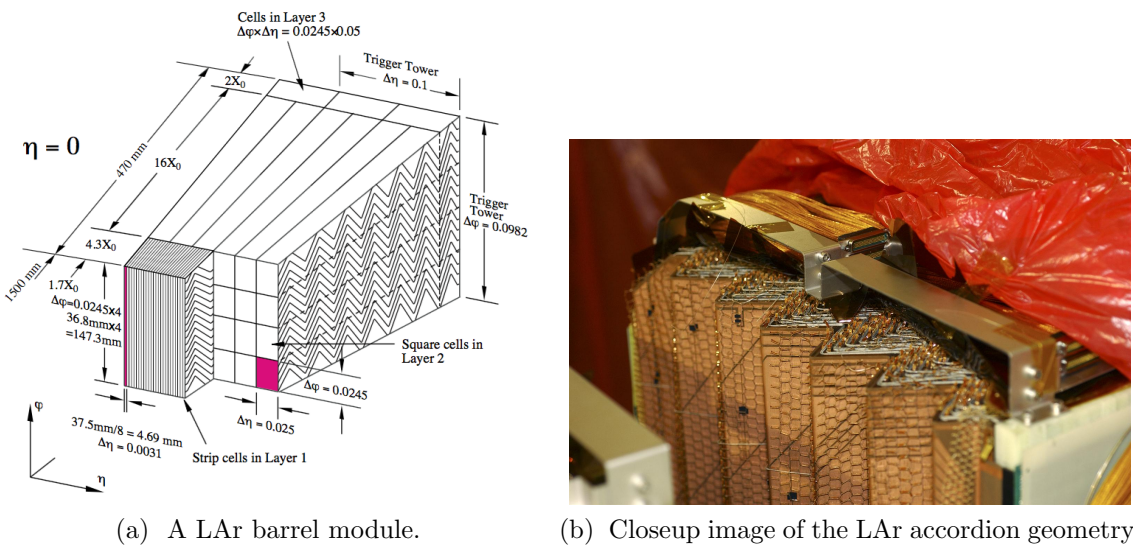


Figure 3.20: The LAr calorimeter uses an accordion geometry to provide uniform coverage in  $\phi$ . Steel-clad lead plates are interleaved with electrodes, consisting of three copper layers separated by polyamide sheets. The barrel module is divided into three layers in depth, with fine segmentation in  $\eta$  in the layer closest the interaction point.

The end-caps, one on either side of the interaction region, measure 63 cm in thickness with inner and outer radii of 33 cm and 209.8 cm, respectively. Each end-cap consists of 1024 lead absorbers with the same accordion geometry as used in the barrel. In the region  $1.5 < |\eta| < 2.5$ , the end-caps present three layers in the longitudinal direction, with fine  $\eta$  segmentation in the front layer. At  $|\eta| = 1.5$ , the granularity of each layer is the same as in the barrel, becoming coarser in the first layer with increasing  $|\eta|$ . Elsewhere, there are two longitudinal layers with coarser transverse granularity.

Finally, the presampler is an instrumented layer of LAr installed in front of the first layer calorimeter, with a thickness of 11 mm in the barrel ( $|\eta| < 1.5$ ) and  $2 \times 2$  mm in the end-caps ( $1.5 < |\eta| < 1.8$ ). The presampler measures the energy lost due to interactions with material between the interaction region and the calorimeters (the beam pipe, inner detector, solenoid, cryostates, and other services and support structures). The total amount of material before and in the electromagnetic calorimeters is shown in figure 3.18 in terms of radiation lengths,  $X_0$ . The cells have a granularity of  $\Delta\eta \times \Delta\phi = 0.025 \times 0.1$ .

In total, the electromagnetic calorimeter has 101,760 readout channels for the barrel, 62,208 channels for the end-caps, 7,808 channels for the barrel presampler, and 1,536 channels for the end-cap presamplers.

## Tile Calorimeter

The tile calorimeter performs hadronic calorimetry in the region  $|\eta| < 1.7$ , occupying the radial range  $2.28 \text{ m} < R < 4.25 \text{ m}$ . Divided into a 5.8 m-long central barrel and two 2.6 m-long extended barrels on either side, it uses steel as the absorber and scintillating tiles as the active material. The total depth is approximately  $7.4\lambda$ .

Each of the three calorimeter sections is divided azimuthally into 64 modules, each spanning  $\Delta\phi = 5.625$ . A module is shown schematically in figure 3.21a. The outer edge of a module is a steel girder which houses the tile calorimeter readout electronics and also provides flux return for the solenoidal magnetic field. The body of the module is a self-supporting structure built from steel absorber plates, with 4 mm-thick spacer plates glued in staggered fashion to 5 mm-thick master plates. The staggered spacing creates the gaps into which the scintillating tiles are inserted, with a steel-to-scintillator volume ratio of approximately 4.7 : 1.

The scintillating tiles use polystyrene as the base material, in which ionizing particles induce the production of ultraviolet light. The polystyrene is doped with wavelength-shifting fluors, 1.5% PTP and 0.044% POPOP, which convert the scintillation light into the visible light. The tiles measure 3 mm thick, and vary between 97 mm-187 mm in radial length and 200 mm-400 mm in azimuthal length. A plastic sleeve envelops each tile, both for the protection of the tile during installation and also to improve the scintillation light collection efficiency due to a reflectivity of  $\sim 95\%$ . At the tile edges, wavelength-shifting fibers transmit the light to photomultiplier tubes housed in the girder. The grouping of the fibers determines the readout cell size, as shown in figure 3.21b; the cells measure  $\Delta\eta \times \Delta\phi = 0.1 \times 0.1$  in

the transverse direction, and are segmented into three layers longitudinally corresponding to depths of approximately  $1.5\lambda$ ,  $4.1\lambda$ , and  $1.8\lambda$ .



Figure 3.21: Left: Schematic view of a tile calorimeter module, showing assembly of the steel absorber, the inserted scintillator tiles, and the readout of lighting through wavelength-shifting fibers to the photomultiplier tubes. Right: Layout of the tile calorimeter cells, defined by the grouping of the readout fibers connecting the scintillating tiles to the photomultiplier tubes.

### Hadronic End-Cap Calorimeters

Outside the tile calorimeter, two hadronic end-cap calorimeters (HEC) perform hadronic calorimetry in the pseudorapidity range  $1.5 < |\eta| < 3.2$ . The HECs use copper and LAr arranged into a flat plate geometry, as shown in figure 3.22. Each HEC consists of two wheels (HEC1 and HEC2), which are further divided into two longitudinal segments. The plates have an inner radius of 372 mm or 475 mm depending on  $z$ , and an outer radius of 2030 mm. HEC1 contains 24 copper plates, each 24 mm thick and spaced by 8.5 mm, plus a 12.5 mm-thick front plate. HEC2 contains 16 copper plates measuring 50 mm in thickness, with a 25 mm-thick front plate. The sampling fractions are thus 4.4% for HEC1 and 2.2% for HEC2.

The gaps contain 3 electrodes spaced by 1.8 mm, the outer two of which supply a nominal operating voltage of 1800 V, and the middle of which performs the readout. The readout pads provide a transverse segmentation of  $\Delta\eta \times \Delta\phi = 0.1 \times 0.1$  for  $|\eta| < 2.5$ , and  $\Delta\eta \times \Delta\phi = 0.2 \times 0.2$  for  $2.5 < |\eta| < 3.2$ . In total, 5,632 channels are read from the HEC.



Figure 3.22: Schematic  $R - \phi$  (left) and  $R - z$  (right) views of the hadronic end-cap calorimeters.

### Forward Calorimeter

The forward calorimeter (FCal) performs both electromagnetic and hadronic calorimetry in the very forward region,  $3.2 < |\eta| < 4.9$ , and also shields the muon system from high particle fluxes. On each side, the FCal is divided into three layers measuring 45 cm in depth, an electromagnetic layer (FCal1) and two hadronic layers (FCal2 and FCal3). All three layers use LAr as the active medium, with very thin gaps due to avoid ion buildup due to the high particle flux. FCal1 uses copper absorbers to optimize the resolution and heat removal. FCal2 and FCal3 use tungsten absorbers, which provides good containment and reduces the lateral spread of hadronic showers. Finally, a passive brass plug behind FCal3 provides shielding for the muon system. The layout of the three layers and shielding plug is shown in figure 3.23.

FCal1 consists of stacked copper plates with 0.27 mm LAr gaps. The electrodes occupy 12,260 holes drilled through the copper plates, and consist of a copper rod coaxial with a copper tube, as shown in figure 3.24a. FCal2 and FCal3 consist of two 2.35 cm-thick copper end-plates spanned by an array electrodes similar to those in FCal1, except with tungsten rods, as shown in figure 3.24b. The arrays contains 10,200 and 8,224 electrodes in FCal2 and FCal3, respectively. In total, the three layers, FCal1, FCal2, and FCal3, contain 1008, 500, and 254 readout channels, respectively, and constitute 208.1 radiation lengths and 9.94 interaction lengths.

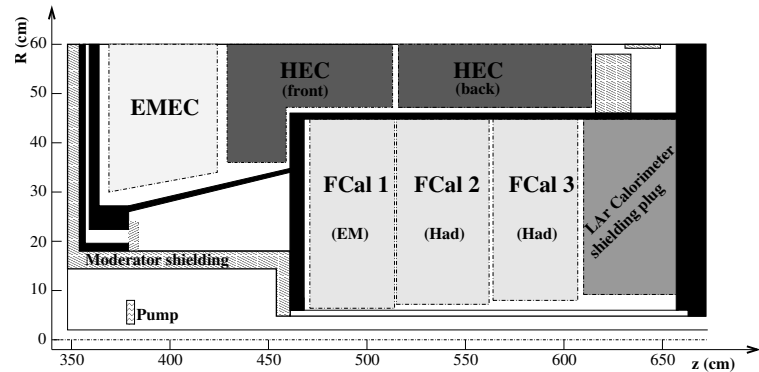


Figure 3.23: Schematic diagram showing the layout of the forward calorimeter in the  $R$ - $z$  plane.

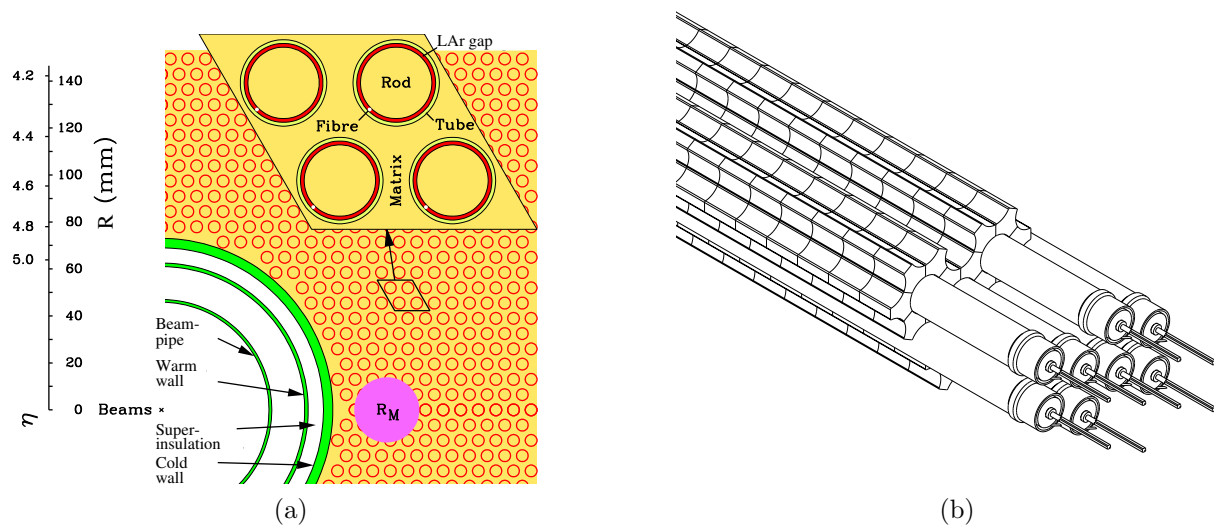


Figure 3.24: Left: the electrode structure of FCal1, showing the matrix of copper tubes and rods. The Molière radius,  $R_M$ , is shown for reference. Right: the absorber matrix in FCal2 and FCal, made from tungsten rods and copper tubes.

### 3.2.5 Muon Spectrometer

The muon spectrometer detects charged particles that penetrate the barrel and end-cap calorimeters. It forms the exterior of the ATLAS detector, occupying the volume of the barrel toroid with four large wheels on each side of the interaction point. Using a combination of several technologies, the muon spectrometer performs precision measurements of muon momenta in the region  $|\eta| < 2.7$ , with a design resolution of 10% for 1 TeV tracks, and also provides triggering on muons for  $|\eta| < 2.4$ .

The structure of the muon spectrometer is shown in figures 3.25 and 3.26. The barrel systems are arranged in three layers with radii of approximately 5 m, 7.5 m, and 10 m, mounted inside and on the eight coils of the barrel toroid magnet with approximate octagonal symmetry. The end-cap systems form four large wheels, located before and after the end-cap toroid magnets at positions of  $|z| \approx 7.4$  m, 10.8 m, 14 m, and 21.5 m.

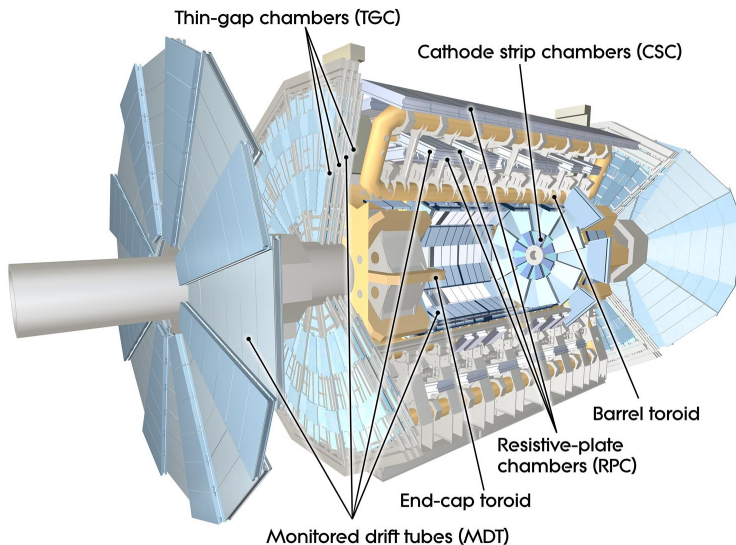


Figure 3.25: 3D model of the ATLAS muon spectrometer. The four different types of detector (MDTs, CSCs, RPCs, and TGCs) and the toroid magnets are shown.

Four different technologies are used for precision measurements and triggering, depending on the location in the detector. Monitored drift tubes (MDTs) perform the precision measurements over most of the volume with  $|\eta| < 2.7$ . Cathode strip chambers (CSCs) replace the MDTs in the innermost wheel for  $2.0 < |\eta| < 2.7$ , to handle the high particle flux. Triggering is performed by resistive plate chambers (RPCs) in the barrel ( $|\eta| < 1.05$ ) and thin gap chambers (TGCs) in the end-caps. The trigger chambers also supplement the MDT position measurements with the hit coordinate in the non-bending plane.



Figure 3.26: Layout of the chambers of the muon spectrometer.

### Monitored Drift Tubes

The muon spectrometer contains 1088 MDT chambers, covering a total area of  $\sim 550 \text{ m}^2$ . The majority of the MDT chambers are rectangular in the barrel and trapezoidal in the end-caps, and are laid out to optimize the solid angle coverage under the constraints of the magnet coils and other structures in the vicinity of the toroid magnet. Each chamber contains several layers of drift tubes, as shown in figure 3.27. The innermost chambers are divided into two groups of tube layers, called *multilayers*, each with four layers of tubes, while the remaining chambers have two groups of three layers of tubes.

The aluminum drift tubes have a radius of 29.97 mm, with a 50  $\mu\text{m}$ -diameter tungsten-rhenium wire forming the anode along the axis of the tube. A cross section of a tube is shown in figure 3.28. The tubes are filled with a mixture of argon and  $\text{CO}_2$  (93:7) with a high pressure of 3 bar, and are operated with a voltage of 3080 V. The average resolution of a single drift tube is 80  $\mu\text{m}$ , and the combined resolution of a chamber is 35  $\mu\text{m}$ . To achieve this precision, the position of the drift tubes and wires must be known to less than 30  $\mu\text{m}$ . Four optical alignment rays inside each MDT chamber continuously monitor the geometry of the chamber with a precision of a few microns, shown in figure 3.27. An inter-chamber optical alignment network monitors the relative positions of chambers relative to their neighbors with a precision of approximately 20  $\mu\text{m}$ . The optical alignment is supplemented with track-based alignment algorithms to align the chambers with poor or absent connection to the optical network, the end-caps with respect to the barrel, and the muon spectrometer with respect to the inner detector.



Figure 3.27: The mechanical structure of a MDT chamber. Two multilayers, each consisting of three or four rows of drift tubes, are separated by aluminum spacers. Four optical alignment rays continuously monitor the geometry of the chamber.

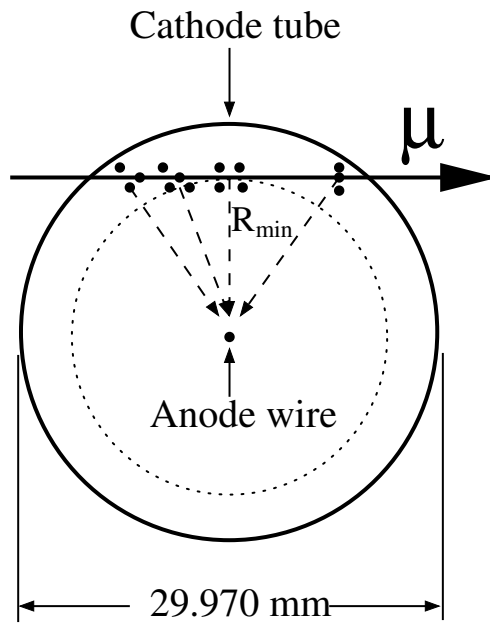


Figure 3.28: Cross section of a drift tube, showing the cathode tube, the anode wire, and an illustration of a muon ionizing the gas as it traverses the tube.

### Cathode Strip Chambers

The rate limit for the safe operation of the MDTs is about  $150 \text{ Hz/cm}^2$ , which is exceeded for  $|\eta| > 2$  in the first layer of the end-cap at  $|z| \approx 7 \text{ m}$ . Accordingly, CSCs are used in this volume of the detector, which can operate up to rates of about  $1 \text{ kHz/cm}^2$ . Eight large and eight small trapezoidal chambers give full coverage in  $\phi$ , as shown in figure 3.29a.

The CSCs are multiwire proportional chambers, with parallel wires running in the radial direction and the two cathodes finely segmented in perpendicular directions to provide measurements in both the  $\eta$  and  $\phi$  directions. The perpendicular cathode segmentation provides position measurements in two dimensions, which helps distinguish hits from nearby particles. In the bending direction, the segmentation corresponds to a readout pitch of 5.31 mm and 5.56 mm for the large and small chambers, respectively. The track coordinate is determined from a relative measurement of the charge induced on 3-5 adjacent strips at the peak of the charge distribution, shown schematically in figure ???. The resolution, dominated by electronic noise in the pre-amplifiers and by the spread of charge along the anode wire due inclined tracks, delta electrons, or a Lorentz force along the wire, is roughly  $60 \mu\text{m}$  per CSC plane. In the non-bending direction, a coarser segmentation leads to a resolution of 5 mm.



Figure 3.29: Left: Layout of the eight large and eight small CSC chambers. Right: Schematic view of the CSC anode wires and perpendicular cathode strips, showing the deposition of charge from a track on several adjacent strips.

### Resistive Plate Chambers

Muon triggering in the barrel ( $|\eta| < 1.05$ ) is performed by 544 RPCs, which exhibit good spatial and timing resolution and an adequate rate capability of  $\sim 1 \text{ kHz/cm}^2$ . The RPCs form three layers, or *stations*, with two on either side of the middle MDT layer and the

third on the inner or outer side of the outer MDT layer, for the small and large sectors, respectively. Each station has two independent layers, each providing a measurement of  $\eta$  and  $\phi$ , resulting in six possible measurements for muons passing through three stations.

An RPC unit consists of two sets of two parallel resistive plates (2 mm-thick phenolic-melaminic plastic laminate) separated by 2 mm by insulating spacers, shown in figure 3.30. The interior is filled with a gas mixture of  $C_2H_2F_4/Iso-C_4H_{10}/SF_6$  (94.7/5/0.3). With an electric field of 4.9 kV/mm, muons traversing the gas induce an avalanche towards the anode, which is read out via capacitive coupling to 25–35 mm-wide copper strips on the exterior face of the RPC. The RPCs achieve a spatial resolution of approximately 10 mm in  $z$  and  $\phi$ , a timing resolution of 1.5 ns, and a detection efficiency of  $\sim 98\%$ .

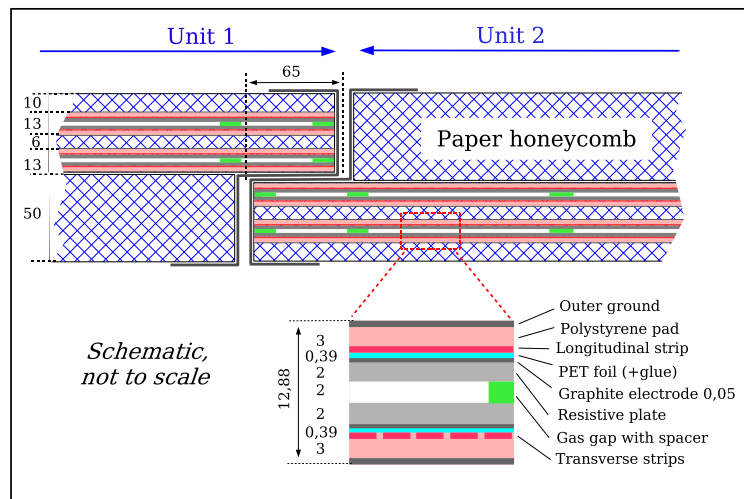


Figure 3.30: Cross section of an RPC, showing two units joined to form a single chamber. Each unit has two sets of two resistive plates (grey) separated by insulating spacers (green). The readout strips (magenta) are on the opposite side of the resistive plates from the gas gap. Outside the detecting elements, the volume of the RPC chamber is filled with paper honeycomb. The dimensions are given in millimeters.

### Thin Gap Chambers

TGCs provide muon triggering in the end-caps, due to their good timing resolution and high rate capability. The TGCs also provide an azimuthal coordinate measurement, which complements the MDT measurement in the radial direction. Nine TGC disks are installed in total: a doublet mounted near the inner MDT end-cap layer, and a triplet and two doublets near the middle MDT end-cap layer. The disks are divided into two concentric annuli, one covering  $1.05 \leq |\eta| \leq 1.92$  and the other covering  $1.92 \leq |\eta| \leq 2.4$ .

The TGCs are multiwire proportional chambers filled with a gas mixture of  $CO_2$  and  $n$ -pentane. The cathode planes are 1.6 mm-thick FR4 (Flame Resistant 4) plates, with the

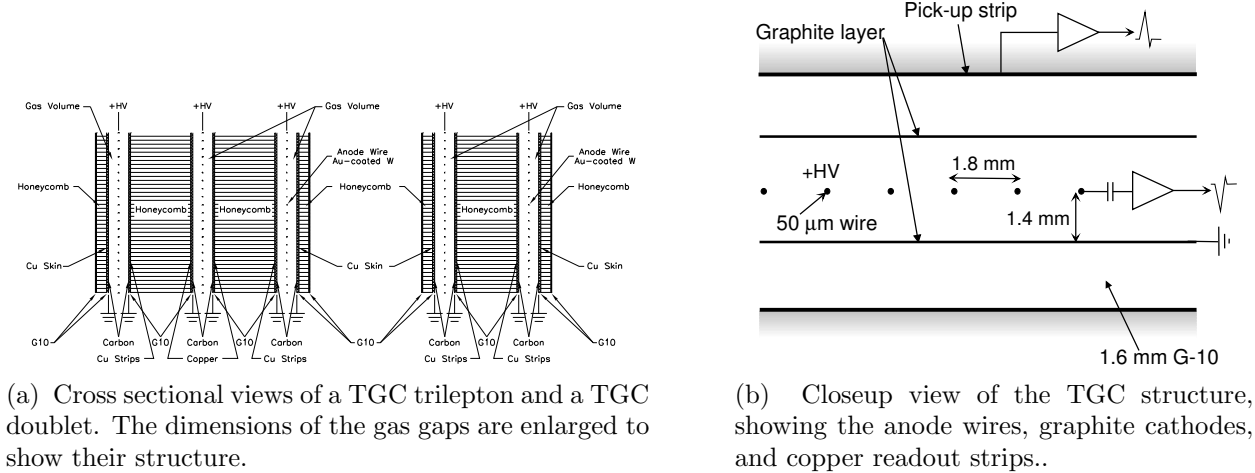


Figure 3.31: The construction of the TGCs.

interior faces coated with graphite and exterior faces cladded with copper. The triplet TGCs have three layers of wires and two layers of copper readout strips, while the doublet TGCs have two layers each of wires and strips, as shown in figure 3.31a. The radial coordinate is measured by the anode wire groups and the azimuthal coordinate by the radial cathode strips. The chambers are “thin” in that the wire to cathode distance, 1.4 mm, is shorter than the wire-to-wire distance of 1.8 mm, as shown in figure 3.31b. The anode wires have a diameter of 50  $\mu\text{m}$  and are operated at a potential of 2.9 kV. The small wire-to-wire distance and high electric field near the anode wires contribute to a good timing resolution of 4 ns. The spatial resolution, 2–6 mm in  $R$  and 3–7 mm in  $\phi$ , is determined by the ganging of readouts: due to the direction of the magnetic field, achieving the required momentum resolution at fixed transverse momentum requires finer resolution at larger pseudorapidities.

### 3.2.6 Trigger and Data Acquisition

During a typical data-taking run during 2012, the LHC beam contains 1377 bunches with a typical bunch spacing of 50  $\mu\text{s}$ , giving an event rate of  $\sim 20 \text{ MHz}$ . In contrast, the ATLAS data acquisition system records events at roughly 400 Hz. The filtering of events is performed by the three-level ATLAS triggering system. The first level, L1, is implemented in hardware, and reduces the event rate to less than 75 kHz. The second level, L2, is implemented in software, and reduces the event rate to less than 3.5 kHz using regions of interest (RoIs) identified by the L1 trigger. The final level of the trigger, the Event Filter, is also implemented in software, and reduce the event rate to less than 400 Hz using the full event information.

The L1 trigger reduces the event rate from 20 MHz to 75 kHz using a limited subset of the event data. While the L1 trigger is processing an event, the full event data is stored in

buffers on the detector. Due to the limited buffer size, the L1 latency must be less than  $2.5\ \mu\text{s}$ , of which  $1\ \mu\text{s}$  is used by the cable propagation time. Therefore, the trigger is implemented in custom hardware processors. The block diagram for the trigger is shown in figure 3.32. The inputs to the trigger include the RPC and TGC detectors in the muon spectrometer and all of the calorimeter system. Two primary systems, the L1 Calorimeter Trigger and the L1 Muon Trigger, select events based on the presence of high- $E_{\text{T}}$  objects or significant total event activity. These include high- $p_{\text{T}}$  muons, electron and photons, jets, hadronically decaying tau leptons, large missing transverse energy, and large total transverse energy.

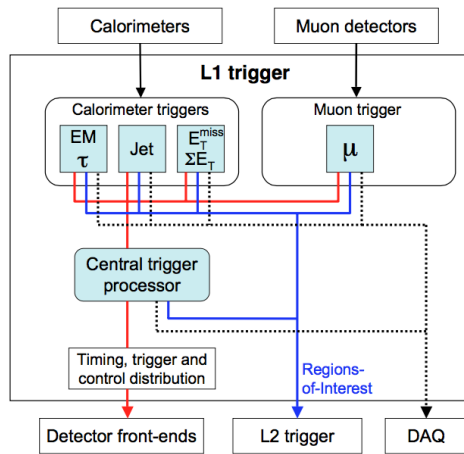


Figure 3.32: Block diagram of the L1 trigger system.

The L1 Calorimeter Trigger uses about 7,000 analogue trigger towers with a reduced granularity,  $\Delta\eta \times \Delta\phi = 0.1 \times 0.1$  for most of the detector. Two subsystems run in parallel: the cluster processor identifies electrons/photon and hadronically decay tau lepton candidates with  $E_{\text{T}}$  above a programmable set of thresholds, while the jet/energy-sum processor identifies jets and calculates the total scalar transverse energy and  $E_{\text{T}}^{\text{miss}}$  using  $\Delta\eta \times \Delta\phi = 0.2 \times 0.2$  blocks of calorimeter cells. Isolation cuts can be applied as well, limiting the energy allowed in the towers surrounding the object of interest and, in the case of electrons/photon, in the hadronic towers behind the electromagnetic towers.

The L1 Muon Trigger searches for a coincidence of hits in consecutive muon trigger stations within a *road*, roughly corresponding to the path of a muon from the interaction point through the detector. The  $p_{\text{T}}$  threshold is encoded in the width of the road, with a narrower road corresponding to a higher  $p_{\text{T}}$  threshold. For low- $p_{\text{T}}$  muons in the RPCs, the algorithm begins with hits in the second RPC doublet, called the *pivot plane*. The trigger requires a hit in the first RPC doublet, within the road defined by the interaction point and the hit in the pivot plane. The high- $p_{\text{T}}$  algorithm is similar, requiring a hit along the road in the third RPC doublet as well as the first two. In the end-caps, the pivot plane is established by the outermost layer of TGCs, with the road corresponding to the path of an infinite-momentum muon originating from the interaction point. To reject backgrounds from

random coincidences, stricter requirements are imposed on the number of coincident hits in the TGC doublets and triplets.

The muon and calorimeter triggers pass their decisions along with the corresponding data to the Central Trigger Processor (CTP). The CTP communicates the total trigger decision to the front ends on the detector, including special triggers such as random triggers or the minimum bias trigger based on scintillator counters. In the event of a passed trigger, the event data is passed to the L2 trigger. The CTP also manages the *luminosity blocks*, an index representing the time at which an event was recorded with coarse ( $\sim 1$  minutes) granularity. A luminosity block is the shortest time interval for which the integrated luminosity can be determined such that the total uncertainty is dominated by systematic effects, rather than limited statistics. In the event of a detector failure, this index allows the rejection of a minimal set of affected events.

The L2 trigger reduces the event rate from a maximum of 75 kHz from the L1 trigger to less than 3.5 kHz. The trigger is implemented in software, and uses only the subset of the event data within the RoIs identified by the L1 trigger, typically 1%-2% of the total. After a successful L1 trigger, the data corresponding to the RoIs, stored in the detector-specific front end electronics, are accumulated in the ROI builder via 1574 readout links. The ROI builder combines the 1574 event fragments into a single data structure, which is passed to the L2 processing farm. At each step of a given trigger algorithm targeting particular signatures, only the relevant RoIs are analyzed. If no signatures remain valid, the event is rejected. Hence the full ROI information is transferred only for events which pass the L2 selection criteria. The typical L2 latency is about 40 ms.

Finally, the event filter reduces the event rate to the final  $\sim$ 400 Hz read out from the detector to disk. Also implemented in software, it runs the same algorithms as used in the offline event reconstruction using the full event information. Based on the objects used for triggering, the triggered events are categorized into one or more *data streams*. The data streams and other data computed by the event filter are appended to the event data, which are then transferred to CERN’s central data-recording facility for storage. An example of the event filter rates from the various streams during a single data-taking run is shown in figure 3.5a. The monthly average rates of each stream during 2012 are shown in figure 3.5b.



(a) Event filter rates for a single data-taking run.

(b) Average monthly event filter rates during 2012.

Table 3.5: The rates of recording events from the event filter for different data streams.

# Bibliography

- [1] L. Evans, *History of the LHC* (May 2010) pp. 1–87.
- [2] L. Rossi, *Superconductivity: its role, its success and its setbacks in the Large Hadron Collider of CERN*,  
Superconductor Science and Technology **23**.3 (Feb. 2010) p. 034001.
- [3] H. Wiedemann, *Particle Accelerator Physics*, SpringerLink: Springer e-Books,  
Springer Berlin Heidelberg, 2007, ISBN: 9783540490456,  
URL: <https://books.google.com/books?id=S8CfmLe87RAC>.
- [4] M. Benedikt et al., *LHC Design Report. 3. The LHC injector chain* (2004).
- [5] O. S. Bruning et al., *LHC Design Report. 1. The LHC Main Ring* (2004).
- [6] G. Papotti et al., *Observations of beam-beam effects at the LHC*,  
arXiv.org (Sept. 2014), arXiv: 1409.5208 [physics.acc-ph].
- [7] The ATLAS Collaboration,  
*The ATLAS Experiment at the CERN Large Hadron Collider*,  
Journal of Instrumentation **3**.08 (Aug. 2008) S08003–438.
- [8] *ATLAS Photos*, CERN, 2012, URL: <http://www.atlas.ch/photos/index.html>.
- [9] M. Alekса et al., *Results of the ATLAS solenoid magnetic field map*,  
Journal of Physics: Conference Series **110**.9 (June 2008) pp. 092018–5.

# Chapter 4

## Luminosity Measurement

### 4.1 Run I Luminosity

The ATLAS Run I data were recorded from 2011 to 2012, with a center-of-mass collision energy of  $\sqrt{s} = 7\text{ TeV}$  in 2011 and  $\sqrt{s} = 8\text{ TeV}$  during 2012. Integrated luminosities of  $L = 5.46\text{ fb}^{-1}$  and  $22.8\text{ fb}^{-1}$  were delivered by the LHC in the two years, of which  $5.08\text{ fb}^{-1}$  and  $21.3\text{ fb}^{-1}$  were recorded by the ATLAS detector. The recorded luminosity accounts for the data acquisition inefficiency, as well as the warm start period, an interval of several minutes after the LHC has declared stable beams during which the tracking detectors are ramped to high voltage and the pixel detector preamplifiers are turned on. After masking data recorded while one or more detector subsystems were not functioning properly,  $4.57\text{ fb}^{-1}$  and  $20.3\text{ fb}^{-1}$  of data are considered usable for physics analyses. The volume of delivered, recorded, and physics-ready data are shown as a function of time in figure 4.1a.

The LHC was typically operated with 1042 and 1368 colliding bunches in 2011 and 2012, respectively, with a bunch spacing of 50 ns. The peak instantaneous luminosity reached values as high as  $\mathcal{L} \sim 8 \times 10^{33}\text{ cm}^{-2}\text{ s}^{-1}$ , corresponding to a peak average pileup value of  $\mu \sim 37$ . The distribution of pileup values in 2011 and 2012 data are shown in figure 4.1b.

### 4.2 Measurement Overview

The instantaneous luminosity at a  $pp$  collider is given by [1, 2]:

$$\mathcal{L} = \frac{R_{\text{inel}}}{\sigma_{\text{inel}}}, \quad (4.1)$$

where  $R_{\text{inel}}$  is the rate of inelastic  $pp$  collisions, and  $\sigma_{\text{inel}}$  is the  $pp$  inelastic cross section. For a storage ring with a revolution frequency  $f_r$  and  $n_b$  colliding bunch pairs, the instantaneous luminosity can be written in terms of the average number of inelastic  $pp$  collisions

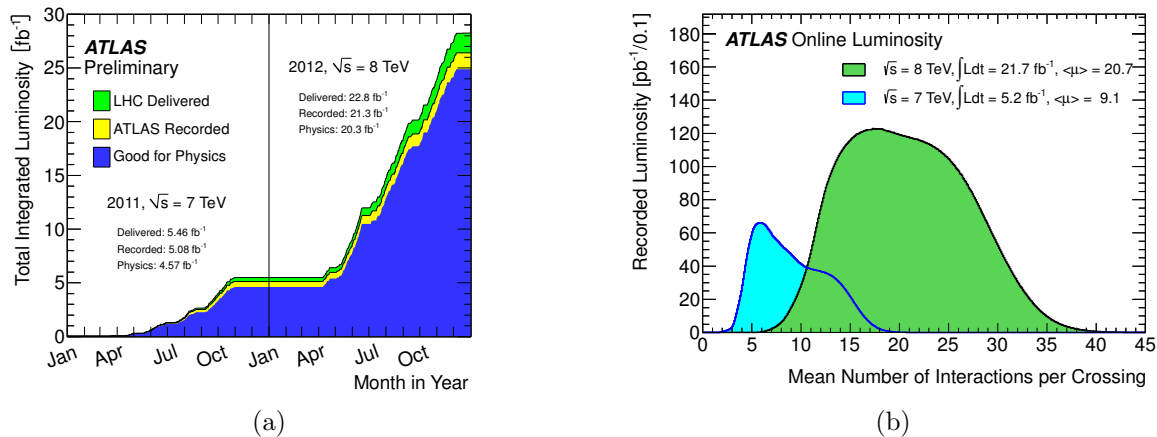


Figure 4.1: Left: The cumulative delivered, recorded, and physics-ready integrated luminosity versus time in 2011-2012. Right: Distribution of the number of interactions per bunch crossing in events recorded in 2011-2012.

per bunch crossing,  $\mu$ , as

$$\mathcal{L} = \frac{\mu f_r n_b}{\sigma_{\text{inel}}}. \quad (4.2)$$

The instantaneous luminosity is measured by ATLAS using several detectors and algorithms, which have some efficiency  $\epsilon$  to detect a  $pp$  interaction and measure the *visible* number of interactions per bunch crossing,  $\mu_{\text{vis}} = \epsilon \mu$ . Defining the visible cross section to be  $\sigma_{\text{vis}} \equiv \epsilon \sigma_{\text{vis}}$ , the instantaneous luminosity as measured by a particular detector is:

$$\mathcal{L} = \frac{\mu_{\text{vis}} f_r n_b}{\sigma_{\text{vis}}}. \quad (4.3)$$

The instantaneous luminosity is measured in intervals of approximately 60 seconds. The visible cross section is a calibration constant for a particular detector, which is determined during dedicated calibration runs in which the luminosity is determined directly from the physical dimensions of the beams. The calibration procedure is described in section 4.4.

### 4.3 Luminosity Detectors

ATLAS performs many redundant luminosity measurements using several detectors. The detectors fall into two categories. *Event counting* detectors have a binary response, returning a 0 or 1 depending on whether a bunch crossing satisfies a set of criteria defined to detect an inelastic  $pp$  collision. Such detectors essentially measure  $p(0; \mu)$ , the probability that an event falls in the zero bin of a Poisson distribution, from which the mean  $\mu$  be calculated. *Hit counting* detectors, on the other hand, count some quantity proportional to the number

of interactions in a given bunch crossing, such as the number of particles identified by a particular detector subsystem. A hit counting measurement typically yields more information about an event at the cost of additional systematic uncertainties.

Ideally, a luminosity detector exhibits the following features:

- The efficiency of the detector should be insensitive to pileup. The visible cross sections are typically measured at  $\mu \approx \mathcal{O}(1)$ , while a typical data-taking run has a peak average pileup of up to  $\mu \sim 40$ ; it is essential that the visible cross section be constant across this range of pileup values.
- The efficiency of the detector should also be constant over long timescales.
- The response of the detector and the readout should fast enough to provide a bunch-by-bunch luminosity measurement. As the LHC bunches are not identical, with different numbers of protons and emittances, it is useful to measure luminosity for each colliding bunch pair, as often as once every 25 ns. The colliding bunch pairs are labeled by the bunch crossing identification number, or BCID, ranging from 1 to 2808; consecutive BCIDs are separated by 25 ns.
- The efficiency should be high enough to yield sufficient statistics. The data are used in increments as short as 20 s, so the statistics collected over this time scale should be high enough that the total uncertainty is dominated by systematic effects. On the other hand, for event counting detectors, the efficiency should not be so high that the detector is saturated; the uncertainty on  $\mu$  is large if  $p(0; \mu)$  is too close to 0 or 1.
- The backgrounds should be low and understandable. Detectors can be sensitive to a wide range of phenomena aside from  $pp$  collisions, which should not be counted as luminosity. For example, some detectors observe a phenomenon called *afterglow*, a small amount of activity in the BCIDs immediately following a collision likely due to photons from nuclear deexcitations in the detector material. The afterglow background is proportional to the luminosity in the colliding BCIDs, and decays away with several time constants. Collisions between a beam and residual gas in the beam pipe, called *beam-gas interactions*, can also contribute a low level of background, and is estimated by observing non-colliding bunches passing through the interaction region.

The central value of the luminosity measurement is determined by the *beam conditions monitor* (BCM) [3], which fulfills most of these desired criteria. The BCM consists of eight diamond-based particle detectors, four on each side of the interaction point at  $|z| = 184$  cm and  $|\eta| = 4.2$ . The detectors have a physical cross section of approximately  $1 \text{ cm}^2$  and are arranged in a cross pattern, with two independent readouts corresponding to the vertical and horizontal pairs. The design purpose of the BCM is to monitor backgrounds and to trigger a beam dump if beam losses towards the inner detector become too high; accordingly, the detector has a very fast readout, and can provide a bunch-by-bunch luminosity measurement

with a time resolution of  $\sim 0.7$  ns. The luminosity is measured using event counting, and can be measured using any combination of the readouts. The configurations used require hits in either the vertical pair (BCMV) or the horizontal pair (BCM), and either coincident hits on both sides of the interaction point (AND) or a single hit on either side (OR). The small size of the active sensor leads to an efficiency of approximately 7% in the OR configuration, which allows for sufficient statistics without saturating the detector.

LUCID (LUminosity measurement using Cherenkov Integrating Detector) [4] provides a supplementary, bunch-by-bunch, event counting-based luminosity measurement. The detector consists of two sets of sixteen Cherenkov detectors surrounding the beampipe at  $z = \pm 17$  m, occupying the pseudorapidity range  $5.6 < |\eta| < 6.0$ . As designed and initially constructed, the Cherenkov detectors are polished aluminum tubes filled with  $C_4F_{10}$  gas. The Cherenkov photons induced by charged particles traversing the gas are collected by photomultiplier tubes (PMTs) located at the far end of the tubes. Additional Cherenkov photons are produced in the quartz window separating the tube volume from the PMT. In this configuration, the typical single-particle yield is 60-70 photoelectrons due to photons created in the gas, and about 40 photoelectrons due to the quartz window. A hit is recorded if the PMT signal exceeds a preset threshold, corresponding to about 15 photoelectrons. However, the higher instantaneous luminosities due to the 50 ns bunch spacing led to saturation of the detectors, and hence on 30 July 2011, the gas was removed from the Cherenkov tubes to reduce the efficiency. The removal of the gas also improved the detector's stability and linearity with respect to pileup. Relative comparisons with other detectors were used to reestablish the detector calibration.

Several detector subsystems nominally designed for physics object reconstruction are also used for hit counting-based luminosity measurements. Algorithms using the tile calorimeter and the forward calorimeters (see section 3.2.4) determine the luminosity from detector currents proportional to the total particle flux in small regions of the calorimeters. The tile calorimeter algorithm monitors the PMT currents corresponding to a few selected cells near  $|\eta| = 1.25$ , where the highest sensitivity to changes in the luminosity is observed. Similarly, the forward calorimeter algorithm monitors the currents in the high voltage lines. In both cases, the detector is unable to provide a bunch-by-bunch measurement, and the current response is not sensitive to the low instantaneous luminosities during the dedicated calibration runs, requiring the calibration to be set using relative comparisons with LUCID or BCM. On the other hand, the detectors exhibit good linearity of response with pileup, and good short-term stability.

Finally, algorithms using the inner detector measure the luminosity by counting reconstructed tracks and vertices<sup>1</sup>. The use of these higher-level objects confers certain benefits, such as low background rates and good long-term stability, at the cost of increased computational requirements, which limit the data rate to  $\mathcal{O}(100)$  Hz. Further, pileup effects can be significant; in particular, the efficiency of the vertex counting algorithm varies by as much

---

<sup>1</sup>Pixel cluster counting, used by the CMS experiment, was also considered, but was not commissioned due to the difficulty of the subtraction of the background due to afterglow.

as 30% up to pileup values of  $\mu = 30$ , limiting its utility to data with low pileup.

## 4.4 Luminosity Calibration: van der Meer Scans

The visible cross sections for the detectors and algorithms described in section 4.3 are calibrated during dedicated runs called van der Meer (vdM) scans [5]. The calibration procedure uses the definition of luminosity in terms of the beam parameters, given for a single colliding bunch by:

$$\mathcal{L} = f_r n_1 n_2 K \int \rho_1(x, y, z, t) \rho_2(x, y, z, t) dx dy dz dt, \quad (4.4)$$

where  $f_r$  is the revolution frequency,  $n_{1,2}$  are the number of particles in the colliding bunches, and  $\rho_{1,2}(x, y, z, t)$  are the time- and position-dependent particle density distribution, normalized so that  $\int \rho_{1,2}(x, y, z, t) dx dy dz = 1$ .  $K$  is a kinematic factor,

$$K = \sqrt{(\vec{v}_1 - \vec{v}_2)^2 - \frac{(\vec{v}_1 \times \vec{v}_2)^2}{c^2}}, \quad (4.5)$$

which, in the limit  $|\vec{v}_{1,2}| \rightarrow c$ , reduces to  $2c \cos \alpha$ , where  $\alpha$  is the crossing angle between the beams. To simplify the current discussion, the crossing angle is assumed to be zero, and the bunch densities are assumed to be functions of  $x$ ,  $y$ , and  $z \pm ct$ , i.e. that the transverse bunch profiles are constant over the duration of the collision<sup>2</sup>. The luminosity can then be expressed as:

$$\mathcal{L} = f_r n_1 n_2 \int \hat{\rho}_1(x, y) \hat{\rho}_2(x, y) dx dy, \quad (4.6)$$

where  $\hat{\rho}_{1,2}(x, y)$  are the transverse particle densities, normalized to unity. Under the further assumption that the transverse particle densities factorize in the horizontal and vertical directions,  $\hat{\rho}(x, y) = \hat{\rho}_x(x) \hat{\rho}_y(y)$ , where  $\hat{\rho}_x(x)$  and  $\hat{\rho}_y(y)$  are also normalized to unity, the luminosity can be written as:

$$\mathcal{L} = f_r n_1 n_2 \Omega_x(\hat{\rho}_{x1}, \hat{\rho}_{x2}) \Omega_y(\hat{\rho}_{y1}, \hat{\rho}_{y2}), \quad (4.7)$$

where  $\Omega_x(\hat{\rho}_{x1}, \hat{\rho}_{x2}) = \int \hat{\rho}_{x1}(x) \hat{\rho}_{x2}(x) dx$ , and similarly for the  $y$  direction<sup>3</sup>. As first proposed by van der Meer, the  $\Omega_{x,y}$  parameters can be determined by measuring the interaction

---

<sup>2</sup>In particular, the *hourglass effect* is neglected. The collisions occur in a drift space, where the beams are focused, or squeezed, onto the interaction point. The transverse size of the beam in direction  $i$  as a function of  $z$  is given by  $\sigma_i^2(z) = \epsilon_i \beta_i^* \left(1 + \frac{(z - z_i^w)^2}{\beta_i^{*2}}\right)$ , where  $\epsilon_i$  is the transverse emittance,  $z_i^w$  is location of the optical waist, and  $\beta_i^*$  is the betatron function at  $z = z_i^w$ . The effect is significant when  $\beta_i^* \lesssim \sigma_z$ ; during the vdM scans,  $\sigma_z \approx 50$  mm, while  $\beta^* = 1.5$  m-11 m, and hence the hourglass effect is neglected.

<sup>3</sup>The formalism can be generalized to the case where the beam profiles do not factorize in  $x$  and  $y$ ; see [Balagura:2011er].

rate as a function of transverse beam displacement,  $R_{x,y}(\delta)$ . Without loss of generality, assume that beam 2 is displaced by  $\delta$  in the  $x$  direction, while beam 1 is held fixed. Then,  $R_x(\delta) = k \int \rho_{x1}(x)\rho_{x2}(x - \delta) dx$  for some constant  $k$ , and

$$\frac{R_x(0)}{\int R_x(\delta) d\delta} = \frac{k \int \rho_{x1}(x)\rho_{x2}(x) dx}{k \int \int \rho_{x1}(x)\rho_{x2}(x - \delta) dx d\delta} \quad (4.8)$$

$$= \int \rho_{x1}(x)\rho_{x2}(x) dx \quad (4.9)$$

$$= \Omega_x(\hat{\rho}_{x1}, \hat{\rho}_{x2}) \quad (4.10)$$

For convenience, define  $\Sigma_{x,y}$  to be the characteristic widths of  $R_{x,y}(\delta)$ , given by:

$$\Sigma_{x,y} = \frac{1}{\sqrt{2\pi}} \frac{\int R_{x,y}(\delta) d\delta}{R_{x,y}(0)}. \quad (4.11)$$

For Gaussian beams,  $\Sigma_{x,y}$  correspond to the Gaussian width of  $R_{x,y}(\delta)$ . Finally, the luminosity is given by

$$\mathcal{L} = \frac{f_r n_1 n_2}{2\pi \Sigma_x \Sigma_y}. \quad (4.12)$$

Equating this with the luminosity defined in equation 4.3, the visible cross section for a given detector and algorithm is given by

$$\sigma_{\text{vis}} = \mu_{\text{vis}}^{\text{MAX}} \frac{2\pi \Sigma_x \Sigma_y}{n_1 n_2}, \quad (4.13)$$

where  $\mu_{\text{vis}}^{\text{MAX}}$  is the visible interaction rate per bunch crossing at the maximum of the scan curve,  $R(\delta)$ . The numbers of particles per bunch,  $n_{1,2}$ , are measured by the LHC Bunch Current Normalization Working Group using bunch current transformers (BCTs) [6–8].

#### 4.4.1 2011 Luminosity Calibration

As an example, the 2011  $pp$  calibration is derived from two pairs of scans in the  $x$ - and  $y$ -directions, performed during the same LHC fill on 15 May 2011 [2]. The beams had 14 colliding bunch pairs,  $\sim 0.8 \times 10^{11}$  protons per bunch,  $\beta^* = 1.5$  m, and a crossing angle of  $\alpha = 240 \mu\text{rad}$ . The resulting transverse beam size was approximately  $\sigma_x \approx \sigma_y \approx 40 \mu\text{m}$ , and the peak average number of interactions per crossing with head-on collisions was  $\mu \approx 2.3$ . The scan was performed in 25 equal steps over a displacement range of  $\delta = \pm 233 \mu\text{m}$ .

Figure 4.2 shows an example scan curve, with the specific visible interaction rate,  $\mu_{\text{vis}}^{\text{sp}} \equiv \mu_{\text{vis}}/(n_1 n_2)$ , plotted as a function of transverse beam separation for the BCMV\_OR algorithm. Normalizing by the bunch current product,  $n_1 n_2$ , eliminates the dependence of the curve on the decreasing beam currents over the course of the scan. The vdm scan curve is fitted with

a Gaussian plus a constant, which is used as  $R_{x,y}(\delta)$  to calculate  $\Sigma_{x,y}$  in equation 4.11.  $\mu_{\text{vis}}^{\text{MAX}}$  is determined from the peak of the fitted function. The measured  $\sigma_{\text{vis}}$  values for both scans and all 14 colliding bunch pairs are shown in figure 4.3. The luminosity-weighted mean  $\sigma_{\text{vis}}$  is taken as the central value, while the scatter of the 28 measurements, which is not consistent with statistical variation, is taken as a systematic uncertainty on the reproducibility of the measurement.

The visible cross sections for several algorithms using during 2011 are shown in table 4.1, along with the efficiency assuming a total inelastic cross section of  $\sigma_{\text{inel}} = (71.34 \pm 0.90) \text{ mb}$  [9].

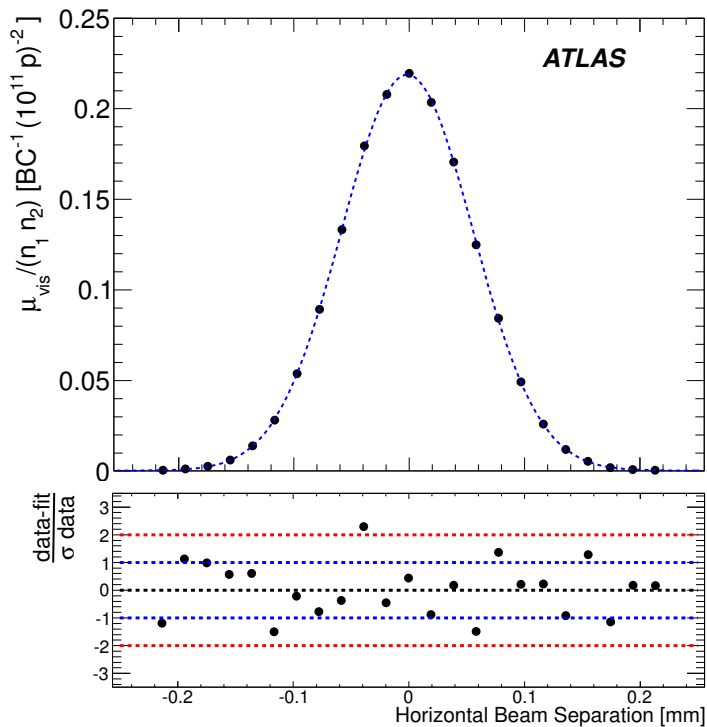


Figure 4.2: An example of a scan curve measured by BCMV\\_OR from the van der Meer scans on 15 May 2011. The specific visible interaction rate  $\mu_{\text{vis}}^{\text{sp}} \equiv \mu_{\text{vis}} / (n_1 n_2)$  is shown as a function of transverse beam separation in the  $x$  direction for a single scan and BCID. The data are fitted with Gaussian plus constant. The bottom plot shows the residual deviation of the data from the fit, divided by the uncertainty on the data.

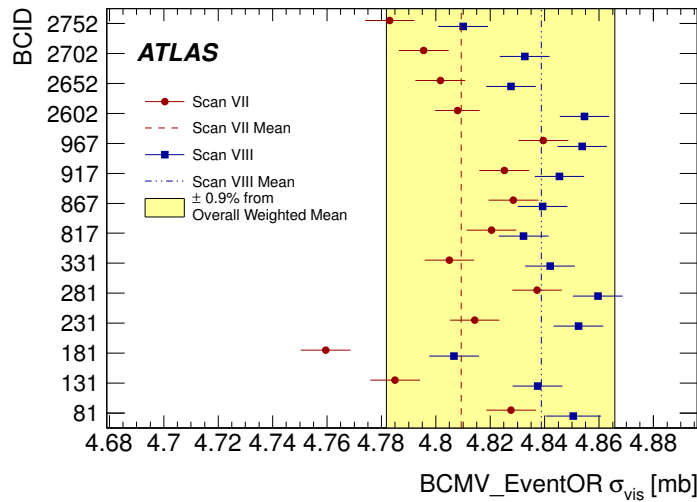


Figure 4.3: Measured  $\sigma_{\text{vis}}$  values from the vdM scans performed in May 2011. The error bars represent statistical uncertainties only. The vertical dashed lines indicate the weighted average over BCIDs from the two sets of scans. The yellow band shows a variation of  $\pm 0.9\%$  from the total weighted average, equal to the systematic uncertainty due to the observed BCID-to-BCID and scan-to-scan variations.

Algorithm	$\sigma_{\text{vis}} \text{ (2011)}$	$\frac{\sigma_{\text{vis}}}{\sigma_{\text{inel}}}$
BCM_VOR	$4.82 \pm 0.07$	0.068
BCM_HOR	$4.78 \pm 0.07$	0.067
BCM_VAND	$0.142 \pm 0.002$	0.002
BCM_HAND	$0.140 \pm 0.002$	0.002
LUCID_OR	$43.3 \pm 0.7$	0.607
LUCID_AND	$13.7 \pm 0.2$	0.192

Table 4.1: Visible cross sections for  $pp$  luminosity measurement algorithms used in 2011. The corresponding efficiency of detecting an inelastic  $pp$  collision is also shown for  $\sigma_{\text{inel}} = 71.34 \text{ mb}$ .

## 4.5 Systematic Uncertainties

The systematic uncertainty on the 2011 and 2012 luminosity measurements are 1.8% and 2.8%<sup>4</sup>, respectively. No single source of uncertainty dominates the total; rather, the uncertainty is due to many sources, each contributing less than 1%. The sources of uncertainty on the 2011 luminosity measurement are shown in table 4.2, divided into uncertainties on the visible cross section measurement during vdm scans and uncertainties on the measurement performed over the course of data taking.

The combined uncertainty on the visible cross sections due to the vdm calibration procedure is 1.5%. The largest source of uncertainty is due to emittance growth and non-reproducibility, reflected in the scatter between BCIDs and between scans in figure 4.3. Other significant sources, each roughly 0.5%, include beam-beam effects, where the two colliding beams deflect each other away from the nominal transverse separation; transverse correlations which violate the assumption that the transverse particle densities factorize as  $\rho(x, y) = \rho_x(x)\rho_y(y)$ ; pileup dependence; and the measurement of the number of protons per bunch,  $n_{1,2}$ .

Uncertainties on the luminosity measurement over the 2011 data-taking period total 0.9%. These uncertainties are dominated by variations in the detector efficiencies during 2011, quantified using relative comparisons between algorithms across the entire year, and pileup dependence, quantified using relative comparisons between algorithms at different pileup values. The relative comparisons are shown in figure 4.4.

The sources contributing to the 2.8% systematic uncertainty in 2012 are similar. The 1% increase from 2011 is largely due to long-term consistency: comparisons with tile and forward calorimeter measurements indicate that the BCMV\_OR efficiency drifted with respect to the calorimeters by as much as 2% over the year. The full 2% is taken as a conservative systematic uncertainty.

## 4.6 Vertex-Based Luminosity Measurement

Primary vertices are points consistent with being the origin of a set of tracks reconstructed by the inner detector, nominally due to inelastic  $pp$  interactions. The reconstruction of tracks and vertices is described in section 5.1. Vertex counting [10] is an appealing luminosity measurement technique for a number of reasons. The backgrounds are very low, and can be controlled by requiring a minimum number of tracks per vertex, chosen here to be five tracks with  $p_T > 400$  MeV. Further, the vertex reconstruction efficiency is expected to be stable throughout the data taking period. However, the technique has two significant drawbacks. First, the data is collected through the standard ATLAS data acquisition system, limiting the event rate during normal physics runs to  $\mathcal{O}(100\text{ Hz})$ . Depending on the trigger used, a correction for the trigger deadtime may also be necessary. Second, the efficiency of the vertex

---

<sup>4</sup>Preliminary uncertainty. The final uncertainty is expected to be around 2%.

Source	Uncertainty
Bunch population product ( $n_1 n_2$ )	0.5%
Beam centering	0.10%
Beam position jitter	0.30%
Emissittance growth/non-reproducibility	0.67% ⊕ 0.55%
Bunch-to-bunch $\sigma_{\text{vis}}$ consistency	0.28%
Fit model	0.31%
Background subtraction	0.29%
Length scale calibration	0.30%
Absolute ID length scale	0.30%
Beam-beam effects	0.50%
Transverse correlations	0.50%
Pileup dependence	0.50%
Afterglow correction	0.2%
BCM Stability	0.2%
Long-term consistency	0.7%
Pileup dependence	0.5%
Total	1.8%

Table 4.2: Systematic uncertainties on the integrated luminosity measured in 2011 using the BCM\_VOR algorithm. The uncertainties are separated into uncertainties on the visible cross section (1.5%) and measurement uncertainties over the year (0.9%).

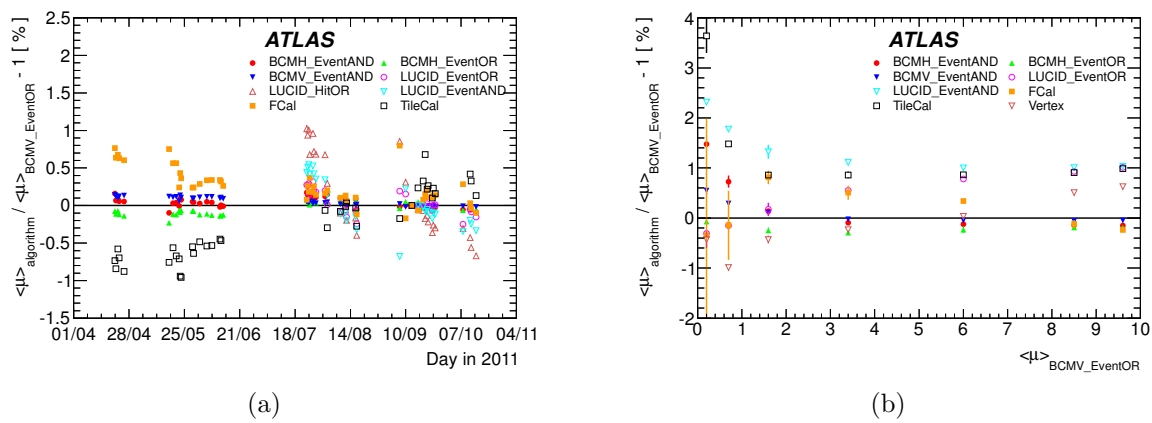


Figure 4.4: Left: Comparison of luminosities measured by different algorithms as a function of time in 2011. Right: Comparison of luminosities measured by different algorithms as a function of the average number of interactions per bunch cross,  $\mu$ , as measured by BCM\_VOR. The data were taken during a single run by separating the beams in the transverse direction, similar to a van der Meer scan.

reconstruction algorithm is significantly nonlinear with pileup, with the efficiency decreasing by  $\sim 30\%$  between pileup values of  $\mu = 1$  and  $\mu = 30$ .

### 4.6.1 Vertex Counting Method

The data for the inner detector-based luminosity measurements are collected through the standard ATLAS data acquisition system. Events are collected with either a random trigger or a trigger requiring hits in the minimum bias trigger scintillators (MBTS), two discs of scintillators mounted on the inner surfaces of the LAr end-cap cryostats ( $2.12 < |\eta| < 3.85$ ). Both triggers can select a specific set of BCIDs, which is essential for special runs where a bunch-by-bunch measurement is necessary, e.g. the vdm scans. The random trigger records a fraction of all bunch crossings in a specific set of colliding BCIDs, enabling an unbiased measurement of  $\mu_{\text{vis}}$  at the cost of lower statistics. The statistics collected worsen at low pileup values, where a large fraction of the triggered events do not contain a collision; hence, the random trigger is used mostly at high pileup. At lower pileup, the statistics can be recovered by using the MBTS trigger, which requires a small number of hits in the MBTS, usually at least two. Care must be taken to avoid bias due to the nontrivial trigger requirements: the trigger inefficiency, prescale, and deadtime must be taken into account. For vertices with at least five tracks, the inefficiency is negligible.

Vertices are reconstructed with two settings: the default reconstruction settings based on tracks with  $p_T > 400 \text{ MeV}$ , and tighter settings (“VtxLumi”) based on tracks with  $p_T > 900 \text{ MeV}$  with stricter requirements on the track quality. The tighter settings were introduced in 2012 to reduce the computational requirements associated with collecting  $\mathcal{O}(100 \text{ Hz})$  of inner detector data over the entire year. The studies described below are based on the 2011 data, where the vertex-based luminosity measurement is only performed on special runs, and use the default reconstruction settings.

The single-bunch instantaneous luminosity is calculated as follows. For the random trigger, the visible interaction rate is  $\mu_{\text{vis}} = \frac{N_{\text{vtx}}}{N_{\text{evt}}}$ , where  $N_{\text{vtx}}$  is the number of vertices recorded in  $N_{\text{evt}}$  triggered events. For the MBTS trigger,  $\mu_{\text{vis}} = \frac{N_{\text{vtx}}}{f_r \Delta t}$ , where  $N_{\text{vtx}}$  is the number of vertices recorded after correcting for the prescale and deadtime,  $f_r = 11245.5 \text{ Hz}$  is the LHC revolution frequency, and  $\Delta t$  is the duration of the measurement.  $\mu_{\text{vis}}$  is then corrected for pileup effects, described below in section 4.6.2, and finally the luminosity is given by equation 4.3.

### 4.6.2 Pileup Effects

The vertex reconstruction efficiency is strongly affected by three pileup-related phenomena:

- Vertex masking: a  $pp$  interaction fails to be reconstructed as a vertex because some or all of its tracks are used by an earlier vertex in the iterative reconstruction algorithm. This is the dominant pileup effect, which causes a large drop in the reconstruction efficiency at high pileup.

- Fake vertices: a vertex passes the cut on the minimum number of tracks due to acquiring tracks from another nearby  $pp$  interaction. This is a subdominant but significant effect, which causes a small increase in the reconstruction efficiency at high pileup.
- Split vertices: a single interaction is reconstructed as two separate vertices. This is a significant effect when considering vertices with two or more tracks, but is negligible for vertices with at least five tracks.

Corrections are derived for vertex masking and fake vertices. The fake vertex correction is derived using truth matching in minimum bias Monte Carlo simulation. The simulation sample was generated using PYTHIA 8, with tune A2M [11, 12]. For a given cut on the minimum number of tracks per vertex,  $n_{\text{trk,min}}$ , a reconstructed vertex is labelled as fake if less than  $n_{\text{trk,min}}$  of its tracks are matched to charged particles originating from the same generated  $pp$  interaction. The average number of reconstructed vertices labelled as fake by Monte Carlo truth matching is shown as a function of pileup in figure 4.6. The fake fractions show a significant dependence on  $\mu$  and on the  $n_{\text{trk,min}}$ .

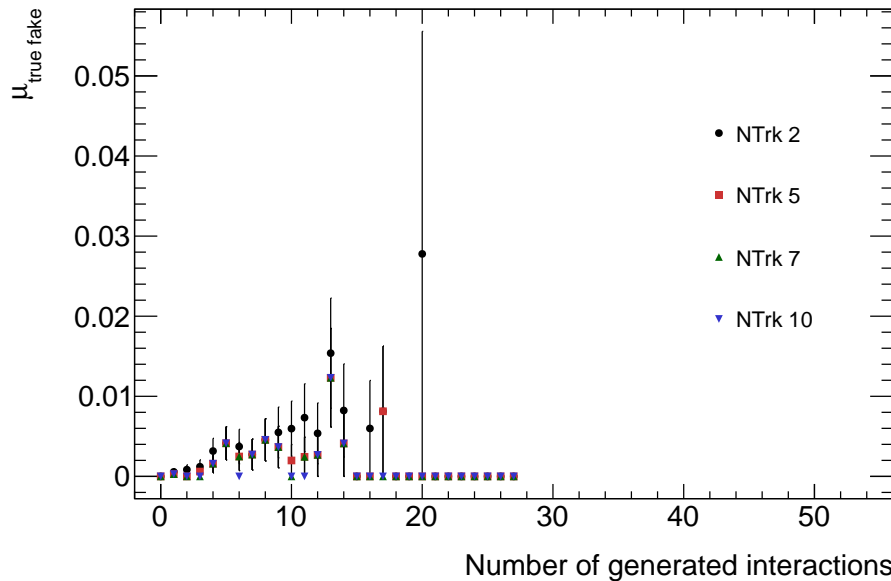


Figure 4.5: Average number of reconstructed vertices without a matched truth interaction, as a function of number of generated interactions per event. The contribution is below 0.1%.

A correction is derived for vertex masking using the distribution of longitudinal distances,  $\Delta z$ , between pairs of vertices in the same event. In the absence of masking, if the interaction region has a Gaussian longitudinal profile with width  $\sigma_z$ , then the  $\Delta z$  distribution would be a Gaussian with width  $\sigma_z \times \sqrt{2}$ . Masking manifests as an absence of reconstructed pairs near  $\Delta z = 0$ , as shown in figure 4.7.

The correction is derived in a data-driven way as follows.

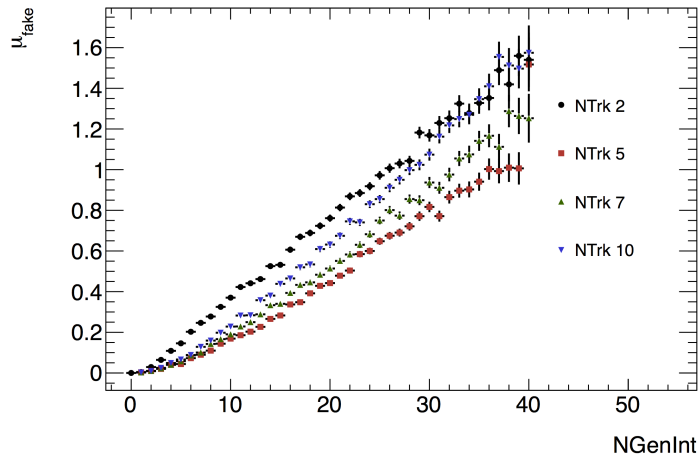


Figure 4.6: Average number of fake vertices per event as a function of the number of generated  $pp$  interactions.

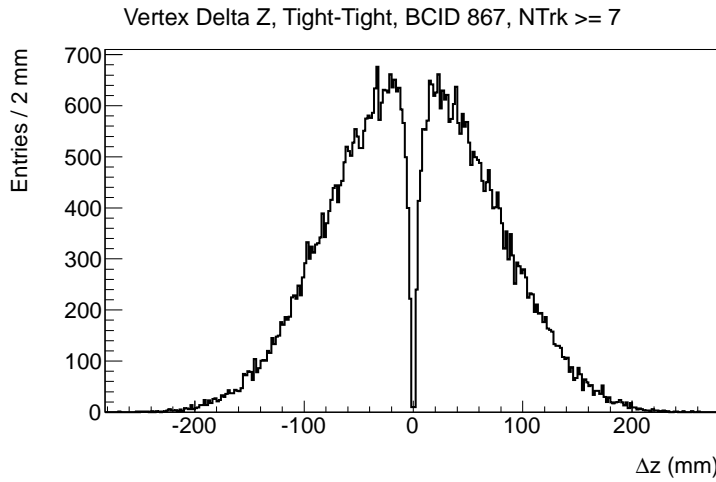


Figure 4.7:  $\Delta z$  distribution between pairs of vertices in the same event, with data from the May Van der Meer scan (ATLAS run 182013).

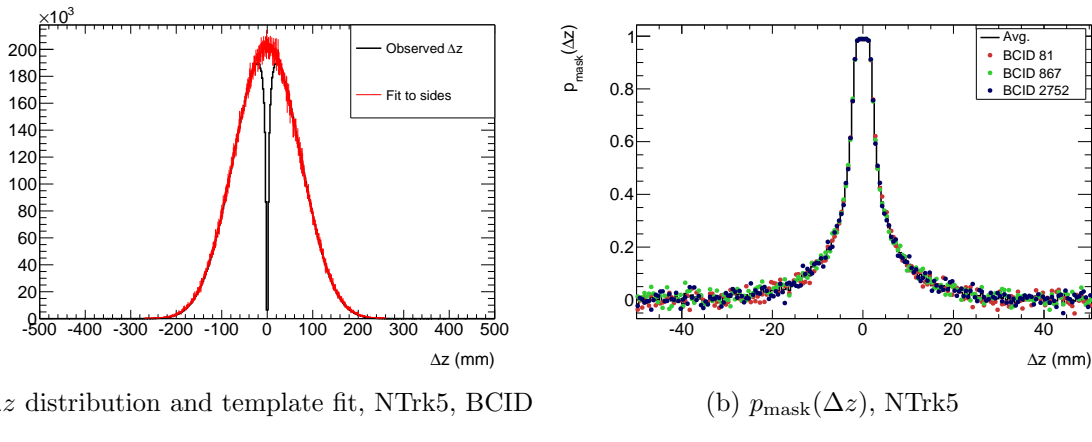
1. In a data sample with exactly two interactions per event, the number of masked pairs is equal to the number of masked vertices. Using data taken at low pileup values and selecting events with exactly two reconstructed vertices, we calculate the 2-vertex masking probability  $p_{\text{mask}}(\Delta z)$ , i.e. the probability that only one of two vertices separated by  $\Delta z$  is reconstructed. This function is assumed to be a universal property of the vertexing algorithm, independent of  $\mu$ .

Specifically, the expected  $\Delta z$  distribution in the absence of masking,  $f_{\text{exp}}(\Delta z)$ , is derived by randomly sampling pairs of points from the observed  $z$ -distribution of reconstructed vertices. Using  $f_{\text{exp}}(\Delta z)$  as a template, the *observed*  $\Delta z$  distribution,

$f_{\text{obs}}(\Delta z)$ , is fitted in the range  $30 \text{ mm} \leq |\Delta z| \leq 300 \text{ mm}$ , where vertex masking is negligible. Finally, the masking probability is defined as:

$$p_{\text{mask}}(\Delta z) = \frac{f_{\text{exp}}(\Delta z) - f_{\text{obs}}(\Delta z)}{f_{\text{exp}}(\Delta z)} \quad (4.14)$$

The masking probability functions derived from minimum bias Monte Carlo and for low- $\mu$  data are shown in figures 4.8 and 4.9.



(a)  $\Delta z$  distribution and template fit, NTrk5, BCID 81

(b)  $p_{\text{mask}}(\Delta z)$ , NTrk5

Figure 4.8: Calibration of the masking correction method on data, using run 182013. Left:  $\Delta z$  distributions and template fits using expected  $\Delta z$  distributions in the range  $30 \text{ mm} \leq \Delta z \leq 300 \text{ mm}$ . Right: pairwise vertex masking probability as a function of the longitudinal distance  $\Delta z$  between the vertices.

2. To derive a correction for a particular data sample at arbitrary  $\mu$ , an *expected*  $\Delta z$  distribution,  $f_{\text{exp}}(\Delta z)$ , is again derived by randomly sample pairs of vertices from the observed primary vertex  $z$ -distribution. Then, the total probability  $p_{\text{mask}}$  that given any two tight vertices, only one is reconstructed can be computed:

$$p_{\text{mask}} = \int_{-\infty}^{\infty} p_{\text{mask}}(\Delta z) f_{\text{exp}}(\Delta z) d(\Delta z). \quad (4.15)$$

3. The total masking probability  $p_{\text{mask}}$  is used to generate a map between the number of reconstructible vertices per event,  $N_{\text{vis}}$ , and the average number of reconstructed vertices per event,  $\mu_{\text{rec}}$ , as follows. Label the generated vertices  $v_i$ ,  $1 \leq i \leq N_{\text{gen}}$ , in the order in which the iterative vertexing algorithm reconstructs the vertices; similarly, let  $p_i$ ,  $1 \leq i \leq N_{\text{vis}}$ , be the probability that vertex  $v_i$  is reconstructed. Proceeding vertex-by-vertex, the  $p_i$  follow a recursion relation:

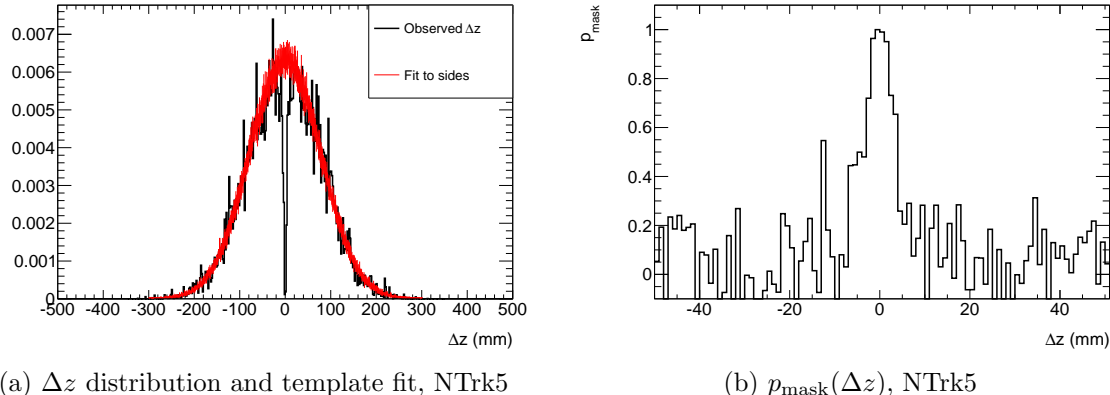


Figure 4.9: Calibration of the masking correction method on simulation, using 8 TeV minimum bias Monte Carlo (pythia 8, tune A2M). Left:  $\Delta z$  distributions and template fits using expected  $\Delta z$  distributions in the range  $30 \text{ mm} \leq \Delta z \leq 300 \text{ mm}$ . Right: pairwise vertex masking probability as a function of the longitudinal distance  $\Delta z$  between the vertices.

$$p_1 = 1 \quad (4.16)$$

$$p_2 = p_1 \times (1 - p_{\text{mask}}) \quad (4.17)$$

$$\dots \quad (4.18)$$

$$p_k = \prod_{i=1}^{k-1} (p_i \times (1 - p_{\text{mask}}) + (1 - p_i) \times 1) \quad (4.19)$$

$$= \prod_{i=1}^{k-1} (1 - p_i p_{\text{mask}}) \quad (4.20)$$

$$= p_{n-1} \times (1 - p_{n-1} p_{\text{mask}}) \quad (4.21)$$

The average number of reconstructed vertices is then:

$$\langle N_{\text{rec}} \rangle = \sum_{i=1}^{N_{\text{vis}}} p_i. \quad (4.22)$$

4. Finally, a map is computed between the average number of reconstructible vertices,  $\mu_{\text{vis}}$ , and the average number of reconstructed vertices,  $\mu_{\text{rec}}(\mu_{\text{vis}})$ , by convoluting  $\mu_{\text{rec}}(N_{\text{vis}})$  with a Poisson distribution:

$$\langle \mu_{\text{rec}} \rangle(\mu_{\text{vis}}) = \sum_{N_{\text{vis}}=0}^{\infty} P(N_{\text{vis}}; \mu_{\text{vis}}) \mu_{\text{rec}}(N_{\text{vis}}). \quad (4.23)$$

### 4.6.3 Vertex-Based Luminosity Measurements in 2011

Due to the low event rate available during physics runs, vertex counting was used to measure luminosity only in three special runs during 2011, where inner detector data were recorded by a special high-rate data stream. The data stream reads out events at  $\mathcal{O}(10\text{ kHz})$ , recording only the inner detector from a small number of bunch crossings, typically less than four. The three runs are the vdM calibration run in May 2011, the pileup scan in September 2011 shown in figure 4.4b, and a high- $\beta^*$  run with a single bunch used to measure the total  $pp$  cross section using the ALFA detector.

#### Van der Meer Scan

An example scan curve from the May 2011 vdM scan is shown in figure 4.10. The trigger used to collect the data required two hits in the MBTS, and selected 3 of the 14 colliding bunch pairs. The peak interaction rate during the fill was  $\mu \sim 2.3$ . The data are corrected for vertex masking and fakes, with the correction factor reaching up to 3% at the peak of the scan curves. Following the protocol described in section 4.4, the visible cross section is determined to be  $(38.50 \pm 0.12)\text{ mb}$ , where the uncertainty reflects the RMS spread between the three bunch crossings and the two scans.

#### Pileup Scan

The September 2011 pileup scan is used to derive systematic uncertainties due to the non-linear response of algorithms with respect to the number of interactions per bunch crossing. The scan was performed at the end of a physics run, displacing the beams in the transverse direction to obtain a sample of data at over a pileup range of  $0.02 \lesssim \mu \lesssim 10$  with otherwise identical conditions. The data was triggered by a random trigger selecting events from two BCIDs, 200 and 999. The data are corrected for vertex masking and fakes, with the correction reaching up to 10% as shown in figure 4.11 with respect to BCM\_VOR. A comparison of the luminosity measurements between vertex counting and BCM\_VOR, shown in figure 4.12, exhibits a slope of about 0.1% per unit of  $\mu$ .

#### ALFA Run

Finally, vertex counting provides a reliable luminosity measurement for the 2011 ALFA run, a special run used for a measurement of the total  $pp$  cross section [13]. The beams contained a single colliding bunch pair with  $\beta^* = 90\text{ m}$  and  $\mu \sim 0.03$ , in order to measure the scattering angle of elastic  $pp$  collisions. A special luminosity analysis is required to address the very low instantaneous luminosity of  $\mathcal{L} \sim 5 \times 10^{27}\text{ cm}^{-2}\text{ s}^{-1}$ , about six orders of magnitude lower than a typical physics fill. The calorimeter methods are unusable due to a

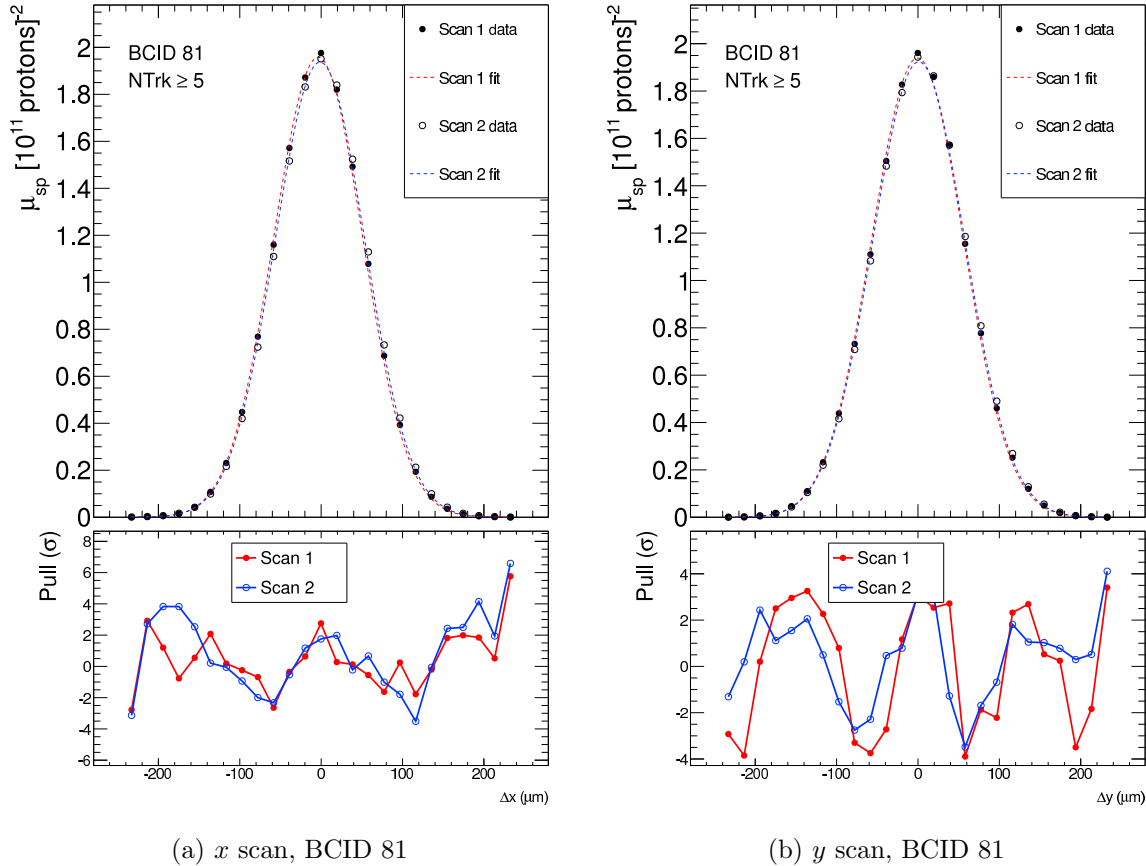


Figure 4.10:  $\mu_{\text{vis}}^{(sp)}$  vs. beam separation, with single gaussian plus constant fits, and pulls.

lack of sensitivity. For BCM and LUCID, the backgrounds at low instantaneous luminosity have a different composition: afterglow is negligible with a single colliding bunch, but beam-gas interactions can be significant, resulting in an extra 0.2% systematic uncertainty. The low-pileup conditions are ideal for vertex counting, eliminating the need to perform pileup corrections. The requirement of at least five tracks with  $p_T > 400$  MeV per vertex suppresses the beam-gas backgrounds. The data were recorded by a random trigger at approximately 1 kHz.

A comparison of luminosity measurements from BCM, LUCID, and vertex counting is shown in figure 4.13. To be consistent with the primary  $pp$  luminosity measurement, the central value is taken from BCM\_VOR; vertex counting shows agreement with this value to within 0.5%.

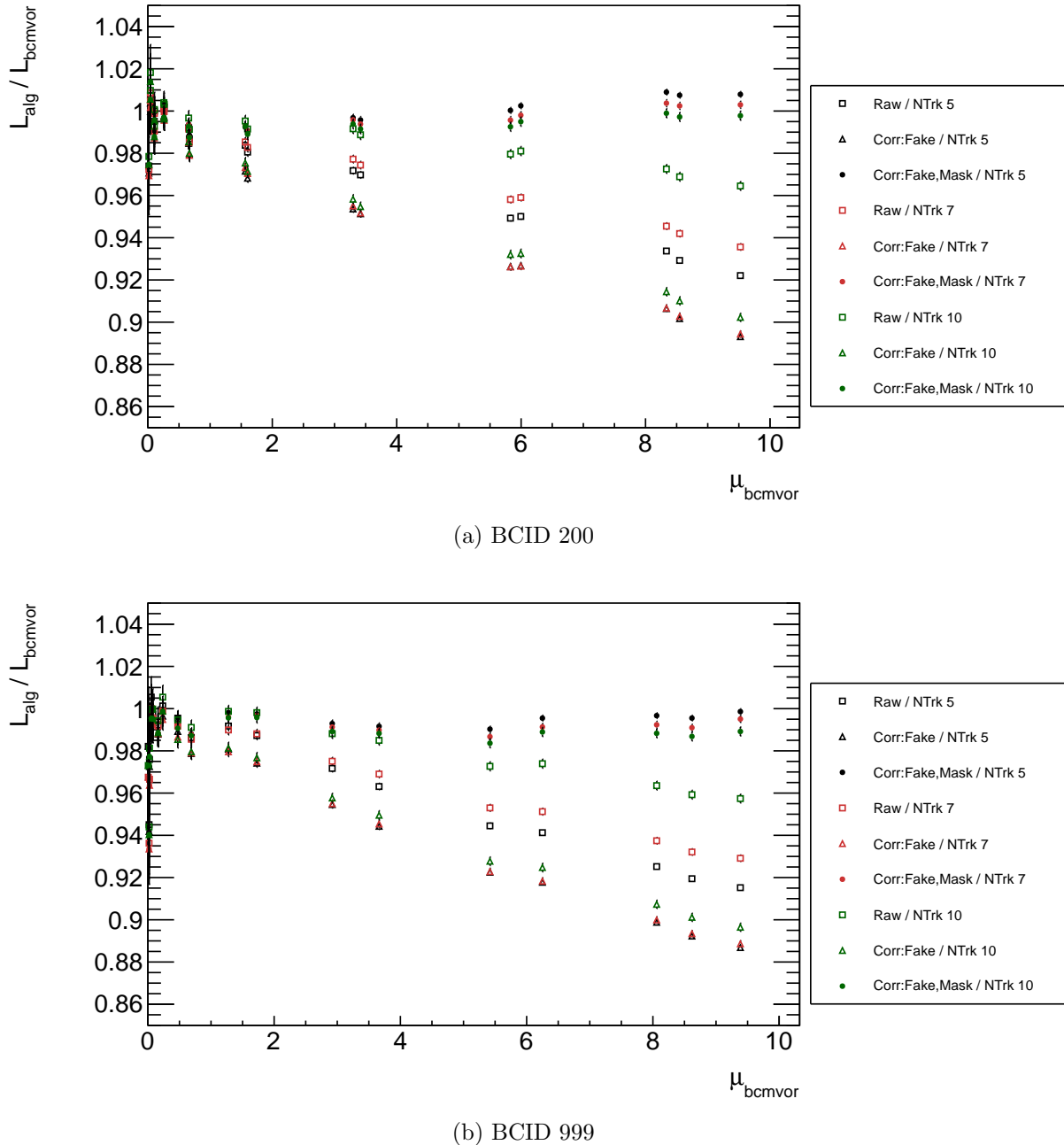


Figure 4.11: Ratio of luminosity values from vertexing to the reference value from BCM\_VOR during the pileup scan in September 2011. The black points show the vertex-based luminosity with  $\geq 5$  tracks, the red with  $\geq 7$  tracks, and the green with  $\geq 10$  tracks. The different shapes show the application of each successive pileup correction: the hollow squares show the vertex-based luminosity with no pileup corrections applied, the hollow triangles are corrected for fake vertices, and the solid circles are corrected for both fake and masked vertices.

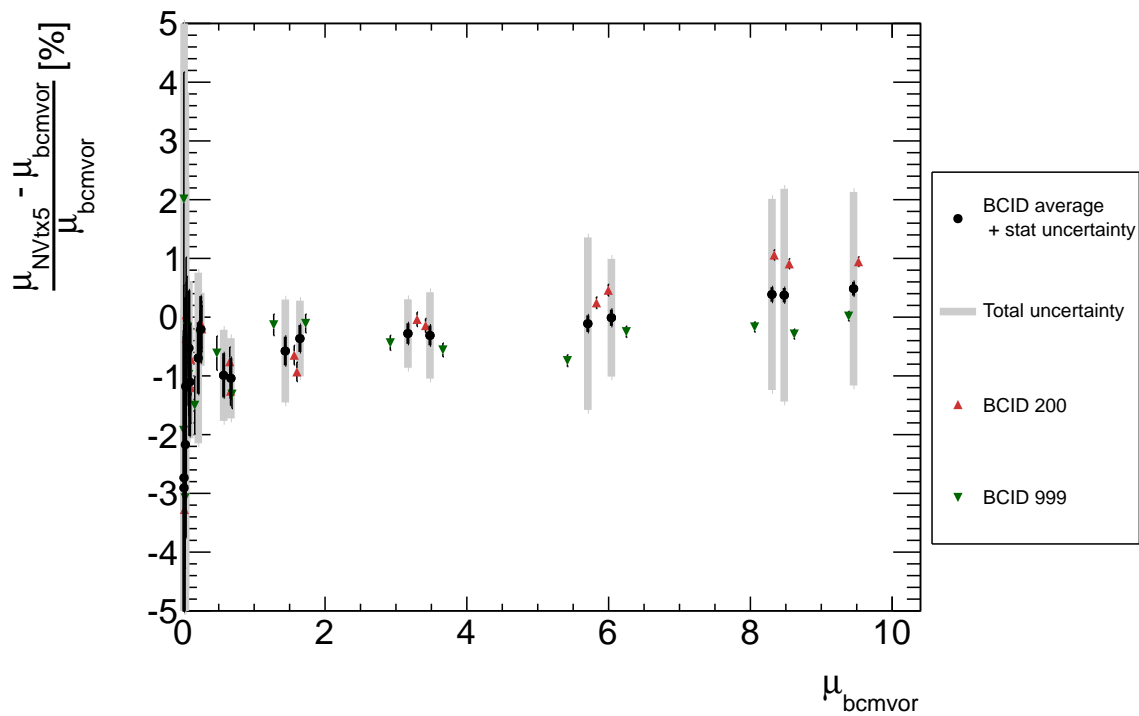


Figure 4.12: Percent difference between luminosities measured by vertex counting and BCM\_VOR during the pileup scan in September 2011. Vertices are required to have at least five tracks. The black points show the central values, taken to be the average between the two colliding BCIDs. The grey bars show the spread between BCIDs and between different track cuts ( $\geq 5$ ,  $\geq 7$ , and  $\geq 10$ ), summed in quadrature.

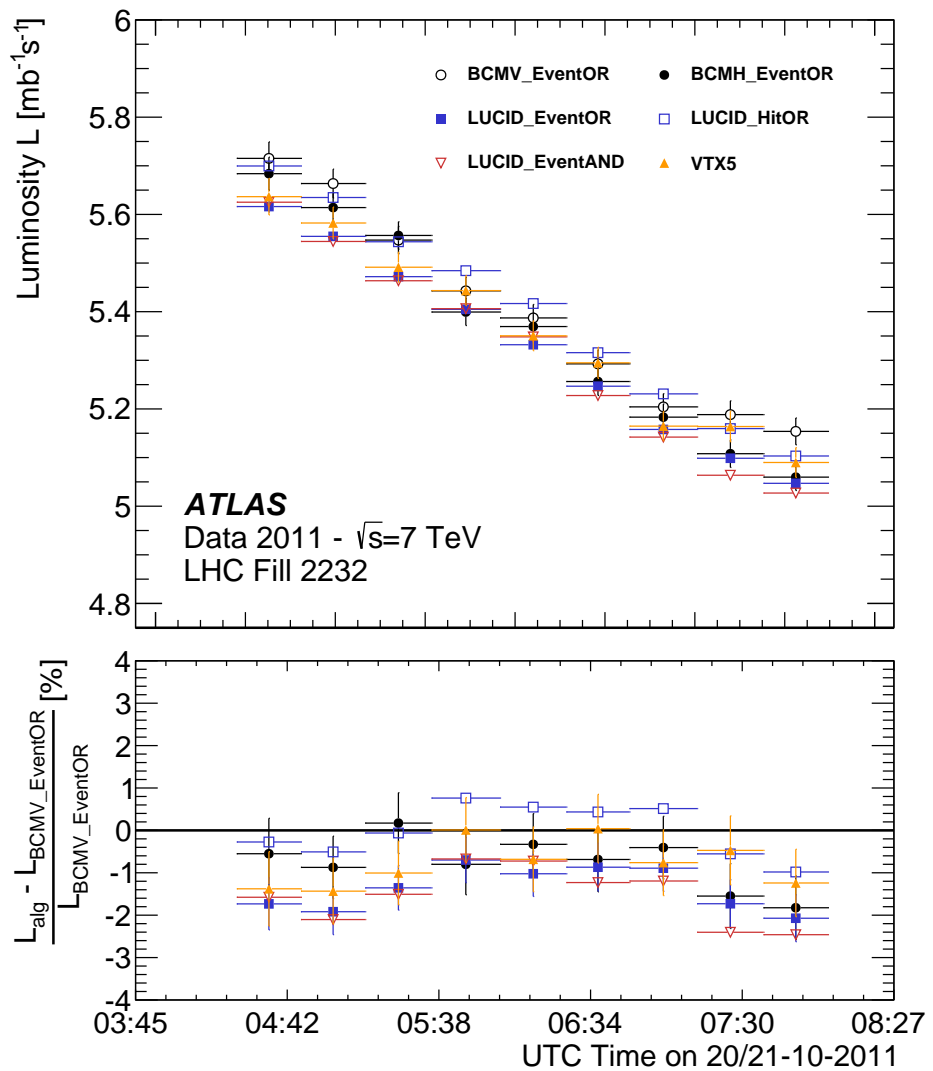


Figure 4.13: Luminosities measured by BCM, LUCID, and vertex counting during the  $\beta^* = 90$  m ALFA run in October 2011.

# Bibliography

- [1] P. Grafström and W. Kozanecki, *Luminosity determination at proton colliders*, Progress in Particle and Nuclear Physics (Jan. 2015) pp. 1–52.
- [2] The ATLAS Collaboration et al., *Improved luminosity determination in  $pp$  collisions at  $\sqrt{s} = 7$  TeV using the ATLAS detector at the LHC*, arXiv **C73.8** (2013) p. 2518, URL: <http://arxiv.org/abs/1302.4393>.
- [3] H. Frais-Kolbl, H. Frais-Koelbl, et al.,  
*The ATLAS Beam Conditions Monitor*, English, JINST **3.02** (2008) P02004–P02004,  
URL: <http://stacks.iop.org/1748-0221/3/i=02/a=P02004?key=crossref.925163f83f527ab642c655fa05d88708>.
- [4] The ATLAS Collaboration,  
*The ATLAS Experiment at the CERN Large Hadron Collider*,  
Journal of Instrumentation **3.08** (Aug. 2008) S08003–438.
- [5] S. van der Meer, *Calibration of the Effective Beam Height in the ISR* (June 1968) pp. 1–4.
- [6] C. Barschel et al., *Results of the LHC DCCT Calibration Studies* (Feb. 2012),  
URL: <http://cds.cern.ch/record/1425904>.
- [7] G. Anders et al.,  
*Study of the Relative LHC Bunch Populations for Luminosity Calibration* (Feb. 2012), URL: <http://cds.cern.ch/record/1427726>.
- [8] A. Alici et al.,  
*Study of the LHC ghost charge and satellite bunches for luminosity calibration*. (Feb. 2012), URL: <http://cds.cern.ch/record/1427728>.
- [9] The ATLAS Collaboration, *Measurement of the total cross section from elastic scattering in  $pp$  collisions at  $\sqrt{s} = 7$  TeV with the ATLAS detector*, Nuclear Physics B **889.C** (Dec. 2014) pp. 486–548.
- [10] S. Pagan Griso, D. Yu, and B. Heinemann, *Luminosity Measurement in  $pp$  Collisions at  $\sqrt{s} = 7$  TeV using Vertex Counting with the ATLAS Detector in 2011* (July 2013) pp. 1–59.
- [11] T. Sjöstrand, S. Mrenna, and P. Z. Skands, *A Brief Introduction to PYTHIA 8.1*, Comput. Phys. Commun. **178** (2008) pp. 852–867, arXiv: 0710.3820 [hep-ph].

- [12] ATLAS Collaboration, *Summary of ATLAS Pythia 8 tunes* (2012).
- [13] The ATLAS Collaboration, *Measurement of the total cross section from elastic scattering in pp collisions at  $\sqrt{s} = 7$  TeV with the ATLAS detector*, Nuclear Physics B **889.C** (Dec. 2014) pp. 486–548,  
URL: <http://dx.doi.org/10.1016/j.nuclphysb.2014.10.019>.

# Chapter 5

## Event Reconstruction

Once recorded by the detector, events are reconstructed using a wide variety of algorithms designed to identify the products of collisions at the center of the detector. The algorithms transform the raw data read out from the detector – hits in the inner detector silicon layers and TRT straws, energy deposits in calorimeter cells, and hits in the muon stations – into a list of physics objects and their energies or momenta. This section describes the techniques used to identify the objects used in the analyses described in chapters 7 and 8.

### 5.1 Track and Vertex Reconstruction

Tracks, nominally due to charged particles traversing the inner detector, are reconstructed using a series of algorithms based on hits in the inner detector [1–3]. The primary “inside-out” algorithm begins by constructing three-dimensional space points associated with the hits in the pixel and SCT layers. Track seeds are formed from sets of three space points in the first four layers of the inner detector (three pixel layers and the innermost SCT layer), constrained to be consistent with a track originating from the interaction region. The track seeds are extended through the remaining SCT layers using a combinatorial Kalman filter. After screening the track candidates to reduce random coincidences and ambiguities from very close tracks, the tracks are extended through the TRT. Finally, the track is refitted using all of the associated hits.

A complementary “outside-in” algorithm identifies tracks with fewer or zero silicon hits, which can arise from hadron decays or photon conversions in the silicon layers, or from track seeds removed during the ambiguity resolution. The algorithm starts from TRT segments, and adds silicon hits proceeding inwards.

Vertices are points consistent with being the origin of a set of tracks. Primary vertices are vertices nominally due to  $pp$  collisions, while secondary vertices arise from other processes like hadron decays or photon conversions. The primary vertex reconstruction algorithm reconstructs vertices one by one, alternately finding a vertex seed and then fitting the corresponding tracks [3, 4]. For most applications, the tracks are required to have  $p_T > 400 \text{ MeV}$ ,

no missing hits along the track in the pixel layers<sup>1</sup> (*holes*), and at most two holes in the SCT layers. The seed finding identifies the global maximum in the distribution of  $z$  coordinates of the tracks. The vertex position is then determined by an adaptive vertex fitting algorithm [5], a  $\chi^2$ -based fit which suppresses the contribution from outlier tracks. Tracks whose impact parameter is inconsistent by more than  $7\sigma$  with the vertex position are then reused to seed a new vertex, until no further seeds can be found.

For most applications, the vertex reconstruction is performed twice. After reconstructing an initial set of primary vertices, the position and size of the interaction region, or *beam spot*, is determined from a fit to the spatial distribution of vertices. The vertices are then reconstructed a second time using the beam spot as a constraint for seed finding and track fitting<sup>2</sup>.

## 5.2 Electrons

The signature of an electron is an energy deposit in the electromagnetic LAr calorimeter and a track pointing at the energy deposit [6, 7]. The electron reconstruction algorithm begins by searching for clusters of energy in the calorimeter, based on a grid of  $N_\eta \times N_\phi = 200 \times 256$  towers of size  $\Delta\eta \times \Delta\phi = 0.025 \times 0.025$ . The tower energy is the sum of the cell energies in all longitudinal layers within the tower. Energy deposits with  $E_T > 2.5$  GeV within a  $3 \times 5$  window of towers form the seeds for both electrons and photons. Seed clusters are rejected if there is a large amount of energy in the adjacent two towers in  $\eta$  or in the hadronic calorimeter behind the cluster.

Next, the reconstruction algorithm searches for a track within a cone of radius  $\Delta R = 0.3$  around the cluster barycenter. Two hypotheses are used for track pattern recognition and fitting: the standard pion hypothesis and an electron hypothesis that allows for larger energy losses due to bremsstrahlung. The cluster and track are required to satisfy one of the following two criteria:

- The barycenter of the cluster and the track extrapolation to the middle layer of the LAr calorimeter satisfy  $\Delta\phi < 0.2$  in the direction of track bending or  $\Delta\phi < 0.05$  in the other direction.
- The barycenter of the cluster and the track extrapolation to the middle layer of the LAr calorimeter, after rescaling the track momentum to the energy of the cluster, satisfy  $\Delta\phi < 0.1$  in the direction of track bending or  $\Delta\phi < 0.05$  in the other direction. This recovers low-energy electrons that potentially lose a significant fraction of their energy before reaching the calorimeter.

---

<sup>1</sup>Excluding missing hits due to an inactive detector element.

<sup>2</sup>For the luminosity measurement using vertices, the beam spot constraint is not applied in order to avoid biases due to changes in the size of the interaction region

For tracks with at least four silicon hits, the track and the cluster must also satisfy  $|\Delta\eta| < 0.05$ . Finally, the cluster and track are rebuilt using algorithms optimized for measurement of the electron properties. The cluster is rebuilt sequentially in all four layers, using an area of  $3 \times 7$  layer-2 cells in the barrel or  $5 \times 5$  layer-2 cells in the end-caps. The tracks of electron candidates are refit using an optimized electron track filter based on the Gaussian Sum Filter (GSF) algorithm [8]. The GSF track and the cluster must satisfy tighter spatial matching criteria:  $\Delta\phi < 0.1$  in the direction of track bending, or  $\Delta\phi < 0.05$  in the opposite direction. GSF tracks with less than four silicon hits are required to satisfy even tighter criteria:  $|\Delta\eta| < 0.35$  or 0.2 in the TRT barrel or end-cap, and  $\Delta\phi < 0.03$  in the direction of track bending or  $\Delta\phi < 0.02$  in the other direction.

### 5.2.1 Identification

Further requirements can be imposed on electron candidates to suppress backgrounds from sources like misidentified hadronic jets, photon conversions, and electrons from hadron decays. Three increasingly stringent sets of cuts are defined, called `loose++`, `medium++`, and `tight++`<sup>3</sup>. The analyses described in chapters 7 and 8 use the tight cuts to select signal electrons. The medium and loose cuts to derive data-driven background estimates. The loose set of cuts impose requirements on the shower shape in the first and second calorimeter layers, the quality of the track, the fraction of energy in hadronic calorimeter cells behind the LAr cells, and the spatial match of the track and the calorimeter cluster. The medium set of cuts contains more stringent versions of the loose cuts, and additionally require a small track impact parameter with respect to the primary vertex, a minimum number of high-threshold TRT hits associated with the track, and a hit in the innermost pixel layer. The tight set of cuts again contain more stringent versions of the medium cuts, with an additional cut on the ratio of the cluster energy to the track momentum ( $E/p$ ) and a veto of candidates associated to a photon conversion vertex.

### 5.2.2 Efficiency Measurements

The efficiency to detect an electron can be factorized into several components: seed cluster detection, reconstruction, and identification [7]. The efficiency to detect a cluster in the electromagnetic calorimeter is very high, above 99% for electrons with  $E_T = 15$  GeV and 99.9% for  $E_T = 45$  GeV. The reconstruction efficiency, covering the matching of a good-quality track to the cluster, and the identification efficiencies, covering the identification cuts with respect to reconstructed electrons, are measured using tag-and-probe techniques targeting  $Z \rightarrow ee$  and  $J/\Psi \rightarrow ee$  events. One electron, the tag, is required to satisfy strict selection criteria, while the second electron, the probe, is used for efficiency measurements.

The combined reconstruction and identification efficiencies are shown in figure 5.1. The reconstruction efficiency makes up 1%-5% of the total efficiency loss for electrons with  $E_T <$

---

<sup>3</sup>An alternative method of identification using a likelihood-based multivariate method has been developed, but is not used in this dissertation.

20 GeV, and less than 1% for electrons with  $E_T > 80$  GeV. The efficiencies are computed for both data and simulation, and the ratio between the two is used to correct the efficiency in simulation. The systematic uncertainty on the reconstruction efficiency is around 0.5% (0.5%–1.5%) for electrons with  $p_T > 25$  GeV ( $p_T < 25$  GeV), and 1%–2% (5%–6%) for the identification efficiency.

### 5.2.3 Energy and Momentum Measurement

For electron candidates with at least four silicon hits, the energy of the electron is taken from the calorimeter measurement, while the trajectory is taken from the GSF track. Candidates with fewer silicon hits are not used in this dissertation. The energy resolution of the calorimeter is parametrized as:

$$\frac{\sigma(E)}{E} = \frac{a}{\sqrt{E}} \oplus \frac{b}{E} \oplus c, \quad (5.1)$$

where  $a$ ,  $b$ , and  $c$  are the sampling, noise, and constant terms, respectively, and generally vary with  $\eta$ . The design value of the sampling term is 9–10% GeV $^{1/2}$  in the central region, and worsens at higher pseudorapidities due to the increased material in front of the calorimeters. The noise term, due to electronics noise and pileup effects, is approximately  $b = 350 \times \cosh \eta$  MeV. The constant term dominates the resolution at high energies, with a design value of  $c = 0.7\%$ .

As the ATLAS calorimeters are non-compensating, the energy measurement is calibrated using a multivariate algorithm trained on single-electron Monte Carlo (MC) simulation to determine the most probable electron energy. The method takes into account differences between data and simulation in the energy scales of each longitudinal layer and other detector effects not modeled in simulation.

After the initial simulation-based calibration, the electron energy scale and resolution are determined using  $Z \rightarrow ee$  events. Residual differences in the energy scale between data and simulation are parametrized as:

$$E^{\text{data}} = E^{\text{simulation}}(1 + \alpha_i), \quad (5.2)$$

where the  $\alpha_i$  quantify the energy scale difference in bins of pseudorapidity. The difference in energy resolution is derived assuming that the  $Z \rightarrow ee$  invariant mass distribution is well-modeled up to a Gaussian constant term,  $c_i$ :

$$\left(\frac{\sigma_E}{E}\right)^{\text{data}} = \left(\frac{\sigma_E}{E}\right)^{\text{simulation}} \oplus c_i, \quad (5.3)$$

where  $i$  again denotes bins in pseudorapidity. Histograms of the  $Z \rightarrow ee$  invariant mass distribution in simulation are then produced for a range of  $\alpha_i$  and  $c_i$  values, and the optimal values are determined using a  $\chi^2$  minimization with respect to data. The energy scale corrections are found to be  $\alpha_i \sim -1\%$  in the barrel,  $\sim 1\%-2\%$  in the barrel/end-cap transition region, and up to  $\sim -4\%$  in the end-caps. The resolution corrections are

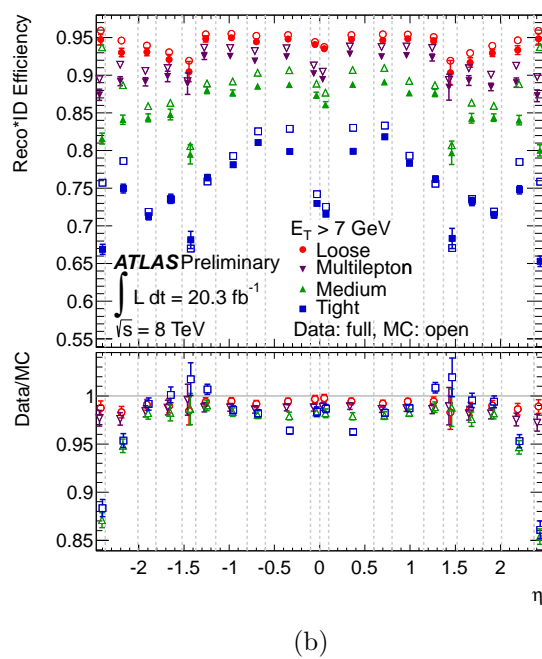
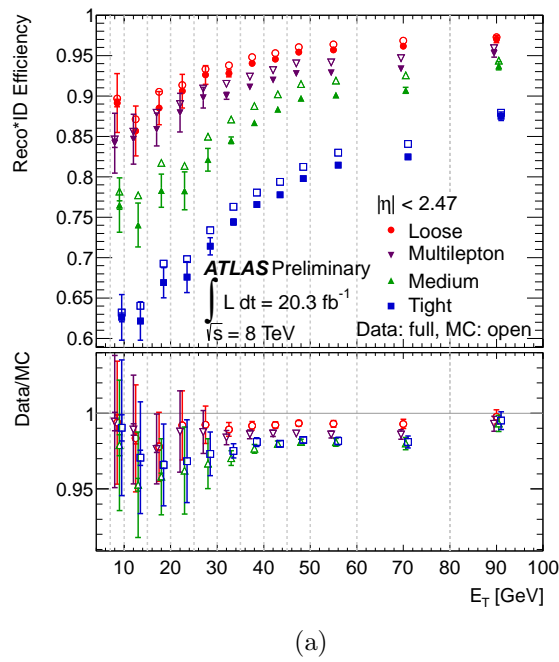


Figure 5.1: The combined reconstruction and identification efficiencies with respect to electrons detected as a cluster in the electromagnetic calorimeter, shown as a function of  $E_T$  (left) and  $\eta$  (right). The error bars show the statistical uncertainty (inner) and the statistical

symmetrized about  $\eta = 0$ , with values of  $c_i \approx 0.8\%$  in the barrel,  $\sim 3.3\%$  in the barrel/end-cap transition region, and  $\sim 0.5\%-2.5\%$  in the end-caps. The energy resolution is shown as a function of  $E_T$  in figure 5.2.

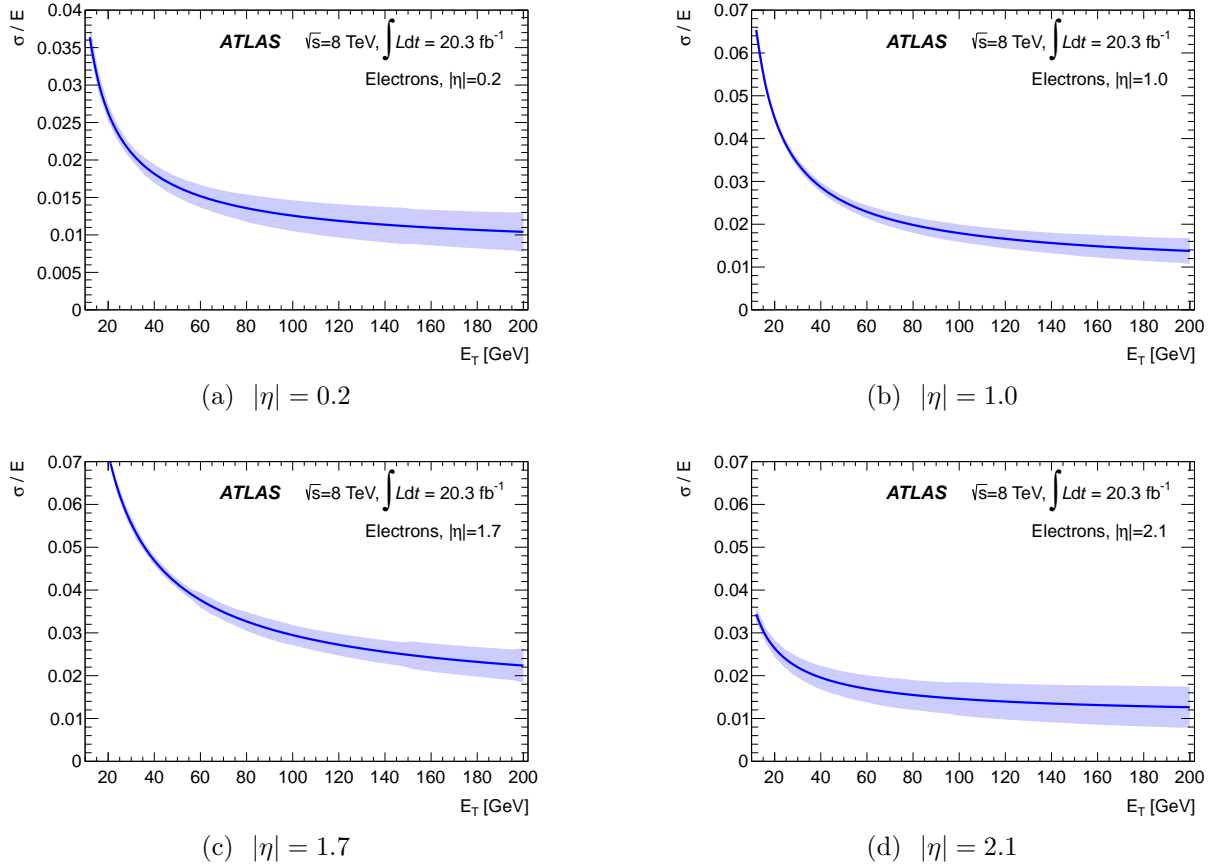


Figure 5.2: Electron energy resolution as a function of  $E_T$  for various values of  $|\eta|$ . The shaded band shows the uncertainty on the resolution [9].

Sources of systematic uncertainty on the energy scale include the closure of the  $Z \rightarrow ee$  method under injections of known energy scale variations, calorimeter gain and pedestal dependence, differences between data and simulation in the calibration of the calorimeter layers, and the modeling of material in front of and within the calorimeter. The total uncertainty ranges from 0.03%-0.22% for  $E_T = 40$  GeV and 0.27%-2.25% for  $E_T = 200$  GeV, with larger uncertainties in the pseudorapidity range  $1.37 < |\eta| < 1.82$  corresponding to the transition region between the barrel and the end-cap.

The systematic uncertainty on the energy resolution is less than 10% for electrons with  $E_T < 50$  GeV, and asymptotically approaches  $\sim 40\%$  for high  $E_T$ . At low energies, the pileup contribution to the noise term,  $b$ , dominates the uncertainty; at higher energy, uncertainty is

due to a mix of the sampling term,  $a$ , the pileup contribution to  $b$ , the modeling of material, and the intrinsic accuracy of the  $Z \rightarrow ee$  method.

## 5.3 Muons

Muons are identified by matching tracks in the muon spectrometer to tracks in the inner detector. The requirements differ based on the instrumentation available in the vicinity of the muon candidate. The analyses described here use *combined* (CB) muons, consisting of matched tracks reconstructed independently in the inner detector and the muon spectrometer. The muon momentum is determined from a statistical combination of the two track's parameters and their corresponding covariance matrices. Combined muons have the highest purity, but suffer from a loss of acceptance near  $\eta \sim 0$ , where the muon spectrometer has gaps to accommodate services for the inner detector and calorimeters, and  $1.1 < \eta < 1.3$ , where some trajectories only pass through one muon station due to incomplete installation. The remaining categories are *standalone* (SA) muons, consisting of a track only in the muon spectrometer; *segment-tagged* (ST) muons, consisting of an inner detector track and one or more track segments in the MDT or CSC chambers; and *calorimeter-tagged* (CaloTag) muons, consisting of an inner detector track matched to a calorimeter energy deposit consistent with the passage of a muon. These categories can recover efficiency in regions of the detector with less instrumentation at the cost of lower muon purity, but are not used in this dissertation.

For all categories of muons, the inner detector track is required to have at least 1 pixel hit, at least 5 SCT hits, at most 2 pixel or SCT holes, and at least 9 TRT hits for  $0.1 < |\eta| < 1.9$ . Energy losses in the calorimeter due to ionization, bremsstrahlung, and electron pair production must also be taken into account.

### 5.3.1 Efficiency Measurements

The efficiency of the reconstructing CB muons is measured as:

$$\epsilon(\text{CB}) = \epsilon(\text{CB}|\text{ID})\epsilon(\text{ID}|\text{MS}), \quad (5.4)$$

where  $\epsilon(\text{CB}|\text{ID})$  is the probability that a muon reconstructed as an inner detector track is also reconstructed as a CB muon, and  $\epsilon(\text{ID}|\text{MS}) \approx \epsilon(\text{ID})$  is the probability that a muon with a track in the muon spectrometer, i.e. a CB or SA muon, is also reconstructed as an inner detector track. The latter approximation is made because  $\epsilon(\text{ID})$  is not directly accessible in data.

The efficiencies are measured using tag-and-probe techniques similar to those described in section 5.2.2, targeting  $Z \rightarrow \mu\mu$  and  $J/\Psi \rightarrow \mu\mu$  events. In this case, the tag muon is required to be a CB muon, and the probe muon is a CB or SA muon in the case of measuring  $\epsilon(\text{ID}|\text{MS})$ , and a CaloTag muon for the measurement of  $\epsilon(\text{CB}|\text{ID})$ . The efficiencies for all types of muon are shown in figure 5.3. CB muons have an efficiency of greater than 97%

in most of the pseudorapidity range, except for significant inefficiencies due to gaps in the muon spectrometer in the ranges  $|\eta| < 0.1$  and  $1.1 < \eta < 1.3$ . The measured efficiencies in data and simulation agree to within  $\sim 2\%$ , and the ratios in each pseudorapidity bin are used as scale factors to correct the efficiency in simulation. The systematic uncertainty on the scale factors is below 0.2% for most of the pseudorapidity range, rising to  $\sim 0.3\%$  near  $|\eta| \sim 2.5$  and  $\sim 0.7\%$  near  $|\eta| \sim 0$ .

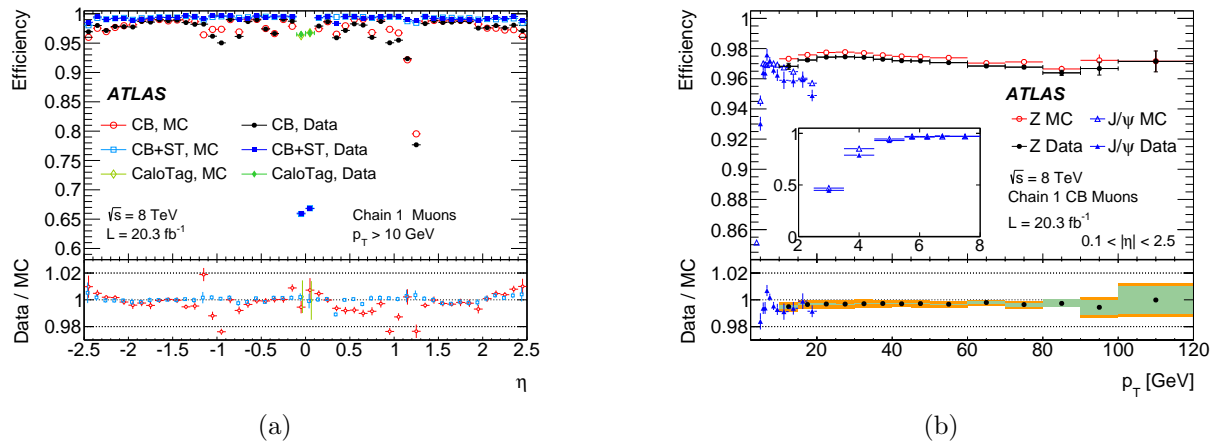


Figure 5.3: Muon reconstruction efficiencies as a function of  $\eta$  for muons with  $p_T > 10$  GeV (left), and as a function of  $p_T$  for muons with  $0.1 < |\eta| < 2.5$  (right). The uncertainty bars on the points indicate statistical uncertainties. The bottom plots show the ratio between the measured and simulated efficiencies, with the combination of statistical and systematic uncertainties indicated by the uncertainty bars.

### 5.3.2 Energy Scale and Resolution

The muon momenta in simulation are scaled and smeared to match the momentum scale and resolution in data. The corrections are derived in bins of  $\eta$  and  $\phi$ , with boundaries chosen to minimize the variation of the correction in each bin, and are applied separately to the transverse momenta measured by the inner detector (ID) and the muon spectrometer (MS). Specifically, the correction is implemented as:

$$p_T^{\text{Cor,Det}} = \frac{p_T^{\text{MC,Det}} + \sum_{n=0}^1 s_n^{\text{Det}}(\eta, \phi) (p_T^{\text{MC,Det}})^n}{1 + \sum_{m=0}^2 \Delta r_m^{\text{Det}}(\eta, \phi) (p_T^{\text{MC,Det}})^{m-1} g_m}, \quad (5.5)$$

where  $\text{Det} = \text{ID}$  or  $\text{MS}$ , the  $\Delta r_m^{\text{Det}}(\eta, \phi)$  parametrize the momentum resolution smearing, the  $s_n^{\text{Det}}(\eta, \phi)$  parametrize the scale corrections, and the  $g_m$  are normally-distributed random

variable with mean 0 and width 1<sup>4</sup>. The constant scale correction term,  $s_0^{\text{MS}}$ , accounts for the difference between data and simulation in the energy lost by muons before reaching the muon spectrometer.  $s_0^{\text{ID}}$  is set to zero due to the negligible energy loss before the inner detector. The linear terms,  $s_1^{\text{ID,MS}}$ , models discrepancies between data and simulation in the magnetic field integral and the radial dimension of the detector. The resolution corrections  $\Delta r_m^{\text{Det}}$  represent deviations from the resolution in data, which is parametrized empirically as:

$$\frac{\sigma(p_T)}{p_T} = \frac{r_0}{p_T} \oplus r_1 \oplus r_2 \cdot p_T, \quad (5.6)$$

where the  $r_0$  term describes energy lost by muons as they traverse the material of the detector, the  $r_1$  term describes multiple scattering, magnetic field inhomogeneities, and local radial displacements, and the  $r_2$  term describes intrinsic resolution effects due to the spatial resolution of the hit measurements and residual misalignment.

The corrections are derived from  $J/\Psi \rightarrow \mu\mu$ ,  $\Upsilon \rightarrow \mu\mu$ , and  $Z \rightarrow \mu\mu$  events using a template maximum likelihood fit, similar to that described in section 5.2.3. The effect of the corrections on the invariant mass distribution of  $Z \rightarrow \mu\mu$  events is shown in figure 5.4, along with the total systematic uncertainty. The muon resolution as measured in  $Z$ ,  $\Upsilon$ , and  $J/\Psi$  events is shown in figure 5.5.

## 5.4 $\tau$ Leptons

The signature of  $\tau$  leptons is significantly more complex than electrons and muons due to the fact that they decay to a diverse set of final states. Tau leptons have a proper decay length of  $87\mu\text{m}$ , and therefore typically decay before reaching the active layers of the detector. The leading decay modes are shown in table 5.1. The branching fractions to  $e\bar{\nu}_e\nu_\tau$  or  $\mu\bar{\nu}_\mu\nu_\tau$  are 17.83% and 17.41%, respectively. The remaining 64.8% of decays are to hadrons plus a neutrino. The hadronic decay modes contain one charged pion in 72% of the decays, and three charged pions in 22% of the decays; the majority of the remainder contain one or more kaons. The hadronic decay modes also frequently contain neutral pions, with 78% containing at least one neutral pion.

In this dissertation, no effort is made to identify or reconstruct leptonic  $\tau$  decays ( $\tau_{\text{lep}}$ ), regarding them only as electrons or muons plus missing transverse energy (see section 5.6). Hadronic  $\tau$  decays ( $\tau_{\text{had}}$ ) are identified using their visible decay products, namely the neutral and charged hadrons, which are collectively called  $\tau_{\text{had-vis}}$ . The signature consists of a narrow jet with one or three tracks, called one-prong or three-prong decays, respectively. Up to two  $\pi^0 \rightarrow \gamma\gamma$  decays are also included. The reconstruction and identification proceeds as follows [11]:

---

<sup>4</sup>Note that this equation does not apply to cases where the resolution in data is better than that in simulation. In these cases, the resolution difference is included in the positive ID and MS variations, and the effect of the positive variation on the physical observables is symmetrized about the nominal value.

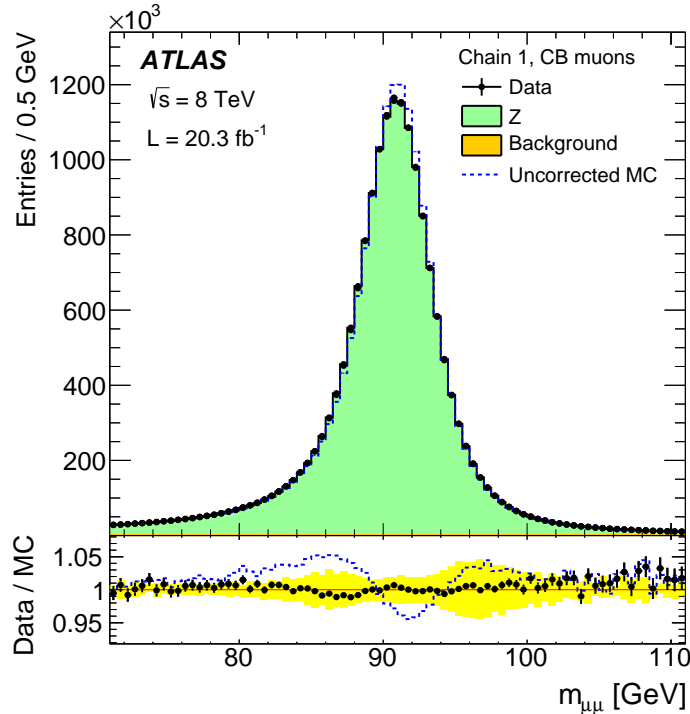


Figure 5.4: Dimuon invariant mass distribution of  $Z \rightarrow \mu\mu$  events, using CB muons. The top panel shows the invariant mass distribution for data (black points), expected  $Z \rightarrow \mu\mu$  signal from MC simulation (green), and expected background from MC simulation (yellow). The muon momentum corrections are applied to the MC simulation, and the total MC prediction is normalized to the data. The dashed histogram shows the background plus signal without muon momentum corrections. The bottom panel shows the ratio of the data to the normalized MC prediction, with the systematic uncertainty on the momentum corrections shown in the yellow band.

Decay	Branching Fraction [%]
$e^- \bar{\nu}_e \nu_\tau$	$17.83 \pm 0.04$
$\mu^- \bar{\nu}_\mu \nu_\tau$	$17.41 \pm 0.04$
$\pi^- \nu_\tau$	$10.83 \pm 0.06$
$\pi^- \pi^0 \nu_\tau$	$25.52 \pm 0.09$
$\pi^- \pi^0 \pi^0 \nu_\tau$	$9.30 \pm 0.11$
$\pi^- \pi^+ \pi^- \nu_\tau$	$9.31 \pm 0.06$
$\pi^- \pi^+ \pi^- \pi^0 \nu_\tau$	$4.62 \pm 0.06$

Table 5.1: Leading branching fractions of the  $\tau$  lepton to final states with leptons or pions. Most of the remaining decays are to final states with kaons. From [10].

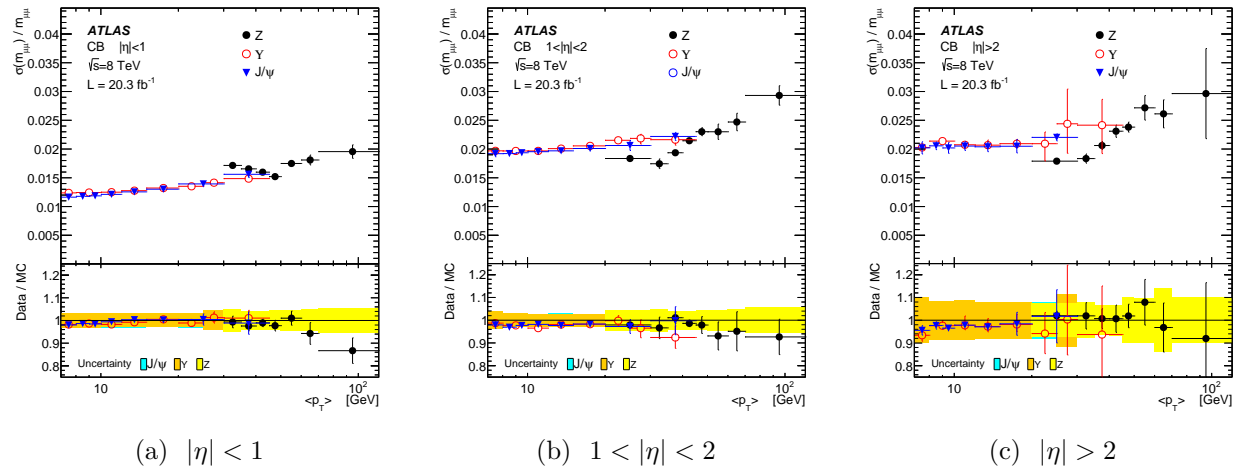


Figure 5.5: Dimuon invariant mass resolution for combined muons as a function of the average muon  $p_T$  in three pseudorapidity regions. The resolution is determined from  $J/\Psi \rightarrow \mu\mu$ ,  $\Upsilon \rightarrow \mu\mu$ , and  $Z \rightarrow \mu\mu$  events. Both muons are required to be in the same pseudorapidity region. The  $J/\Psi$  and  $\Upsilon$  data are plotted as a function of  $\bar{p}_T = \frac{p_{T1} + p_{T2}}{2}$ , while  $Z$  data are plotted as a function of  $p_T^* = m_Z \sqrt{\frac{\sin \theta_1 \sin \theta_2}{2(1 - \cos \alpha_{12})}}$ , where  $\theta_{1,2}$  are the polar angles of the two muons and  $\alpha_{12}$  is the angle between the two muons, which removes the correlation between  $m_{\mu\mu}$  and  $\bar{p}_T$ . The lower panels show the ratio between data and the corrected MC, with bands representing the uncertainty on the MC corrections for the three calibration samples.

- Jets are reconstructed using the anti- $k_t$  algorithm with a distance parameter of  $R = 0.4$ , built from TopoClusters calibrated with a local hadronic calibration. Jets with  $p_T > 10$  GeV and  $|\eta| < 2.5$  are used as seeds for  $\tau$  lepton candidates.
- For each jet seed, the  $\tau$  vertex is chosen to be the primary vertex with the greatest  $\sum p_T$  of tracks in a cone of radius  $\Delta R = 0.2$  around the jet seed. This vertex defines the  $\tau_{\text{had-vis}}$  direction, i.e. is used to determine the  $\eta$  and  $\phi$  of the  $\tau$  candidate.
- $\pi^0$  candidates, consisting of a pair clusters within  $\Delta R < 0.2$  of the  $\tau$  candidate, are identified using a multivariate boosted decision tree (BDT) algorithm. The algorithm identifies up to two  $\pi^0$ s.
- BDT-based identification algorithms are used to discriminate hadronic  $\tau$  decays from the backgrounds, primarily due to jets with low track multiplicity. The BDTs use many input variables describing the energy cluster, the spatial arrangement and energy of the tracks, and the neutral pions. Separate BDTs are trained for one-prong and three-prong  $\tau$  decays, using simulated  $Z \rightarrow \tau\tau$ ,  $W \rightarrow \tau\nu$ , and  $Z' \rightarrow \tau\tau$  decays for signal and collision data samples for the background. Three working points with different identification efficiencies are defined: BDT-loose, BDT-medium, and BDT-tight.

The performance of the identification algorithms is shown in figure 5.6. The correction factors applied to simulated samples to equalize the efficiencies in simulation and real data are shown in figure 5.7. The correction factors are derived by measuring the efficiencies in data and simulation, using a tag-and-probe method targeting  $Z \rightarrow \tau_{\text{lep}}\tau_{\text{had}}$  events. For the BDTight working point, the corrections range from 94%-96%, and carry uncertainties between 2.0%-2.2%.

- An additional BDT-based algorithm rejects one-prong  $\tau$  candidates consistent with an electron. The most powerful discriminating variables are the ratio of high- to low-threshold TRT hits on the track and the ratio of energies deposited in the electromagnetic and hadronic calorimeters. The electron rejection power versus the  $\tau$  efficiency, derived from simulated  $Z \rightarrow ee$  events, is shown in figure 5.8.

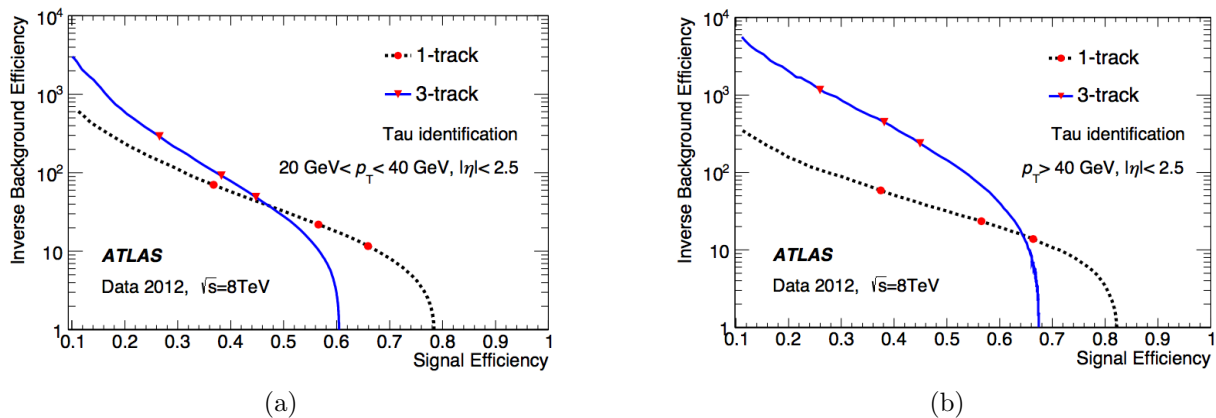


Figure 5.6: Inverse background efficiency (rejection power) versus signal efficiency for the BDT-based offline  $\tau$  identification algorithm. (a) shows the efficiency for  $\tau$  leptons with  $20 \text{ GeV} < p_T < 40 \text{ GeV}$ , and (b) shows the efficiency for  $\tau$  leptons with  $p_T > 40 \text{ GeV}$ . The three points on each curve correspond to the BDT-tight, BDT-medium, and BDT-loose working points, in order of increasing signal efficiency and decreasing background rejection power. The background consists of simulated multijet events, while the signal consists of simulated  $Z$ ,  $W$ , and  $Z'$  events decaying to  $\tau$  leptons.

### 5.4.1 Energy Scale and Resolution

The hadronic  $\tau$  reconstruction and identification are based on calorimeter cells calibrated at the local hadronic scale. Several corrections are applied to correct the energy to a  $\tau$ -specific energy scale (TES). First, corrections are derived using simulated  $Z \rightarrow \tau\tau$ ,  $W \rightarrow \tau\nu$ , and  $Z' \rightarrow \tau\tau$  events, generated with PYTHIA8. These corrections are determined as a function of the reconstructed  $\tau_{\text{had-vis}}$  energy and pseudorapidity based on the medium identification

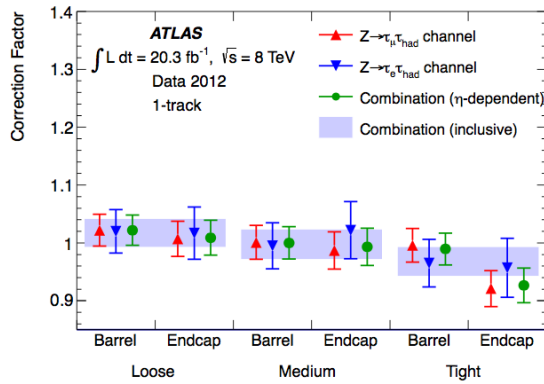


Figure 5.7: Correction factors applied to simulation to equalize the efficiency to that measured in data, as measured in  $Z$  tag-and-probe data. The error bars show the combined statistical and systematic uncertainty.

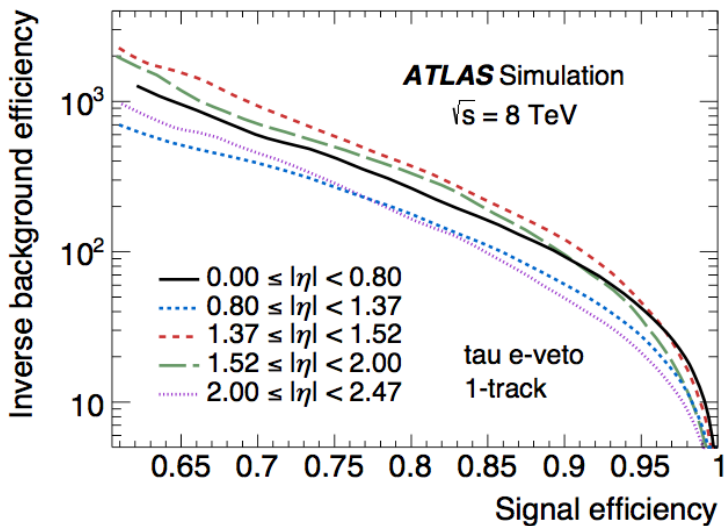


Figure 5.8: Electron rejection power versus 1-track  $\tau_{\text{had}}$  efficiency for the electron rejection BDT.

working point. A small pseudorapidity correction, reaching up to  $|\Delta\eta| = 0.01$ , corrects a bias due to underestimated cluster energies in poorly-instrumented regions of the calorimeter. To account for pileup, 90–420 MeV per additional reconstructed vertex is subtracted from the reconstructed  $\tau_{\text{had-vis}}$  energy, depending on  $\eta$ . The simulated  $\tau_{\text{had-vis}}$  energy resolution after these corrections is shown in figure 5.9, and ranges between about 20% at very low energy to about 5% above a few hundred GeV.

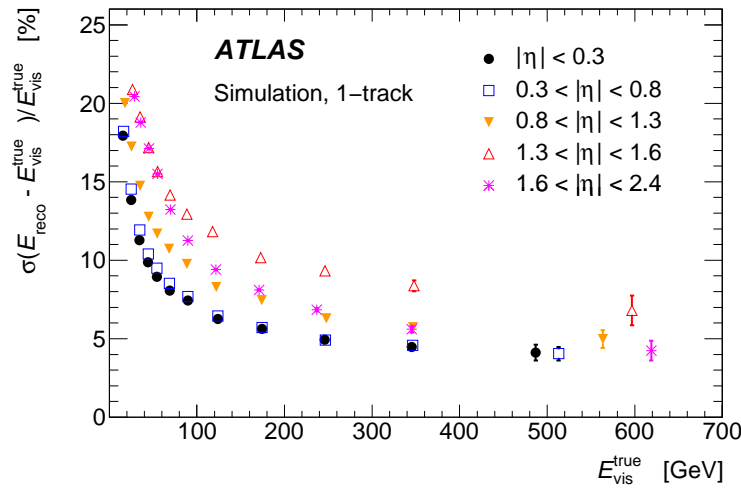


Figure 5.9: Energy resolution for hadronically decaying  $\tau$  leptons with one associated track in various pseudorapidity regions. The resolution is the standard deviation of a Gaussian fit to the distribution of  $\frac{E_{\text{reco}} - E_{\text{true-vis}}}{E_{\text{true-vis}}}$  in bins of  $E_{\text{true-vis}}$  and  $|\eta_{\text{true-vis}}|$ .

Finally, data-driven corrections and systematic uncertainties on the  $\tau$  energy scale are derived using a *deconvolution* method [12]. The method combines the systematic uncertainties on the single-particle response of the calorimeters based on the well-known branching fractions of hadronically decaying  $\tau$  leptons. A TES correction of about 1% is determined. Including additional systematic uncertainties covering the detector modeling, pileup, non-closure of the calibration method, and the hadronic shower model, the total TES uncertainty is 2 – 3% for one-prong decays and 2 – 4% for three-prong decays.

## 5.5 Jets

Jets play an important complementary role to leptons in the analyses described in the following chapters. The new physics scenarios considered often produce jets in addition to the three required leptons. If the new particles are colored, as in strongly produced supersymmetry, then high- $p_T$  jets can be produced in cascade decays. Alternatively, if the new particles decay via the weak interaction, then the decays will often contain hadronically decaying weak bosons. From the background point of view, due to the colored initial state in  $pp$  collisions,

jets are produced copiously at the LHC. Despite the stringent lepton identification cuts, jets misidentified as leptons or containing semileptonic decays can constitute a significant source of backgrounds to trilepton final states.

The reconstruction of jets in the calorimeter is based on topological clusters of energy [12, 13]. The reconstruction steps are shown in figure 5.10. Clusters are formed by grouping together calorimeter cells based on their signal-to-noise ratio,  $S/N$ , where the  $N$  includes electronic noise and contributions from pileup interactions. Cells with  $S/N > 4$  form the cluster seeds, which are then expanded to include all connected cells with  $S/N > 2$ . Finally, cells along the perimeter with  $S/N > 0$  are added to the cluster. The cluster energies are then calibrated according to one of two scales: the electromagnetic (EM) scale assumes that the cell energy is due to an electromagnetic shower, while the local cell signal weighting (LCW) method classifies energy deposits as electromagnetic or hadronic in origin. The jets used in this dissertation are constructed from cells calibrated at the LCW scale.

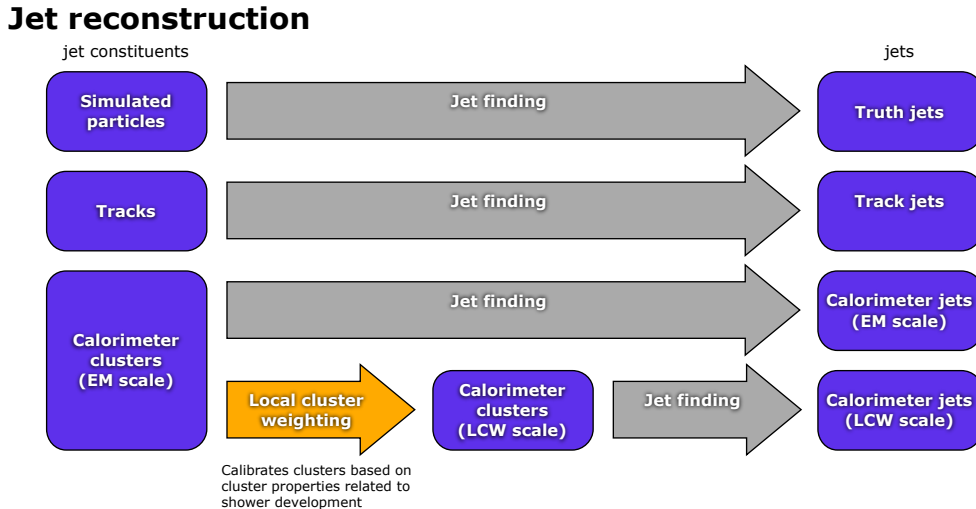


Figure 5.10: Overview of the jet reconstruction, showing the inputs to and outputs from the jet finding algorithms. The bottom two rows show the reconstruction of calorimeter jets, while the top two rows show jets built from truth particles in simulation and from tracks.

Next, the jet finding algorithms group the calibrated clusters into collections of jets. The algorithm used in this dissertation is the anti- $k_t$  algorithm with a distance parameter of  $R = 0.4$ , implemented in FASTJET [14, 15]. A distance measure between objects,  $d_{i,j}$ , and between objects and the beam,  $d_{i,B}$ , is defined as

$$d_{i,j} = \min(k_{t,i}^{2p}, k_{t,j}^{2p}) \frac{\Delta_{ij}^2}{R^2}, \quad (5.7)$$

$$d_{i,B} = k_{t,i}^{2p}, \quad (5.8)$$

where  $k_{t,i}$  is the transverse momentum of object  $i$ ,  $\Delta_{i,j} = \sqrt{(y_i - y_j)^2 + (\phi_i - \phi_j)^2}$  is the geometrical distance in rapidity ( $y_{i,j}$ ) and azimuthal angle ( $\phi_{i,j}$ ), and  $p$  is a parameter that controls the relative importance of energy versus geometrical ( $\Delta_{ij}$ ) scales, taken to be  $p = -1$  for the anti- $k_t$  algorithm. The algorithm combines objects sequentially by considering the smallest distance in the event. If the smallest distance is between two objects  $i$  and  $j$ , then the objects are combined. If the smallest distance is between object  $i$  and the beam  $B$ , then  $i$  is classified as a jet and removed from the object list. The algorithm continues until there are no objects left.

Loose quality cuts are applied to reject events with jets due to non-collision sources, such beam-gas collisions between protons in one beam and the residual gas in the beam pipe, beam-halo events due to collisions with upstream collimators, muons from cosmic rays, and calorimeter noise. The cuts have an efficiency of above 99.8% for retaining real jets.

### 5.5.1 Energy Scale and Resolution

The jet energy is calibrated in several steps, as shown in figure 5.11. First, pileup and origin corrections are applied. Energy contributions from pileup interactions in the same or nearby bunch crossings are subtracted based on simulation, with the correction determined in bins of jet  $p_T$  and  $\eta$  as a function of the number of reconstructed vertices in the event and the average number of interactions per crossing expected from the instantaneous luminosity. The geometry of the jet is corrected to point from the primary event vertex, rather than the nominal center of the ATLAS detector.

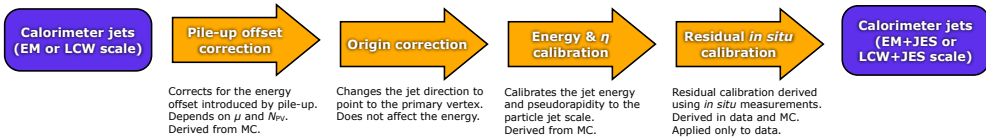


Figure 5.11: Overview of the jet calibration scheme.

The energy and pseudorapidity of the jet are initially calibrated based on the relationship between jets reconstructed from calorimeter clusters and jets reconstructed from truth particles in simulation. Then, *in situ* corrections are applied to the calibrated jets to correct for effects not described by the initial simulation-based calibration. The corrections are based on balancing the transverse momenta of jets against other well-calibrated objects. Jets in the central region, with detector rapidity  $|\eta_{\text{det}}| < 1.2$ , are calibrated against photons and leptonically decaying  $Z$  bosons. Jets with high transverse momentum,  $p_T > 210$  GeV, are also calibrated using multijet events, balancing the high- $p_T$  jet against several low- $p_T$  jets. Jets with  $1.2 < |\eta_{\text{det}}| < 2.8$  are calibrated against central jets with  $|\eta_{\text{det}}| < 0.8$ ; due to a lack of statistics with which to derive the calibration, more forward jets, with  $\pm 2.8 < \eta_{\text{det}} < 4.5$ , are assigned the same calibration as jets with  $\eta_{\text{det}} = \pm 2.8$ . The *in situ* calibrations shift the jet energy in data down by about 2% for  $p_T < 100$  GeV, and decreases with increasing  $p_T$ .

A large number of systematic uncertainties are assigned to the in situ calibration procedure, related to the modeling of the detector and physics processes in simulation and to the in situ methods themselves. The uncertainties are summarized in figure 5.12. Additionally, systematic uncertainties related to the pileup correction, high- $p_T$  jets, jet flavor, and differences simulation settings are assigned where appropriate.

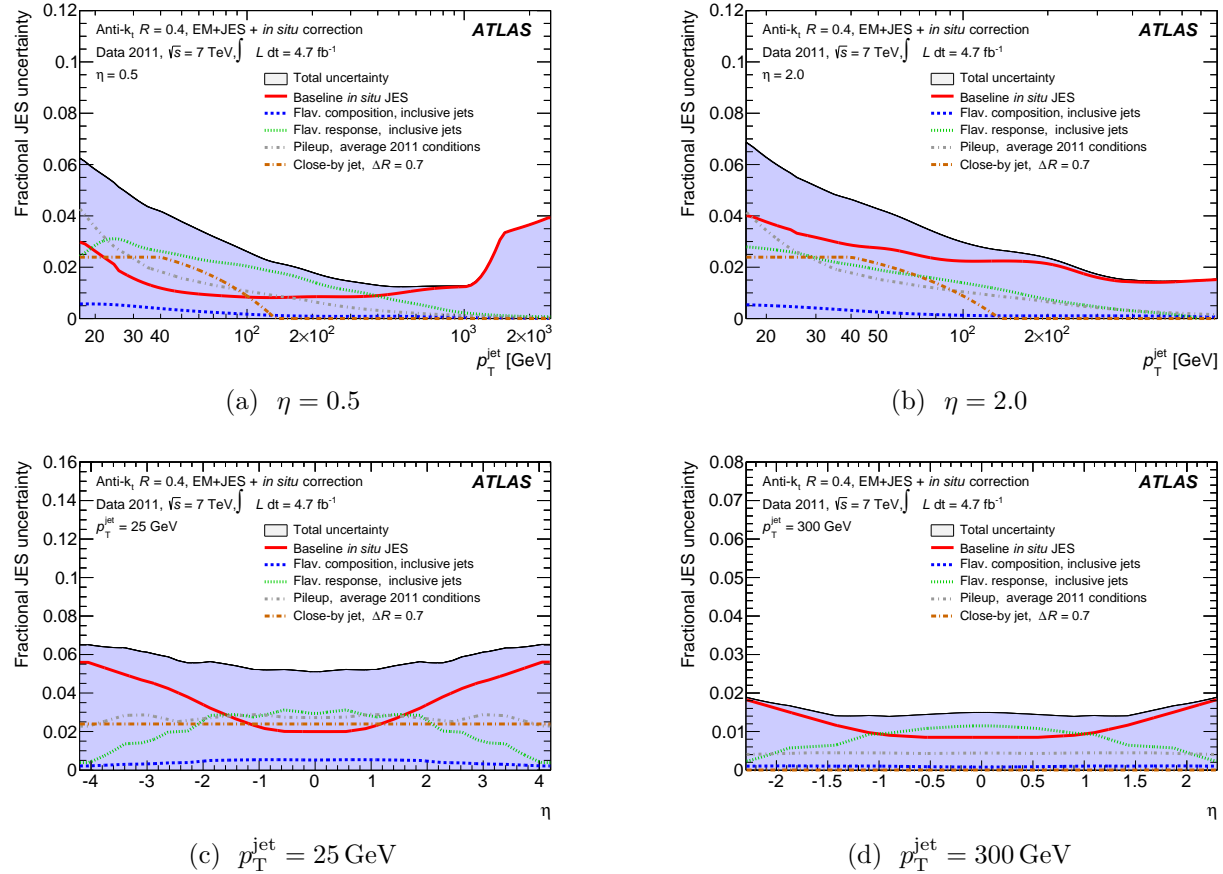


Figure 5.12: Sample-dependent fractional jet energy scale (JES) systematic uncertainty as a function of  $p_T^{\text{jet}}$  (top) and  $\eta$  (bottom), at fixed values of  $\eta$  or  $p_T^{\text{jet}}$ , respectively. The jets are reconstruction using the anti- $k_T$  algorithm with a radius parameter of  $R = 0.4$  from clusters at the LCW scale, and are calibrated as described in the text. The shaded area shows the total systematic uncertainty, while the colored lines show the contribution of various individual sources of uncertainty.

### 5.5.2 Pileup Suppression

Jets due to pileup interactions can be suppressed using the track information, at the cost of introducing some pileup-dependence to the jet reconstruction inefficiency. For a given

jet and primary vertex, the *jet vertex fraction* (JVF) is defined as the ratio of the  $\sum p_T$  of tracks associated with the jet and matched to the primary vertex to the  $\sum p_T$  of all tracks associated to the jet, shown schematically in figure 5.13. Specifically, letting  $\mathcal{T}$  be the set of tracks associated to the jet, the JVF is defined as:

$$\text{JVF} = \frac{\sum_{i \in \mathcal{T}} p_{T,i} \Theta_V(i)}{\sum_{i \in \text{jet}} p_{T,i}}, \quad (5.9)$$

where  $\Theta_V(i) = 1$  if the track  $i$  is matched to the primary vertex and 0 otherwise. If  $\mathcal{T}$  is empty, then  $\text{JVF} \equiv -1$ . In this dissertation, the primary vertex is chosen as the vertex with the highest  $\sum p_T^2$  of tracks, and  $\text{JVF} > 0.5$  is required for jets with  $20 \text{ GeV} < p_T < 50 \text{ GeV}$ .

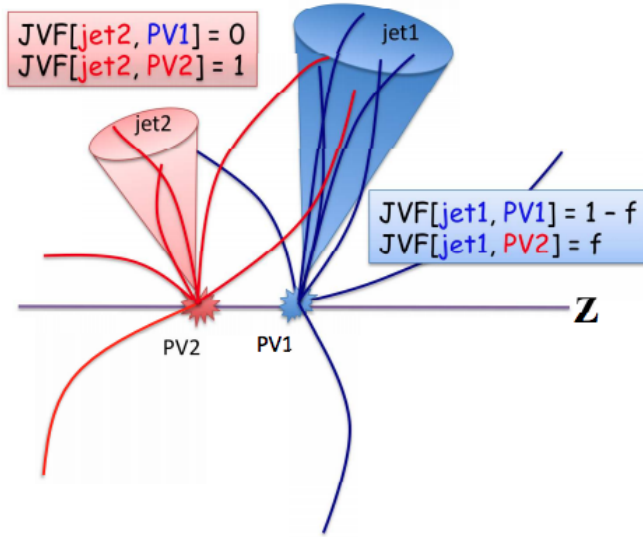


Figure 5.13: Schematic representation of the jet vertex fractions in the case of two jets and two primary vertices.  $f$  is the fraction of track  $p_T$  in jet 1 due to tracks associated with vertex PV2.

### 5.5.3 $b$ -tagging

The model-independent trilepton analysis (chapter 7) also makes use of the tagging of jets due to  $b$  quarks. Jets containing  $b$  quarks have several features which distinguish them from jets due to light quarks or gluons.  $B$  hadrons have proper decay lengths of approximate 0.5mm, long enough to be observed in the form of tracks or vertices reconstructed away from the primary interaction point. They also have large masses compared to other hadrons, leading to wider jets with more particles.

The algorithm used to tag  $b$ -jets is an artificial neural network called the MV1 algorithm [16]. The neural network uses three simpler likelihood-based algorithms as inputs [17, 18]:

- **IP3D:** Uses the transverse and longitudinal impact parameters of the tracks associated with a jet.
- **SV1:** Attempts to reconstruct a secondary vertex from the tracks associated with a jet. The most sensitive variable is the decay length significance between the secondary vertex and the primary event vertex. Additionally, the algorithm uses the invariant mass of tracks associated with the secondary vertex, the ratio of the energy of tracks assigned to the vertex to the energy of all tracks within the jet, and the number of two-track vertex candidates within the jet.
- **JetFitter:** Constructs a line connecting the primary vertex with one or more points associated with  $b$ - or  $c$ -hadron decays using a Kalman filter. The algorithm makes use of variables similar to the SV1 algorithm, along with the flight length significance between decays. Note that the algorithm does not require secondary vertices, allowing for the identification of decays with only one track.

The MV1 algorithm is trained on simulated data, using  $b$ -jets as signal and light quark jets as background, and returns a tag weight for each jet. The tag weight is used to establish working points with a given signal efficiency and background rejection power, as shown in figure 5.14a. The model-independent triplepton analysis uses the working point with 80% signal efficiency. The performance of the algorithm as a function of transverse momentum is shown in figure 5.14b.

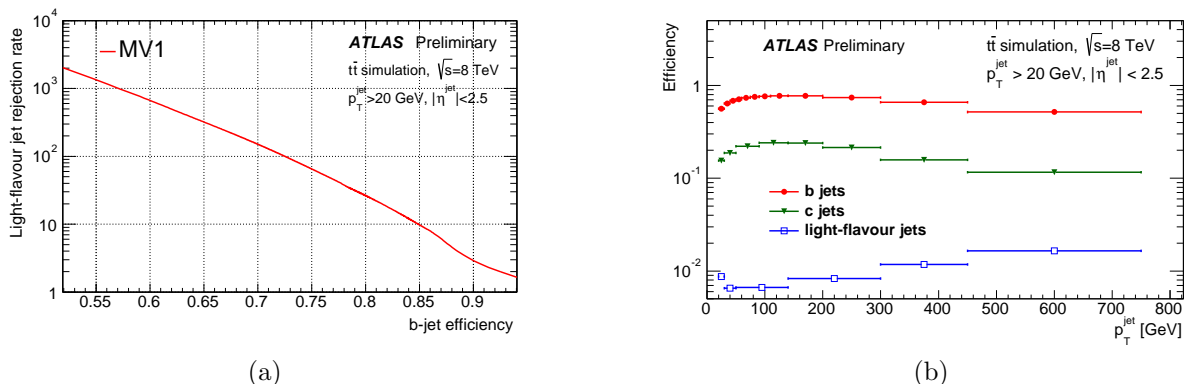


Figure 5.14: Performance of the MV1  $b$ -tagging algorithm. The inclusive signal efficiency versus background rejection is shown at left. The signal and background efficiencies at the 70% working point are shown as a function of  $p_T$  at right.

## 5.6 Invisible Particles

Neutrinos interact only via the weak interaction, and hence escape the detector without interacting with any of the detector components. The same is true for any new stable, neutral, and colorless particles, such as the lightest supersymmetric particle in  $R$  parity-conserving scenarios or sterile neutrinos. The presence of such particles can only be inferred through the overall imbalance of the transverse momentum<sup>5</sup> of the other visible collision products,  $\mathbf{E}_T^{\text{miss}} = (E_x^{\text{miss}}, E_y^{\text{miss}})$ .

The missing transverse momentum is defined as the negative vector sum of the visible objects in the event [19, 20]. The energies are mostly determined from calorimeter measurements, except for muons. To avoid using calorimeter energy deposits multiple times, the algorithm assigns energy to deposits to a single object according to a strict order: electrons are identified first, followed by photons, hadronically decaying  $\tau$  leptons, jets, and muons. Depending on the analysis requirements, the energy of a given physics object can be determined using the full reconstruction algorithm, or the energy deposits can be calibrated to the EM or LCW scales. Finally, topological clusters and tracks not assigned to physics objects are included in  $\mathbf{E}_T^{\text{miss}}$  calculation as the so-called soft term. The missing transverse energy is given by:

$$E_{x(y)}^{\text{miss}} = - \left( E_{x(y)}^e + E_{x(y)}^\gamma + E_{x(y)}^\tau + E_{x(y)}^{\text{jets}} + E_{x(y)}^\mu + E_{x(y)}^{\text{soft}} \right), \quad (5.10)$$

where each term on the right represents the total momentum of the reconstructed objects in the  $x$  or  $y$  directions.

The measured  $\mathbf{E}_T^{\text{miss}}$  receives contributions from sources besides invisible particles, including calorimeter noise, particles falling in insensitive regions of the detector, energy mismeasurements, and pileup interactions. These effects are mitigable to varying degrees. Particles falling outside the detector acceptance contribute irreducibly to the  $\mathbf{E}_T^{\text{miss}}$  resolution. For physics objects like electrons or jets, the noise and pileup contributions are suppressed by the reconstruction algorithms and identification cuts. To reduce the noise and pileup contributions to the soft term, the cells are grouped into topological clusters. Rejecting events where the  $\mathbf{E}_T^{\text{miss}}$  is parallel or antiparallel to the physics objects can mitigate the impact of energy mismeasurements.

## 5.7 Object Selection

The analyses described in this dissertation search for energetic leptons and jets produced in the decays of new heavy particles. The leptons and jets typically have large transverse momenta and are well-separated from other objects in the event, due to the large difference in the mass scale between the final decay products (leptons or hadrons with mass  $m \lesssim 10$  GeV)

---

<sup>5</sup>The longitudinal momentum imbalance,  $E_z^{\text{miss}}$ , is not useful in  $pp$  collisions due to the unknown longitudinal momenta of the initial colliding partons.

and the parents ( $W/Z$  bosons or the new particles themselves, with mass  $m \gtrsim 80$  GeV). The new particles typically have short lifetimes, and hence the leptons and jets are produced promptly at the location of the initial proton-proton interaction, consistent with originating from the selected primary vertex. These properties can be used to suppress backgrounds due to Standard Model processes and detector effects, described in chapter 6.

### 5.7.1 Leptons

The events used in this dissertation are required to have at least three reconstructed electrons, muons, or hadronically decaying  $\tau$  leptons. A summary of the lepton selections is shown in tables 5.2 and 5.3. Leptons are required to satisfy the following requirements:

- **Transverse momentum:** Electrons and muons must have  $p_T > 15$  GeV, while hadronically decaying  $\tau$  leptons must have  $p_T > 20$  GeV. The transverse momentum cut is driven by the availability of triggers with which to perform data-driven estimates of backgrounds due to sources like semileptonically decays in jets or misidentified jets (see section 6.2.1).
- **Geometrical acceptance:** Electrons are required to have  $|\eta| < 2.47$ , excluding the transition region  $1.37 < |\eta| < 1.52$  between the barrel and end-cap calorimeters. Muons and  $\tau$  leptons are required to have  $|\eta| < 2.5$ .
- **Particle identification:** To suppress the reducible backgrounds, the leptons must satisfy strict requirements related to particle identification. Electrons candidates must satisfy the `tight++` set of identification cuts. Electrons are neglected if they fall in a region affected by the presence of a dead front end board in the first or second sampling layer, a dead high voltage supply, or a masked cell in the core. Muons are required to be *combined*, with associated hits in the inner detector and muon spectrometer. Specifically, associated inner detector track must have:
  - A B-layer hit, unless the muon passes through a deactivated region of the B-layer.
  - $\geq 1$  pixel hit and  $\geq 5$  SCT hits, including any deactivated sensors along the trajectory.
  - $\leq 2$  total missing hits in the pixel and SCT, excluding deactivated sensors along the trajectory.
  - A successful extension into the TRT, with  $\geq 6$  TRT hits, of which  $< 90\%$  are classified as outlier hits.

Finally,  $\tau$  leptons must satisfy the `BDT-tight` selection criteria.

- **Impact parameter:** The inner detector track associated with electrons and muons must be consistent with originating from the event primary vertex. The transverse impact parameter significance, defined as the transverse impact parameter  $d_0$  divided

by its uncertainty  $\sigma_{d_0}$ , is required to satisfy  $\frac{d_0}{\sigma_{d_0}} < 3$ . Similarly, the longitudinal impact parameter  $z_0$  is required to satisfy  $z_0 \sin \theta < 0.5$  mm. These requirements suppress leptons from semileptonic heavy flavor decays.

- **Isolation:** To further reduce the impact of non-prompt and misidentified leptons, the leptons are required to be isolated from other activity in the event. The cuts on electrons and muons are similar, and limit the amount of nearby activity as measured by inner detector tracks and calorimeter energy deposits:

- For both electrons and muons, a cut is applied on `ptcone30`, the sum of transverse momenta of tracks associated to the same primary vertex as the lepton within a cone of radius  $\Delta R = 0.3$ .
- For muons, a cut is applied on `Etcone30`, the scalar sum of transverse energies of calorimeter cells within  $\Delta R < 3.0$  of the muon track.
- For electrons, a cut is applied on `TopoEtcone30`, the sum of topological calorimeter clusters within a cone of  $\Delta R < 3.0$ . The use of topological clusters reduces the impact of pileup and out-of-cone leakage.

In this dissertation, the electron and muon isolation variables are required to be less than 10% of the lepton transverse momentum for leptons with  $p_T < 100$  GeV, and less than  $10 \text{ GeV} + 0.01 \times p_T$  for leptons with  $p_T \geq 100$  GeV.

Isolation requirements are also applied at the trigger level. For the lowest- $p_T$  unprescaled electron and muon triggers, `ptcone20`, the sum of transverse momenta of all tracks within a cone of radius  $\Delta R = 0.2$ , is required to satisfy  $\text{ptcone20}/p_T < 0.1$ .

Cut	Electrons	Muons
Object ID	<code>Tight++</code>	Combined Tight
Leading (trigger) $E_T/p_T$	$E_T > 26$ GeV	$p_T > 26$ GeV
Subleading $E_T/p_T$	$E_T > 15$ GeV	$p_T > 15$ GeV
Trigger Acceptance	$( \eta  < 2.47) \&\& !(1.37 <  \eta  < 1.52)$	$ \eta  < 2.4$
Acceptance	$( \eta  < 2.47) \&\& !(1.37 <  \eta  < 1.52)$	$ \eta  < 2.5$
Calo. Isolation ( $E_T, p_T < 100$ GeV)	$\text{TopoEtcone30} < 0.1 \times E_T$	$\text{Etcone30} < 0.1 \times p_T$
Calo. Isolation ( $E_T, p_T > 100$ GeV)	$\text{TopoEtcone30} < 10 \text{ GeV} + 0.01 \times E_T$	$\text{Etcone30} < 10 \text{ GeV} + 0.01 \times p_T$
Track Isolation ( $E_T, p_T < 100$ GeV)	$\text{ptcone30} < 0.1 \times E_T$	$\text{ptcone30} < 0.1 \times p_T$
Track Isolation ( $E_T, p_T > 100$ GeV)	$\text{ptcone30} < 10 \text{ GeV} + 0.01 \times E_T$	$\text{ptcone30} < 10 \text{ GeV} + 0.01 \times p_T$
Track $d_0$	$\frac{d_0}{\sigma_{d_0}} < 3$	$\frac{d_0}{\sigma_{d_0}} < 3$
Track $z_0$	$z_0 \sin \theta < 0.5$ mm	$z_0 \sin \theta < 0.5$ mm

Table 5.2: Electron and muon selection criteria.

### 5.7.2 Jets and Missing Transverse Energy

Jets are required to have  $p_T > 30$  GeV, in order to limit the presence of pileup jets. For the geometrical acceptance, jets must lie in the range  $|\eta| < 4.5$ , so that the jet falls within

Cut	Taus
Object ID	BDT Tight
$p_T$	$p_T > 26 \text{ GeV}$
Acceptance	$ \eta  < 2.5$

Table 5.3: Tau selection criteria.

instrumented regions of the detector. Pileup jets are additionally suppressed with a cut on the JVF (section 5.5.2): for jets with  $p_T < 50 \text{ GeV}$ , the JVF must be at least 0.5.

Jets consistent with originating from the decay of a  $b$ -hadron are identified using the MV1 algorithm [16], with an efficiency of 80%.

The missing transverse momentum,  $\mathbf{E}_T^{\text{miss}}$ , is calculated using the MET\_Egamma10NoTau\_RefFinal algorithm. Calorimeter cells associated with electrons or photons with  $p_T > 10 \text{ GeV}$  are calibrated specifically to the corresponding object. Cells associated with  $\tau$  leptons are calibrated as jets, rather than as hadronically decaying  $\tau$  leptons, due to the ambiguity between jets and  $\tau$  leptons when using BDT-loose  $\tau$  leptons in the data-driven reducible background estimate, described in section 6.2.4.

### 5.7.3 Overlap Removal

Objects are frequently reconstructed as multiple objects; for example, a muon with a hard bremsstrahlung emission might be reconstructed as a muon, an electron, and a jet. In order to resolve ambiguities, the following overlap removal procedure is applied:

- If  $\Delta R(e, e) < 0.1$ , remove the lower  $p_T$  electron, to avoid “a potential bias in the simulation of the reconstruction efficiency for two real, close-by same-flavour leptons” [21].
- If  $\Delta R(e, \text{jet}) < 0.2$ , remove the jet. This addresses the ambiguity between electrons and jets.
- If  $0.2 < \Delta R(\text{jet}, e) < 0.4$  and  $p_T(\text{jet}) > 30 \text{ GeV} + 0.05 * p_T(e)$ , remove the electron. This suppresses the reducible electron background.
- If  $\Delta R(\mu, e) < 0.1$ , remove the electron. This addresses cases where a muon radiates a hard photon, which is then reconstructed as an electron.
- If  $\Delta R(\mu, \text{jet}) < 0.1$ , and:

$$\begin{aligned} p_T^{\text{jet}} < 0.5 p_T^\mu & : p_T^\mu < 200 \text{ GeV}, \text{ or} \\ p_T^{\text{jet}} < 100 \text{ GeV} & : p_T^\mu \geq 200 \text{ GeV}, \end{aligned} \quad (5.11)$$

remove the jet. This is intended to reduce efficiency loss due to the next step from jets induced by muons at high muon  $p_T$ .

- If  $\Delta R(\text{jet}, \mu) < 0.3$ , remove the muon. This requirement suppresses the reducible muon backgrounds.

# Bibliography

- [1] T. Cornelissen et al.,  
*Concepts, Design and Implementation of the ATLAS New Tracking (NEWT)* (2007).
- [2] The ATLAS Collaboration, *Performance of the ATLAS Silicon Pattern Recognition Algorithm in Data and Simulation at  $\sqrt{s} = 7$  TeV* (July 2010) pp. 1–14,  
URL: <https://cds.cern.ch/record/1281363>.
- [3] The ATLAS Collaboration, *Performance of the ATLAS Inner Detector Track and Vertex Reconstruction in the High Pile-Up LHC Environment* (Mar. 2012) pp. 1–20.
- [4] The ATLAS Collaboration, *Performance of primary vertex reconstruction in proton-proton collisions at  $\sqrt{s} = 7$  TeV in the ATLAS experiment* (July 2010) pp. 1–10, URL: <http://cds.cern.ch/record/1281344>.
- [5] W. Waltenberger, R. Frühwirth, and P. Vanlaer, *Adaptive vertex fitting*, Journal of Physics G: Nuclear and Particle Physics **34**.12 (Nov. 2007) N343–N356,  
URL: <http://stacks.iop.org/0954-3899/34/i=12/a=N01?key=crossref.1572e0c569f8431ab1d721e989956caa>.
- [6] The ATLAS Collaboration,  
*Electron reconstruction and identification efficiency measurements with the ATLAS detector using the 2011 LHC proton–proton collision data*, The European Physical Journal C **74**.7 (July 2014) pp. 2941–38.
- [7] The ATLAS Collaboration, *Electron efficiency measurements with the ATLAS detector using the 2012 LHC proton-proton collision data* (June 2014) pp. 1–50.
- [8] The ATLAS Collaboration, *Improved electron reconstruction in ATLAS using the Gaussian Sum Filter-based model for bremsstrahlung* (May 2012) pp. 1–22.
- [9] The ATLAS Collaboration, *Electron and photon energy calibration with the ATLAS detector using LHC Run 1 data*, The European Physical Journal C **74**.10 (Oct. 2014) pp. 3071–48.
- [10] K. Olive et al., *Review of Particle Physics*, Chin.Phys. **C38** (2014) p. 090001.
- [11] The ATLAS Collaboration, *Identification and energy calibration of hadronically decaying tau leptons with the ATLAS experiment in pp collisions at  $\sqrt{s} = 8$  TeV*, arXiv.org (Dec. 2014), arXiv: 1412.7086 [hep-ex].

- [12] The ATLAS Collaboration, *Jet energy measurement with the ATLAS detector in proton-proton collisions at  $\sqrt{s} = 7$  TeV*, English, arXiv.org 3 (Dec. 2011) pp. 2304–118, arXiv: 1112.6426 [hep-ex], URL: <http://link.springer.com/10.1140/epjc/s10052-013-2304-2>.
- [13] The ATLAS Collaboration, *Jet energy measurement and its systematic uncertainty in proton-proton collisions at  $\sqrt{s} = 7$  TeV with the ATLAS detector*, English, The European Physical Journal C **75**.1 (Jan. 2015) pp. 17–101, URL: <http://link.springer.com/10.1140/epjc/s10052-014-3190-y>.
- [14] M. Cacciari, G. P. Salam, and G. Soyez, *The anti- $k_t$  jet clustering algorithm*, arXiv **0804**.04 (2008) pp. 063–063, URL: <http://stacks.iop.org/1126-6708/2008/i=04/a=063?key=crossref.2ffef838d94c2b899ee27950c18ee8d2>.
- [15] M. Cacciari, G. P. Salam, and G. Soyez, *FastJet User Manual*, arXiv **C72** (2012) p. 1896, URL: <http://arxiv.org/abs/1111.6097>.
- [16] The ATLAS Collaboration, *Calibration of the performance of b-tagging for c and light-flavour jets in the 2012 ATLAS data* (July 2014) pp. 1–19.
- [17] The ATLAS Collaboration, *Expected Performance of the ATLAS Experiment, Detector, Trigger and Physics* (July 2009) pp. 1–1852.
- [18] The ATLAS Collaboration, *Commissioning of the ATLAS high-performance b-tagging algorithms in the 7 TeV collision data* (July 2011) pp. 1–22, URL: <https://cds.cern.ch/record/1369219>.
- [19] The ATLAS Collaboration, *Performance of missing transverse momentum reconstruction in proton-proton collisions at  $\sqrt{s} = 7$  TeV with ATLAS*, English, The European Physical Journal C **72**.1 (Jan. 2012) pp. 1844–35, URL: <http://link.springer.com/10.1140/epjc/s10052-011-1844-6>.
- [20] The ATLAS Collaboration, *Performance of Missing Transverse Momentum Reconstruction in ATLAS studied in Proton-Proton Collisions recorded in 2012 at 8 TeV* (Aug. 2013) pp. 1–41, URL: <https://cds.cern.ch/record/1570993>.
- [21] D. L. Adams et al., *Recommendations of the Physics Objects and Analysis Harmonisation Study Groups 2014* (July 2014) pp. 1–41, URL: <https://cds.cern.ch/record/1700874>.

# Chapter 6

## Background Estimation

The relevant Standard Model processes contributing to multilepton final states are diboson production ( $WZ$ ,  $ZZ$ ), production of a top quark pair in association with an weak gauge boson ( $t\bar{t} + V$ ), and triboson production ( $VVV^{(*)}$ , where  $V = W$  or  $Z$ ). Examples tree-level Feynman diagrams of these processes are shown in figure 6.1. These backgrounds, called *prompt* backgrounds, are estimated using Monte Carlo (MC) simulation, as described in section 6.1. Significant backgrounds also arise from processes where at least one reconstructed lepton is due to the semileptonic decay of a hadron, the misidentification of a jet, or the asymmetric conversion of a photon in the detector; such backgrounds are called *reducible* backgrounds. These backgrounds are estimated using either MC simulation or a data-driven technique called the *fake factor* method, which is described in section 6.2.1.

### 6.1 Prompt Backgrounds

The prompt backgrounds are estimated using Monte Carlo simulation. The hard-scattering processes are modeled by dedicated event generators, possibly including the emission of additional partons. Additional QCD radiation is modeled using a parton shower. The detector response to the simulated events is simulated with the ATLAS simulation framework [1] using the GEANT4 toolkit [2]. Pileup is included by overlaying simulated minimum-bias interactions from PYTHIA [3] on the hard scattering event. Simulated events are assigned weights to reproduce the observed pileup distributions in data, and also to account for small differences in the trigger, reconstruction, and identification efficiencies between simulation and data.

The details of the modeling of each sample are described below. The generator, parton shower, PDF set, underlying event tune, and accuracy of theoretical cross section for samples are summarized in table 6.1.

- SHERPA [4] is used to model  $WW$ ,  $WZ$ , and  $ZZ$  production. Both bosons in the events decay leptonically. Up to three jets are included in the matrix element. An important feature of SHERPA is that it accurately models the  $W + \gamma^*$  and  $Z + \gamma^*$  contributions

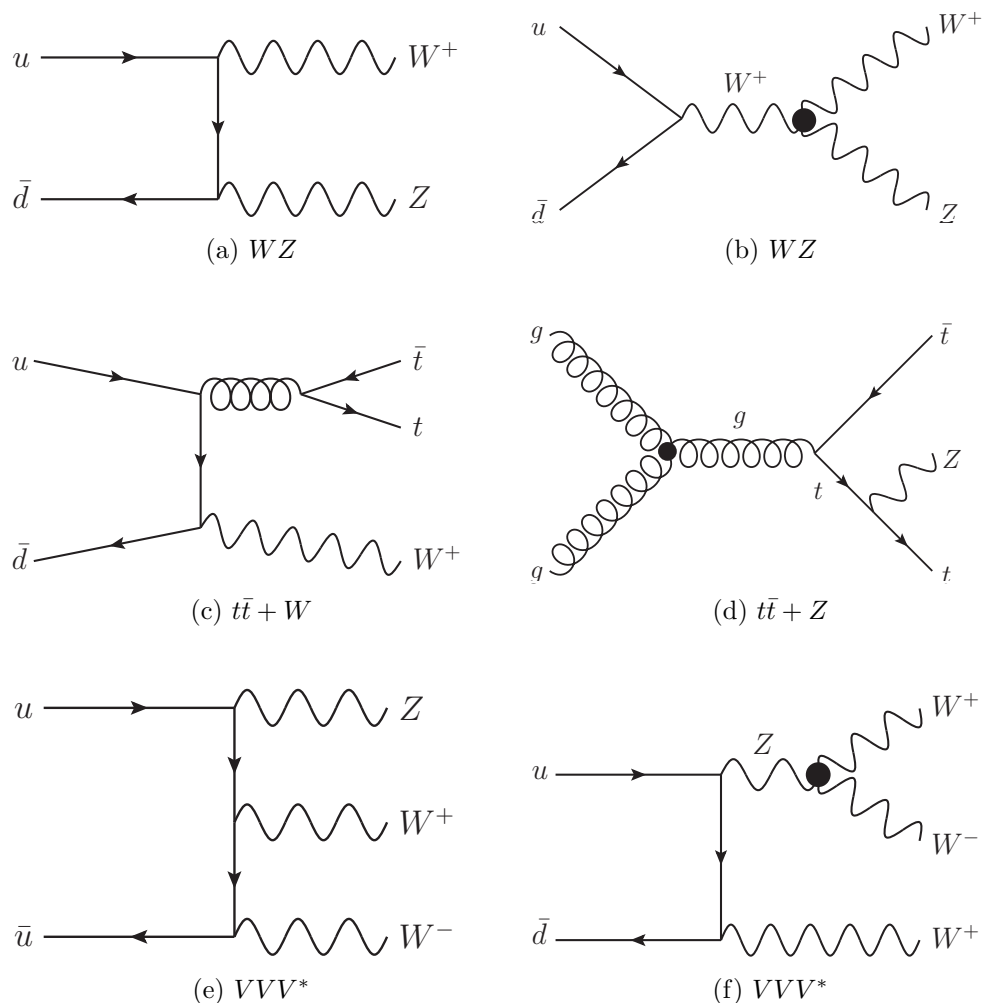


Figure 6.1: Example tree-level Feynman diagrams of Standard Model processes leading to trilepton final states.

Process	Generator	Parton shower and hadr.	PDF set	UE tune	Cross section
$WZ$	SHERPA 1.4.3	SHERPA	CT10 [6]	SHERPA	NLO
$ZZ$	SHERPA 1.4.5	SHERPA	CT10	SHERPA	NLO
$t\bar{t} + W/Z$	MADGRAPH 5.1.3.33	PYTHIA 6.426	CTEQ6L1 [7]	AUET2B [8]	NLO
$VVV^{(*)}$	MADGRAPH 5.1.3.33	PYTHIA 6.426	CTEQ6L1	AUET2B	LO
$Z + \gamma$	SHERPA	SHERPA	CT10	SHERPA	LO

Table 6.1: Summary of the primary background MC samples used in this analysis. The generator, parton shower and hadronization, PDF, underlying event tune, and the order of the cross section calculation are shown for each sample.

down to very low  $\gamma^*$  masses; for electron decays, a cut of  $m(ee) > 100$  MeV is applied, while for muon and tau decays, SHERPA naturally cuts off the divergence. To increase the statistics in the phase space relevant for this analysis, the  $WZ$  samples requires at least two leptons have  $p_T > 5$  GeV. Finally, the  $WZ$  sample also treats the  $b$  and  $c$  quarks as massive, which improves the modeling of heavy flavor jets at the cost of increased computation time.

- SHERPA is also used to model  $Z + \gamma$  production, where the photon converts asymmetrically in the detector and is reconstructed as an electron. The events are reweighted to account for observed mismodeling in the conversion rate, described in section 10.1.1.
- $t\bar{t} + V$  production is modeled with MADGRAPH [5], with PYTHIA for the parton shower.
- $WWW^{(*)}$ ,  $ZWW^{(*)}$ , and  $ZZZ^{(*)}$  are modeled using MADGRAPH, with PYTHIA for the parton shower. Their contributions to all the signal regions are negligible.

## 6.2 Reducible Backgrounds

The reducible backgrounds encompass a variety of processes in which one or more reconstructed lepton arises due to a non-prompt process or a misidentification. Sources of such leptons include semileptonic hadron decays, misidentified jets, particles penetrating the calorimeter and leaving hits in the muon spectrometers, and asymmetric photon conversions in the detector. The backgrounds are estimated using simulation or a data-driven technique, depending on the source. The contribution from  $Z + \gamma$ , where the photon converts asymmetrically and is reconstructed as an electron, is estimated from Monte Carlo, with scale factors applied to account for an observed overestimation in the photon-to-electron conversion rate (see section 10.1.1). Other reducible contributions are estimated using a data-driven technique called the *fake factor* method.

### 6.2.1 Fake Factor Method

The fake factor method estimates the reducible backgrounds in each signal region by characterizing the fake or non-prompt leptons in terms of quantities sensitive to the fake process,

such as isolation, impact parameter, or particle identification cuts. Two orthogonal sets of leptons are defined: *numerator* leptons ( $N$ ) satisfy the nominal signal lepton selection criteria, while *denominator* leptons ( $D$ ) satisfy most of the nominal selection criteria, except with inverted requirements on quantities sensitive to the fake process. The reducible background is estimated in a data-driven way from a control region consisting of events with a mix of numerator and denominator leptons, together with a parametrization of the relationship between numerators and denominators.

The relationship between numerator and denominator objects is called the *fake factor*,  $f$ , defined as the ratio of the number of fake leptons satisfying the numerator criteria to those satisfying the denominator criteria. The fake factor is measured in a control region enriched in fake leptons. The success of the method depends largely on the extrapolation of the  $f$  from the measurement control region to the signal regions. To capture the dependence on the event kinematics,  $f$  can be measured as a function of various lepton or event variables; in this dissertation, the fake factors are all measured in bins of lepton  $p_T$  and  $\eta$ .

Once  $f$  has been measured, the reducible background is determined as follows. In signal events with three or more leptons, any subset of the leptons could be real or fake. For example, an event might contain two real leptons from a Drell-Yan process plus a fake third lepton. Such an event is labeled  $\ell_1^R \ell_2^R \ell_3^F$ , indicating the “truth” classification of the three leptons as either real ( $R$ ) or fake ( $F$ ) (the ordering of the letters corresponds to some canonical order of the leptons, such as  $p_T$  ordering). On the other hand, if an event contained, say,  $W \rightarrow l\nu$  plus two fake leptons, the event would be labeled  $\ell_1^R \ell_2^F \ell_3^F$  (or  $\ell_1^F \ell_2^R \ell_3^F$  or  $\ell_1^F \ell_2^F \ell_3^R$ ).

The quantity we desire to determine is the number of events containing three real leptons,  $n_{\ell_1^R \ell_2^R \ell_3^R}$ . The quantity actually measured in a signal region is the number of events containing three numerator objects,  $n_{\ell_1^N \ell_2^N \ell_3^N}$ . Any of these numerators could be real or fake, so the sample can be decomposed as:

$$n_{\ell_1^N \ell_2^N \ell_3^N} = n_{\ell_1^R \ell_2^R \ell_3^R} + n_{\ell_1^R \ell_2^R \ell_3^F} + n_{\ell_1^R \ell_2^F \ell_3^R} + n_{\ell_1^R \ell_2^F \ell_3^F} + \quad (6.1)$$

$$+ n_{\ell_1^F \ell_2^R \ell_3^R} + n_{\ell_1^F \ell_2^R \ell_3^F} + n_{\ell_1^F \ell_2^F \ell_3^R} + n_{\ell_1^F \ell_2^F \ell_3^F} \quad (6.2)$$

The reducible background prediction is  $n_{\ell_1^N \ell_2^N \ell_3^N} - n_{\ell_1^R \ell_2^R \ell_3^R}$ , the number of signal events where at least one lepton is fake. To determine the other terms, we use events with one or more denominator leptons. For example, consider  $\ell_1^D \ell_2^N \ell_3^N$  events, where the first lepton is a denominator and the remaining leptons are numerators. Assuming that the denominator lepton is always a fake lepton, the number of  $\ell_1^D \ell_2^N \ell_3^N$  events, each weighted by the fake factor  $f$  corresponding to the denominator lepton (represented schematically by  $n_{\ell_1^D \ell_2^N \ell_3^N} f_1$ ), equals the number of  $\ell_1^N \ell_2^N \ell_3^N$  events where the first lepton is fake:

$$n_{\ell_1^D \ell_2^N \ell_3^N} f_1 = n_{\ell_1^F \ell_2^R \ell_3^R} + n_{\ell_1^F \ell_2^R \ell_3^F} + n_{\ell_1^F \ell_2^F \ell_3^R} + n_{\ell_1^F \ell_2^F \ell_3^F}. \quad (6.3)$$

Similarly, the remaining permutations of numerators and denominators yield:

$$n_{\ell_1^N \ell_2^D \ell_3^N} f_2 = n_{\ell_1^R \ell_2^F \ell_3^R} + n_{\ell_1^R \ell_2^F \ell_3^F} + n_{\ell_1^F \ell_2^F \ell_3^R} + n_{\ell_1^F \ell_2^F \ell_3^F} \quad (6.4)$$

$$n_{\ell_1^N \ell_2^N \ell_3^D} f_3 = n_{\ell_1^R \ell_2^R \ell_3^F} + n_{\ell_1^R \ell_2^F \ell_3^F} + n_{\ell_1^F \ell_2^R \ell_3^F} + n_{\ell_1^F \ell_2^F \ell_3^F} \quad (6.5)$$

$$n_{\ell_1^D \ell_2^D \ell_3^N} f_1 f_2 = n_{\ell_1^F \ell_2^F \ell_3^R} + n_{\ell_1^F \ell_2^F \ell_3^F} \quad (6.6)$$

$$n_{\ell_1^D \ell_2^N \ell_3^D} f_1 f_3 = n_{\ell_1^F \ell_2^R \ell_3^F} + n_{\ell_1^F \ell_2^F \ell_3^F} \quad (6.7)$$

$$n_{\ell_1^N \ell_2^D \ell_3^D} f_2 f_3 = n_{\ell_1^R \ell_2^F \ell_3^F} + n_{\ell_1^F \ell_2^F \ell_3^F} \quad (6.8)$$

$$n_{\ell_1^D \ell_2^D \ell_3^D} f_1 f_2 f_3 = n_{\ell_1^F \ell_2^F \ell_3^F} \quad (6.9)$$

These equations contain eight equations and eight unknowns, so the system can be solved for the reducible background prediction:

$$\ell_1^N \ell_2^N \ell_3^N - \ell_1^R \ell_2^R \ell_3^R = (\ell_1^N \ell_2^N \ell_3^D f_3 + \ell_1^N \ell_2^D \ell_3^N f_2 + \ell_1^D \ell_2^N \ell_3^N f_1) \quad (6.10)$$

$$- (\ell_1^N \ell_2^D \ell_3^D f_2 f_3 + \ell_1^D \ell_2^N \ell_3^D f_1 f_3 + \ell_1^D \ell_2^D \ell_3^N f_1 f_2) \quad (6.11)$$

$$+ \ell_1^D \ell_2^D \ell_3^D f_1 f_2 f_3 \quad (6.12)$$

Note that throughout this method, we have assumed that the leptons used for the measurement of  $f$  and the denominator leptons in trilepton events are always fake leptons. In practice, real leptons contaminate both of these samples, and is accounted for using simulation, where the lepton can be classified as real or fake using the truth record of the event.

The remainder of this chapter presents the measurement of the fake factors  $f$  for electrons, muons, and tau leptons.

### 6.2.2 Electron Fake Factors

The background estimation for fake electrons targets the reducible contribution from two sources: semileptonic heavy flavor decays and misidentified light hadrons. The electron denominator objects are defined by inverting either the IsEM electron identification criteria<sup>1</sup> or the track impact parameter cut (exclusive OR), as shown in table 6.2; the electron must pass all the remaining cuts listed in table 5.2. Additionally, an inefficiency is observed for loose offline electrons with respect to the loose electron triggers. This is due to the lack of Gaussian sum filter (GSF) tracking [9] at the trigger level. The inefficiency is mitigated by imposing the `tight++` requirement on the  $\Delta\eta$  and  $\Delta\phi$  between the electron track and associated calorimeter cluster, with the goal of cutting out electrons with large amounts of bremsstrahlung, whose tracks are not reconstructed by the non-GSF algorithm in the trigger.

The fake factors are measured in a control sample of single-electron events, using the entire  $20.3 \text{ fb}^{-1}$  2012 dataset. The triggers used to collect events are listed in table 6.3;

---

<sup>1</sup>The parameter space between `medium++` and `loose++`, rather than `tight++` and `medium++`, is used for two reasons. First, for the model-independent trilepton analysis (chapter 7), electrons passing `medium++` and failing `loose++` are used to define a validation region to test the fake factor method. Second, requiring the electrons to fail `medium++` reduces the prompt contamination in the denominator sample.

Criteria	Numerator	Denominator
IsEM ID	<code>tight++</code>	<code>!medium++ &amp;&amp; loose++</code>
Impact Parameter Significance	$\frac{ d_0 }{\sigma_{d_0}} < 3$	$3 < \frac{ d_0 }{\sigma_{d_0}} < 10$

Table 6.2: Electron denominator definitions. The denominators are taken to be an exclusive OR combination of the two selection inversions. Additionally, denominator objects must pass the tight requirement on the  $\Delta\eta$  and  $\Delta\phi$  between the track and the cluster.

photon triggers are used where available ( $p_T > 24$  GeV), and loose electron triggers are used otherwise ( $15$  GeV  $< p_T < 24$  GeV).

$p_T$ range (GeV)	Trigger	Average 2012 Prescale
15-17	EF_e5_loose0	56080.5
17-24	EF_e15vh_loose0	1549.7
24-45	EF_g20_loose	4412.6
45-65	EF_g40_loose	348.3
65-85	EF_g60_loose	80.9
85-105	EF_g80_loose	28.5
105-125	EF_g100_loose	13.0
125-210	EF_g120_loose	1.0
>210	EF_g200_etcut	1.0

Table 6.3: Trigger used to collect electron numerator and denominator objects.

Events are required to have  $m_T < 40$  GeV and  $E_T^{\text{miss}} < 40$  GeV to suppress contamination from single- $W$  production, where  $m_T$  is the transverse mass of the electron and missing transverse energy in the event. The events are also required to have exactly one electron, numerator or denominator, in order to suppress prompt contamination from  $Z \rightarrow ll$  events. The electrons are required to be trigger-matched to the trigger used to collect the event in the relevant  $p_T$  range. The residual prompt contamination, comprised mostly of  $W$  and  $Z$  events with smaller contributions from Drell-Yan,  $t\bar{t}$  and single- $t$ , is subtracted using Monte Carlo. The numerator and denominator event yields, as well as the predicted prompt contamination, are shown in figure 6.2. The prompt contamination consists primarily of  $W$  and  $Z$  events. The relative size of the prompt contamination is quite large for numerator objects, reaching up to  $\sim 60\%$  for  $p_T \sim 50$  GeV, despite the cuts intended to reduce the  $W$  contribution. The fake factors are binned two-dimensionally in  $p_T$  and  $\eta$ , shown in figure 6.3. The  $p_T$  dependence of the fake factors is shown in figure 6.4, for the inclusive sample (left) and for various  $|\eta|$  ranges (right).

To help clarify the origin of the structure in  $\eta$  observed at low  $p_T$ , the numerator and denominator counts are also shown versus  $\eta$  for  $p_T < 24$  GeV in figure 6.5. The numerator counts are relative flat versus  $\eta$  in the central region, and grow for  $|\eta| \gtrsim 2$ . Conversely, the

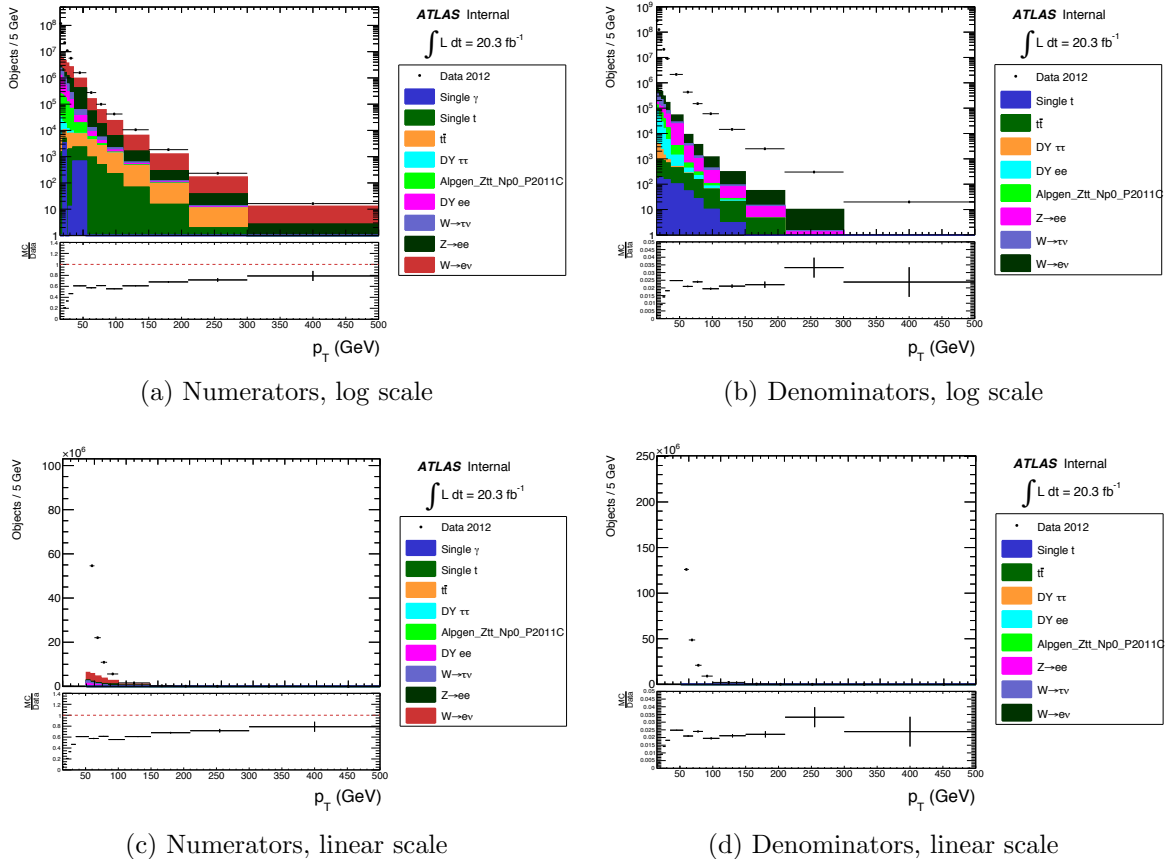
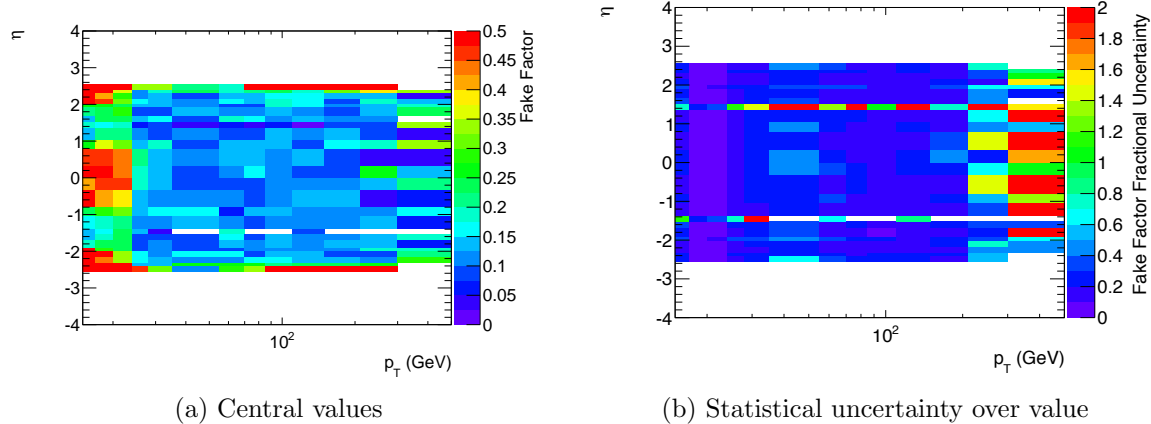
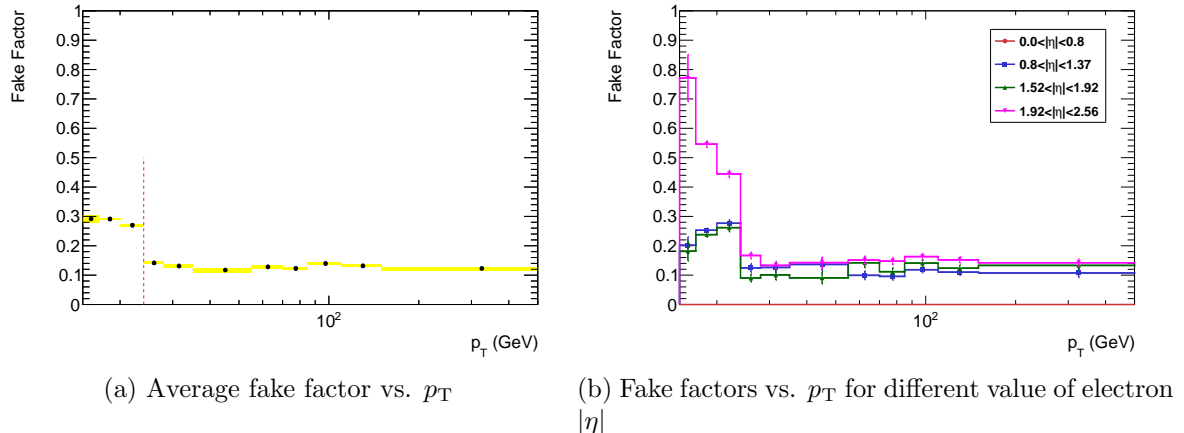


Figure 6.2: Numerator and denominator electron object counts. The data sample consists of all single-electron events in the 2012 dataset, with cuts to reduce prompt contamination as described in the text. The markers represent object counts from 2012 data, and the colored histograms indicate the prompt subtractions estimated from Monte Carlo.

denominators exhibit a significant increase near the barrel-endcap overlap region, and also for  $|\eta| \gtrsim 2$ .

The following sources of systematic uncertainty are considered:

- **Prompt subtraction:** The presence of real, prompt leptons from Standard Model processes in the sample used to measure the fake factors is accounted for using Monte Carlo simulation. Uncertainties on the simulated samples include luminosity; cross section uncertainties; and reconstruction, trigger, and identification efficiency scale factors. These lead to a maximum uncertainty of about 20% where the prompt subtraction is largest.
- **Trigger efficiency correction:** As mentioned previously, an inefficiency is observed in the loose electron triggers for offline `loose++` electrons. This is due to the lack of

Figure 6.3: Electron fake factors parametrized in  $p_T$  and  $\eta$ .Figure 6.4: Electron fake factors projected in  $p_T$ . The denominator requirements are different below and above 24 GeV, where the triggers switch from EF\_eXX to EF\_gXX; below, the additional requirements on  $\Delta\eta_1$  and  $\Delta\phi_2$  cause a large drop in the denominators, and a large increase in the fake factor values.

GSF tracking in the trigger. For the fake factor derivation, this affects electrons in the range  $15 \text{ GeV} < p_T < 24 \text{ GeV}$ , where photon triggers are not available. Imposing the `tight++` cut on the track-cluster matching (the  $\Delta\eta$  and  $\Delta\phi$  between the electron track and calorimeter cluster) mitigates most, but not all, of the inefficiency, by cutting out electrons with large amounts of bremsstrahlung whose track are not reconstructed in the trigger. Based on a comparison of loose electron and photon triggers in the range  $24 \text{ GeV} < p_T < 85 \text{ GeV}$ , a correction of about 8% is applied to loose electron-triggered events, and the same value is taken as systematic uncertainty.

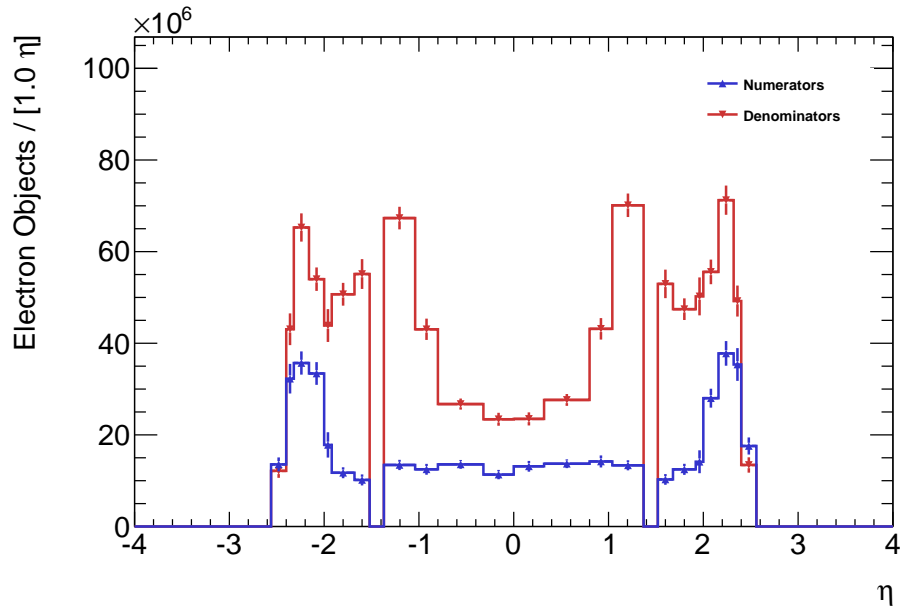


Figure 6.5: Electron numerator and denominator object counts versus  $\eta$  for  $p_T < 24$  GeV.

- **Extrapolation to signal region:** Two systematic uncertainties are assigned to account for bias due to the extrapolation of fake factors from the control region to the signal region. First, the cuts on  $m_T$  and  $E_T^{\text{miss}}$  are varied from  $< 40$  GeV to  $< 25$  GeV and  $< 55$  GeV. A  $p_T$ -dependent systematic uncertainty of up to 15% is assigned. Second, Monte Carlo-based truth studies indicate that the fake factor values are quite different for heavy- and light-flavor jets, so a difference in heavy flavor fraction between the control and signal regions will bias the fake factors. The effect of this is estimated using a  $t\bar{t}$  Monte Carlo sample, and a flat systematic uncertainty of 20% is assigned. See appendix 10.1.1 for more information.

The systematic and total uncertainties on the fake factors are shown as a function of  $p_T$  in figure 6.6.

### 6.2.3 Muon Fake Factors

The muon fake factor method is similar to that used in the ATLAS same-sign dilepton search on the 7 TeV dataset [10]. The method targets non-prompt muons from semileptonic heavy flavor decays, punch-through, and decays-in-flight of long-lived mesons by inverting the isolation requirements. Specifically, the denominator muons are defined as follows:

- Pass all numerator muon requirements in table 5.2, except the requirements on  $\text{Etcone30}$ ,  $\text{ptcone30}$ , and  $\frac{d_0}{\sigma_{d_0}}$ .

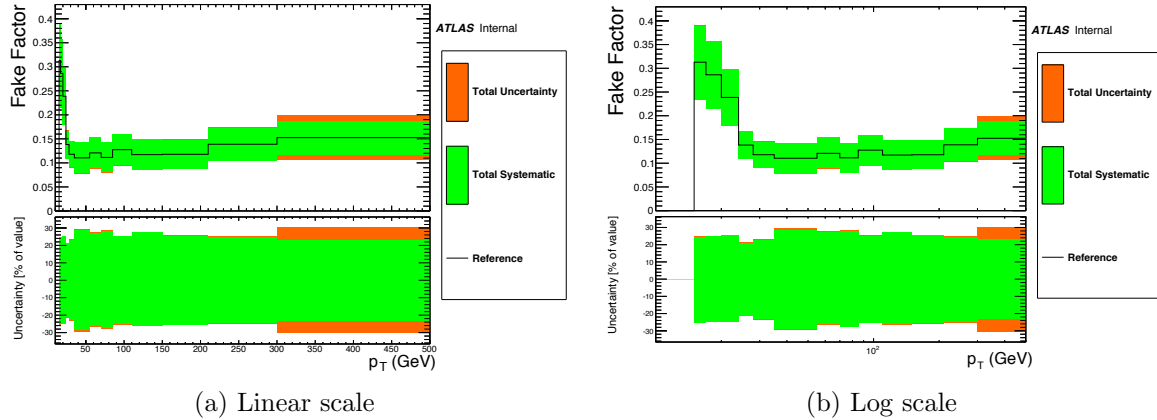


Figure 6.6: Electron fake factors vs.  $p_T$  with systematic and total uncertainties. The statistical uncertainty includes both the data and prompt subtraction Monte Carlo statistics.

- Loosen impact parameter cut:

$$\left| \frac{d_0}{\sigma_{d_0}} \right| < 10 \quad (6.13)$$

- Invert isolation:

$$\text{Etcone30, ptcone30} > \begin{cases} 0.15p_T & : p_T < 100 \text{ GeV} \\ 15 + 0.01p_T \text{ GeV} & : p_T > 100 \text{ GeV} \end{cases} \quad (6.14)$$

$$\frac{\text{Etcone30}}{p_T} < 2.0 \quad (6.15)$$

$$\frac{\text{ptcone30}}{p_T} < 2.0 \quad (6.16)$$

$$(6.17)$$

- If  $p_T < 40$  GeV, apply the same overlap requirement as the signal regions, removing the muon if  $\Delta R(\mu, \text{jet}) < 0.3$ . This overlap requirement is not applied for muons with  $p_T > 40$  GeV, which increases the statistical precision at the expense of additional systematic uncertainty. This is denoted by “dR” or “non-dR” below, for example in figure 6.9.

The muon fake factors are measured in a same-sign dimuon sample, triggered by the `EF_2mu13` trigger. The use of same-sign muons suppresses the prompt contamination from  $Z/\gamma^*$  events. The measurement uses only muons with large track impact parameter significance,  $\left| \frac{d_0}{\sigma_{d_0}} \right| > 3$ , to obtain a sample enriched in non-prompt muons (if both muons satisfy this requirement, then both are counted in the measurement). An extrapolation factor is derived from Monte Carlo to account for the fact that the signal region requires  $\left| \frac{d_0}{\sigma_{d_0}} \right| < 3$ , as detailed below.

Two sets of fake factors are measured, depending on the jet activity in the event. In the following, jets are required to have  $p_T > 30$  GeV, and be separated from muons with  $\Delta R(\mu, \text{jet}) > 0.3$ .

- **Inclusive:** Applied to events with zero jets. The measurement uses the entire same-sign dimuon sample.
- **Two-Jet:** Applied to events with one or more jet. The measurement uses same-sign dimuon events with at least two jets with  $p_T > 30$  GeV.

Fake muons from the two-jet sample are expected to come primarily from  $W + \text{jets}$  and  $t\bar{t}$  processes, while the inclusive sample also includes contributions from  $b\bar{b}$ . Figure 6.7 shows the  $p_T$  distributions of numerator and denominator muons in the measurement sample along with the expected prompt contributions.

The extrapolation factor from the measurement control region, with  $|\frac{d_0}{\sigma_{d_0}}| > 3$ , to the signal region, with  $|\frac{d_0}{\sigma_{d_0}}| < 3$ , is derived from various Monte Carlo samples. The extrapolation factor is simply the ratio of fake factors derived in Monte Carlo using the control region cut ( $|\frac{d_0}{\sigma_{d_0}}| > 3$ ) to those using the signal region cut ( $|\frac{d_0}{\sigma_{d_0}}| < 3$ ). The central value is taken from the POWHEG  $t\bar{t}$  sample, using all truth-level non-prompt muons, as shown in figure 6.8. A systematic uncertainty is assigned by comparing with other samples (MC@NLO  $t\bar{t}$  and PYTHIA8  $b\bar{b}$  and  $c\bar{c}$ ), and using only same-sign dimuon events in these samples.

The fake factors are parametrized one-dimensionally in  $p_T$  and  $\eta$ , as there are insufficient statistics to do a full two-dimensional parametrization. The fake factor is computed as:

$$f(p_T, \eta) = \frac{f(p_T) \times f(\eta)}{\langle f \rangle} \quad (6.18)$$

where  $\langle f \rangle$  is the total average fake factor. The measured fake factors are shown in figures 6.9 and 6.10.

The sources of systematic uncertainty considered are listed below, and the fractional systematic uncertainty is shown in figure 6.11.

- **Prompt subtraction:** The normalization of the simulated prompt subtraction samples is varied by  $\pm 10\%$ , leading to a systematic uncertainty of 1-6%.
- **Topological dependence:** The difference between the inclusive and two-jet fake factors is taken as a systematic uncertainty. The uncertainty is symmetrized, using the full difference as both upward and downward uncertainty, and ranges from 3% to 36%.
- **Dependence on  $d_0$  significance:** As mentioned previously, the extrapolation factor is derived in a number of different Monte Carlo samples. The largest deviation of 24% is taken as a systematic uncertainty.

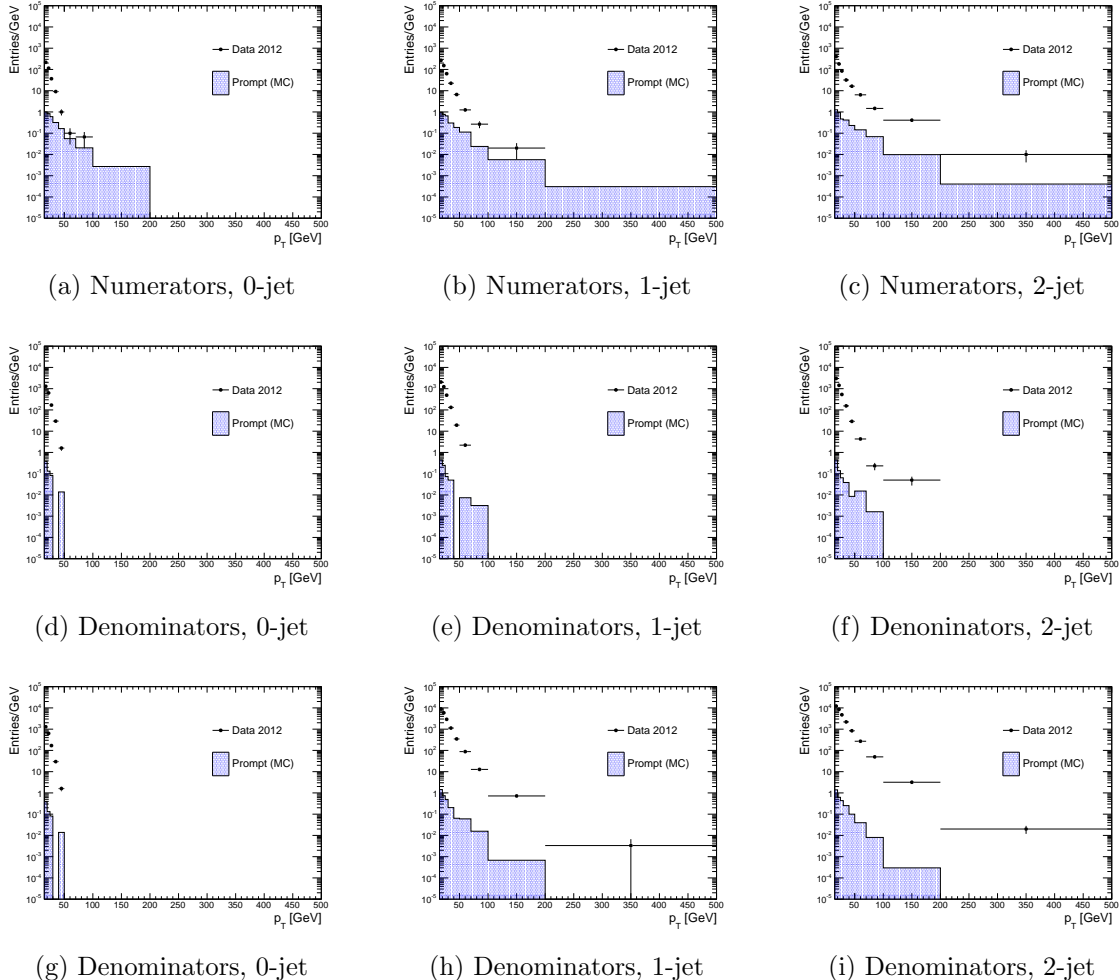


Figure 6.7:  $p_T$  spectrum of muons used in fake factor measurement. The left plots show events with zero jets, the middle plots show events with one jet, and the right plots show events with two or more jets. All numerator events require both numerator and denominator be separated from a jet by  $\Delta R > 0.3$ ; the same requirement is applied to denominators in the second row of plots, while the third row shows denominators that are not required to be isolated from nearby jets.

- **Light flavor fraction:** As with the electron fake factors, the fake factor values are quite different for muons originating from light flavor (LF) sources ( $\pi/K$  decay or punch-through) versus heavy flavor (HF) decays. The systematic uncertainty is described in detail in [11]; in brief, it uses the difference in momenta measured by the inner detector and muon spectrometer as a discriminant between HF and LF fakes, estimates the difference in HF/LF fraction between the control and signal regions, and finally uses HF and LF fake factors measured in Monte Carlo to estimate the effect of

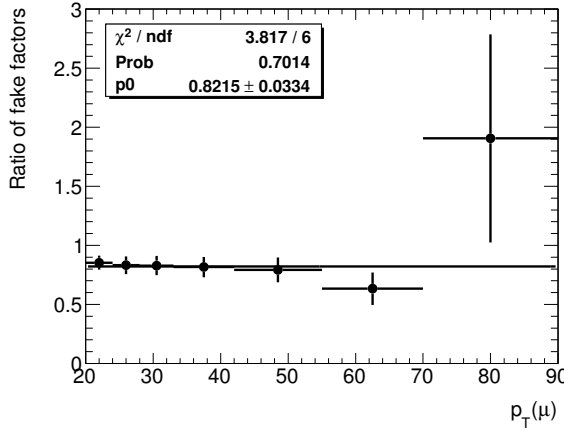


Figure 6.8: Ratio between the fake factors for muons with  $|d_0|/\sigma(d_0) > 3$  compared to fake factor with nominal numerator and denominator definitions. These fake factors are derived from a POWHEG  $t\bar{t}$  sample.

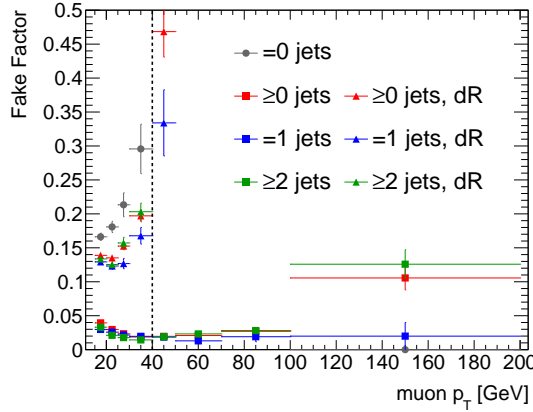


Figure 6.9: Muon fake factors as a function of  $p_T$ . Two sets of fake factors are plotted, with and without the “dR” requirement. The vertical dashed line at 40 GeV indicates the point at which the fake factors switch from the “dR” points, where the denominators are required to be separated from nearby jets, to the lower, non-“dR” points where the jet-isolation requirement is dropped to improve the statistics.

the discrepancy in HF/LF fraction. A systematic uncertainty of 2% to 21% is assigned.

### 6.2.4 Tau Lepton Fakes

The detector signature of hadronically decaying tau leptons, consisting of a jet with one or more associated tracks, is not as distinctive as the signature of electrons and muons. Differentiating between jet, which are copiously produced in proton-proton collisions, and

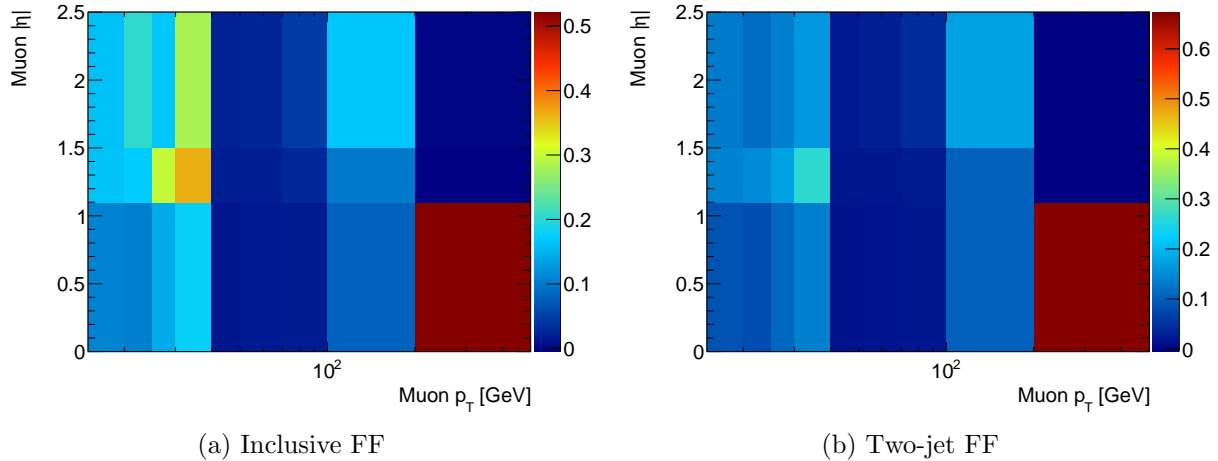


Figure 6.10: Muon fake factors as functions of  $p_T$  and  $|\eta|$ . The left plot shows fake factors measured in the inclusive control sample and applied to events with zero jets. The right plot shows fake factors measured in events with two jets, and applied to events with at least one jet.

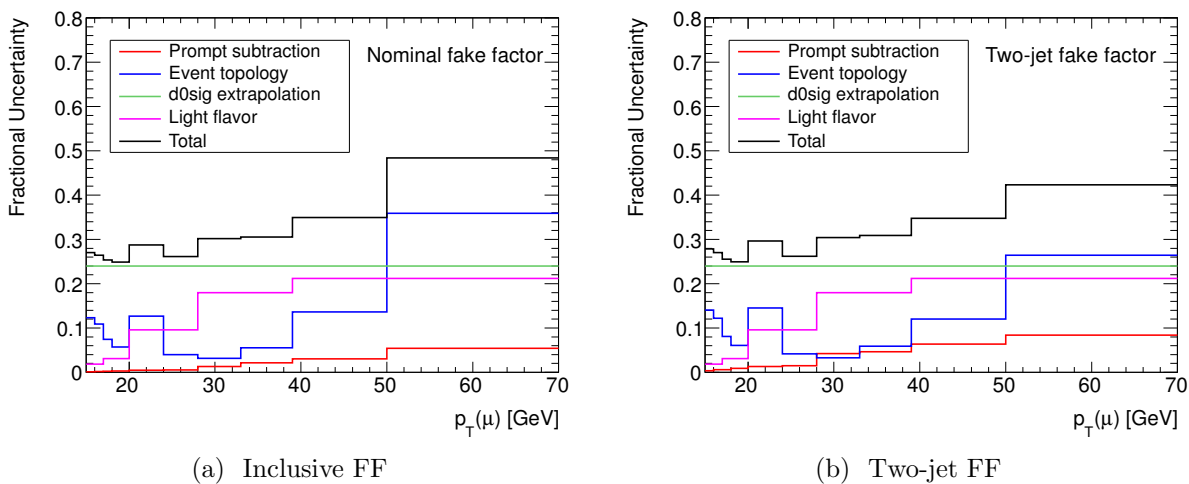


Figure 6.11: Systematic uncertainties on muon fake factor as a function of  $p_T(\mu)$ . The left plot shows the uncertainties for the inclusive fake factor, while the right shows the uncertainty for the two-jet fake factor.

hadronically decaying tau leptons is difficult, and accordingly the reducible backgrounds in events containing a hadronically decaying tau lepton is much larger.

The tau identification algorithm (section 5.4) employs a multivariate discriminant based on calorimeter shower shapes and tracking information. The fake rate is strongly dependent on the jet fragmentation, in particular whether the parton initiating the jet is a gluon, light quark, or heavy quark. In constructing the denominator definition, a tighter efficiency working point reduces the dependence on the initial parton, thereby improving the extrapolation of the fake factors to the signal regions; on the other hand, the working point must be loose enough to collect sufficient statistics. The denominator definition requires tau candidates to have a **BDTScore** which fails the **BDT-Medium** selection threshold, but exceeds 0.9 times the  $p_T$ -dependent **BDT-Loose** threshold. In simulation, this definition is seen to be relatively insensitive to the type of parton initiating the jet. The fake factors are measured two-dimensionally in bins of  $p_T$  and  $|\eta|$ , and a correction is applied as a function of the highest MV1  $b$ -tag weight of all jets in the event.

### Fake Factor Measurement

The tau lepton fake factors are measured using a tag-and-probe method in a sample targeting  $W+jets$  events. Events are required to have a muon satisfying the numerator criteria (tag) plus a hadronic tau candidate (probe). To avoid biasing the fake factors, no other requirements are imposed to reject the prompt contamination (for example, requiring the muon and  $\tau_{\text{had-vis}}$  to have the same sign biases the sample towards gluon-initiated jets). The prompt contamination, dominantly from  $Z+jets$  and  $t\bar{t}$  production, is subtracted using simulation.

The muon- $\tau_{\text{had-vis}}$  invariant mass and  $\tau_{\text{had-vis}} p_T$  spectra for numerators and denominators are shown in figure 6.12, along with the prompt contribution estimated from simulation. Figure 6.13 shows the resulting fake factors.

### Systematic Uncertainties

The following sources of systematics uncertainties on the tau fake factors are considered:

- Uncertainties on the simulation-based estimates of the prompt contamination.
- Uncertainties associated with the binning choice.
- Dependence of the fake factors on the flavor of the initiating parton.

The uncertainty due to the prompt contamination estimation is derived by fluctuating the normalizations of the Monte Carlo samples by their theoretical uncertainties. The resulting variations in the fake factors are between 5%-17%, and are largest for  $30 \text{ GeV} \lesssim p_T \lesssim 40 \text{ GeV}$ , where the contribution from  $Z \rightarrow \tau_\mu \tau_{\text{had}}$  is greatest.

To estimate the effect of the binning, the fake factors are reapplied to the same sample they were derived from. The results are shown in figure 6.14. An uncertainty of 5% is assigned.

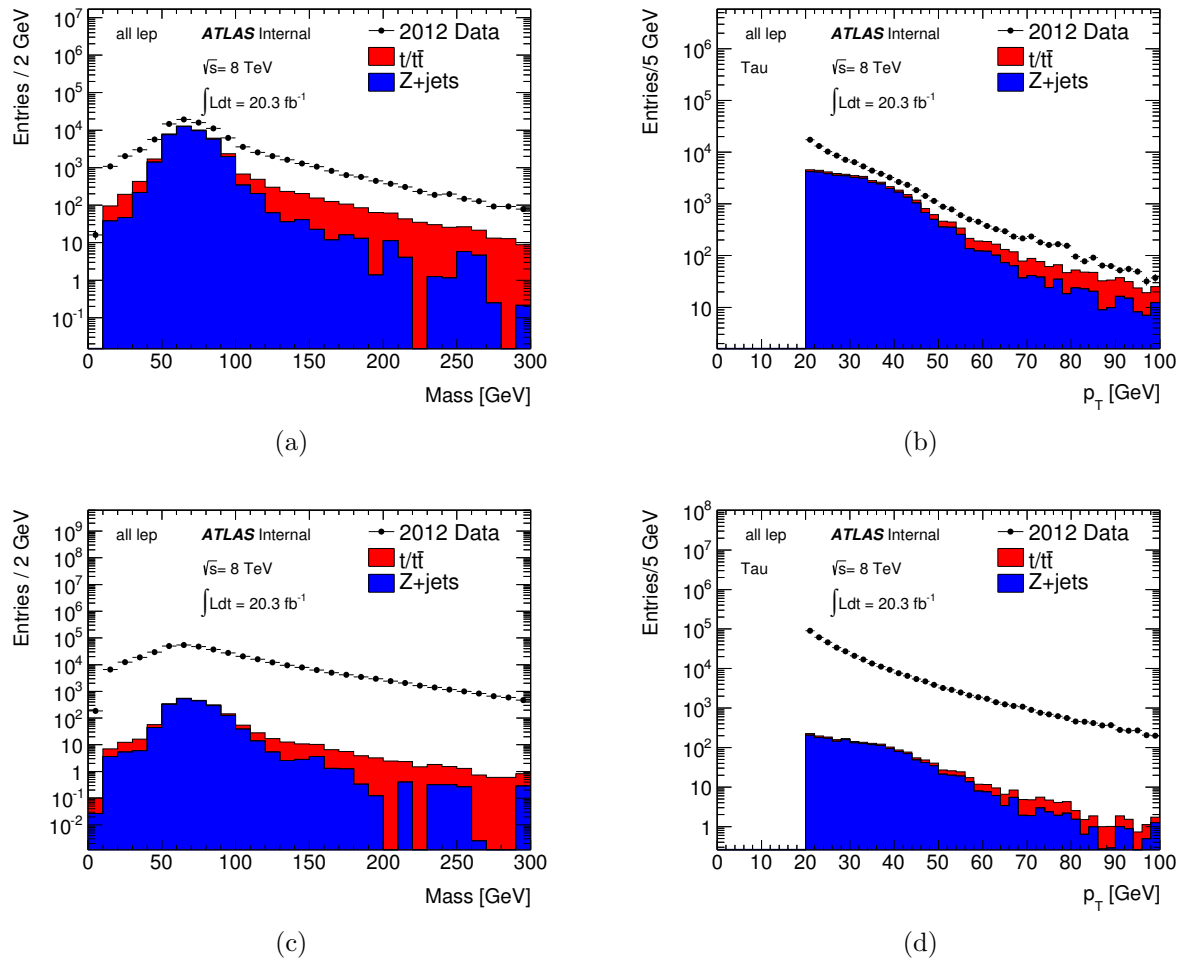


Figure 6.12: Invariant mass of the muon and  $\tau_{\text{had-vis}}$  pair (left) and  $p_T$  of the tau candidate (right). The top plots show the distributions for numerator  $\tau_{\text{had-vis}}$  candidates, while the bottom plots show the distributions for denominator  $\tau_{\text{had-vis}}$  candidates. The filled histograms show the prompt contamination estimated from simulation.

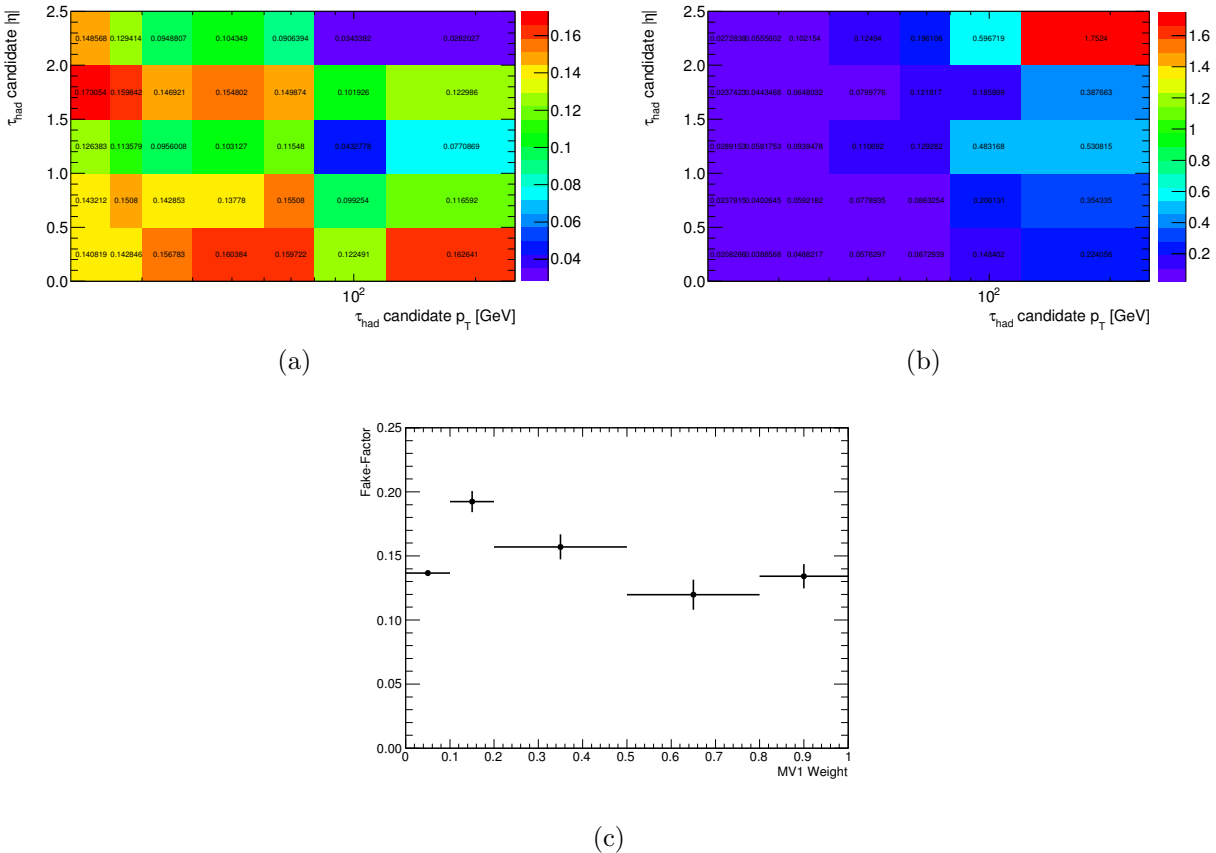


Figure 6.13: Tau fake factors binned in  $p_T$  and  $|\eta|$  (left), and the corresponding statistical uncertainty (right). The correction for the maximum MV1  $b$ -tag weight of all jets in the event is also shown (bottom). The fake factors are derived from  $W+jets$  events.

Finally, to estimate the effect of differences in flavor composition between the measurement sample and the signal regions, the fake factors are applied to a  $t\bar{t}$  validation region. In simulation, this validation region is observed to have a substantially different flavor composition from the  $W+jets$  measurement sample. A systematic uncertainty of 25% covers the observed differences between the fake background estimate and the data.

In total, the systematic uncertainties are in the range 25%-30%, and are largest around  $30 \text{ GeV} \lesssim p_T \lesssim 40 \text{ GeV}$ .

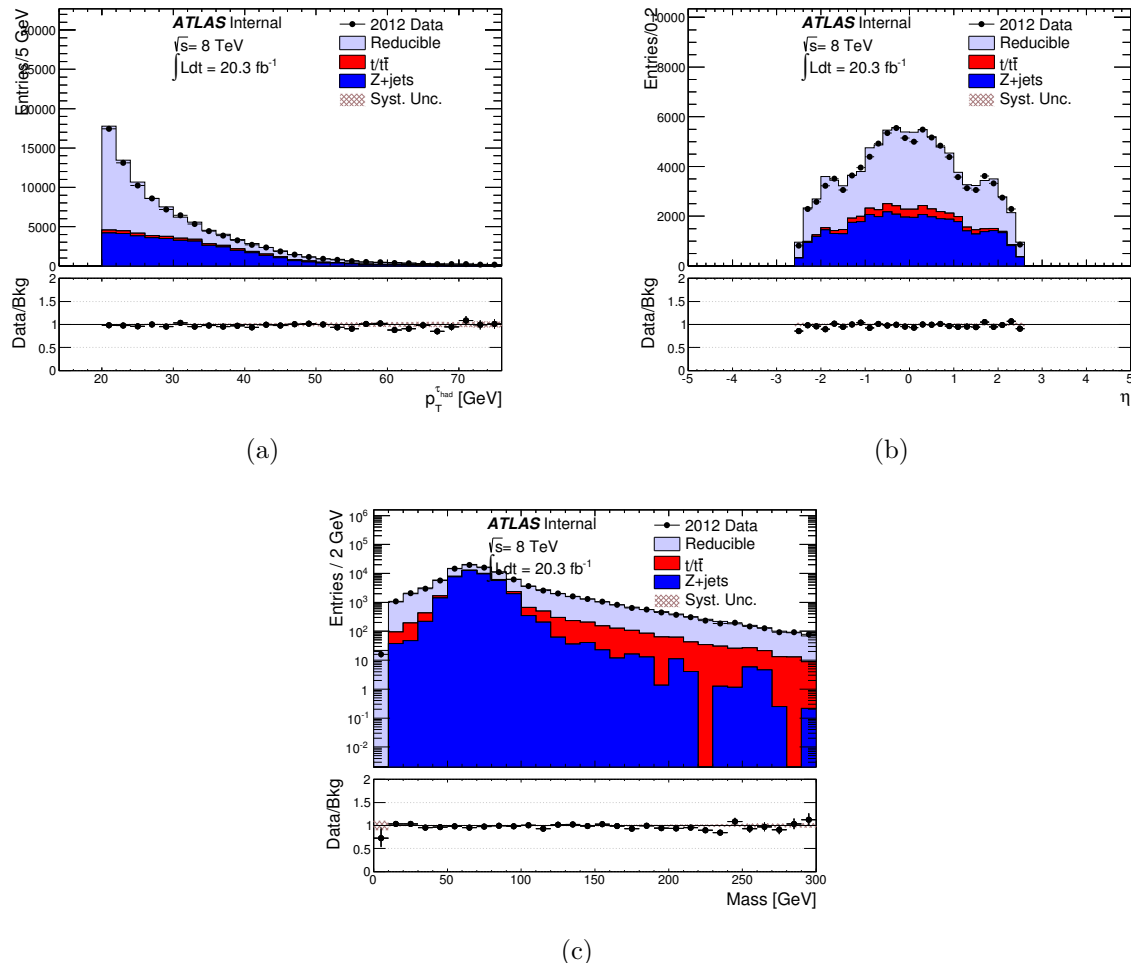


Figure 6.14: Results of the closure test, comparing the data to the fake factor-based background estimate in a  $t\bar{t}$  validation region. The  $\tau_{\text{had-vis}} p_T$  (left),  $|\eta|$  (right), and the dilepton invariant mass (bottom) are shown.

# Chapter 7

## Model-Independent Trilepton Search

Events containing three or more leptons are useful probes of phenomena beyond the Standard Model. The production of three or more leptons is predicted by many models of phenomena beyond the Standard Model, as described in section 2.2. The expected Standard Model backgrounds are typically small; depending on the flavor and charge of the three leptons, such events primarily arise from diboson production ( $WZ$ ,  $ZZ$ ), or from single boson ( $W$ ,  $Z/\gamma^*$ ) or  $t\bar{t}$  production along with one or more leptons from misidentified or semileptonically decaying jets. This dissertation presents two such searches: a model-independent search for nonresonant production of three or more leptons in many signal regions, and a signature-driven search for resonance trilepton production in the context of heavy leptons.

This chapter presents a search for physics beyond the Standard Model using events containing three or more leptons [1]. The search uses  $20.3 \text{ fb}^{-1}$  of  $pp$  collision data taken at  $\sqrt{s} = 8 \text{ TeV}$  with the ATLAS detector. Many signal regions are defined based on the properties of the leptons, jets, and overall momentum imbalance of the event, with the goal of being broadly sensitive to the nonresonant production of trilepton final states by phenomena beyond the Standard Model. The results are first presented in a model-independent fashion, establishing upper limits on the production of events with three or more charged leptons from non-Standard Model sources. The limits are then confronted against a model predicting new doubly charged scalar particles.

### 7.1 Event Selection

This section describes the selection of events containing at least three leptons in the  $pp$  collision data and Monte Carlo simulation samples.

#### 7.1.1 Triggering

Collisions events for this analysis are triggered using the unprescaled single-electron or single-muon triggers with the lowest transverse momentum thresholds. At least one of the following

triggers must have fired:

- `EF_e24vhi_medium1`: One electron with  $p_T > 24$  GeV. The electron must satisfy cuts similar to the `medium++` identification criteria at the trigger level, an isolation requirement of  $\frac{p_T^{\text{cone}20}}{p_T} < 0.1$ , and cuts on the leakage into the hadronic calorimeter.
- `EF_e60_medium1`: One electron with  $p_T > 60$  GeV. The electron must also satisfy the medium identification cuts, but the isolation and leakage requirements are removed.
- `EF_mu24i_tight`: One muon with  $p_T > 24$  GeV, satisfying an isolation requirement of  $\frac{p_T^{\text{cone}20}}{p_T} < 0.12$ .
- `EF_mu36_tight`: One muon with  $p_T > 36$  GeV, with no isolation requirement.

The triggers with higher transverse momentum thresholds remove the isolation requirements in order to improve the efficiency at higher  $p_T$ . Triggered events are required to have an offline lepton matched to the trigger object within  $\Delta R = \sqrt{(\Delta\eta)^2 + (\Delta\phi)^2} < 0.1$ . To avoid trigger turn-on effects near the  $p_T$  threshold, the offline lepton must have  $p_T > 26$  GeV. Additionally, trigger-matched muon must have  $|\eta| < 2.4$  to avoid uninstrumented regions of the detector.

### 7.1.2 Trilepton Event Selection

After successful triggering and overlap removal, events are required to have at least three selected leptons, of which at most one is a hadronically decaying tau lepton. The primary event vertex, chosen as the reconstructed vertex with the highest  $\sum p_T^2$  of tracks, must have at least three tracks. Finally, events are rejected if they contain “bad jets” not associated to real energy deposits in the calorimeters due to  $pp$  collisions, i.e. from electronics problems or cosmic rays [2].

## 7.2 Analysis Strategy

The analysis defines a large number of nonexclusive signal regions, designed to target new physics models and to compartmentalize the expected backgrounds. First, the events are divided into six categories as follows. First, the events are divided into three categories based on the properties of any opposite-sign, same-flavor (OSSF) lepton pairs in the event:

- **on- $Z$** : events containing an OSSF lepton pair consistent with the decay of a  $Z$  boson, with invariant mass within 20 GeV of  $m_Z$ ;
- **off- $Z$ , OSSF**: events containing an OSSF pair that do not fall in the on- $Z$  category; and

- **off- $Z$ , mixed:** events containing no OSSF pairs.

The on- $Z$  category also includes events containing three leptons (two of which form an OSSF pair) with invariant mass within 20 GeV of  $m_Z$ , to include events containing a  $Z$  boson where a photon from final state radiation converts and is reconstructed as a prompt electron.

Next, the events are further divided into two categories based on the number of electron or muon candidates in the event:

- **3L:** events containing at least three electrons or muons, and
- **2L+ $\tau_{\text{had}}$ :** events containing exactly two electrons or muons and a hadronically decaying tau lepton.

After dividing the events into these six exclusive categories, many signal regions are defined based on the lower bound in various kinematic variables. An ordering is imposed on the leptons for the sake of disambiguation: in the 3L category, the leptons are ordered by  $p_T$ , while in the 2L category, the electrons or muons are ordered by  $p_T$ , and the  $\tau_{\text{had}}$  is the third lepton. The variables used to define the signal regions are:

- $H_T^{\text{leptons}}$ : the scalar sum of the transverse momenta of the leading three leptons. Events containing new particles with masses significantly greater than  $m_W$  or  $m_Z$  will typically have larger  $H_T^{\text{leptons}}$  than the Standard Model backgrounds.
- Minimum  $p_T^\ell$ : the  $p_T$  of the softest of the leading three leptons. As with  $H_T^{\text{leptons}}$ , the  $p_T$  of leptons produced in the decays of heavy particles will tend to be larger than those from the expected Standard Model backgrounds.
- $H_T^{\text{jets}}$ : the scalar sum of the transverse momenta of all selected jets in the event. This variable is sensitive to the strongly produced new physics, where leptons are produced in the decays of heavy colored particles, such as squarks. Such events often contain hard jets in addition to the three leptons. Conversely, the Standard Model  $WZ$  and  $ZZ$  backgrounds are weakly produced, and have softer  $H_T^{\text{jets}}$  distributions.
- $E_T^{\text{miss}}$ : the magnitude of the missing transverse momentum in the event. In models of new physics, leptons can be produced in association with new invisible particles, such as stable neutralinos in  $R$ -parity conserving supersymmetry, or with neutrinos in leptonic  $W$  decays. Requiring large  $E_T^{\text{miss}}$  can distinguish such signals from the Standard Model backgrounds, where the  $E_T^{\text{miss}}$  is primarily due to neutrinos from  $W$  or  $\tau$  decays. Requiring large  $E_T^{\text{miss}}$  also suppresses backgrounds due to  $Z+\text{jets}$ , where the jet decays semileptonically or is misidentified as a lepton.
- $m_{\text{eff}}$ : the scalar sum of  $H_T^{\text{jets}}$ ,  $E_T^{\text{miss}}$ , and the  $p_T$  of all identified leptons in the event. As with  $H_T^{\text{leptons}}$  by itself, multilepton production due to the decays of heavy particles will typically have a harder  $m_{\text{eff}}$  distribution than the Standard Model backgrounds.

Variable	Meaning					
$H_T^{\text{jets}}$	$\Sigma p_T$ of all jets in the event					
$m_T^W$	Transverse mass of $W$ -boson candidate (on- $Z$ events only)					
Variable	Meaning	Lower Bounds [GeV]		Additional Requirements		
$H_T^{\text{leptons}}$	$\Sigma p_T$ of leading three leptons	0	200	500	800	
Min. $p_T^\ell$	$p_T$ of softest (third) lepton	0	50	100	150	
$E_T^{\text{miss}}$	Missing transverse momentum	0	100	200	300	$H_T^{\text{jets}} < 150$ GeV
$E_T^{\text{miss}}$		0	100	200	300	$H_T^{\text{jets}} \geq 150$ GeV
$m_{\text{eff}}$		0	600	1000	1500	
$m_{\text{eff}}$	All transverse activity	0	600	1200		$E_T^{\text{miss}} \geq 100$ GeV
$m_{\text{eff}}$		0	600	1200		$m_T^W \geq 100$ GeV, on- $Z$
Variable	Meaning	Lower Bounds				
$b$ -tags	Number of $b$ -tagged jets	1	2			

Table 7.1: Kinematic signal regions defined in the analysis.

- $m_T^W$ : for events in the on- $Z$  categories, the transverse mass of the missing transverse momentum,  $\vec{p}_T^{\text{miss}}$ , and the highest- $p_T$  lepton not associated with a  $Z$  boson candidate, defined as:

$$m_T^W = \sqrt{2|\vec{p}_T^\ell| |\vec{p}_T^{\text{miss}}| (1 - \cos(\Delta\phi))}, \quad (7.1)$$

where  $\Delta\phi$  is the azimuthal angle between the transverse momentum of the lepton,  $\vec{p}_T^\ell$ , and the missing transverse momentum,  $\vec{p}_T^{\text{miss}}$ .

- $N_{b\text{-tags}}$ , the number of  $b$ -tagged jets. New physics scenarios related to the hierarchy problem (section 2.2) often couple preferentially to the third generation, due to the dominant effect of the top quark in the running of the Higgs mass.

The signal regions are defined in table 7.1. The signal regions use one of  $H_T^{\text{leptons}}$ , the minimum  $p_T^\ell$ ,  $E_T^{\text{miss}}$ ,  $m_{\text{eff}}$ , and  $n_b$  as binning variables.  $H_T^{\text{jets}}$ ,  $E_T^{\text{miss}}$ , and  $m_T^W$  are used to impose additional requirements on the signal regions. In total, 138 signal regions are defined.

## 7.3 Systematic Uncertainties

Systematic uncertainties are assigned to the signal and background predictions to account for possible modelling inaccuracies. The sources of uncertainty considered are:

- Uncertainties on the reducible background estimates from the data-driven estimation method, as described in section 6.2.1. The uncertainties ranges between 20% to 30% for the electron fake factors, 25% to 50% for the muon fake factors, and 25% to 30% for the tau lepton fake factors.

Sample	Uncertainty
$t\bar{t} + V$	30% [3, 4]
$ZZ$	4.3%
$WZ$	7.6%

Table 7.2: Systematic uncertainties used for the MC samples that contribute to the background estimates.

- Simulated Monte Carlo samples, whether signal or background, must be normalized to the integrated luminosity of the data. The weight assigned to each event is:

$$w = \frac{\mathcal{L}\sigma_{\text{process}}}{N_{\text{sim}}}, \quad (7.2)$$

where  $\mathcal{L}$  is the integrated luminosity of the data,  $\sigma_{\text{process}}$  is the cross section of the simulated process, and  $N_{\text{sim}}$  is the number of simulated events. The integrated luminosity carries an uncertainty of 2.8%, as described in section 4.5. The cross sections are taken from calculations with uncertainties due to various sources, including the fixed order of the calculation, the choice of renormalization and factorization scales, and the PDFs. For the dominant  $WZ$  and  $ZZ$  backgrounds, the predictions from SHERPA are compared to those from the next-to-leading-order generator VBFNLO. The generators show good agreement, and the systematic uncertainty on the cross section is determined from VBFNLO by varying the factorization and renormalization scales up and down by factors of two. The uncertainties are shown in table 7.2.

No systematic uncertainty is assigned to the normalization of the  $Z + \gamma$  sample. Rather, a large uncertainty of 30% is assigned due to the reweighting procedure described in section 10.1.1. The  $VVV^{(*)}$  sample is also not assigned an uncertainty due to its small contribution to the signal regions.

- Events are also weighted to account for differences between data and Monte Carlo simulation in the lepton trigger, reconstruction, and identification efficiencies. The scale factors and associated uncertainties are provided by the relevant ATLAS combined performance groups. The electron (section 5.2.2) and muon (section 5.3.1) scale factors are close to unity, with uncertainties in the range 1-5%. The scale factors for the tau lepton identification efficiency range from 94-96% for the BDTTight working point, and carry uncertainties between 2.0-2.2% (section 5.4).
- The lepton energy scales carry uncertainty which has a small effect on the signal regions due to leptons or events near  $E_T$  or  $p_T$  thresholds, as described in sections 5.2.3, 5.3.2, and 5.4.1.

- The jet energies are scaled and smeared according to recommendations from the `JetEtMiss` combined performance group (section 5.5.1). The uncertainty affects the  $H_T^{\text{jets}}$  and  $m_{\text{eff}}$  distributions, and also the lepton-jet overlap removal procedure.
- The lepton and jet energy uncertainties are also propagated to the missing transverse energy,  $E_T^{\text{miss}}$ .
- The efficiencies of the  $b$ -tagging algorithm carry uncertainties which are parameterized based on matching the identified  $b$ -jets to truth  $b$ -jets.
- Finally, the Monte Carlo samples carry statistical uncertainty due to simulating a finite number of events.

The dominant sources of uncertainty depend on the signal region, but are generally due to Monte Carlo statistical uncertainties, the fake factor uncertainties, and theoretical cross section uncertainties.

## 7.4 Background Validation

The background estimates are verified in several dedicated validation regions, which are orthogonal to the signal regions. Events containing two leptons are used to test the selection of prompt leptons and their corresponding scale factors and energy corrections. The reducible backgrounds are tested in  $t\bar{t}$  validation regions, where the events are required to have two same-sign leptons to target semileptonic decays where one lepton arises from a reducible process. Finally, the fake factor method is validated in events with modified, intermediate lepton selections, where the signal leptons are between the numerator and denominator definitions used in the nominal reducible background estimate.

### 7.4.1 Dilepton Validation Regions

Three dilepton validation regions target the three flavors of leptons:  $ee$ ,  $\mu\mu$ , and  $\mu\tau_{\text{had}}$ . The  $ee$  and  $\mu\mu$  regions require an opposite-sign lepton pair of the appropriate flavor. The invariant mass distributions of the dilepton system in these regions are shown in figure 7.1. Some disagreement is observed in the  $ee$  invariant mass distribution; this discrepancy is covered by the electron energy scale systematic uncertainties.

The  $ee$  and  $\mu\mu$  validation regions are also used to generate scale factors to account for efficiency differences between simulation and data when applying cuts on lepton isolation or impact parameter. The scale factors are computed from events with a dilepton pair with invariant mass within 10 GeV of  $m_Z$ , and are shown in figure 7.2. The scale factors are mostly consistent with unity to within 0.5%, except for isolation requirements on the low- $p_T$  leptons, where the scale factors deviate from unity by up to 2%.

The  $\mu\tau_{\text{had}}$  region applies addition cuts to reduce the large contribution from fake tau leptons in  $W+\text{jets}$  events:

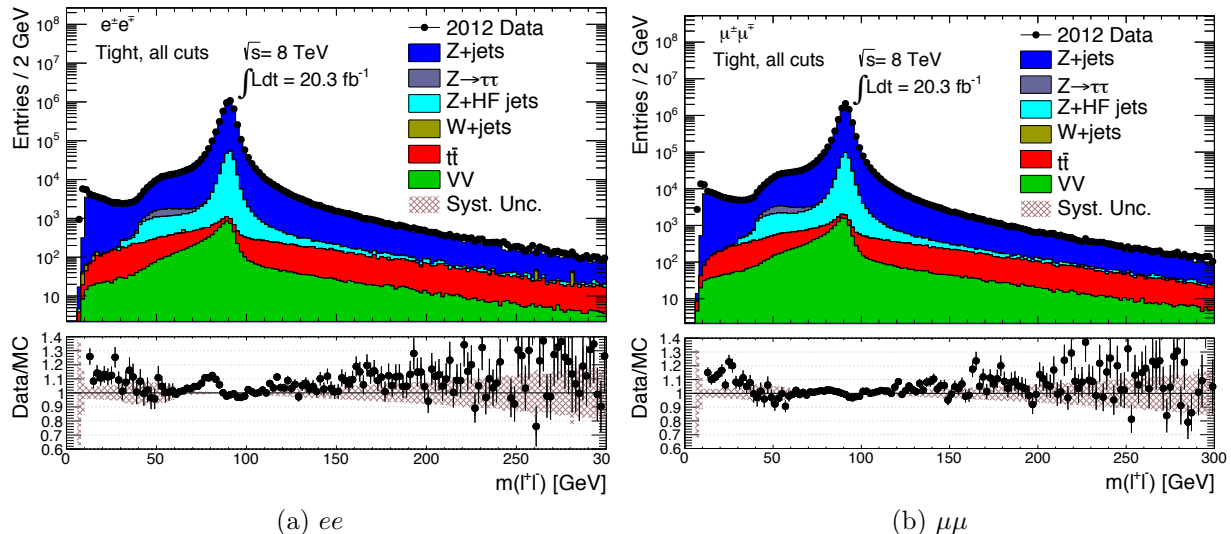


Figure 7.1: Dilepton invariant mass distributions for the  $ee$  (left) and  $\mu\mu$  (right) validation regions.

- $\cos \Delta\phi(\mu, E_T^{\text{miss}}) + \cos \Delta\phi(\tau, E_T^{\text{miss}}) > -0.15$ ,
- $\Delta\phi(\mu, \tau_{\text{had}}) > 2.4$ ,
- $m_T^\mu < 50$  GeV,
- $42 < m_Z^{\text{vis.}} < 82$  GeV, and
- $p_T^\mu < 40$  GeV.

The  $p_T$  distribution of the  $\tau_{\text{had-vis}}$  is shown in figure 7.3.

### 7.4.2 $t\bar{t}$ Validation Regions

In signal regions that veto  $Z$  bosons and require large  $H_T^{\text{jets}}$  or  $E_T^{\text{miss}}$ , a large reducible background component is expected from  $t\bar{t}$  events, where both  $W$  bosons decay leptonically and a third lepton arises from a misidentified jet or semileptonic heavy flavor decay. This process is tested in the  $t\bar{t}$  validation regions, which require at least one  $b$ -tagged jet with  $p_T > 30$  GeV, exactly two electrons or muons with the same charge, and  $H_T^{\text{jets}} < 500$  GeV. The requirement that the leptons have the same sign vetoes dilepton  $t\bar{t}$  events with two prompt leptons from  $W$  decays, while the  $H_T^{\text{jets}}$  requirement reduces the potential contamination from new BSM phenomena. Note that events containing hadronically decaying tau leptons are used to derive a systematic uncertainty on the tau fake factors due to the flavor composition of the events (section 6.2.4), and so are not used as a validation region.

The  $E_T^{\text{miss}}$  distribution of events in the  $t\bar{t}$  validation region is shown in figure 7.4.

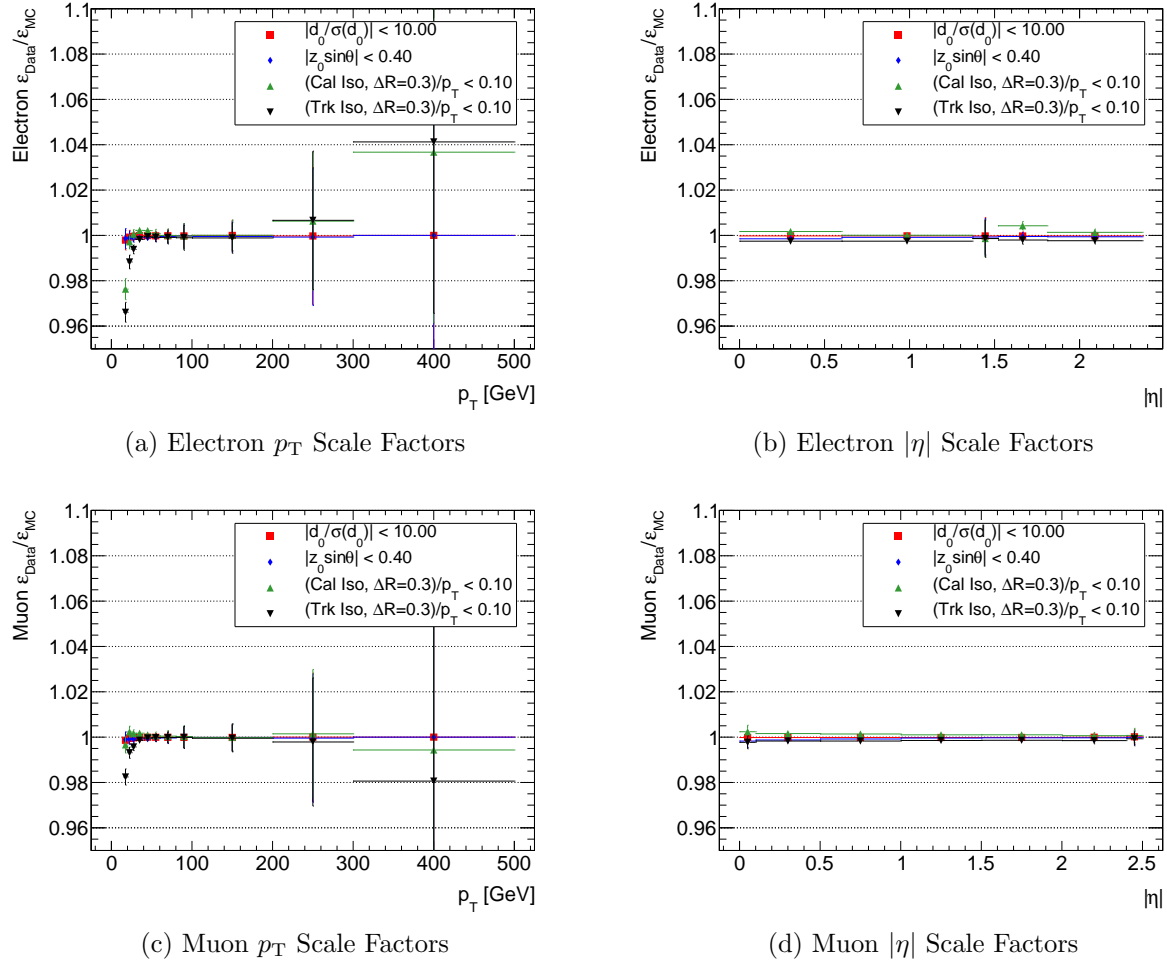


Figure 7.2: Scale factors for electrons and muons as functions of  $p_T$  (left) and  $|\eta|$  (right).

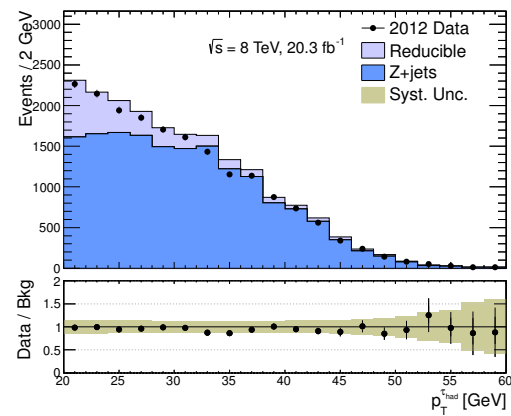


Figure 7.3:  $p_T$  distribution of the  $\tau_{\text{had-vis}}$  candidates in the  $\mu\tau_{\text{had}}$  validation region.

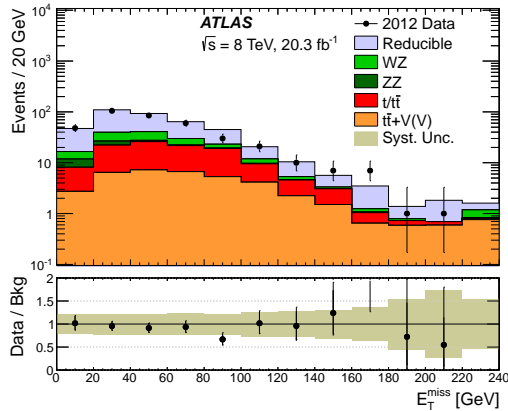


Figure 7.4:  $t\bar{t}$  validation regions for all flavor ( $e, \mu$ ) combinations.

### 7.4.3 Intermediate Fake Factor Validation Regions

The fake factor method is further validated in regions containing events with two signal (numerator) leptons and one “intermediate” lepton, which fulfills selection criteria looser than the numerator criteria but tighter than the denominator criteria. Separate fake factors are derived for intermediate leptons; these are defined schematically as  $\langle \text{intermediate} \rangle / \langle \text{denominator} \rangle$ , rather than  $\langle \text{numerator} \rangle / \langle \text{denominator} \rangle$ . Specifically, the intermediate leptons satisfy most of the numerator criteria except for:

- **Electrons:** the electron must pass the `medium++` cuts, but fail the `tight++` cuts.
- **Muons:** the candidate must have either its track or calorimeter transverse isolation energy satisfy  $0.10 < \text{iso}/p_T < 0.15$ .
- **Taus:** the tau candidate must pass the `Medium-BDT` identification requirement, but fail the `tight-BDT` identification requirement.

The first two regions, targeting reducible electrons and muons, require an OSSF pair of electrons or muons, plus a third intermediate electron or muon of the opposite flavor. The events are largely due to  $Z \rightarrow ee$  or  $Z \rightarrow \mu\mu$  events, with an additional lepton that is either prompt and fails the signal lepton criteria, or is due to a reducible process. The  $p_T$  and  $\eta$  distributions of the intermediate electrons and muons are shown in figure 7.5.

The events containing an intermediate  $\tau_{\text{had}}$  are much more abundant than intermediate electrons or muons, so three  $\tau_{\text{had}}$  validation regions are defined, mirroring the signal region categories. Events are required to contain two electrons or muons plus an intermediate  $\tau_{\text{had}}$ , and are separated into on- $Z$ , off- $Z$ /OSSF, and off- $Z$ /mixed categories, depending on the two electrons or muons. The  $p_T$  and  $\eta$  of the intermediate  $\tau_{\text{had}}$  is shown for each category in figure 7.6.

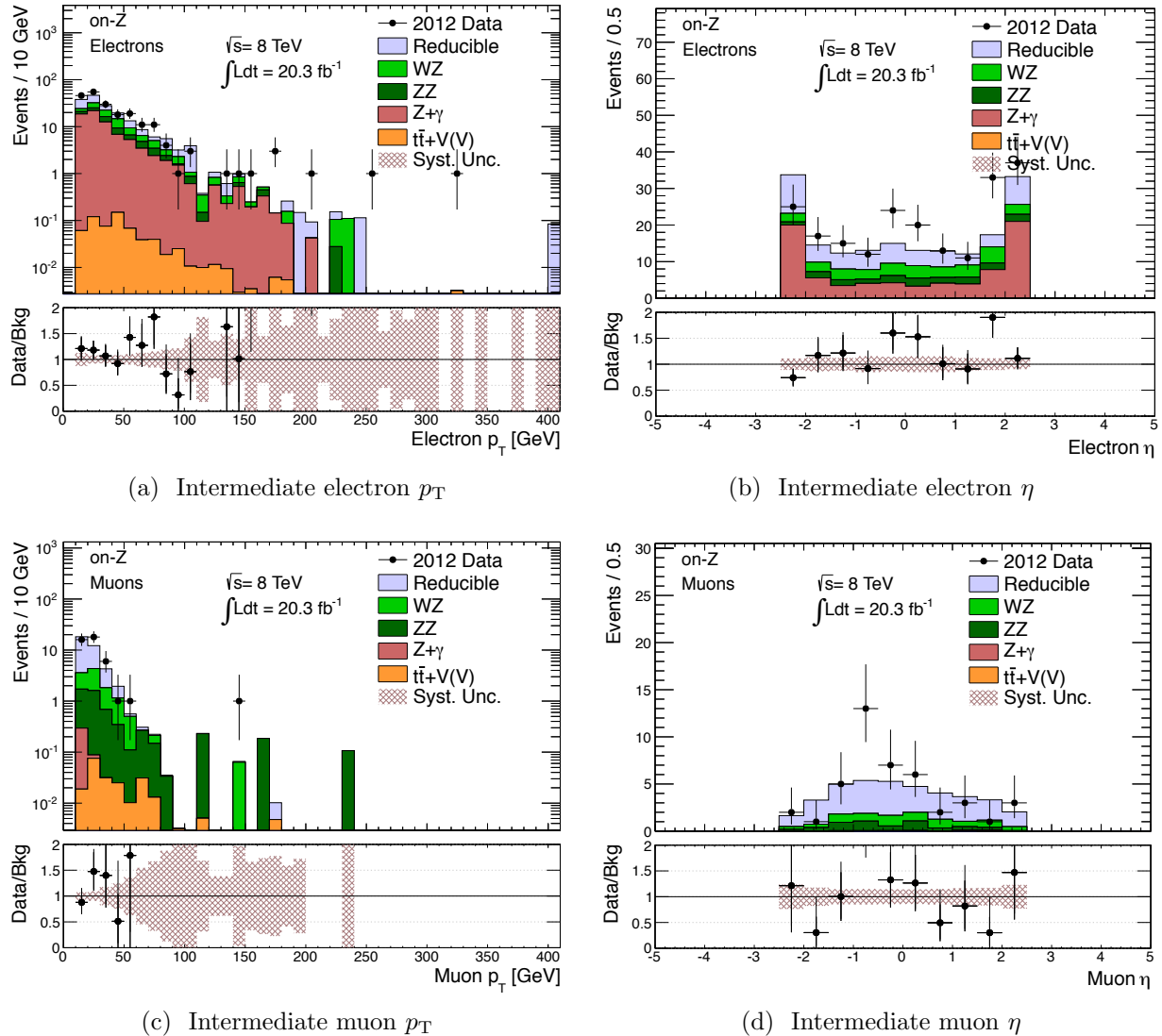


Figure 7.5:  $p_T$  and  $\eta$  distributions of the off- $Z$  electron (top) or muon (bottom) satisfying the intermediate selection criteria. The other two leptons in the event are required to satisfy the numerator selection criteria and form an opposite-sign, same-flavor pair, with different flavor from the intermediate lepton.

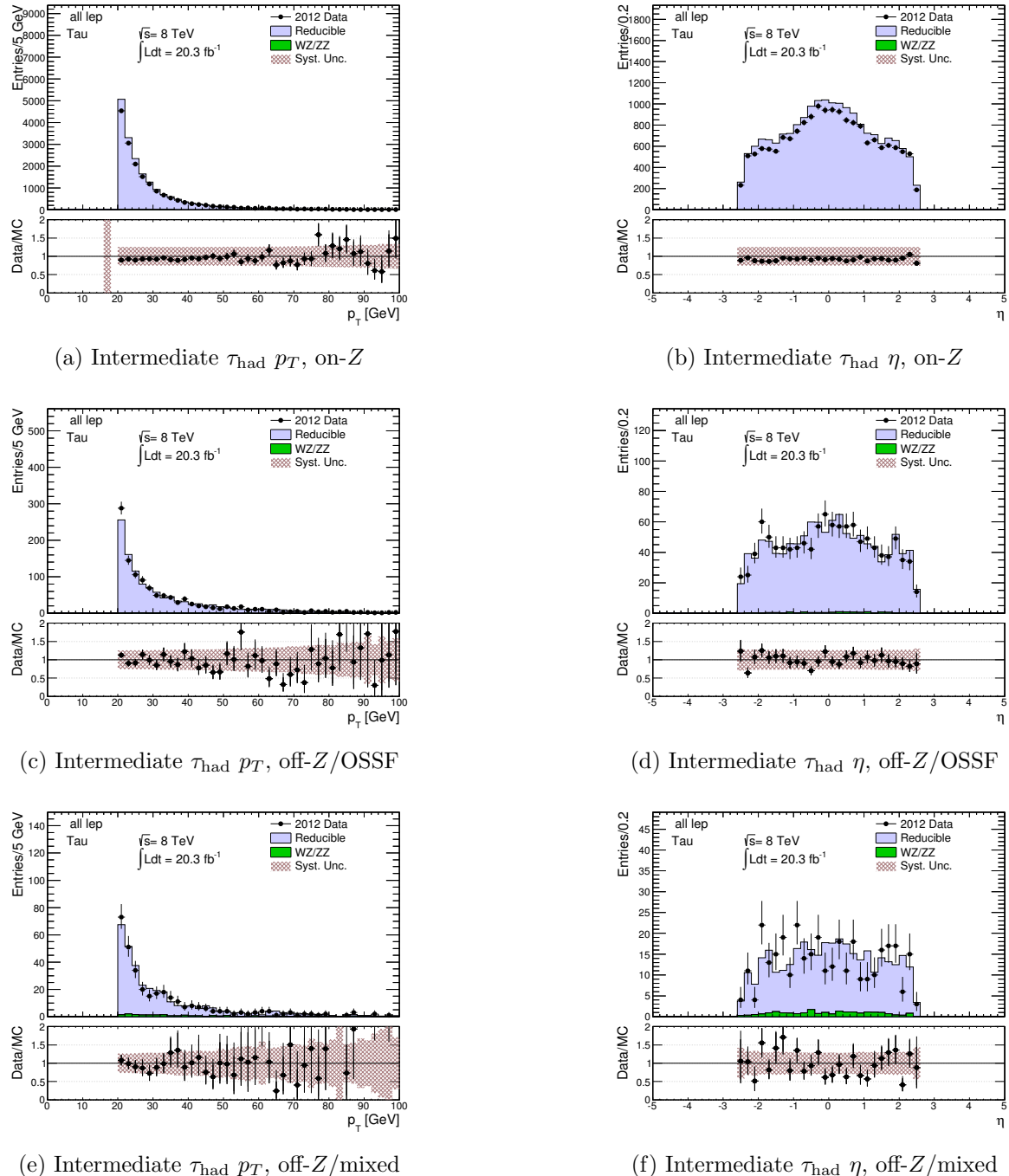


Figure 7.6:  $p_T$  and  $\eta$  distributions of the intermediate  $\tau_{\text{had}}$  in the on- $Z$ , off- $Z$ /OSSF, and off- $Z$ /mixed intermediate validation regions.

## 7.5 Results and Limits

The results of the search as organized as follows. For each category, the distributions of the various kinematic variables ( $H_T^{\text{leptons}}$ ,  $H_T^{\text{jets}}$ ,  $m_{\text{eff}}$ ,  $E_T^{\text{miss}}$ ,  $m_T^W$ ,  $N_{\text{jets}}$ ,  $N_{b\text{-tags}}$ , and the  $p_T$  of the third lepton) are produced (where applicable). Then, in each of the 138 signal regions, the number of observed and expected events are compared, and, absent any significant deviations, 95% confidence level (CL) upper limits are derived on the number of events from new physics,  $N_{95}$ , and the corresponding *visible cross section*,  $\sigma_{95}^{\text{vis}}$ , defined as

$$\sigma_{95}^{\text{vis}} = \frac{N_{95}}{\mathcal{L}}, \quad (7.3)$$

where  $\mathcal{L} = 20.3 \text{ fb}^{-1}$  is the integrated luminosity of the data.

The plots for the  $H_T^{\text{leptons}}$  signal regions are shown here for demonstrative purposes. The full set of plots is available at [[model-independent-webpage](#) ]. The  $H_T^{\text{leptons}}$  distributions are shown in figure 7.7. The observed and expected event counts in the three corresponding signal regions ( $H_T^{\text{leptons}} > 200 \text{ GeV}$ ,  $H_T^{\text{leptons}} > 500 \text{ GeV}$ , and  $H_T^{\text{leptons}} > 800 \text{ GeV}$ ) are shown in table 7.3. Finally, the upper limits on  $\sigma_{95}^{\text{vis}}$  are shown in figure 7.8.

The deviations between the observed and expected in all 138 signal regions are shown in figure 7.9, in units of the total uncertainty on the background expectation.

Figure 7.7:  $H_T^{\text{leptons}}$  distributions in the six categories.

Table 7.3: Observed and expected event counts in the  $H_T^{\text{leptons}}$  signal regions, along with the inclusive counts for the entire category.

## 7.6 Model Testing

The 95% CL upper limits on trilepton event production from new physics derived in section 7.5 provide a useful tool with which to confront models of new physics producing trilepton final states. To facilitate the comparison of the model-independent limits with the

Figure 7.8: 95% CL upper limits on the visible cross section of trilepton event production from new physics,  $\sigma_{95}^{\text{vis}}$ , in each  $H_T^{\text{leptons}}$  signal region.

Figure 7.9: Deviations between the observed event counts and the background expectations in each signal region, in units of the total uncertainty on the background prediction.

predictions of a model (i.e. a set of simulated events from an event generator), per-lepton fiducial efficiencies are provided to quantify approximately the efficiency of triggering, reconstructing and selecting fiducial leptons at truth level. The definition of fiducial truth leptons is as follows:

- **Transverse momentum:** Electrons and muons are required to have  $p_T > 10$  GeV, while tau leptons are required to have  $p_T > 15$  GeV.
- **Pseudorapidity:** The same pseudorapidity cuts as the reconstructed signal leptons are applied. Electrons must have  $|\eta| < 2.47$ , excluding the region  $1.37 < |\eta| < 1.52$ , and muons and tau leptons must have  $|\eta| < 2.5$ .
- **Isolation:** For electrons and muons, the sum of the transverse momenta of all charged particles with  $p_T > 1$  GeV within a cone of radius  $\Delta R = 0.3$  of the lepton, denoted `truth_ptcone30`, must satisfy  $\text{truth\_ptcone30}/p_T < 0.15$ . Similarly, the `truth_Etcone30`, defined as the sum of all stable, visible particles within a cone of radius  $\Delta R = 0.3$ , is required to satisfy  $\text{truth\_Etcone30}/p_T < 0.15$ .
- **Origin and Decay:** Leptons must originate from the hard scattering interaction (as opposed to the interaction with the detector as simulated by GEANT4), and not arise from the decay of a hadron. Electrons and muons are also required to be stable; tau leptons are required to decay hadronically.

The per-lepton fiducial efficiencies are measured in a sample of simulated  $WZ$  events. The efficiencies are determined separately for electrons, muons, hadronically decaying taus, electrons from tau decays, and muons from tau decays. Fiducial leptons are matched to reconstructed leptons satisfying the selection criteria (section 5.7.1), within a cone of  $\Delta R = 0.1$  for electrons and muons and  $\Delta R = 0.2$  for hadronically decaying taus and electrons and muons from  $\tau$  decays. The efficiency,  $\epsilon_\ell$ , is the ratio of the number of matched reconstructed leptons to the number of fiducial leptons within the geometrical acceptance. For electrons, hadronically decaying taus, and electrons from tau decays, the efficiency is measured separately in bins of  $p_T$  and  $|\eta|$ , with the efficiency of a given lepton taken to be  $\epsilon_\ell(p_T, \eta) \equiv \epsilon_\ell(p_T) \cdot \epsilon_\ell(|\eta|)/\langle \epsilon_\ell \rangle$ , where  $\langle \epsilon_\ell \rangle$  is the average efficiency of the inclusive sample. For muons, the efficiency is measured in bins of  $p_T$  for  $|\eta| < 0.1$  and  $|\eta| > 0.1$ .

The efficiencies are shown in tables 7.4 and 7.5. Given a model of new physics, they can be used to compute the number of events expected in each of the signal regions; for example, an event with three leptons  $\ell_1$ ,  $\ell_2$ , and  $\ell_3$  has an efficiency  $\epsilon = \epsilon_{\ell_1} \epsilon_{\ell_2} \epsilon_{\ell_3}$  to be reconstructed and selected.

### 7.6.1 Example: Doubly Charged Scalar Particles

An example of confronting models of new physics with the model-independent limits in section 7.5, limits are established on a model of predicting doubly charged scalar particles

$p_T$ [GeV]	Prompt $e$		Prompt $\mu$		$\tau \rightarrow e$		$\tau \rightarrow \mu$		$\tau_{\text{had}}$
	$ \eta  > 0.1$	$ \eta  < 0.1$	$ \eta  > 0.1$	$ \eta  < 0.1$	$ \eta  > 0.1$	$ \eta  < 0.1$	$ \eta  > 0.1$	$ \eta  < 0.1$	
10–15	0.045±0.001	0.021±0.001	0.003±0.002	0.027±0.002	0.013±0.001	0.005±0.003	-	-	
15–20	0.484±0.003	0.704±0.003	0.37±0.01	0.384±0.005	0.539±0.005	0.29±0.02	0.071±0.003	-	
20–25	0.571±0.003	0.808±0.002	0.42±0.01	0.47±0.01	0.62±0.01	0.35±0.03	0.25±0.01	-	
25–30	0.628±0.002	0.855±0.002	0.45±0.01	0.52±0.01	0.68±0.01	0.39±0.03	0.31±0.01	-	
30–40	0.681±0.002	0.896±0.001	0.50±0.01	0.57±0.01	0.71±0.01	0.42±0.03	0.31±0.01	-	
40–50	0.713±0.002	0.920±0.001	0.52±0.01	0.60±0.01	0.75±0.01	0.42±0.04	0.31±0.01	-	
50–60	0.746±0.002	0.932±0.001	0.52±0.01	0.64±0.01	0.76±0.01	0.42±0.03	0.31±0.01	-	
60–80	0.767±0.002	0.940±0.001	0.52±0.01	0.67±0.01	0.78±0.01	0.42±0.03	0.32±0.01	-	
80–100	0.800±0.003	0.940±0.002	0.52±0.01	0.68±0.02	0.79±0.02	0.42±0.04	0.32±0.02	-	
100–200	0.820±0.003	0.940±0.002	0.52±0.01	0.70±0.03	0.81±0.02	0.42±0.05	0.32±0.02	-	
200–400	0.83±0.01	0.94±0.01	0.52±0.05	0.72±0.08	0.91±0.06	-	-	-	0.29±0.05
400–600	0.83±0.04	0.93±0.02	0.50±0.20	-	-	-	-	-	-
≥ 600	0.83±0.05	0.92±0.08	-	-	-	-	-	-	-

Table 7.4: The fiducial efficiency for electrons, muons, and taus in different  $p_T$  ranges ( $\epsilon_{fid}(p_T)$ ). For electrons and muons from tau decays, the  $p_T$  is that of the electron or muon, not the tau. The uncertainties shown reflect the statistical uncertainties of the simulated samples only.

$ \eta $	Prompt $e$	$\tau \rightarrow e$	$\tau_{\text{had}}$
0.0–0.1	0.640±0.003	0.37±0.01	0.24±0.01
0.1–0.5	0.699±0.001	0.41±0.01	0.31±0.01
0.5–1.0	0.702±0.001	0.41±0.01	0.28±0.01
1.0–1.5	0.660±0.002	0.37±0.01	0.21±0.01
1.5–2.0	0.605±0.002	0.36±0.01	0.25±0.01
2.0–2.5	0.602±0.002	0.38±0.01	0.25±0.01

Table 7.5: The fiducial efficiency for electrons and taus in different  $\eta$  ranges ( $\epsilon_{fid}(\eta)$ ). For electrons from tau decays, the  $\eta$  is that of the electron, not the tau. The uncertainties shown reflect the statistical uncertainties of the simulated samples only.

within the context of left-right symmetry [5–8]. The model contains several scalar particles of charge 0,  $\pm 1$ , and  $\pm 2$ , the neutral component of which generates neutrino mass via the type II seesaw mechanism (section ??). Only pair production of the doubly charged particles,  $H_{L,R}^{\pm\pm}$ , is considered here, where  $L$  denotes coupling to  $SU(2)_L$  or  $SU(2)_R$ . The phenomenology of the particles is similar, differing in their couplings to left- and right-handed fermions and in their pair production cross sections due to different gauge couplings.

The  $H_{L,R}^{\pm\pm}$  decay to two charged leptons, and in general do not conserve lepton flavor. In scenarios where the  $H_{L,R}^{\pm\pm}$  decay to electrons or muons, the strongest limits are derived from same-sign dilepton signatures. An ATLAS search at  $\sqrt{s} = 8$  TeV excluded  $H_L^{\pm\pm}$  masses below 465 GeV – 550 GeV and  $H_R^{\pm\pm}$  masses below 370 GeV – 435 GeV, depending on the flavor of the lepton pair ( $e^\pm e^\pm$ ,  $e^\pm \mu^\pm$ , or  $\mu^\pm \mu^\pm$ ) [9]. If the  $H_{L,R}^{\pm\pm}$  decay to  $e^\pm \tau^\pm$  or  $\mu^\pm \tau^\pm$ , however, then competitive limits can be established using model-independent trilepton limits.

The model is confronted against the model-independent limits in the off- $Z$ , OSSF categories, using the  $H_T^{\text{leptons}}$  signal regions and combining the **3L** and **2L+ $\tau_{\text{had}}$**  categories. Events are simulated using PYTHIA8 using the MSTW2008 leading order PDF set, with mass hypotheses in 50 GeV increments between 50 GeV – 600 GeV, plus an additional point at a mass of 1 TeV. The  $H_T^{\text{leptons}} > 200$  GeV signal regions are used for  $H^{\pm\pm}$  mass hypotheses below 200 GeV, while the  $H_T^{\text{leptons}} > 500$  GeV signal regions are used for larger mass hypotheses. The resulting observed and expected limits are shown in figure 7.10. For left-handed doubly charged particles, masses below 400 GeV (400 GeV) are excluded for 100% branching fraction to  $e^\pm \tau^\pm$  ( $\mu^\pm \tau^\pm$ ), compared to expected limits of  $350 \pm 50$  GeV ( $370 \pm 20$  GeV).

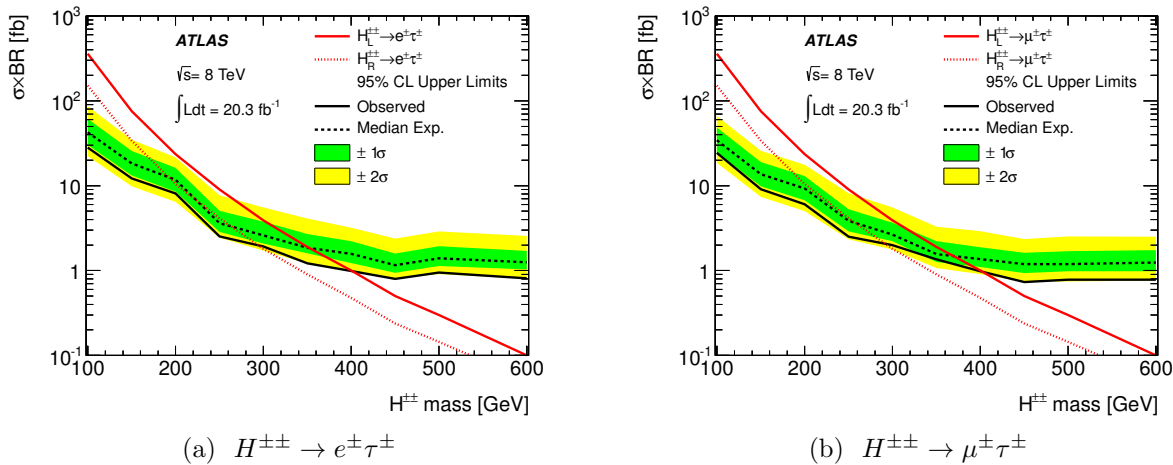


Figure 7.10: Observed and expected 95% CL limits on the cross section times branching ratio for  $H^{\pm\pm}$  decaying to  $e^\pm \tau^\pm$  (left) and  $\mu^\pm \tau^\pm$  (right). The solid and dashed red lines show the expected cross section times branching ratio for left- and right-handed  $H^{\pm\pm}$ , respectively.

# Bibliography

- [1] The ATLAS Collaboration, *Search for new phenomena in events with three or more charged leptons in  $pp$  collisions at  $\sqrt{s} = 8$  TeV with the ATLAS detector*, arXiv.org (Nov. 2014), arXiv: 1411.2921v2 [hep-ex], URL: <http://arxiv.org/abs/1411.2921v2>.
- [2] The ATLAS Collaboration, *Jet energy measurement and its systematic uncertainty in proton–proton collisions at  $\sqrt{s} = 7$  TeV with the ATLAS detector*, English, The European Physical Journal C **75**.1 (Jan. 2015) pp. 17–101, URL: <http://link.springer.com/10.1140/epjc/s10052-014-3190-y>.
- [3] M. V. Garzelli et al.,  *$Z^0$ -boson production in association with a  $t\bar{t}$  pair at next-to-leading order accuracy with parton shower effects*, English, Physical Review D **85**.7 (Apr. 2012) pp. 074022–6, URL: <http://link.aps.org/doi/10.1103/PhysRevD.85.074022>.
- [4] J. M. Campbell and R. K. Ellis,  *$t\bar{t}W^\pm$  production and decay at NLO*, English, Journal of High Energy Physics **2012**.7 (July 2012) pp. 52–12, URL: [http://link.springer.com/10.1007/JHEP07\(2012\)052](http://link.springer.com/10.1007/JHEP07(2012)052).
- [5] J. C. Pati and A. Salam, *Lepton Number as the Fourth Color*, Phys.Rev. **D10** (1974) pp. 275–289.
- [6] R. N. Mohapatra and J. C. Pati, *Left-Right Gauge Symmetry and an Isoconjugate Model of CP Violation*, English, Phys.Rev. **D11**.3 (1975) pp. 566–571, URL: <http://link.aps.org/doi/10.1103/PhysRevD.11.566>.
- [7] G. Senjanovic and R. N. Mohapatra, *Exact Left-Right Symmetry and Spontaneous Violation of Parity*, English, Phys.Rev. **D12**.5 (1975) pp. 1502–1505, URL: <http://link.aps.org/doi/10.1103/PhysRevD.12.1502>.
- [8] T. G. Rizzo, *Doubly Charged Higgs Bosons and Lepton Number Violating Processes*, Phys.Rev. **D25** (1982) pp. 1355–1364.

- [9] *Search for anomalous production of prompt same-sign lepton pairs and pair-produced doubly charged Higgs bosons with  $\sqrt{s} = 8$  TeV  $pp$  collisions using the ATLAS detector*, English, **2015**.3 (Mar. 2015) pp. 41–48,  
URL: [http://link.springer.com/article/10.1007/JHEP03\(2015\)041](http://link.springer.com/article/10.1007/JHEP03(2015)041).

# Chapter 8

## Trilepton Resonance Search

The sensitivity of a search using events with many electrons or muons can be enhanced significantly if the leptons are produced resonantly, allowing the use of a mass constraint. Searches for resonant dilepton production have a rich history, including the discoveries of the  $J/\psi$  [1, 2], the  $\Upsilon$  [3], and the  $Z$  boson [4]. At the LHC, the resonant four-lepton channel proved instrumental in the recent discovery of the Higgs boson [5, 6]. Resonant dilepton searches have placed strong constraints on a variety of new physics scenarios, such as new gauge bosons [7, 8] and doubly-charged scalar particles [9].

This chapter presents a search for the resonant production of three leptons using  $20.3\text{ fb}^{-1}$  of  $pp$  collision data at  $\sqrt{s} = 8\text{ TeV}$ . Trilepton resonances have been used previously at lower energies to place constraints on lepton flavor violation in muon and tau lepton decays [10, 11]. This analysis targets high-mass heavy leptons,  $L^\pm$ , decaying to three leptons via an intermediate on-shell  $Z$  boson,  $L^\pm \rightarrow Z + \ell \rightarrow \ell\ell\ell$ , where  $\ell = e$  or  $\mu$ . The final state is fully reconstructible, giving both a trilepton and a  $Z$  mass constraint with which to discriminate the signal from the background.

The chapter is organized as follows. Section 8.1 describes the models of new physics used to motivate the analysis. Section 8.2 describes the search strategy, including the event selection and the identification of trilepton resonance candidates. Section 8.3 lists the sources of systematic uncertainty on the signal and background estimates. The background estimates are validated in section 8.4. Finally, the results and interpretations are shown in sections 8.6 and 8.7.

### 8.1 Signal Models

The search is motivated by two models of phenomena beyond the Standard Model: the type III neutrino seesaw model [12] and extra generations of vector-like leptons [13], discussed earlier in sections ?? and ???. Both models propose heavy, charged, and colorless fermions which are made unstable by mixing with Standard Model leptons. The type III seesaw model also includes a neutral heavy lepton,  $N^0$ , with the same mass as the  $L^\pm$ .

The new particles are pair produced via gauge interactions,  $q\bar{q} \rightarrow L^\pm L^\mp$  or  $q\bar{q}' \rightarrow L^\pm N^0$ , as shown in figure 8.1. The production cross sections depend on how the new particles couple to  $SU(2)_L \times U(1)_Y$ : the type III seesaw fermions transform in the adjoint representation of  $SU(2)_L$  and have zero hypercharge,  $(\mathbf{3}, 0)$ , while the heavy lepton in the generic vector-like lepton model inherits its gauge couplings from its  $SU(5)$  multiplet,  $(1, -1)$ . The different gauge couplings, plus the various production modes, lead to significant differences in production rates. The production cross sections of the two models are shown in figure 8.2.

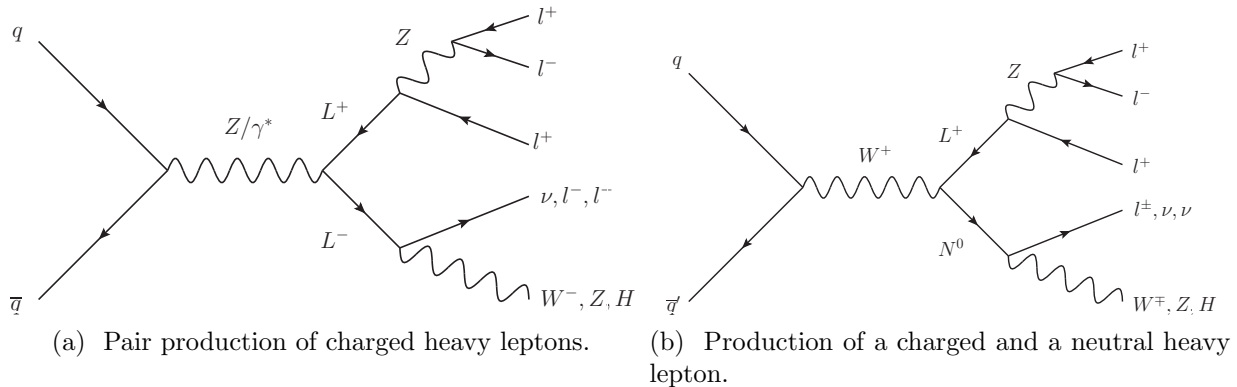


Figure 8.1: Production and decay of new heavy leptons to final states with a trilepton resonance.

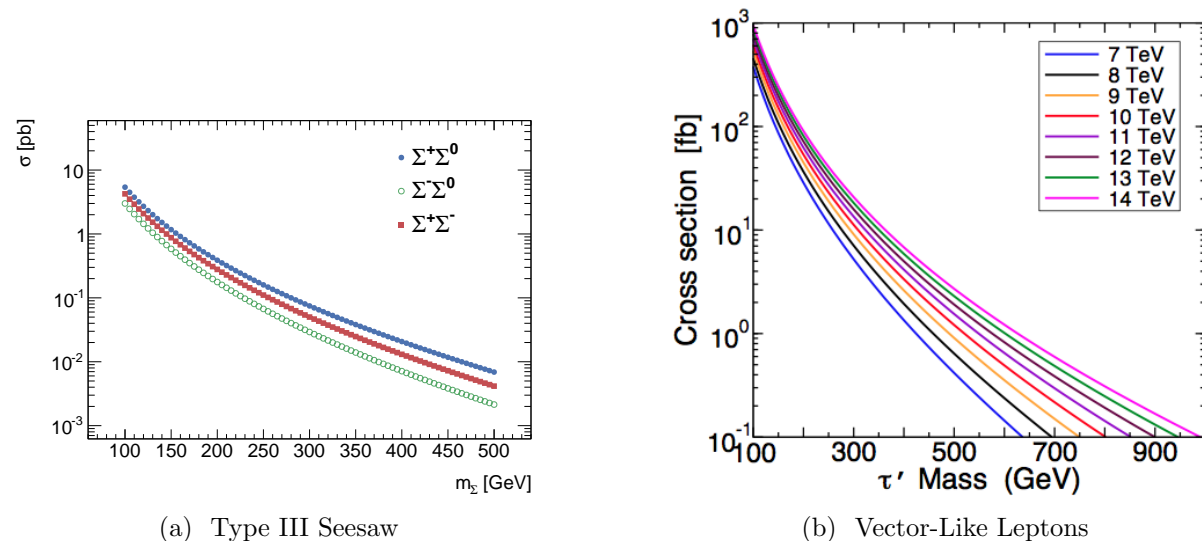


Figure 8.2: Production cross sections at  $\sqrt{s} = 8$  TeV for heavy lepton pair production for the type III seesaw model (left) and the vector-like leptons model (right).

The heavy leptons are made unstable by introducing mixing terms with the Standard Model leptons. For example, consider a single extra generation of fermions transforming in the adjoint representation of  $SU(2)_L$ , as in the type III seesaw model:

$$\Sigma \equiv \begin{pmatrix} N^0/\sqrt{2} & L^+ \\ L^- & -N^0/\sqrt{2} \end{pmatrix}. \quad (8.1)$$

The Lagrangian contains Yukawa terms mixing the heavy leptons with Standard Model leptons,  $\ell = e, \mu, \tau$ :

$$-\mathcal{L} \ni \sum_{\ell=e, \mu, \tau} \sqrt{2}\phi^0 \bar{\Psi} Y_{L\ell} \psi_\ell + \text{h.c.}, \quad (8.2)$$

where  $\Psi \equiv L_R^{+c} + L_R^-$  is a Dirac spinor representing the four charged degrees of freedom,  $\psi_\ell$  are Dirac spinors corresponding to the Standard Model leptons,  $\phi \equiv (\phi^+, \phi^0)^T \equiv (\phi^+, (v+H+i\eta)/\sqrt{2})^T$  is the Higgs doublet, and  $Y_{L\ell}$  are Yukawa couplings. After electroweak symmetry breaking, the mass matrices take the form

$$-\mathcal{L} \ni \sum_{\ell=e, \mu, \tau} \begin{pmatrix} \bar{\psi}_{\ell, R} & \bar{\Psi}_R \end{pmatrix} \begin{pmatrix} m_l & 0 \\ Y_{L\ell} v & M_{L^\pm} \end{pmatrix} \begin{pmatrix} \psi_{\ell, L} \\ \Psi_L \end{pmatrix} + \begin{pmatrix} \bar{\psi}_{\ell, L} & \bar{\Psi}_L \end{pmatrix} \begin{pmatrix} m_l & Y_{L\ell}^\dagger v \\ 0 & M_{L^\pm} \end{pmatrix} \begin{pmatrix} \psi_{\ell, R} \\ \Psi_r \end{pmatrix}. \quad (8.3)$$

Diagonalizing the mass matrices leads to off-diagonal terms in the gauge interactions, with couplings proportional to the mixing parameters  $V_{L\ell} = \frac{v}{\sqrt{2}} M_{L^\pm}^{-1} Y_{L\ell}$ . These couplings enable the decay of the heavy leptons to a boson ( $W$ ,  $Z$ , or  $h$ ) plus a Standard Model lepton or neutrino, with partial widths given by:

$$\Gamma(N^0 \rightarrow \ell^- W^+) = \Gamma(N^0 \rightarrow \ell^+ W^-) = \frac{g^2}{64\pi} |V_{L\ell}|^2 \frac{M_{L^\pm}^3}{M_W^2} \left(1 - \frac{M_W^2}{M_{L^\pm}^2}\right)^2 \left(1 + 2\frac{M_W^2}{M_{L^\pm}^2}\right), \quad (8.4)$$

$$\sum_\ell \Gamma(N^0 \rightarrow \nu_\ell Z) = \frac{g^2}{64\pi c_W^2} \sum_\ell |V_{L\ell}|^2 \frac{M_{L^\pm}^3}{M_Z^2} \left(1 - \frac{M_Z^2}{M_{L^\pm}^2}\right)^2 \left(1 + 2\frac{M_Z^2}{M_{L^\pm}^2}\right), \quad (8.5)$$

$$\sum_\ell \Gamma(N^0 \rightarrow \nu_\ell H) = \frac{g^2}{64\pi} \sum_\ell |V_{L\ell}|^2 \frac{M_{L^\pm}^3}{M_H^2} \left(1 - \frac{M_H^2}{M_{L^\pm}^2}\right)^2, \quad (8.6)$$

$$\sum_\ell \Gamma(L^+ \rightarrow \nu_\ell W^+) = \frac{g^2}{32\pi} \sum_\ell |V_{L\ell}|^2 \frac{M_{L^\pm}^3}{M_W^2} \left(1 - \frac{M_W^2}{M_{L^\pm}^2}\right)^2 \left(1 + 2\frac{M_W^2}{M_{L^\pm}^2}\right), \quad (8.7)$$

$$\Gamma(L^+ \rightarrow \ell^+ Z) = \frac{g^2}{64\pi c_W^2} |V_{L\ell}|^2 \frac{M_{L^\pm}^3}{M_Z^2} \left(1 - \frac{M_Z^2}{M_{L^\pm}^2}\right)^2 \left(1 + 2\frac{M_Z^2}{M_{L^\pm}^2}\right), \quad (8.8)$$

$$\Gamma(L^+ \rightarrow \ell^+ H) = \frac{g^2}{64\pi} |V_{L\ell}|^2 \frac{M_{L^\pm}^3}{M_H^2} \left(1 - \frac{M_H^2}{M_{L^\pm}^2}\right)^2. \quad (8.9)$$

The branching fractions of the charged and neutrino heavy leptons are shown as function of  $m_{L^\pm}$  in figure 8.3. Note that these branching fractions are common to all the models considered in this analysis (aside from the possibility of only having a charged heavy lepton).

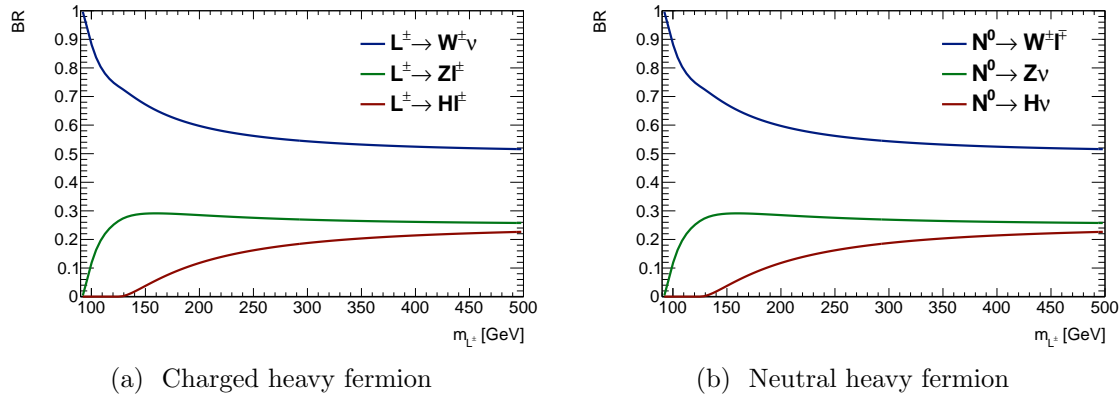


Figure 8.3: Branching ratios of a heavy lepton decaying via mixing with Standard Model leptons.

Constraints on the mixing parameters  $V_{L\ell}$  can be derived from precision measurements of the  $Z$  width, and constraints on products of the mixing parameters from flavor violation experiments like  $\mu \rightarrow e\gamma$  [14–17]:

$$|V_{Le}| < 5.5 \times 10^{-2} \quad (8.10)$$

$$|V_{L\mu}| < 6.3 \times 10^{-2} \quad (8.11)$$

$$|V_{L\tau}| < 6.3 \times 10^{-2} \quad (8.12)$$

$$|V_{Le} V_{L\mu}| < 1.7 \times 10^{-7} \quad (8.13)$$

$$|V_{Le} V_{L\tau}| < 4.2 \times 10^{-4} \quad (8.14)$$

$$|V_{L\mu} V_{L\tau}| < 4.9 \times 10^{-4}. \quad (8.15)$$

### 8.1.1 Signal Monte Carlo Samples

Signal events are generated using Monte Carlo simulation, with eleven mass hypotheses in the range  $100 \text{ GeV} \leq m_{L^\pm} \leq 400 \text{ GeV}$  for the vector-like leptons model and ten mass hypothesis in the range  $100 \text{ GeV} \leq m_{L^\pm, N^0} \leq 500 \text{ GeV}$  for the type III seesaw model. The samples are summarized in table 8.1. The events are generated with MADGRAPH 4.5.2 and 5.2.2.1 [18], for the vector-like leptons and type III seesaw models, respectively, using the CTEQ6L1 [19] PDF set and the AU2 underlying event tune [20]. Showering is performed with PYTHIA 8 [21]. Decays of the heavy leptons in the vector-like leptons model are performed using BRIDGE [22], while decays in the type III seesaw samples are performed by MADGRAPH.

The cross sections for both samples are calculated at leading order (LO) in QCD, and are shown in table 8.1.

For the type III seesaw model, the charged and neutral heavy leptons are generated with identical masses. The simulated decay modes are listed in table 8.2. The mixing parameters are chosen to be  $V_{Le} = 0.055$ ,  $V_{L\mu} = 0.063$ , and  $V_{L\tau} = 0$ , yielding a mix of  $ee$ ,  $e\mu$ , and  $\mu\mu$  decays. For the vector-like leptons model, one heavy lepton is required to decay via  $L^\pm \rightarrow Z(\ell\ell)\ell$ , where  $\ell = e, \mu, \tau$ . The two heavy leptons are constrained to decay to the same flavor of Standard Model lepton, which is chosen with equal probability to be an electron, muon, or tau. For both models, the events are reweighted to correspond to electron-only or muon-only mixing scenarios.

The type III seesaw samples were simulated with no intrinsic width for the  $Z$  bosons. As a result, the signal peaks are slightly narrower than would be expected if the  $Z$  width were correctly included. As described below in section 8.5.1, the limit setting is performed by fitting the trilepton mass distributions with analytical functions. In order to incorporate the missing  $Z$  width into the signal peaks, the peak width parameters determined from the vector-like lepton samples are used for the type III seesaw model.

Mass [GeV]	Cross Section [pb]	Equivalent $L$ [ $\text{fb}^{-1}$ ]
Type III Seesaw		
100	1.273	$7.7 \times 10^2$
120	2.138	$2.9 \times 10^2$
160	0.853	$6.5 \times 10^2$
200	0.346	$1.4 \times 10^3$
250	0.135	$3.5 \times 10^3$
300	0.0604	$3.8 \times 10^3$
350	0.02969	$7.2 \times 10^3$
400	0.01566	$1.3 \times 10^4$
450	0.008733	$2.3 \times 10^4$
450	0.00504	$4.0 \times 10^4$
Vector-Like Leptons		
100	0.378	$1.1 \times 10^4$
110	0.264	$9.2 \times 10^3$
120	0.193	$1.0 \times 10^4$
130	0.142	$1.3 \times 10^4$
140	0.106	$1.7 \times 10^4$
160	0.0645	$2.7 \times 10^4$
180	0.0407	$4.3 \times 10^4$
200	0.0265	$6.7 \times 10^4$
250	0.0104	$1.8 \times 10^5$
300	0.00457	$4.1 \times 10^5$
400	0.00115	$1.7 \times 10^6$

Table 8.1: Masses  $m_{L^\pm}$ , production cross sections, and equivalent luminosities of the signal Monte Carlo samples.

Production Mode	Decay 1	Decay 2
$pp \rightarrow N^0 L^+$	$N^0 \rightarrow \ell^+ W^-$	$L^+ \rightarrow \ell^+ Z$
$pp \rightarrow N^0 L^+$	$N^0 \rightarrow \ell^- W^+$	$L^+ \rightarrow \ell^+ Z$
$pp \rightarrow N^0 L^+$	$N^0 \rightarrow \nu_\ell Z$	$L^+ \rightarrow \ell^+ Z$
$pp \rightarrow N^0 L^+$	$N^0 \rightarrow \nu_\ell H$	$L^+ \rightarrow \ell^+ Z$
$pp \rightarrow N^0 L^-$	$N^0 \rightarrow \ell^- W^+$	$L^- \rightarrow \ell^- Z$
$pp \rightarrow N^0 L^-$	$N^0 \rightarrow \ell^+ W^-$	$L^- \rightarrow \ell^- Z$
$pp \rightarrow N^0 L^-$	$N^0 \rightarrow \nu_\ell Z$	$L^- \rightarrow \ell^- Z$
$pp \rightarrow N^0 L^-$	$N^0 \rightarrow \nu_\ell H$	$L^- \rightarrow \ell^- Z$
$pp \rightarrow L^- L^+$	$L^- \rightarrow \ell^- Z$	$L^+ \rightarrow \ell^+ Z$
$pp \rightarrow L^- L^+$	$L^- \rightarrow \nu_l W^-$	$L^+ \rightarrow \ell^+ Z$
$pp \rightarrow L^- L^+$	$L^- \rightarrow \ell^- H$	$L^+ \rightarrow \ell^+ Z$
$pp \rightarrow L^- L^+$	$L^- \rightarrow \ell^- Z$	$L^+ \rightarrow \nu_l W^+$
$pp \rightarrow L^- L^+$	$L^- \rightarrow \ell^- Z$	$L^+ \rightarrow \ell^+ H$

Table 8.2: Decays simulated for the type III seesaw signal samples.

## 8.2 Search Strategy

### 8.2.1 Event Selection and Heavy Lepton Reconstruction

The event selection is very similar to that used in the model-independent analysis, described in section 7.1. In particular, the same definitions are used for leptons and jets, in order to make use of the same fake factor method to estimate the reducible backgrounds. Events containing a heavy lepton candidate are selected as follows.

- Events are triggered using the lowest-threshold unprescaled single-electron and single-muon triggers, `EF_e24vhi_medium1`, `EF_e60_medium1`, `EF_mu24i_tight`, and `EF_mu36_tight` (section 7.1.1).
- The primary event vertex must have at least three tracks with  $p_T > 400$  MeV.
- Events are required to have at least three electrons or muons ( $eee$ ,  $e\mu\mu$ ,  $\mu\mu e$ ,  $\mu\mu\mu$ ) satisfying the lepton selection criteria (table 5.2).
- Events must have one  $Z$  candidate, consisting of a same-flavor, opposite-sign pair of leptons with  $|m_{l+l-} - m_Z| < 10$  GeV. The  $Z$  mass is taken to be  $m_Z = 91.1876$  GeV [23].
- Four-lepton events with two leptonic  $Z$  candidates with  $|m_{\ell\ell} - m_Z| < 10$  GeV are rejected to suppress the Standard Model  $ZZ$  background. The efficiency loss for signal events is low; see tables 8.4 and 8.5.
- If an event contains more than three leptons, a unique trilepton candidate in each event is chosen as follows:

- Choose the same-flavor, opposite-sign pair with invariant mass closest to  $m_Z$ .
- Choose the third (“off- $Z$ ”) lepton to be the closest in  $\Delta R$  to the reconstructed  $Z$  four-momentum.
- For low heavy lepton mass hypotheses,  $m_{L^\pm} \lesssim 200$  GeV, the  $Z$  and the third lepton will tend to be collimated. The expected background and signal  $\Delta R$  distributions for selected trilepton candidate are shown in figure 8.4. Imposing a cut on the  $\Delta R(Z, \ell_3)$  of the trilepton candidates improves the signal significance, and also provides a useful control region defined by inverting the cut. The value of the cut is chosen by comparing the expected sensitivities of the analysis with different cuts values, described in appendix 10.2.1. A flat cut of  $\Delta R(Z, \ell_3) < 3.0$  is used, independent of the heavy lepton mass hypothesis.

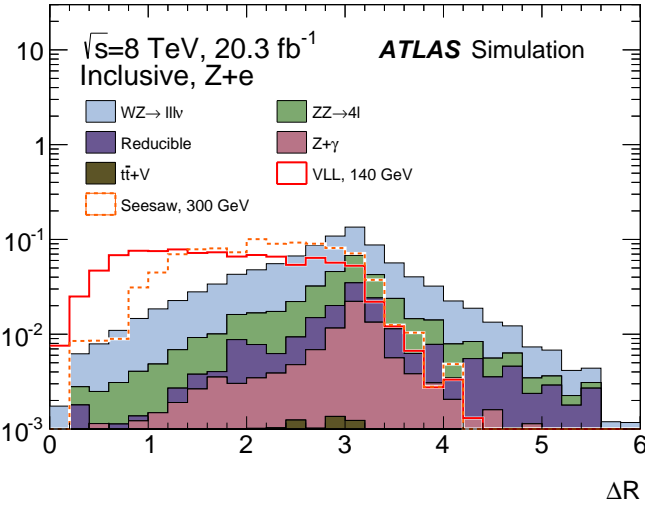


Figure 8.4: Expected  $\Delta R(Z, \ell_3)$  distributions for background and signal in the inclusive signal region.

- The variable of interest used to apply the trilepton mass constraint is  $\Delta m \equiv m_{3\ell} - m_{\ell^+\ell^-}$ , where the invariant mass of the two leptons associated with a  $Z$  boson decay is subtracted by the trilepton mass. This method reduces the impact of the lepton energy or momentum resolutions on the width of the resonance peak, at the cost of introducing some width due to the intrinsic width of the  $Z$ ,  $\Gamma_Z = 2.4952 \pm 0.0023$  GeV [23]. Over most of the mass range, this variable reduces the width of the signal peaks, as shown in table 8.3.

Table 8.3: Comparison of the full-width, half-maximum of the signal peaks between the  $\Delta m$  and  $m_{3\ell}$  variables.

After identifying the trilepton candidates, six mutually exclusive signal regions are defined. First, to target the flavor structure of the heavy lepton mixing, events are divided into two flavor channels,  $Z + e$  and  $Z + \mu$ , depending on the flavor the off- $Z$  lepton. Second, as the heavy leptons are pair produced, signal events will contain additional activity due to the decay of the second heavy lepton. Events are divided into three exclusive categories based on other activity in the event:

- $4\ell$ : events containing a fourth lepton, either an electron or a muon, passing the normal lepton criteria.
- $3\ell + jj$ : events containing exactly three leptons and a dijet with  $60.385 \text{ GeV} < m_{jj} < 150.9 \text{ GeV}$ .
- $3\ell$ -only: all other events, i.e. events with three leptons and no jet pair satisfying the invariant mass requirement.

The choice of these three categories is motivated in figure 8.5, which shows the fraction of events with various activity from the decay of the other heavy lepton. The additional activity includes extra leptons and neutrinos, and jets from  $W/Z/h$  decays. Assuming that the mixing with tau leptons is zero ( $V_{\tau L} = 0$ ), the requirements of a fourth lepton or a hadronically decaying boson are very efficient on signal. If the second heavy fermion is charged, then the only decay mode that fails both requirements is  $L^\pm \rightarrow W^\pm(\tau^\pm\nu)\nu$ . If the second heavy fermion is neutral, then only the  $N^0 \rightarrow Z(\nu\nu)\nu$  and a small fraction of  $N^0 \rightarrow H\nu$  decays fail both requirements. Categorization targeting neutrinos is less effective at separating signal from the large  $WZ$  background (see figures 10.8-10.11).

In some cases, it is useful to consider the events without dividing into these three categories, distinguishing events only by the flavor of the off- $Z$  lepton. This is referred to as the “Inclusive” signal region below.

### 8.2.2 Performance on Fiducial Signal Events

The performance of the cuts and heavy lepton candidate selection is shown in tables 8.4 and 8.5 in terms of efficiency on fiducial events. The fiducial selection requires the event to have three truth-level leptons satisfying  $p_T > 15 \text{ GeV}$  and  $|\eta| < 2.5$ , of which two form a  $Z$  candidate with  $|m_{\ell^+\ell^-} - m_Z| < 10 \text{ GeV}$ , the third lepton is of the correct flavor, and the trilepton mass satisfies  $|m_{3\ell} - m_{L^\pm}| < 5 \text{ GeV}$ . The final efficiency to reconstruct and select fiducial events for each signal region is shown as a function of signal mass  $m_{L^\pm}$  in figure 8.6.

Note that cut imposing a flavor requirement on the reconstructed off- $Z$  lepton has a different efficiency between the vector-like lepton sample and the seesaw sample. This is a consequence of the initial flavor content of the samples: the vector-like lepton samples are divided into two samples with 100% branching fraction to either bachelor electron or bachelor muon, while the seesaw samples is a single mixed sample containing both electron and muon decays.

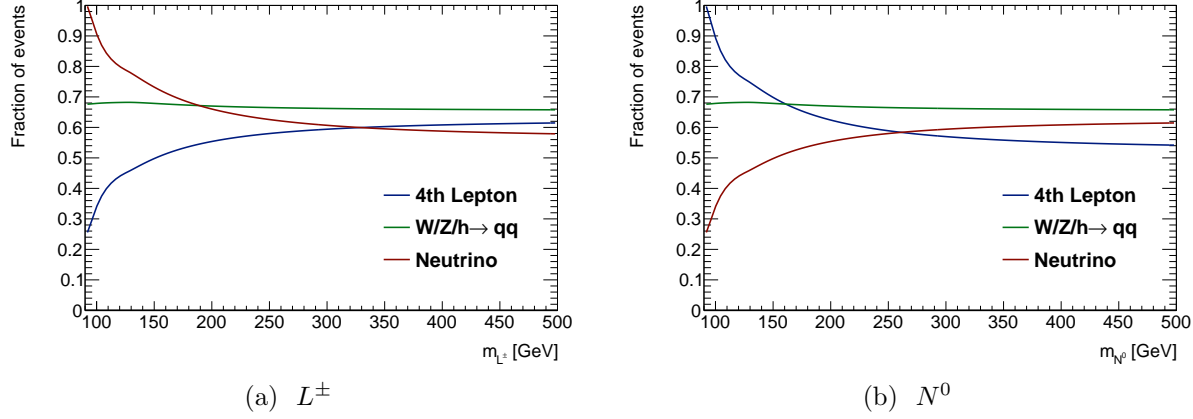


Figure 8.5: Fraction of events with various activity on the opposite side of the event, for  $L^\pm L^\mp$  events at left, and  $L^\pm N^0$  events at right. The left plot, showing the opposite side activity for a  $L^\pm L^\mp$  final state, is identical for the seesaw and vector-like lepton model.

Process	Preselection	Bachelor $e$	$ m_{\ell^+\ell^-} - m_Z  < 10$ GeV	$!2Z$	$\Delta R < 3.0$	$4\ell$	$3\ell + jj$	$3\ell$ -only
VLL, 100 GeV	$0.348 \pm 0.008$	$0.318 \pm 0.008$	$0.306 \pm 0.008$	$0.303 \pm 0.008$	$0.298 \pm 0.008$	$0.054 \pm 0.004$	$0.096 \pm 0.005$	$0.147 \pm 0.006$
VLL, 110 GeV	$0.478 \pm 0.006$	$0.435 \pm 0.006$	$0.421 \pm 0.006$	$0.417 \pm 0.006$	$0.401 \pm 0.006$	$0.076 \pm 0.003$	$0.11 \pm 0.004$	$0.215 \pm 0.005$
VLL, 120 GeV	$0.535 \pm 0.006$	$0.491 \pm 0.006$	$0.467 \pm 0.006$	$0.457 \pm 0.006$	$0.424 \pm 0.006$	$0.104 \pm 0.004$	$0.117 \pm 0.004$	$0.204 \pm 0.005$
VLL, 130 GeV	$0.604 \pm 0.006$	$0.539 \pm 0.006$	$0.509 \pm 0.006$	$0.494 \pm 0.006$	$0.445 \pm 0.006$	$0.125 \pm 0.004$	$0.127 \pm 0.004$	$0.194 \pm 0.005$
VLL, 140 GeV	$0.643 \pm 0.006$	$0.578 \pm 0.006$	$0.559 \pm 0.006$	$0.538 \pm 0.006$	$0.491 \pm 0.006$	$0.153 \pm 0.004$	$0.164 \pm 0.004$	$0.174 \pm 0.005$
VLL, 160 GeV	$0.663 \pm 0.006$	$0.593 \pm 0.006$	$0.572 \pm 0.006$	$0.552 \pm 0.006$	$0.499 \pm 0.006$	$0.175 \pm 0.005$	$0.148 \pm 0.004$	$0.176 \pm 0.005$
VLL, 180 GeV	$0.698 \pm 0.006$	$0.62 \pm 0.006$	$0.594 \pm 0.006$	$0.573 \pm 0.007$	$0.505 \pm 0.007$	$0.197 \pm 0.005$	$0.163 \pm 0.005$	$0.144 \pm 0.005$
VLL, 200 GeV	$0.707 \pm 0.006$	$0.624 \pm 0.007$	$0.596 \pm 0.007$	$0.577 \pm 0.007$	$0.52 \pm 0.007$	$0.209 \pm 0.006$	$0.167 \pm 0.005$	$0.145 \pm 0.005$
VLL, 250 GeV	$0.751 \pm 0.007$	$0.654 \pm 0.007$	$0.626 \pm 0.007$	$0.615 \pm 0.007$	$0.548 \pm 0.008$	$0.245 \pm 0.007$	$0.152 \pm 0.005$	$0.151 \pm 0.005$
VLL, 300 GeV	$0.771 \pm 0.007$	$0.662 \pm 0.008$	$0.63 \pm 0.008$	$0.625 \pm 0.008$	$0.547 \pm 0.008$	$0.258 \pm 0.007$	$0.169 \pm 0.006$	$0.121 \pm 0.005$
VLL, 400 GeV	$0.776 \pm 0.007$	$0.669 \pm 0.008$	$0.642 \pm 0.008$	$0.641 \pm 0.008$	$0.562 \pm 0.008$	$0.277 \pm 0.007$	$0.181 \pm 0.006$	$0.103 \pm 0.005$
Seesaw, 100 GeV	$0.381 \pm 0.006$	$0.351 \pm 0.005$	$0.336 \pm 0.005$	$0.334 \pm 0.005$	$0.308 \pm 0.005$	$0.08 \pm 0.003$	$0.096 \pm 0.003$	$0.131 \pm 0.004$
Seesaw, 120 GeV	$0.517 \pm 0.004$	$0.474 \pm 0.004$	$0.45 \pm 0.004$	$0.44 \pm 0.004$	$0.403 \pm 0.004$	$0.128 \pm 0.003$	$0.128 \pm 0.003$	$0.148 \pm 0.003$
Seesaw, 160 GeV	$0.611 \pm 0.005$	$0.548 \pm 0.005$	$0.532 \pm 0.005$	$0.516 \pm 0.005$	$0.464 \pm 0.005$	$0.167 \pm 0.004$	$0.141 \pm 0.003$	$0.157 \pm 0.003$
Seesaw, 200 GeV	$0.657 \pm 0.005$	$0.591 \pm 0.005$	$0.574 \pm 0.005$	$0.559 \pm 0.005$	$0.5 \pm 0.005$	$0.203 \pm 0.004$	$0.146 \pm 0.003$	$0.152 \pm 0.004$
Seesaw, 250 GeV	$0.671 \pm 0.007$	$0.605 \pm 0.007$	$0.592 \pm 0.007$	$0.582 \pm 0.007$	$0.505 \pm 0.007$	$0.221 \pm 0.006$	$0.14 \pm 0.005$	$0.144 \pm 0.005$
Seesaw, 300 GeV	$0.729 \pm 0.007$	$0.649 \pm 0.007$	$0.633 \pm 0.007$	$0.626 \pm 0.007$	$0.541 \pm 0.008$	$0.23 \pm 0.006$	$0.167 \pm 0.006$	$0.144 \pm 0.005$
Seesaw, 350 GeV	$0.72 \pm 0.007$	$0.651 \pm 0.008$	$0.638 \pm 0.008$	$0.635 \pm 0.008$	$0.553 \pm 0.008$	$0.251 \pm 0.007$	$0.157 \pm 0.006$	$0.146 \pm 0.006$
Seesaw, 400 GeV	$0.717 \pm 0.007$	$0.641 \pm 0.008$	$0.627 \pm 0.008$	$0.623 \pm 0.008$	$0.529 \pm 0.008$	$0.243 \pm 0.007$	$0.15 \pm 0.006$	$0.136 \pm 0.005$
Seesaw, 450 GeV	$0.762 \pm 0.008$	$0.67 \pm 0.009$	$0.66 \pm 0.009$	$0.657 \pm 0.009$	$0.554 \pm 0.009$	$0.267 \pm 0.008$	$0.184 \pm 0.007$	$0.103 \pm 0.006$
Seesaw, 500 GeV	$0.72 \pm 0.007$	$0.636 \pm 0.008$	$0.611 \pm 0.008$	$0.608 \pm 0.008$	$0.525 \pm 0.008$	$0.24 \pm 0.007$	$0.151 \pm 0.006$	$0.134 \pm 0.005$

Table 8.4: Fraction of fiducial events remaining at various stages in the cutflow for the  $Z + e$  signal regions. Only statistical uncertainties due to finite Monte Carlo statistics are shown. The preselection cut requires three selected leptons, with one same-flavor opposite-sign pair, as well as the general event selection cuts listed above.

Process	Preselection	Bachelor $\mu$	$ m_{l^+l^-} - m_Z  < 10 \text{ GeV}$	$!2Z$	$\Delta R < 3.0$	$4l$	$3l + jj$	Else
VLL, 100 GeV	$0.52 \pm 0.007$	$0.508 \pm 0.007$	$0.472 \pm 0.007$	$0.461 \pm 0.007$	$0.456 \pm 0.007$	$0.064 \pm 0.004$	$0.14 \pm 0.005$	$0.252 \pm 0.006$
VLL, 110 GeV	$0.61 \pm 0.004$	$0.593 \pm 0.004$	$0.568 \pm 0.004$	$0.554 \pm 0.004$	$0.536 \pm 0.004$	$0.119 \pm 0.003$	$0.142 \pm 0.003$	$0.275 \pm 0.004$
VLL, 120 GeV	$0.67 \pm 0.003$	$0.648 \pm 0.004$	$0.617 \pm 0.004$	$0.596 \pm 0.004$	$0.561 \pm 0.004$	$0.149 \pm 0.003$	$0.139 \pm 0.003$	$0.273 \pm 0.003$
VLL, 130 GeV	$0.702 \pm 0.003$	$0.676 \pm 0.003$	$0.642 \pm 0.003$	$0.614 \pm 0.003$	$0.569 \pm 0.003$	$0.163 \pm 0.003$	$0.143 \pm 0.002$	$0.263 \pm 0.003$
VLL, 140 GeV	$0.723 \pm 0.003$	$0.701 \pm 0.003$	$0.667 \pm 0.003$	$0.634 \pm 0.003$	$0.585 \pm 0.003$	$0.173 \pm 0.003$	$0.156 \pm 0.002$	$0.256 \pm 0.003$
VLL, 160 GeV	$0.752 \pm 0.003$	$0.727 \pm 0.003$	$0.685 \pm 0.003$	$0.65 \pm 0.003$	$0.592 \pm 0.003$	$0.212 \pm 0.003$	$0.156 \pm 0.002$	$0.223 \pm 0.003$
VLL, 180 GeV	$0.77 \pm 0.003$	$0.746 \pm 0.003$	$0.69 \pm 0.003$	$0.659 \pm 0.003$	$0.593 \pm 0.003$	$0.227 \pm 0.003$	$0.161 \pm 0.002$	$0.205 \pm 0.003$
VLL, 200 GeV	$0.779 \pm 0.003$	$0.751 \pm 0.003$	$0.69 \pm 0.003$	$0.66 \pm 0.003$	$0.584 \pm 0.003$	$0.239 \pm 0.003$	$0.161 \pm 0.002$	$0.184 \pm 0.002$
VLL, 250 GeV	$0.786 \pm 0.003$	$0.752 \pm 0.003$	$0.676 \pm 0.003$	$0.657 \pm 0.003$	$0.579 \pm 0.003$	$0.268 \pm 0.003$	$0.162 \pm 0.002$	$0.149 \pm 0.002$
VLL, 300 GeV	$0.789 \pm 0.002$	$0.76 \pm 0.003$	$0.68 \pm 0.003$	$0.667 \pm 0.003$	$0.578 \pm 0.003$	$0.288 \pm 0.003$	$0.163 \pm 0.002$	$0.127 \pm 0.002$
VLL, 400 GeV	$0.787 \pm 0.002$	$0.753 \pm 0.003$	$0.665 \pm 0.003$	$0.656 \pm 0.003$	$0.563 \pm 0.003$	$0.292 \pm 0.003$	$0.166 \pm 0.002$	$0.106 \pm 0.002$
Seesaw, 100 GeV	$0.535 \pm 0.006$	$0.521 \pm 0.006$	$0.484 \pm 0.006$	$0.471 \pm 0.006$	$0.46 \pm 0.006$	$0.192 \pm 0.005$	$0.121 \pm 0.004$	$0.147 \pm 0.004$
Seesaw, 120 GeV	$0.677 \pm 0.004$	$0.66 \pm 0.004$	$0.613 \pm 0.004$	$0.589 \pm 0.004$	$0.546 \pm 0.004$	$0.212 \pm 0.004$	$0.119 \pm 0.003$	$0.215 \pm 0.004$
Seesaw, 160 GeV	$0.745 \pm 0.004$	$0.723 \pm 0.004$	$0.685 \pm 0.004$	$0.658 \pm 0.004$	$0.595 \pm 0.005$	$0.252 \pm 0.004$	$0.14 \pm 0.003$	$0.202 \pm 0.004$
Seesaw, 200 GeV	$0.743 \pm 0.004$	$0.717 \pm 0.005$	$0.668 \pm 0.005$	$0.651 \pm 0.005$	$0.588 \pm 0.005$	$0.263 \pm 0.004$	$0.152 \pm 0.004$	$0.173 \pm 0.004$
Seesaw, 250 GeV	$0.761 \pm 0.006$	$0.735 \pm 0.006$	$0.673 \pm 0.007$	$0.662 \pm 0.007$	$0.585 \pm 0.007$	$0.284 \pm 0.006$	$0.144 \pm 0.005$	$0.157 \pm 0.005$
Seesaw, 300 GeV	$0.785 \pm 0.006$	$0.764 \pm 0.006$	$0.695 \pm 0.007$	$0.688 \pm 0.007$	$0.601 \pm 0.007$	$0.295 \pm 0.007$	$0.171 \pm 0.006$	$0.135 \pm 0.005$
Seesaw, 350 GeV	$0.78 \pm 0.006$	$0.757 \pm 0.007$	$0.688 \pm 0.007$	$0.681 \pm 0.007$	$0.59 \pm 0.008$	$0.294 \pm 0.007$	$0.155 \pm 0.006$	$0.141 \pm 0.005$
Seesaw, 400 GeV	$0.753 \pm 0.007$	$0.727 \pm 0.007$	$0.642 \pm 0.008$	$0.634 \pm 0.008$	$0.544 \pm 0.008$	$0.277 \pm 0.007$	$0.15 \pm 0.006$	$0.118 \pm 0.005$
Seesaw, 450 GeV	$0.762 \pm 0.008$	$0.732 \pm 0.008$	$0.658 \pm 0.008$	$0.653 \pm 0.009$	$0.555 \pm 0.009$	$0.285 \pm 0.008$	$0.152 \pm 0.006$	$0.119 \pm 0.006$
Seesaw, 500 GeV	$0.755 \pm 0.007$	$0.729 \pm 0.007$	$0.654 \pm 0.008$	$0.65 \pm 0.008$	$0.551 \pm 0.008$	$0.275 \pm 0.007$	$0.155 \pm 0.006$	$0.122 \pm 0.005$

Table 8.5: Fraction of fiducial events remaining at various stages in the cutflow for the  $Z + \mu$  signal regions. Only statistical uncertainties due to finite Monte Carlo statistics are shown. The preselection cut requires three selected leptons, with one same-flavor opposite-sign pair, as well as the general event selection cuts listed above.

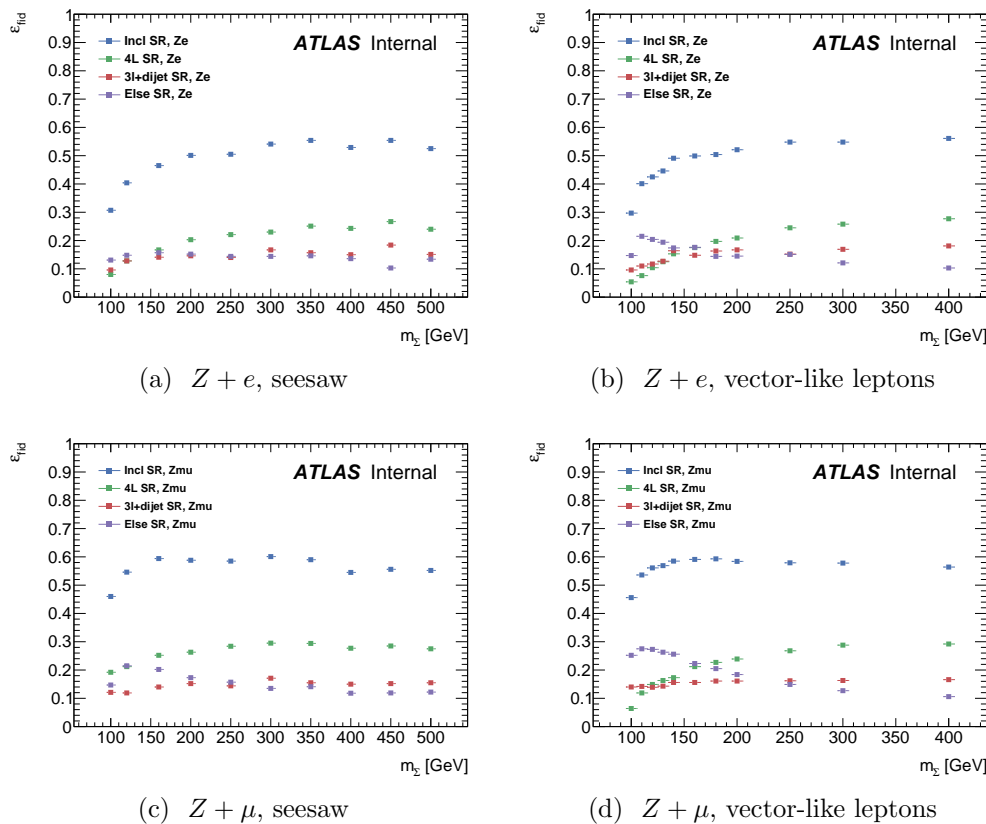


Figure 8.6: Efficiencies of cuts defining each signal region on fiducial  $Z(l\bar{l})l$  events at each simulated mass point. For the  $Z + e$  signal regions, the branching fraction is set to be  $BR(L^\pm \rightarrow X + e/\nu_e) = 100\%$ ; similarly, for the  $Z + \mu$  signal regions, the branching fraction is set to be  $BR(L^\pm \rightarrow X + \mu/\nu_\mu) = 100\%$ .

## 8.3 Systematic Uncertainties

The signal predictions and background estimates are assigned systematic uncertainties from several sources. In approximate order of significance, these are:

- **Diboson shape uncertainty:** A systematic uncertainty is assigned to the modeling of the diboson  $\Delta m$  spectra by comparing SHERPA to POWHEG. SHERPA is used as a central value, with uncertainty given by the symmetric difference between SHERPA and POWHEG. As shown below in section 8.5.2, the shapes of the  $4\ell$  and  $3\ell$ -only signal regions are consistent with the inclusive signal region, so the shape uncertainty taken from the inclusive signal region. The comparison for the  $WZ$  background is shown in figure 8.7.

In the case of the  $ZZ$  background, the procedure is complicated by the fact that the POWHEG sample is filtered to remove events with same-flavor, opposite-sign lepton pairs with  $m_{l+l-} < 4$  GeV (`mll14`). In order to compare the samples in a common phase space, the `mll14` filter is emulated on the SHERPA sample by rejecting events that contain a same-flavor, opposite-sign pair of truth leptons with  $m_{l+l-} < 4$  GeV. SHERPA, SHERPA with `mll14` filter, and POWHEG are compared in figure 8.8. The events from the POWHEG sample are weighted using the ratio of SHERPA to SHERPA with `mll14` filter. The final comparison of background shapes is shown in figure 8.9.

- **Monte Carlo statistics:** The Monte Carlo samples carry statistical uncertainty due to containing a finite number of events.
- **Monte Carlo sample normalizations:** As discussed in section 7.3, the signal and background Monte Carlo samples are normalized to the measured luminosity of the data using theoretical cross sections. The uncertainty on the measured luminosity is 2.8%, while the uncertainties on the  $WZ$ ,  $ZZ$ , and  $t\bar{t} + V$  backgrounds are 7.6%, 4.3%, and 22%, respectively. A cross section uncertainty is not assigned to the  $Z + \gamma$  backgrounds; instead, as described next, a large uncertainty is assigned due to applying scale factors to correct the simulated rate of photon conversions. Similarly, an uncertainty is not assigned for the  $VVV^{(*)}$  cross section, due to its small contribution to the signal regions.
- **Charge flip scale factors:** The rate of trilepton events due to  $Z + \gamma$ , where the photon converts asymmetrically and is reconstructed as an electron, is observed to be overestimated in Monte Carlo. As detailed in section 10.1.1, the events are reweighted to correct this overestimation, with a corresponding uncertainty of 30%.
- **Fake factor method:** The systematic uncertainty on the fake factors is described in sections 6.2.2 and 6.2.3. They range from 20%-30% for electrons and 25%-50% for muons.

- **Lepton scale factors:** Scale factors are applied to equalize the lepton trigger, reconstruction, and identification efficiencies between data and simulation (sections 5.2.2 and 5.3.1). The scale factors are typically close to unity, and the corresponding uncertainties range from 1%-5%.
- **Lepton energy and momentum corrections:** To improve agreement between data and simulation, the electron energy is scaled in data, and the electrom energy and muon momenta are smeared in Monte Carlo (see sections 5.2.3 and 5.3.2). The corrections carry small systematic uncertainties that primarily affect the analysis due to leptons migrating between passing and failing the selection, or lepton pairs moving in or out of the  $Z$  mass window.
- **Jet energy scale and resolution:** Like the leptons, systematic uncertainties are assigned to the jet energy scale and resolution (see section 5.5.1). The jet energy uncertainties have a small impact on this analysis, only affecting the normalization of the  $3\ell + jj$  signal regions when the dijet mass is pushed in or out of the window  $m_W - 20 \text{ GeV} < m_{jj} < m_H + 25 \text{ GeV}$ .

Figures 8.10 and 8.11 show the fractional uncertainty due to each source of uncertainty in 20 GeV bins for each signal region, as well as the total systematic uncertainty and expected statistical uncertainty. Note that the uncertainties shown are bin-by-bin uncertainties from the Monte Carlo and fake factor predictions, and do not directly reflect the final uncertainties incorporated in the fit-based limit setting; this is discussed in section ??.

The impact of each uncertainty in each signal region, in terms of fractional uncertainty on the total normalization, is shown for background in figure 8.6, and some example signal points in figures 8.7–8.9.

	$Z + e$				$Z + \mu$			
	Total	$4\ell$ SR	$3\ell + jj$ SR	$3\ell$ -only SR	Total	$4\ell$ SR	$3\ell + jj$ SR	$3\ell$ -only SR
$\sigma_{ZZ}$	0.9	3.9	0.9	0.8	0.7	3.8	0.4	0.6
$\sigma_{WZ}$	4.9	0.1	4.6	5.1	5.3	—	4.9	5.6
$\sigma_{t\bar{t}V}$	0.4	1.5	2.9	0.1	0.4	0.9	2.9	0.1
Luminosity	2.6	2.8	2.7	2.6	2.5	2.6	2.4	2.5
$\gamma$ conv. SFs	2.0	—	1.2	2.1	—	—	—	—
$\ell$ efficiency	1.6	1.8	1.6	1.6	0.9	0.9	1.0	0.9
$e$ reducible SFs	1.7	—	0.5	1.9	0.1	0.9	0.1	0.1
$\mu$ reducible SFs	0.3	—	0.3	0.3	3.4	0.6	4.3	3.5
JES/JER	0.1	$^{+0.2}_{-0.0}$	3.3	0.4	0.1	0.2	3.2	0.5
LES/LER	0.6	$^{+1.0}_{-0.3}$	$^{+0.3}_{-1.2}$	$^{+0.7}_{-0.4}$	0.1	0.1	0.2	0.1
MC Statistics	2.4	5.0	4.3	2.6	1.2	3.5	2.8	1.2
Total	6.9	7.4	8.4	7.1	7.0	6.0	8.7	7.2

Table 8.6: The impact of significant sources of uncertainty on the background prediction in each signal region, in terms of percent of the total background normalization.

	$Z + e$				$Z + \mu$			
	Incl SR	$4\ell$ SR	$3\ell + jj$ SR	$3\ell$ -only SR	Incl SR	$4\ell$ SR	$3\ell + jj$ SR	$3\ell$ -only SR
Luminosity	2.8	2.8	2.8	2.8	2.8	2.8	2.8	2.8
$l$ scale factors	1.7	1.7	1.7	1.6	1.1	1.1	1.1	1.0
MC Statistics	2.1	4.5	3.7	3.0	1.4	2.7	2.7	2.2
JES/JER	0.0	0.2	3.6	3.0	0.2	0.3	3.0	2.2
LES/LER	0.1	0.4	0.1	0.1	0.1	0.2	0.2	0.2
Total	3.9	5.6	6.1	5.3	3.3	4.0	5.1	4.3

Table 8.7: The impact of different sources of systematic uncertainty on the signal prediction for the type III seesaw model with  $m_{L^\pm} = 160$  GeV, in terms of percent of the total signal normalization.

	$Z + e$				$Z + \mu$			
	Incl SR	$4\ell$ SR	$3\ell + jj$ SR	$3\ell$ -only SR	Incl SR	$4\ell$ SR	$3\ell + jj$ SR	$3\ell$ -only SR
Luminosity	2.8	2.8	2.8	2.8	2.8	2.8	2.8	2.8
$l$ scale factors	1.8	1.7	1.8	1.9	1.2	1.2	1.2	1.2
MC Statistics	3.0	5.7	4.9	4.7	2.2	3.7	3.8	3.6
JES/JER	0.1	—	1.6	1.7	0.2	0.3	2.0	2.3
LES/LER	0.4	0.1	1.0	0.4	0.3	0.0	0.9	0.3
Total	4.5	6.5	6.2	6.0	3.8	4.8	5.3	5.3

Table 8.8: The impact of different sources of systematic uncertainty on the signal prediction for the type III seesaw model with  $m_{L^\pm} = 300$  GeV, in terms of percent of the total signal normalization.

	$Z + e$				$Z + \mu$			
	Incl SR	$4\ell$ SR	$3\ell + jj$ SR	$3\ell$ -only SR	Incl SR	$4\ell$ SR	$3\ell + jj$ SR	$3\ell$ -only SR
Luminosity	2.8	2.8	2.8	2.8	2.8	2.8	2.8	2.8
$l$ scale factors	1.8	1.8	1.8	2.0	1.3	1.4	1.3	1.3
MC Statistics	3.0	5.5	4.8	4.8	2.4	4.0	3.9	4.1
JES/JER	—	—	1.7	1.9	0.3	0.5	1.8	2.5
LES/LER	0.4	0.5	2.1	1.7	0.4	1.6	2.8	2.2
Total	4.5	6.4	6.4	6.4	3.9	5.4	6.0	6.1

Table 8.9: The impact of different sources of systematic uncertainty on the signal prediction for the type III seesaw model with  $m_{L^\pm} = 500$  GeV, in terms of percent of the total signal normalization.

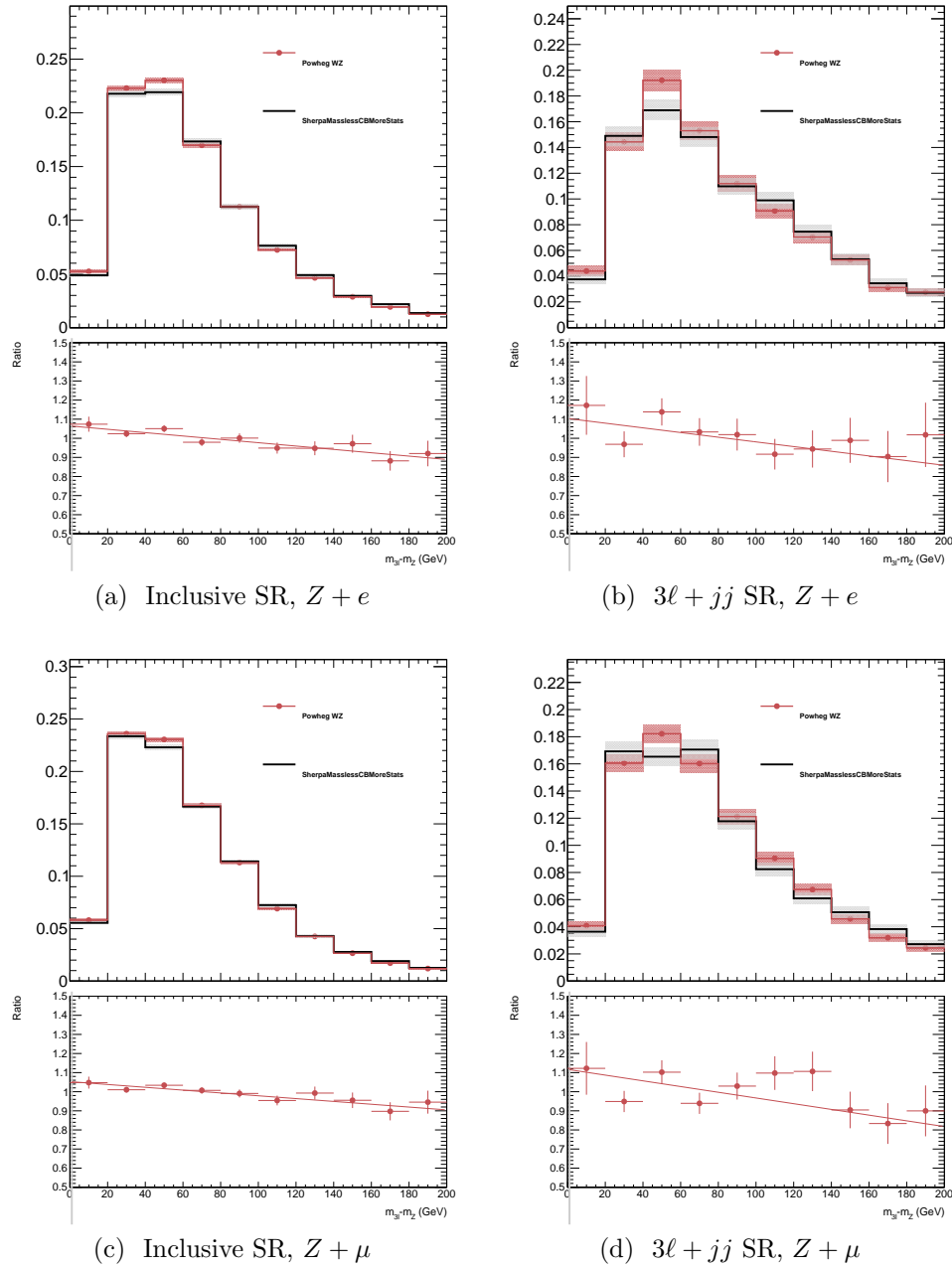


Figure 8.7: Comparison of the  $\Delta m$  distributions between POWHEG and SHERPA for the  $WZ$  backgrounds. The 4L signal region is omitted due to the negligible number of  $WZ$  events with four leptons.

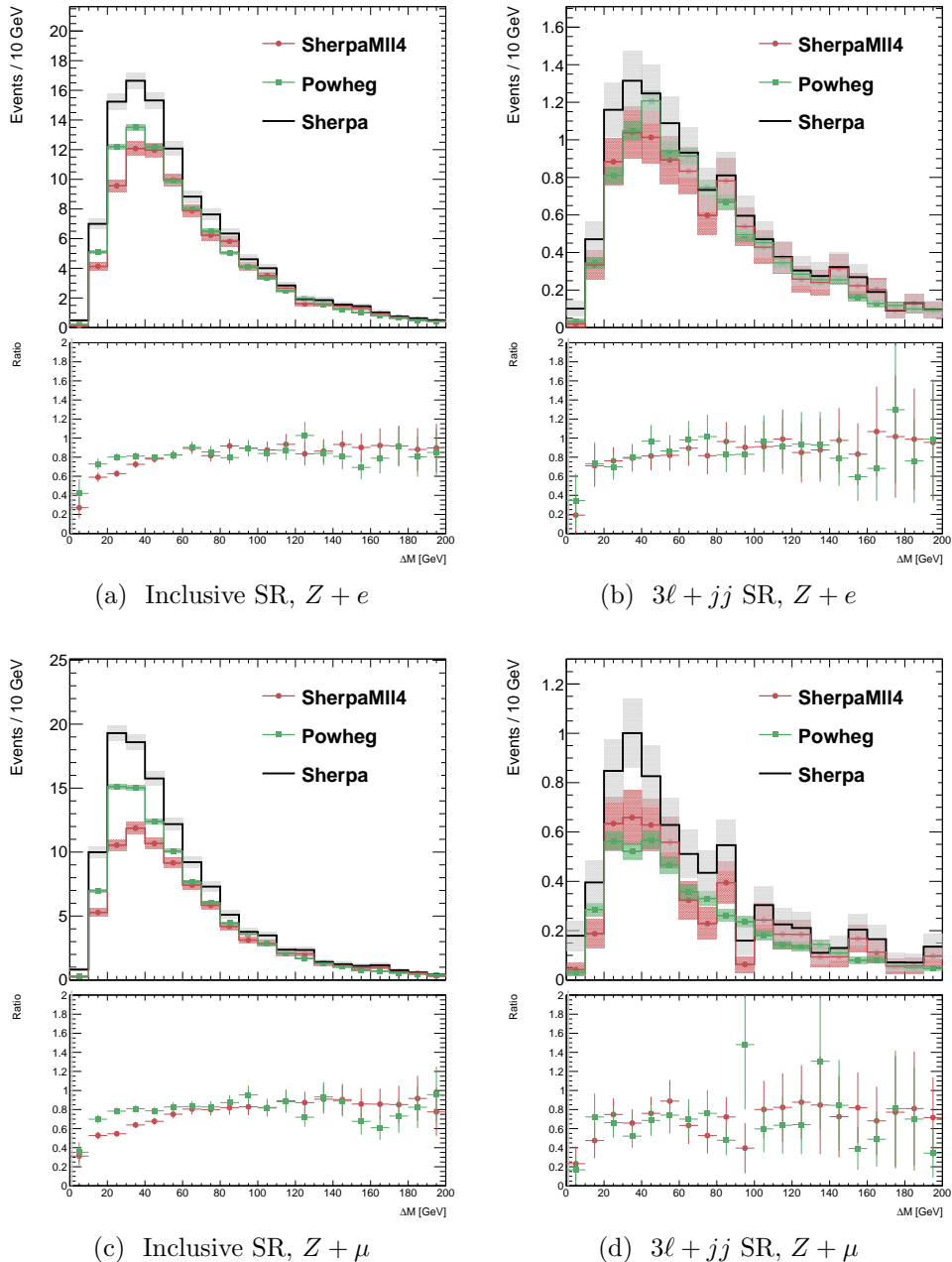


Figure 8.8: Comparison of SHERPA, SHERPA with mll4 filter, and POWHEG.

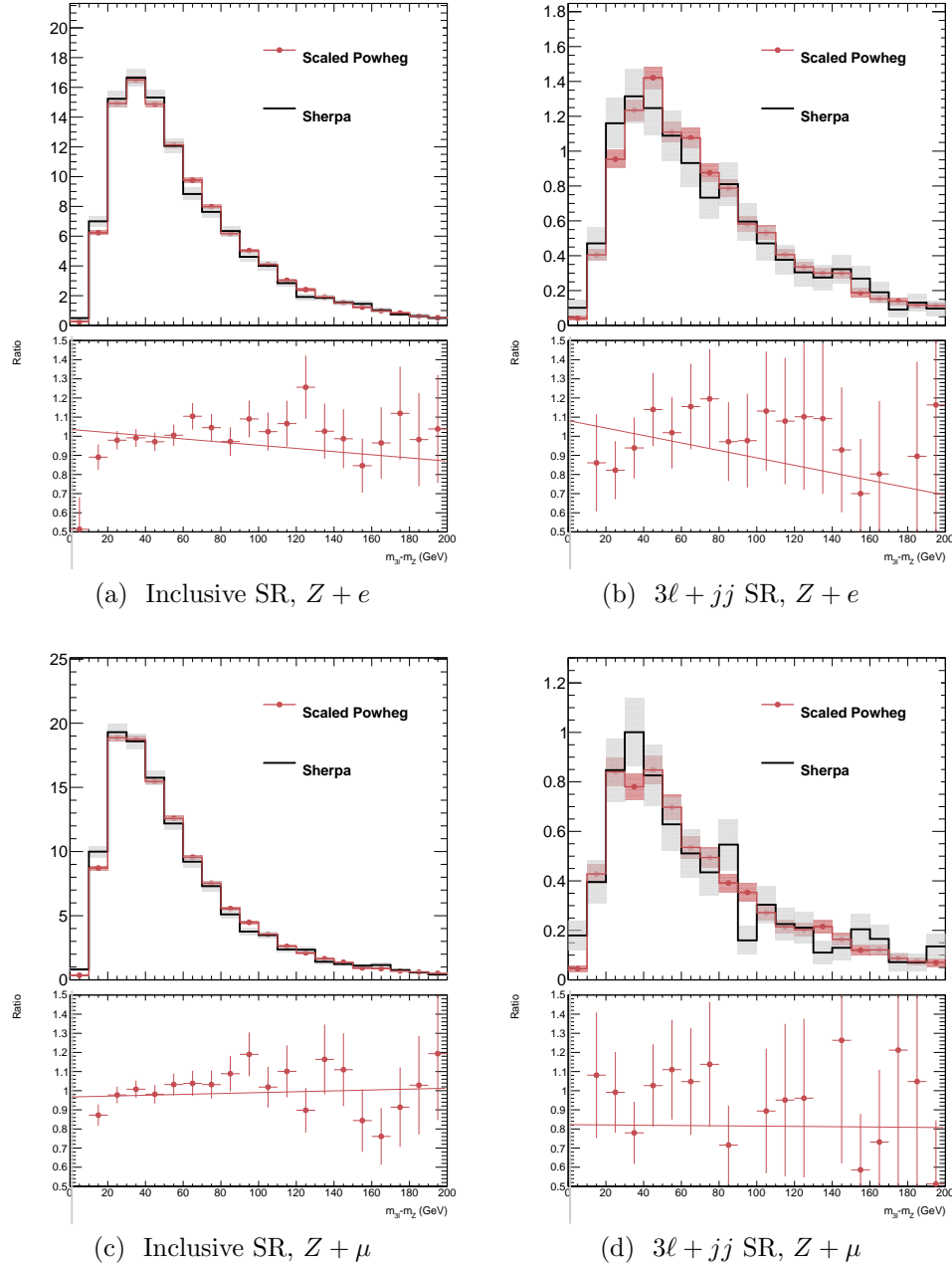


Figure 8.9: Comparison of the  $\Delta m$  distributions between POWHEG and SHERPA for the  $ZZ$  backgrounds. The POWHEG events are weighted to account for the mll4 filter.

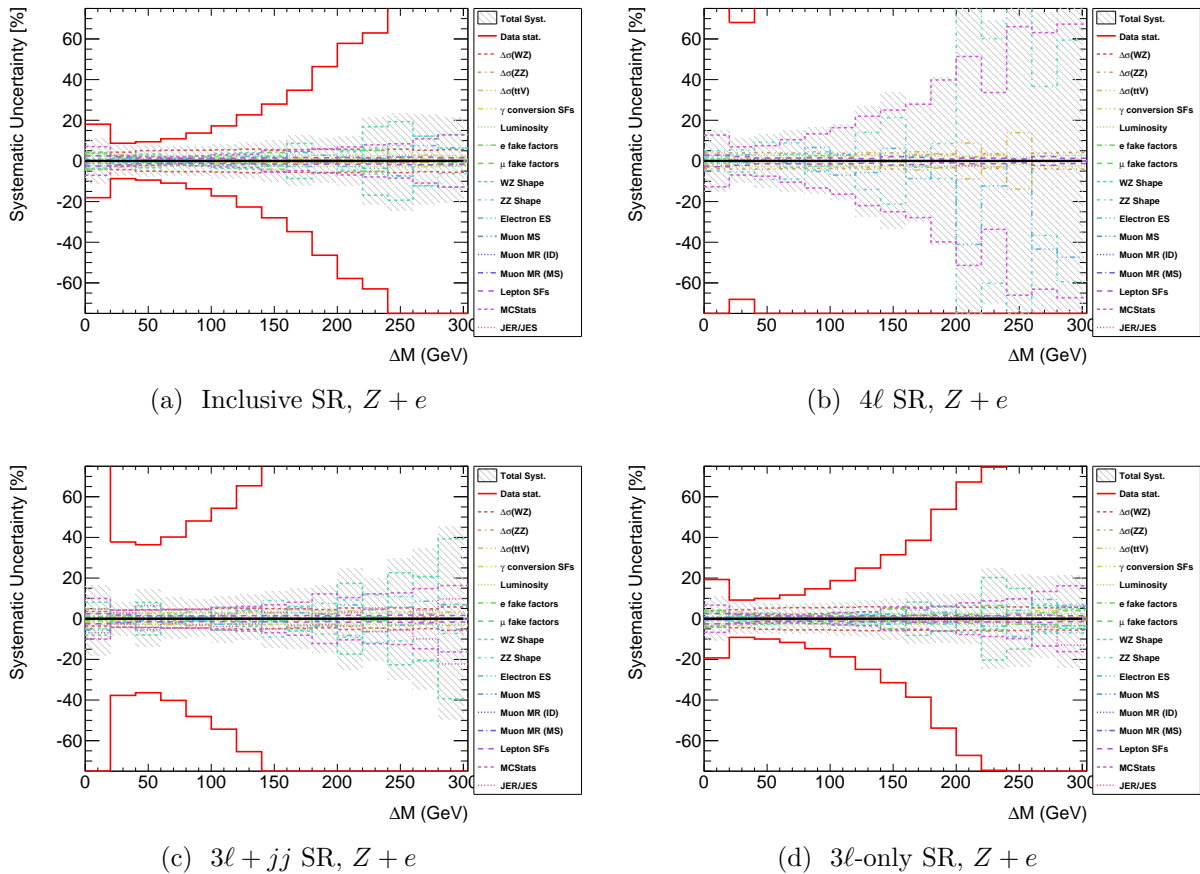


Figure 8.10: Systematics summary plots for each signal region in the  $Z + e$  flavor channel. The contribution from each source of systematic uncertainty is shown in 20 GeV bins, along with the total systematic uncertainty and the expected statistical uncertainty. Note that these uncertainties reflect bin-by-bin uncertainties on the Monte Carlo predictions, and do not necessarily correspond to the final uncertainty after fitting the background shapes.

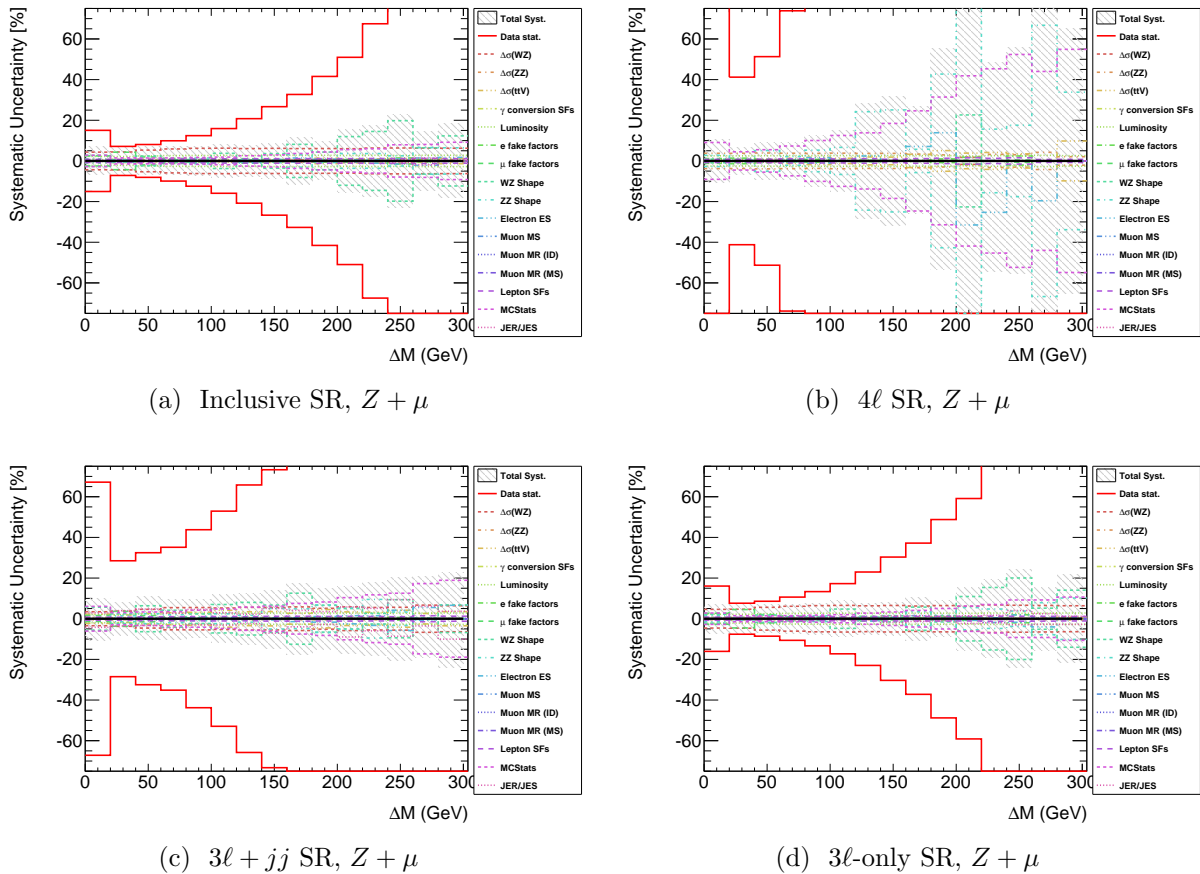


Figure 8.11: Systematics summary plots for each signal region in the  $Z + \mu$  flavor channel. The contribution from each source of systematic uncertainty is shown in 20 GeV bins, along with the total systematic uncertainty and the expected statistical uncertainty. Note that these uncertainties reflect bin-by-bin uncertainties on the Monte Carlo predictions, and do not necessarily correspond to the final uncertainty after fitting the background shapes.

## 8.4 Background Validation

For each flavor channel, four validation regions are defined to test the background predictions from the Monte Carlo simulation samples and the fake factor procedure. Each region starts from the set of events with three selected electrons or muons, two of which form an opposite-sign, same-flavor (OSSF) pair of leptons.

The **high  $\Delta R$**  region contains events with large separation between the  $Z$  candidate momentum and the off- $Z$  lepton momentum,  $\Delta R(Z, \ell_3) > 3$ . Events are also required to have exactly three leptons, and to satisfy  $\Delta m < 200 \text{ GeV} - m_Z$ , to limit signal contamination from hypotheses with larger  $m_{L^\pm}$  where the  $Z$  and the off- $Z$  lepton are less collimated. The region has a similar background composition to the signal regions with three leptons, and tests the  $WZ$ ,  $ZZ$ , and reducible background predictions.

The **ZZ** region contains events with two OSSF lepton pairs with invariant mass within 10 GeV of  $m_Z$ . The region tests the  $ZZ$  background prediction.

The **off-Z** region contains events with exactly three leptons, with an OSSF pair within 50 GeV of  $m_Z$ , but no OSSF pairs with invariant mass within 20 GeV of  $m_Z$ . As the event does not contain a  $Z$  candidate, the trilepton selection is modified: the highest mass OSSF pair is selected, and the third lepton is chosen to be the remaining lepton. In the  $Z + e$  flavor channel, this region tests the  $Z + \gamma$  background prediction. In the  $Z + \mu$  channel, the region is dominated by  $ZZ$ , where one lepton is not selected, and the other two leptons originate from an off-shell  $Z^*/\gamma^*$ .

The **WZ** region contains events with exactly three leptons, two of which form an OSSF pair within 10 GeV of  $m_Z$ , and the third of which satisfies  $40 \text{ GeV} < m_T^W < 90 \text{ GeV}$ . Additionally, the validation region requires  $40 \text{ GeV} < E_T^{\text{miss}} < 100 \text{ GeV}$  and zero jets, which suppresses signal contamination.

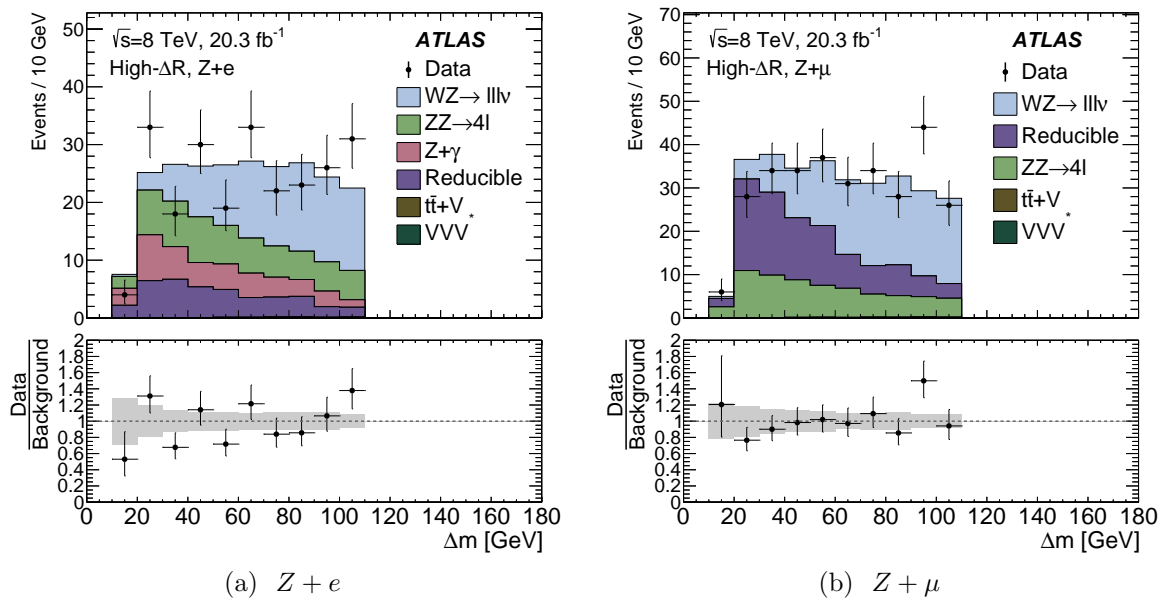
The definition of each validation region and the backgrounds tested are summarized in table 8.10. The total number of observed and predicted events in each region is shown in table 8.11, and the corresponding  $\Delta m$  distributions are shown in figures 8.12-8.15. Good agreement is seen in most validation regions, with the observed and predicted normalizations agreeing to better than  $1.5\sigma$ . A deficit of data with respect to the background prediction is seen in the off- $Z$ ,  $Z + \mu$  validation region, corresponding to  $2.3\sigma$ . The region is dominated by contributions from  $ZZ$ , where only three leptons pass the selection requirements and no same-flavour, opposite-sign lepton pair is reconstructed with invariant mass within 20 GeV of  $m_Z$ .

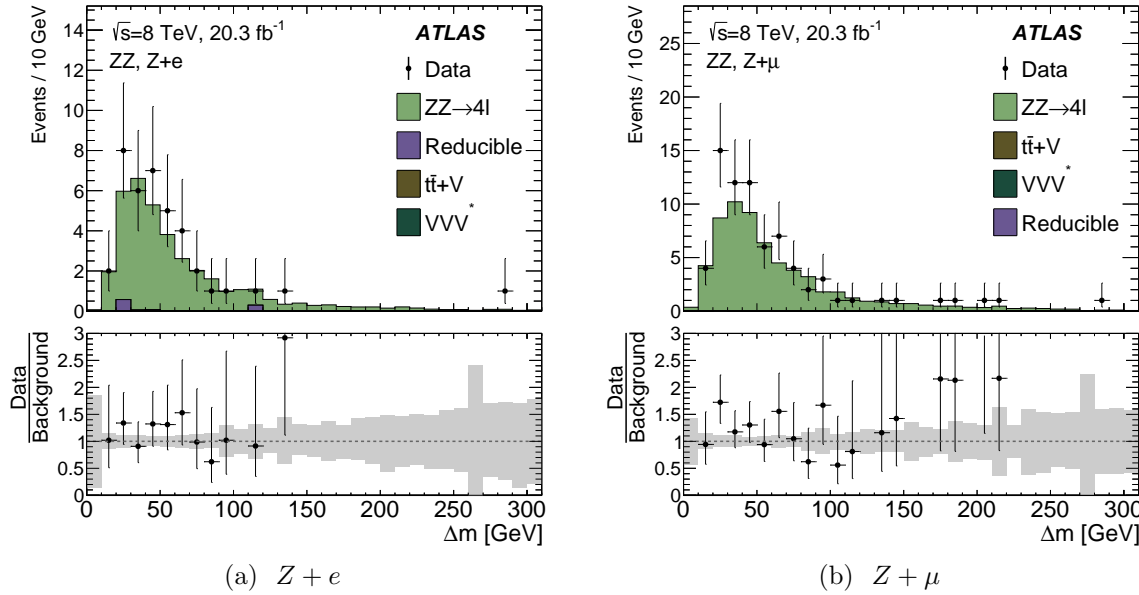
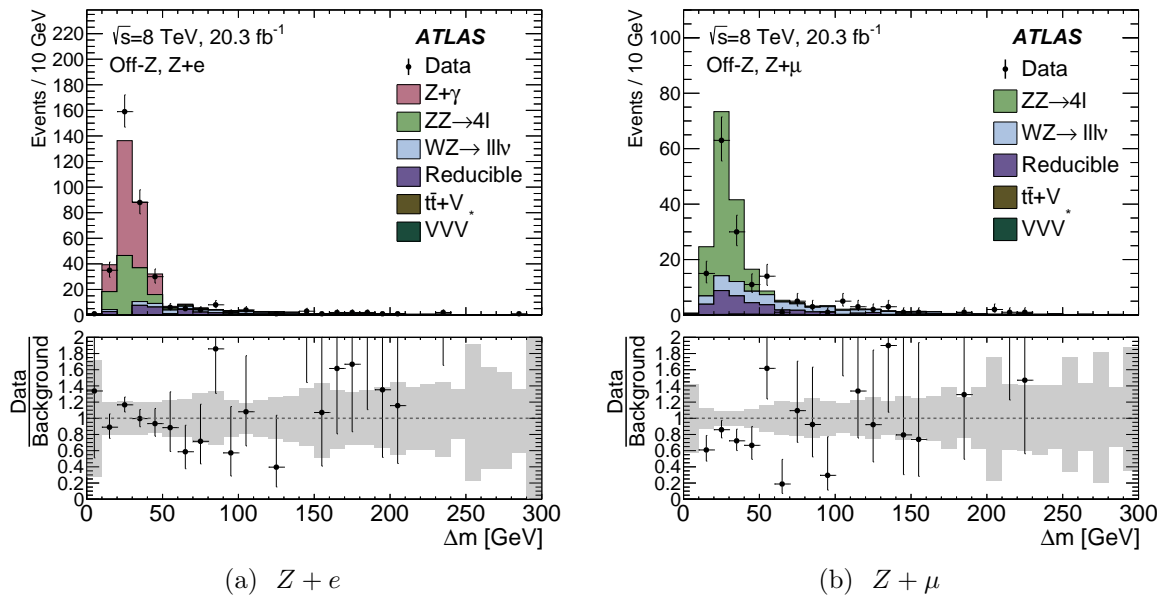
Control Region	Definition	Background Tested
High $\Delta R$	$\Delta R(Z, \ell_3) > 3.0$ $\Delta m < 200 \text{ GeV} - m_Z$	$WZ, ZZ$ , and reducible
Off $Z$	Reject events with $ m_\mu - m_Z  < 20 \text{ GeV}$	$Z + \gamma$ ( $Z + e$ events) and $ZZ$ ( $Z + \mu$ events)
Two $Z$	Require 2 $Z$ candidates ( $ m_\mu - m_Z  < 10 \text{ GeV}$ )	$ZZ$
$WZ$	3 leptons, 0 jets, $40 \text{ GeV} < m_T^W < 90 \text{ GeV}$ , $40 \text{ GeV} < E_T^{\text{miss}} < 100 \text{ GeV}$	$WZ$

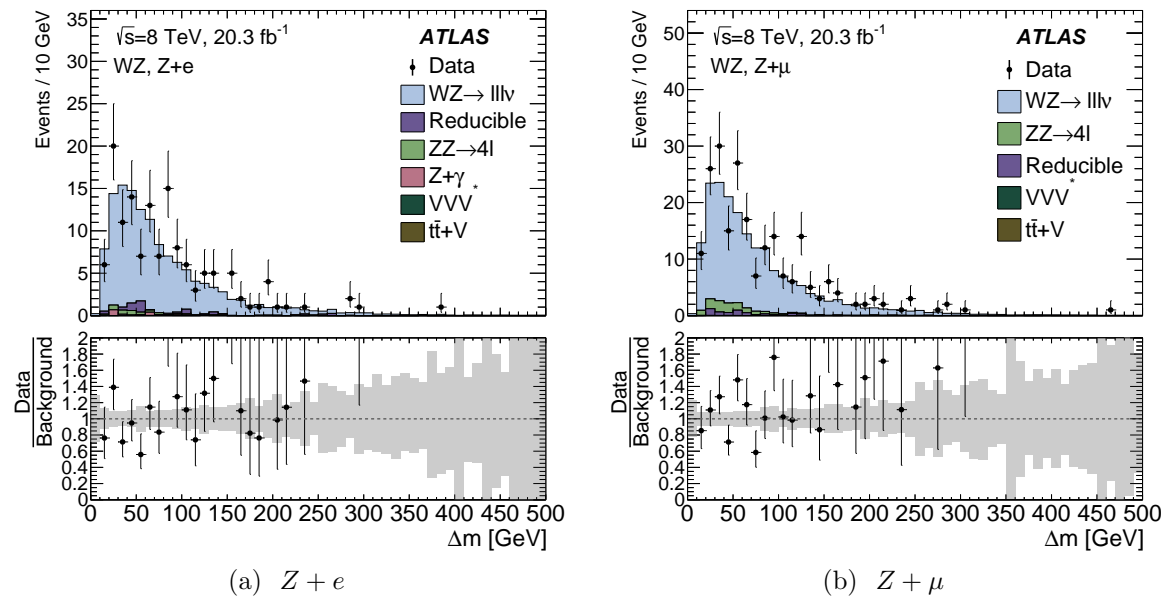
Table 8.10: Definitions and targeted backgrounds of the four validation regions.

Channel	Validation Region	Data	Background Prediction	$\frac{\text{Data} - \text{Bkgd}}{\sigma_{\text{bkgd}}}$
$Z + e$	High- $\Delta R$	239	$239 \pm 14$	0.0
$Z + e$	Off- $Z$	360	$349 \pm 44$	+0.2
$Z + e$	$ZZ$	39	$37 \pm 2$	+0.3
$Z + e$	$WZ$	140	$133 \pm 10$	+0.4
$Z + \mu$	High- $\Delta R$	302	$301 \pm 12$	+0.1
$Z + \mu$	Off- $Z$	163	$200 \pm 8$	-2.3
$Z + \mu$	$ZZ$	74	$63 \pm 3$	+1.2
$Z + \mu$	$WZ$	222	$193 \pm 14$	+1.5

Table 8.11: Summary of the number of events observed and predicted for each validation region. The uncertainty on the background prediction is the total systematic uncertainty. The difference between the observed and predicted number of events divided by the combined statistical and systematic uncertainty on the prediction is also shown.

Figure 8.12:  $\Delta m$  distributions for the high  $\Delta R$  validation regions.

Figure 8.13:  $\Delta m$  distributions for the  $ZZ$  validation regions.Figure 8.14:  $\Delta m$  distributions for the off- $Z$  validation regions.

Figure 8.15:  $\Delta m$  distributions for the  $WZ$  validation regions.

## 8.5 Signal and Background Fit Model

The numbers of signal and background candidate events in data are determined from an unbinned maximum-likelihood fit of a combination of signal and background models to the  $\Delta m$  distributions in each signal region. The signal and background processes are modeled with analytical probability density functions (p.d.f.s). The parameters of the p.d.f.s are determined from fits to the  $\Delta m$  distributions predicted by simulation or the fake factor procedure. Then, in each flavor channel, the data is fitted with the combined signal and background model, performed simultaneously on the three categories. In each signal region, the normalization of the dominant background ( $ZZ$  or  $WZ$ ) is a free parameter in the fit. The normalizations of all other backgrounds are constrained to fluctuate according to Gaussian probability distributions with mean and width values equal to the estimates and the total uncertainties before fitting. The resulting uncertainties on the fit parameters are incorporated in the limit setting as Gaussian-distributed nuisance parameters. Similarly, the shape uncertainty between the  $\Delta m$  distributions predicted by SHERPA and POWHEG is incorporated as a Gaussian-distributed nuisance parameter multiplying a template given by the difference between the two p.d.f.s.

### 8.5.1 Signal Modeling

The  $\Delta m$  distributions for the type III seesaw and vector-like leptons scenarios contain two distinct pieces: a peak associated with the correct identification of the three leptons due to the heavy lepton decay, and a broader component due to cases where the trilepton candidate does not originate from a heavy lepton decay. Accordingly, the distributions are modeled using the sum of two functions: a Voigtian for the peak and a Landau function for the combinatorial component. The signal parametrization is given by the following expression:

$$\mathcal{S}(m_L^\pm) = f_V F_V(\Delta m; \Gamma_V, m_V, \sigma_V) + (1 - f_V) F_L(\Delta m; \sigma_L, m_L), \quad (8.16)$$

$$(8.17)$$

where  $f_V$  denotes the fraction of events in the Voigtian;  $\Gamma_V$ ,  $m_V$  and  $\sigma_V$  are the width, mean and gaussian smearing term of the Voigtian; and  $\sigma_L$  and  $m_L$  are the width and mean of the Landau distribution.

The  $\Delta m$  distributions at each simulated mass point for both the type III seesaw and the vector-like leptons models are fitted with  $\mathcal{S}(m_L^\pm)$ , separately for each flavor channel and category. An example fit from the 300 GeV mass hypothesis of the vector-like leptons model is shown in figure 8.16. The full fit results from the inclusive categories are shown in tables 10.3-10.6.  $f_V$  roughly corresponds to how often the correct three leptons from the resonant decay are reconstructed and selected, and ranges from  $\sim 60\%$  ( $\sim 70\%$ ) at  $m_{L^\pm} = 120$  GeV to 58% (55%) at  $m_{L^\pm} = 400$  GeV for the type III seesaw (vector-like leptons) model. As mentioned in section 8.1.1, the type III seesaw samples were simulated

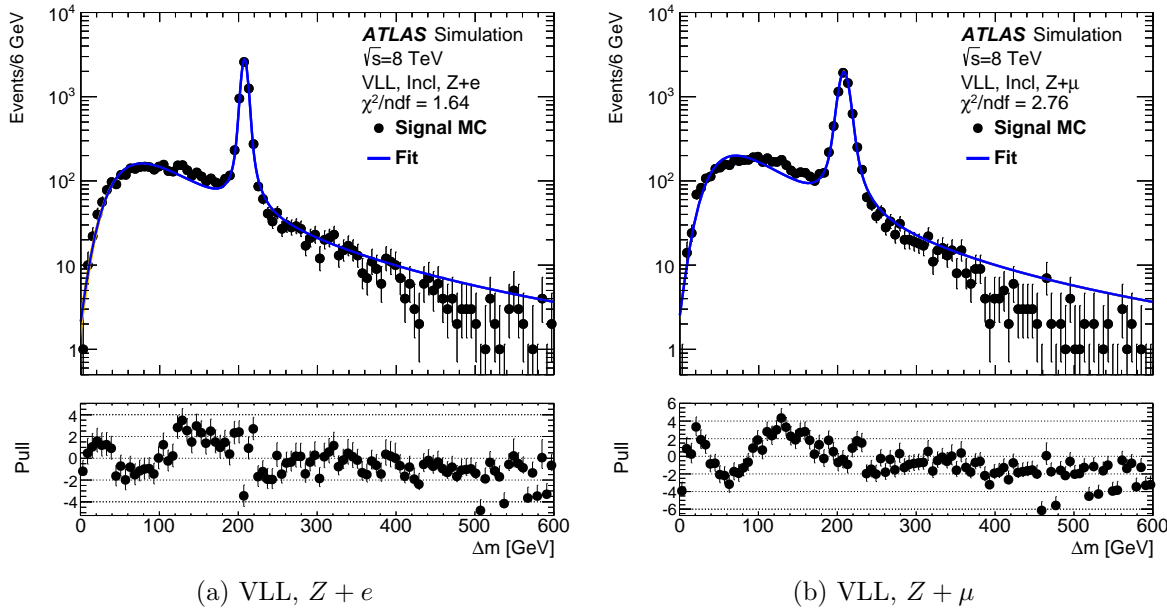


Figure 8.16: Fit of a Landau and a Voigtian to the inclusive distribution of the  $\Delta m$  at 300 GeV for the vector-like leptons model for  $Z + e$  final states (a) and  $Z + \mu$  final states (b).

without intrinsic  $Z$  width, and hence the width parameters determined from the vector-like leptons samples are used instead.

Signal hypotheses at intermediate mass points between the simulated values are obtained by linearly interpolating the fit parameters determined at the nearest simulated points above and below. To validate the linear interpolation between the mass points, a closure test was performed comparing the fit parameters determined at a simulated mass point with the values obtained from a linear interpolation between the adjacent simulated points. The resulting fit for the 160 GeV mass point is shown in Fig. ??.

### 8.5.2 Background Fits

The dominant diboson backgrounds are modeled using a Bukin function, a 5-parameter function designed to model asymmetric peaks:

$$\mathcal{P}(x; x_p, \sigma_p, \xi, \rho) = A_p \exp \left[ \frac{\xi \sqrt{\xi^2 + 1} (x - x_1) \sqrt{2 \log 2}}{\sigma_p (\sqrt{\xi^2 + 1} - \xi)^2 \log(\sqrt{\xi^2 + 1} + \xi)} + \rho \left( \frac{x - x_i}{p_p - x_i} \right)^2 - \log 2 \right], \quad (8.18)$$

where  $\rho = \rho_1$  and  $x = x_i$  for  $x < x_1$ , and  $\rho = \rho_2$  and  $x_i = x_2$  for  $x \leq x_2$ . The function describes the diboson  $\Delta m$  distribution well, in particular successfully modeling the turn-on region at low values of  $\Delta m$ . However, the fit parameters are strongly correlated, with some pairs exceeding 99% correlation. To reduce the number of free parameters, two parameters,  $\sigma_p$  and  $\xi_p$ , are constrained to be linear functions of  $x_p$  using pseudoexperiments. 100 toy datasets are generated from the fitted 5-parameter Bukin function, and the Bukin function fit is repeated on each dataset. The scatter plots of  $\sigma_p$  versus  $x_p$  and  $\xi_p$  versus  $x_p$  are shown in figure ??, along with the linear least squares fits used to constrain  $\sigma_p$  and  $\xi_p$ .

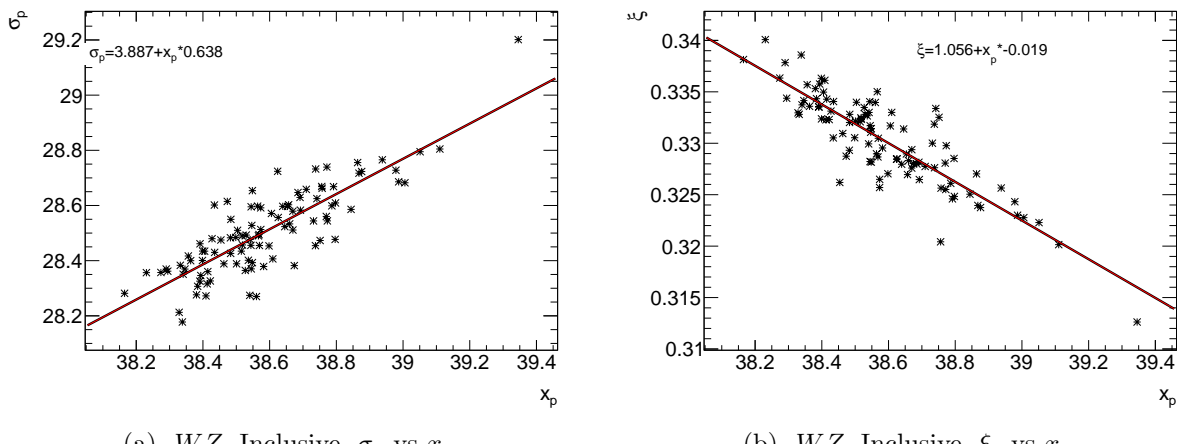


Figure 8.17: Parameter correlation for 100 toy experiments, including the linear fit for the inclusive  $WZ$  region.

The shapes of the diboson  $\Delta m$  distributions in the categorized signal regions are compared to the inclusive signal regions using unbinned Kolmogorov-Smirnov tests, shown in figures 8.19 and 8.20 and tables 8.12 and 8.13. The shapes of the  $\Delta m$  distributions in the  $4\ell$  and  $3\ell$ -only signal regions are consistent with the inclusive regions; therefore, to take advantage of the larger statistics in the inclusive signal region, the shape from the inclusive signal region is used to model the  $4\ell$  and  $3\ell$ -only signal regions. The fits for the inclusive and  $3\ell + jj$  signal regions are shown in figures 8.21 and 8.22.

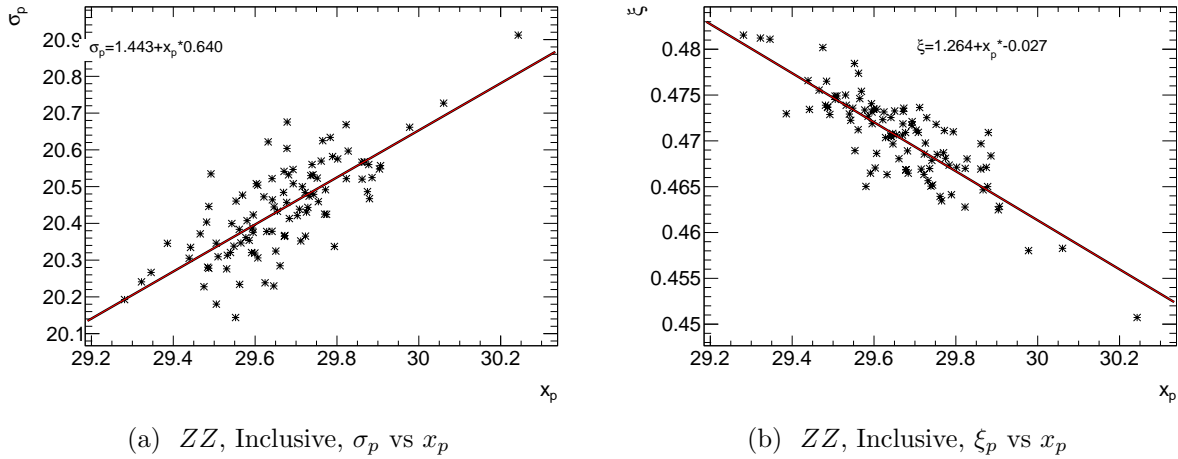


Figure 8.18: Parameter correlation for 100 toy experiments, including the linear fit for the inclusive  $ZZ$  region.

Signal Region	KS probability	$D$
$4\ell, Z + e$	0.4109	0.060
$3\ell + jj, Z + e$	0.001	0.122
$3\ell\text{-only}, Z + e$	0.782	0.019
$4\ell, Z + \mu$	0.520	0.043
$3\ell + jj, Z + \mu$	0.130	0.098
$3\ell\text{-only}, Z + \mu$	0.946	0.016

Table 8.12: Results of Kolmogorov-Smirnov tests comparing the  $ZZ$   $\Delta m$  shapes between the categorized signal regions and the inclusive signal regions. The Kolmogorov-Smirnov probability and test statistic are shown.

Signal Region	KS probability	$D$
$3\ell + jj, Z + e$	0.0	0.165
$3\ell\text{-only}, Z + e$	0.012	0.016
$3\ell + jj, Z + \mu$	0.0	0.152
$3\ell\text{-only}, Z + \mu$	0.0349	0.012

Table 8.13: Results of Kolmogorov-Smirnov tests comparing the  $WZ$   $\Delta m$  shapes between the categorized signal regions and the inclusive signal regions. The Kolmogorov-Smirnov probability and test statistic are shown.

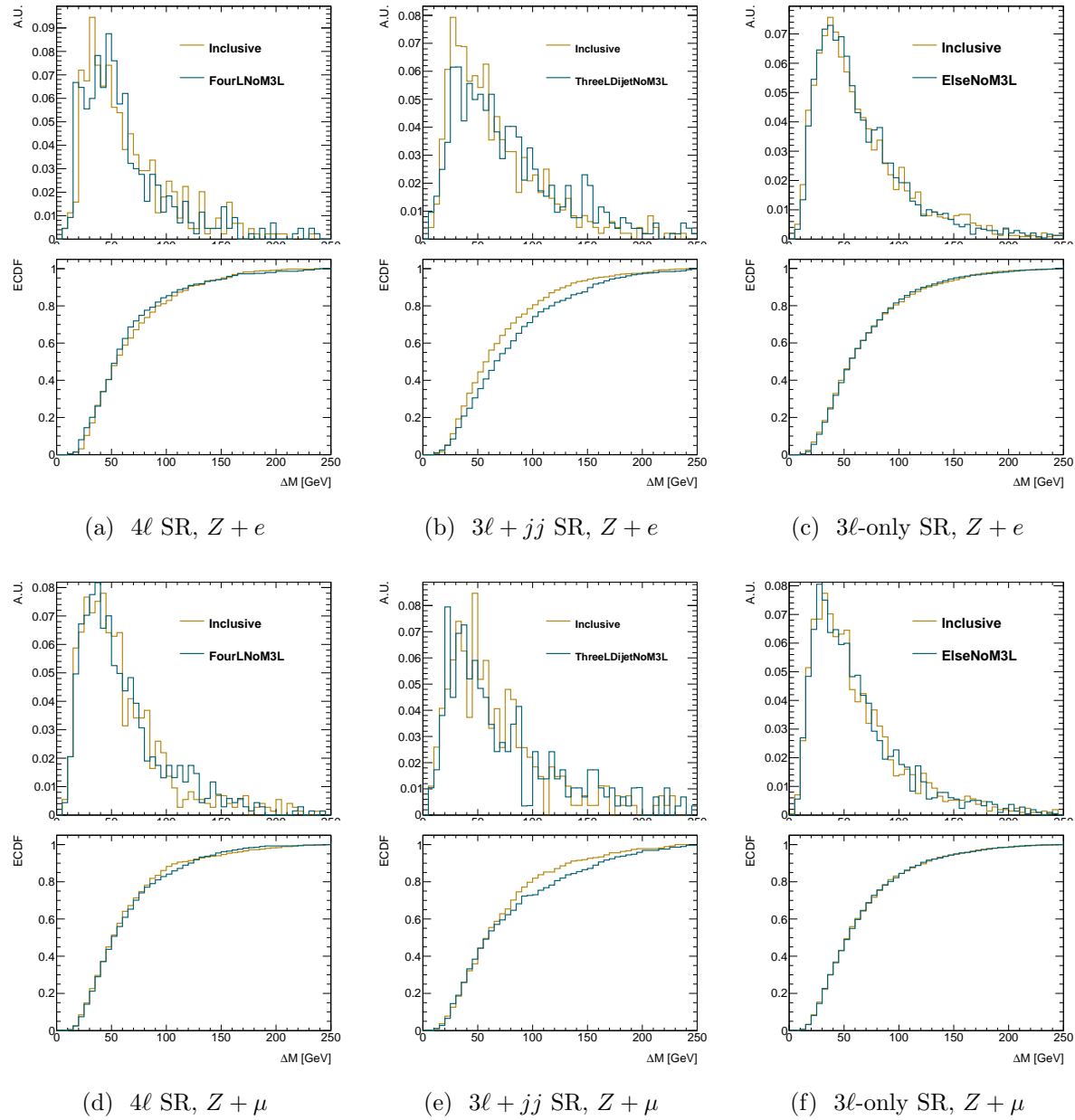


Figure 8.19: Comparison of  $ZZ \Delta m$  shapes between the inclusive signal region and the categorized signal regions, with empirical distribution functions.

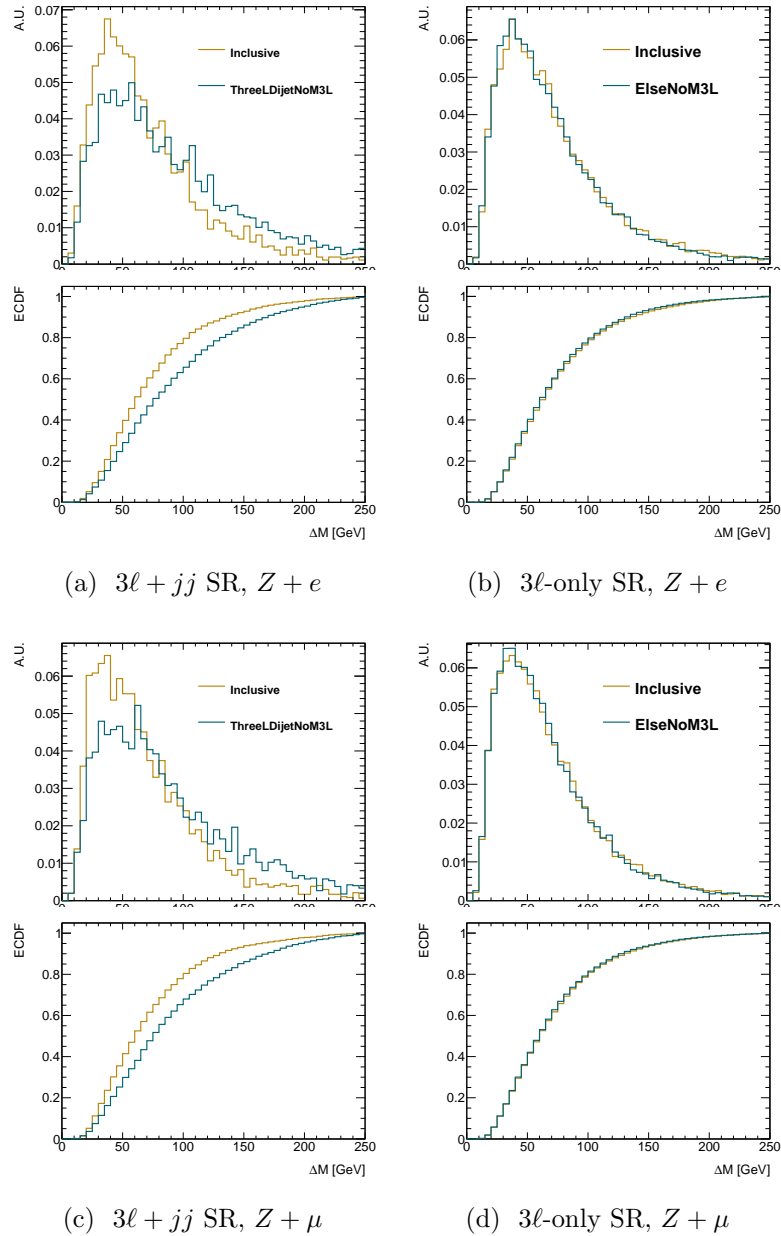


Figure 8.20: Comparison of  $WZ$   $\Delta m$  shapes between the inclusive signal region and the categorized signal regions, with empirical distribution functions. The  $4\ell$  signal regions are not shown due to the lack of  $WZ$  events with four leptons.

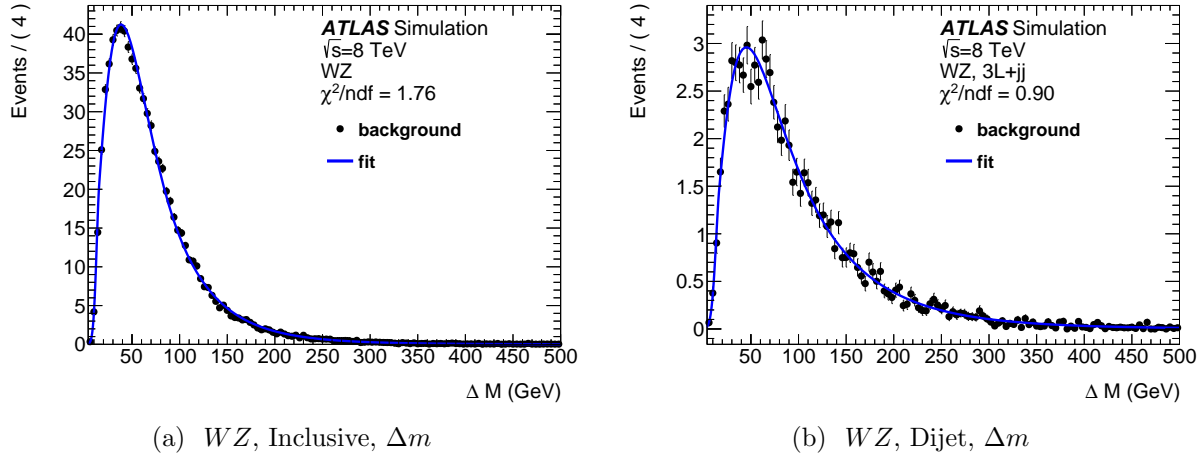


Figure 8.21:  $\Delta m$  distributions from Monte Carlo and Bukin function fits for the  $WZ$  background. The inclusive (left) and  $3\ell + jj$  (right) signal regions are shown.

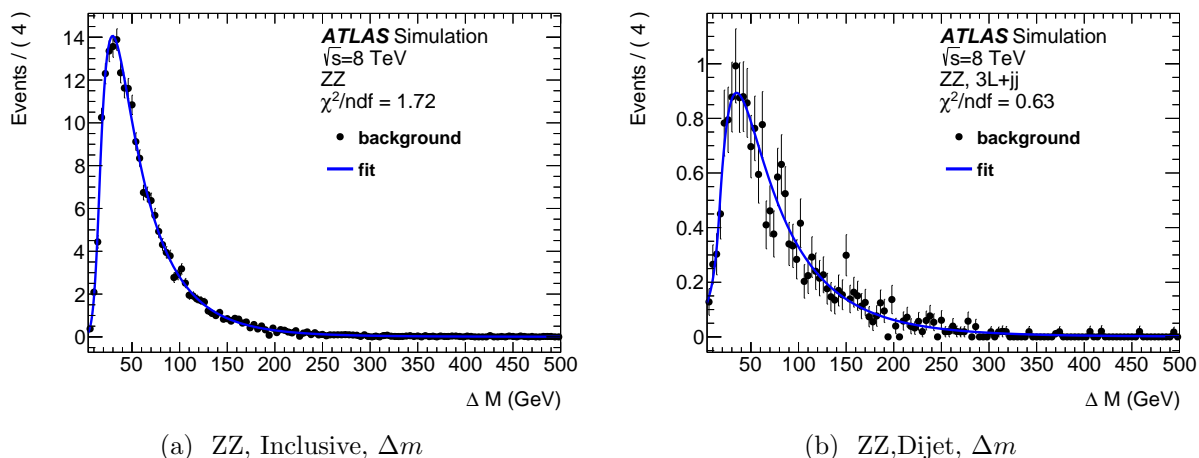


Figure 8.22:  $\Delta m$  distributions from Monte Carlo and Bukin function fits for the  $ZZ$  background. The inclusive (left) and  $3\ell + jj$  (right) signal regions are shown.

The most important remaining backgrounds are due to reducible processes and  $Z(l\bar{l}) + \gamma$ . The  $Z(l\bar{l}) + \gamma$  background is only significant in the  $Z + e$  signal regions. Due to the limited statistics from the fake factor estimate, the individual categories are combined into a single inclusive distribution for electron and muons. The reducible backgrounds are fitted with Landau distributions, shown in figure 8.23. The individual regions are then normalized to the expectations from the individual categories<sup>1</sup>.

The  $Z(l\bar{l}) + \gamma$  background is only significant in the  $3\ell$ -only,  $Z + e$  signal region. This background is modeled with the sum of a Landau and a Gaussian, shown in figure 8.24a. The remaining small contributions from  $t\bar{t} + V$  and triboson processes are modeled together with a Landau function, shown in figure 8.24b.

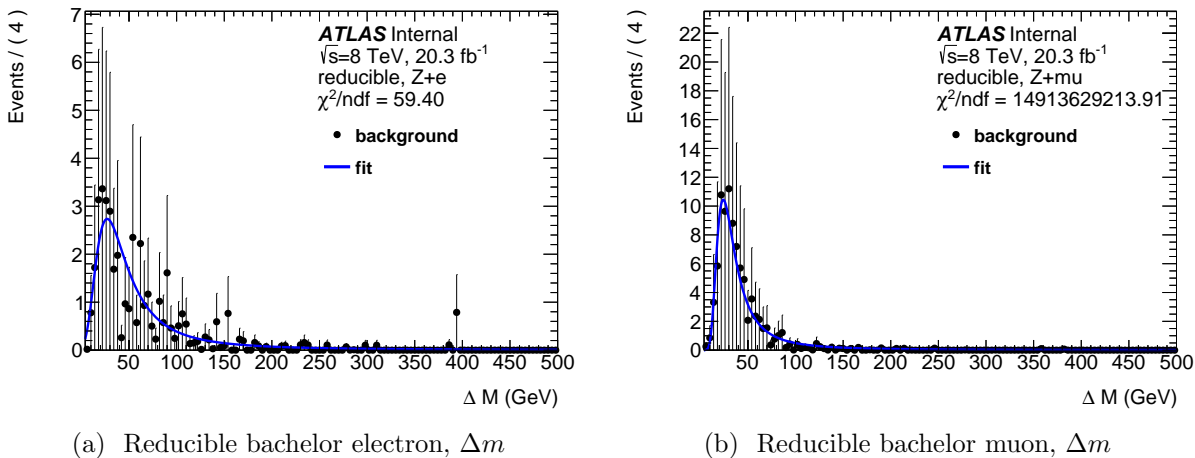


Figure 8.23: The shape of the reducible background is taken from the estimates from the fake factor method. The distribution is parametrized with a Landau for both bachelor lepton flavors. Due to the limited statistics in the categorized signal regions, the shape is determined in the inclusive signal region, and only the normalization varies in the categorized signal regions.

<sup>1</sup>In categories where the fake factor method predicts overall normalization that is negative but consistent with zero within statistical uncertainties, which can occur due to the prompt subtraction, the normalization is set to zero.

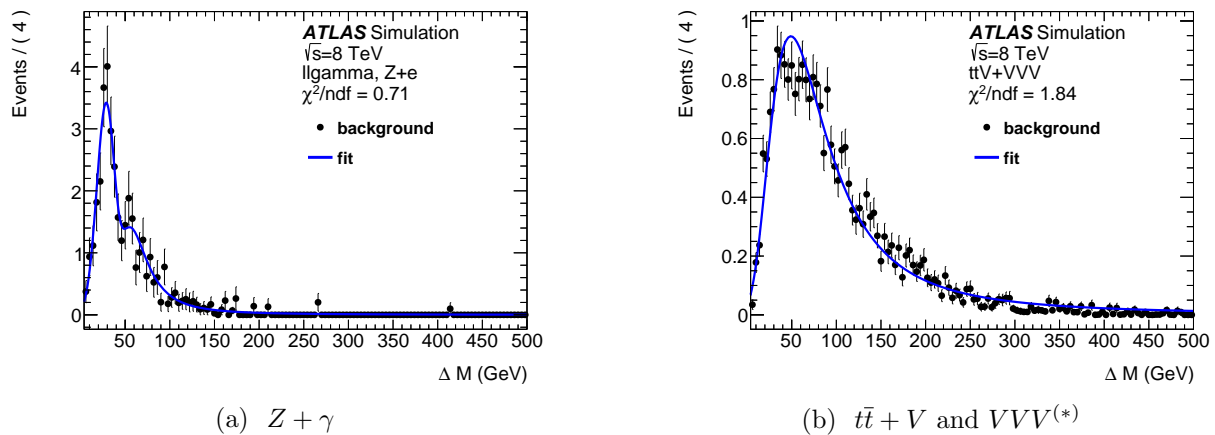


Figure 8.24:  $\Delta m$  distributions for the  $Z + \gamma$  (left) and  $t\bar{t} + V$  plus  $VVV^{(*)}$  (right) backgrounds. For the  $Z + \gamma$  background, the inclusive,  $Z + e$  signal region is shown; the background is negligible in the  $Z + \mu$  signal regions. For the  $t\bar{t} + V$  plus  $VVV^{(*)}$  background, the combination of the  $Z + e$  and  $Z + \mu$  inclusive signal regions is shown.

## 8.6 Results

The total number of observed events each signal region is shown in table 8.14. The predicted backgrounds before and after performing the unbinned maximum-likelihood fit in the background-only hypothesis are also shown. The  $\Delta m$  distributions for the pre-fit background estimates and the data are shown in figure 8.25, with examples signals from the vector-like leptons model with  $m_{L^\pm} = 140$  GeV and the type III seesaw model with  $m_{L^\pm} = 300$  GeV also shown. The data agree with the background expectation in all cases, and no clear peak indicating resonant trilepton production is seen in any of the signal regions.

Table 8.14: Observed and expected number of events in the six signal regions, before and after the combined unbinned maximum-likelihood fit. The pre-fit uncertainties represent the total systematic uncertainties on the background estimates. The post-fit uncertainties are determined by the maximum-likelihood fit.

Process	$Z + e$			$Z + \mu$		
	4l SR	$3\ell + jj$ SR	3 $\ell$ -only SR	4 $\ell$ SR	$3\ell + jj$ SR	3 $\ell$ -only SR
Before combined background-only fit						
$ZZ$	$10.9 \pm 0.6$	$11.7 \pm 0.8$	$91 \pm 5$	$21.4 \pm 1.1$	$7.5 \pm 0.6$	$90 \pm 5$
$WZ$	$0.08 \pm 0.01$	$35.3 \pm 3.1$	$337 \pm 28$	—	$46 \pm 4$	$480 \pm 40$
$Z + \gamma$	—	$2.3 \pm 0.8$	$35 \pm 11$	—	—	—
Reducible	—	$1.6 \pm 0.5$	$38 \pm 14$	$1.5 \pm 0.3$	$8.8 \pm 3.0$	$79 \pm 22$
$t\bar{t} + V, VVV^{(*)}$	$1.2 \pm 0.2$	$7.8 \pm 1.7$	$2.3 \pm 0.4$	$1.5 \pm 0.2$	$9.5 \pm 2.1$	$3.3 \pm 0.5$
Total Background	$12.2 \pm 0.7$	$59 \pm 4$	$504 \pm 34$	$24.4 \pm 1.2$	$72 \pm 6$	$650 \pm 50$
After combined background-only fit						
$ZZ$	$15 \pm 4$	$13.4 \pm 2.3$	$107 \pm 9$	$22 \pm 5$	$10.1 \pm 1.6$	$88 \pm 8$
$WZ$	$0.08 \pm 0.03$	$39 \pm 6$	$393 \pm 28$	$0.02 \pm 0.02$	$56 \pm 9$	$460 \pm 40$
$Z + \gamma$	—	$2.2 \pm 0.8$	$34 \pm 11$	—	—	—
Reducible	—	$1.8 \pm 1.2$	$37 \pm 13$	$1.8 \pm 0.9$	$10.2 \pm 2.8$	$92 \pm 24$
$t\bar{t} + V, VVV^{(*)}$	$1.1 \pm 0.3$	$7.5 \pm 1.7$	$2.5 \pm 0.6$	$1.5 \pm 0.4$	$9.1 \pm 2.1$	$3.3 \pm 0.8$
Total Background	$16 \pm 4$	$64 \pm 7$	$574 \pm 34$	$25 \pm 5$	$85 \pm 10$	$640 \pm 40$
Data	16	64	573	25	86	651

Good agreement is seen between the pre-fit and post-fit normalizations for the  $4\ell$  and  $3\ell + jj$  categories in the  $Z + \mu$  flavour channel. The largest change in normalization due to the fit is in the  $4\ell$  category for the  $Z + e$  flavour channel, where the fitted  $ZZ$  normalization exceeds the prediction by 35%. The  $WZ$  and  $ZZ$  normalizations increase by roughly 15% in the  $3\ell + jj$  and  $3\ell$ -only categories in the  $Z + e$  flavour channel, and 30% in the  $3\ell + jj$  category in the  $Z + \mu$  flavour channel. The projections of the fit results in the background-

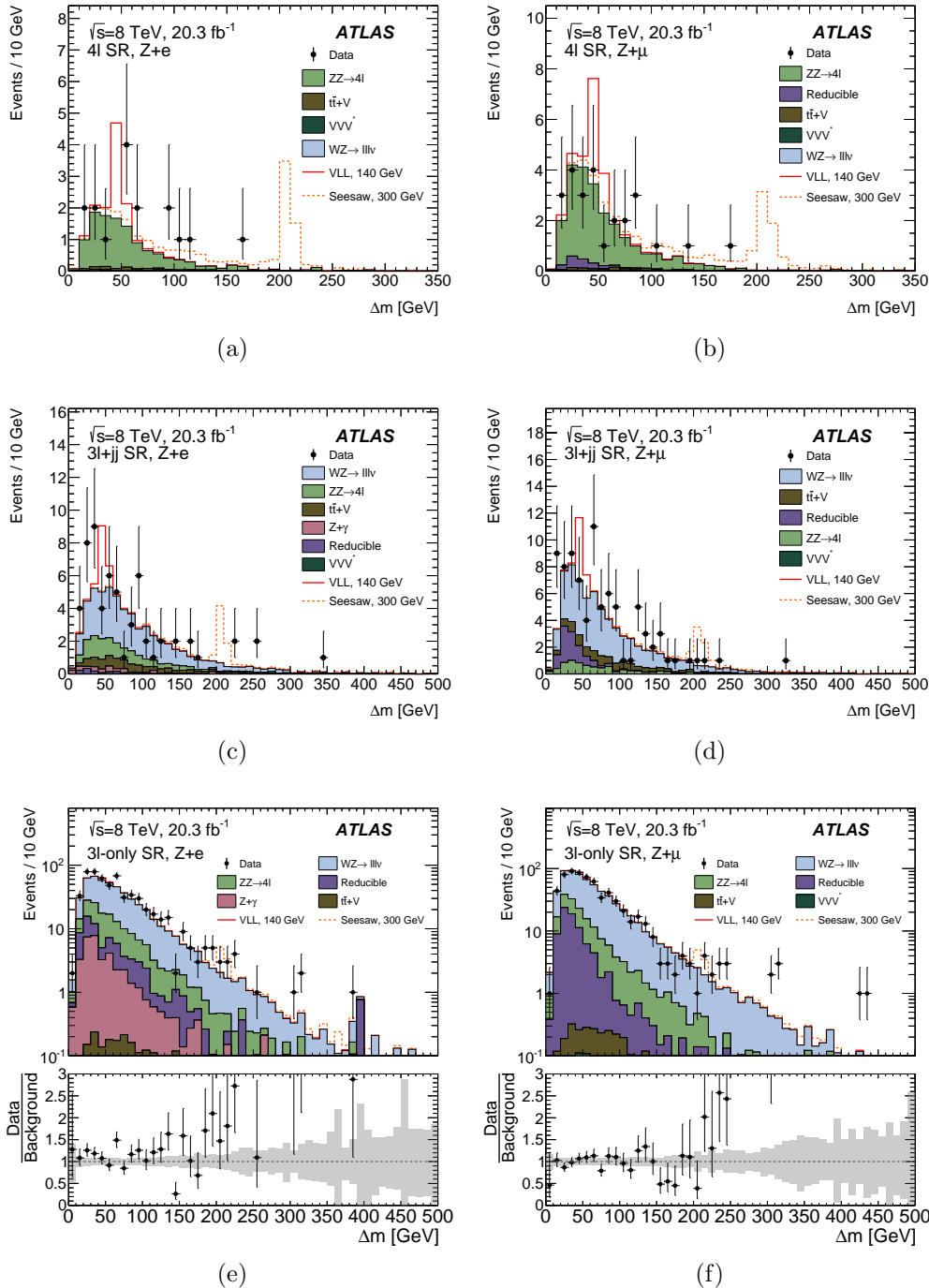


Figure 8.25: The  $\Delta m = m_{3\ell} - m_{\ell^+\ell^-}$  distributions for the  $4\ell$  (top),  $3\ell + jj$  (middle), and  $3\ell$ -only (bottom) categories, divided into the  $Z + e$  (left) and  $Z + \mu$  (right) flavour channels. The observed data are shown as black points, while the pre-fit background expectations are shown in the coloured histograms. Also shown are examples for signal contributions for a 140 GeV  $L^\pm$  in the vector-like leptons model and a 300 GeV  $L^\pm$  in the type III seesaw model. The error bars on the data points represent statistical uncertainties, and the shaded bands represent the systematic uncertainties on the background predictions.

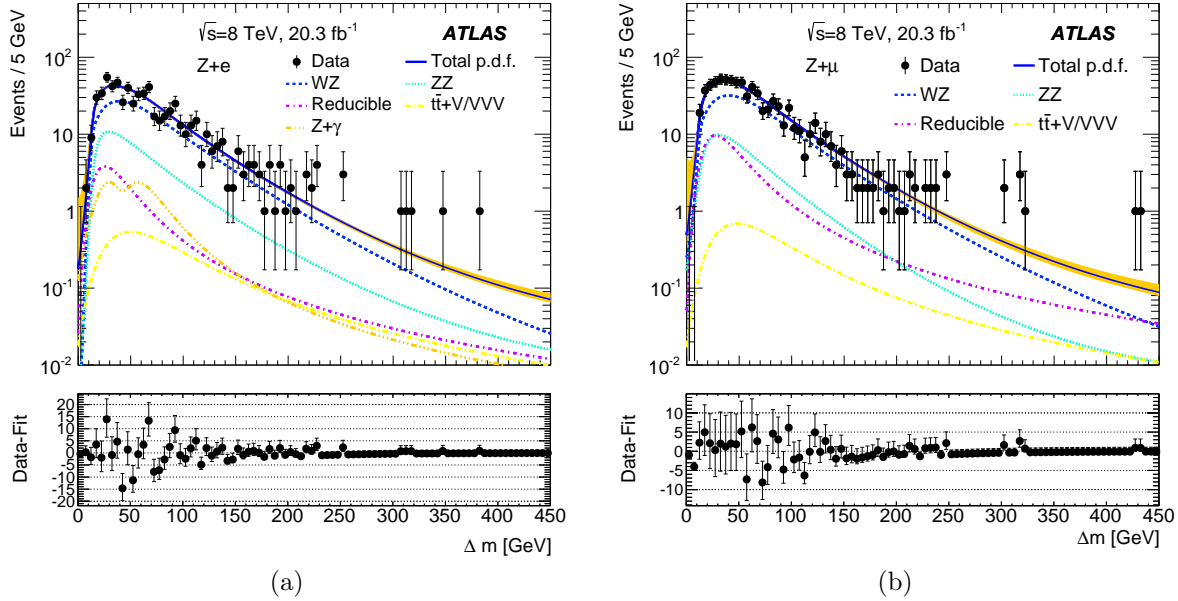


Figure 8.26: Projections onto the  $\Delta m$  variable of the background-only unbinned maximum-likelihood fits, shown superimposed on the data with the three categories in each flavour channel added together. The  $Z + e$  flavour channel is shown in (a), and the  $Z + \mu$  channel is shown in (b). The contributions of the separate background components to the total background-only fit are also shown. The error bars on the data points represent statistical uncertainties. Good agreement is observed between the background model and the data.

only hypothesis are shown in figure 8.26 for the combination of the three categories in each flavour channel.

## 8.7 Interpretation

The data are well described by the combined fit to the three categories in each flavour channel. The consistency of the data with the background-only hypothesis is evaluated by scanning the local  $p_0$ -value for the  $\Delta m$  distribution in 3 GeV intervals for signal mass hypotheses in the range  $100 - 400$  GeV for the vector-like leptons model, and  $100 - 500$  GeV for the seesaw model, using the unbinned maximum-likelihood fit described in section 8.5 with the signal strength set to zero. The agreement is expressed in terms of the  $p_0$ -value, the probability that, assuming the background-only hypothesis is true, an experiment would yield at least as many events as observed in the current measurement. The  $p_0$  values are calculated using the frequentist hypothesis test based on the profile likelihood ratio test statistic and approximated with asymptotic formulae [24]. The results are shown in figure 8.27. The minimum  $p_0$ -value is  $p_0 = 0.02$  at a mass of 183 GeV for the  $Z + e$  flavour channel, and

$p_0 = 0.05$  at a mass of 109 GeV for the  $Z + \mu$  flavour channel.

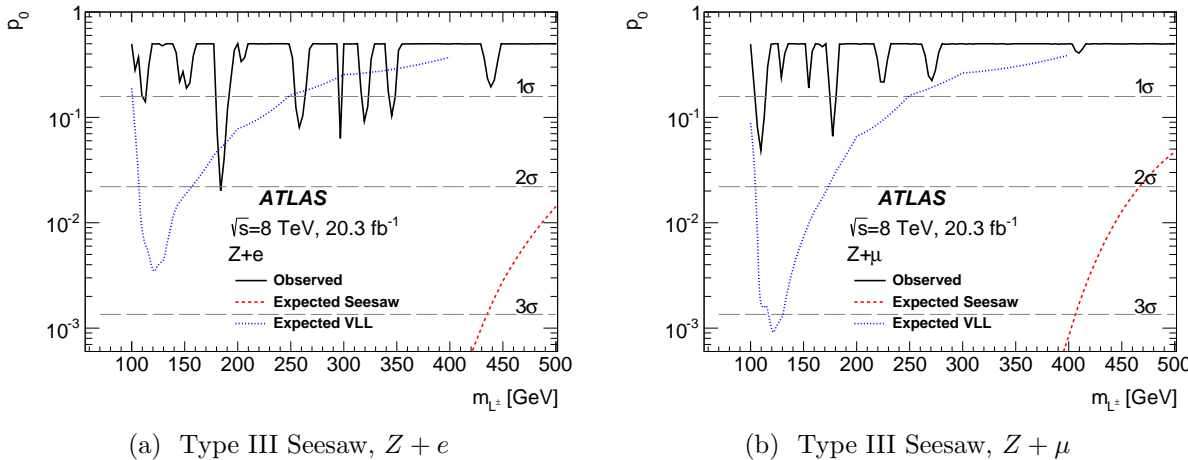


Figure 8.27:  $p_0$ -values for the background-only hypothesis as a function of the heavy lepton mass and the corresponding expected  $p$ -values for the vector-like lepton model (blue) and the type-III seesaw model.

### 8.7.1 Limits on Models

Since no significant excess above the background expectation is observed, the fit model is used to derive 95% confidence level (CL) exclusion limits on the heavy lepton pair-production cross section,  $\sigma$ , using the  $CL_s$  method [25]. The limits are shown for the vector-like leptons model in figure 8.28, and for the type III seesaw model in figure 8.29, evaluated in the same 3 GeV intervals as the  $p_0$ -values. The vector-like leptons model is excluded for electron-only mixing in the heavy lepton mass ranges 129–144 GeV and 163–176 GeV, with an expected exclusion in the range 109–152 GeV. The corresponding observed (expected) exclusion for the muon-only mixing scenario is 114–153 GeV and 160–168 GeV (105–167 GeV). The significantly higher production cross sections for the type III seesaw model lead to an observed (expected) exclusion in the electron-only mixing scenario in the heavy lepton mass range 100–430 GeV (100–436 GeV). For the muon-only mixing scenario, the observed exclusion is in the ranges 100–401 GeV and 419–468 GeV, while the expected exclusion is 100–419 GeV.

#### Model-Independent Limits

The constraints shown in figures 8.28 and 8.29 are relevant to the specific VLL and type III seesaw models considered, and are not necessarily applicable to other scenarios predicting trilepton resonances with an intermediate  $Z$  boson. A more model-independent observable is the *visible cross section*,  $\sigma_{\text{vis}}$ , defined as the number of observed events with  $Z + \ell$ -induced trilepton resonances for a given resonance mass divided by the integrated luminosity of the

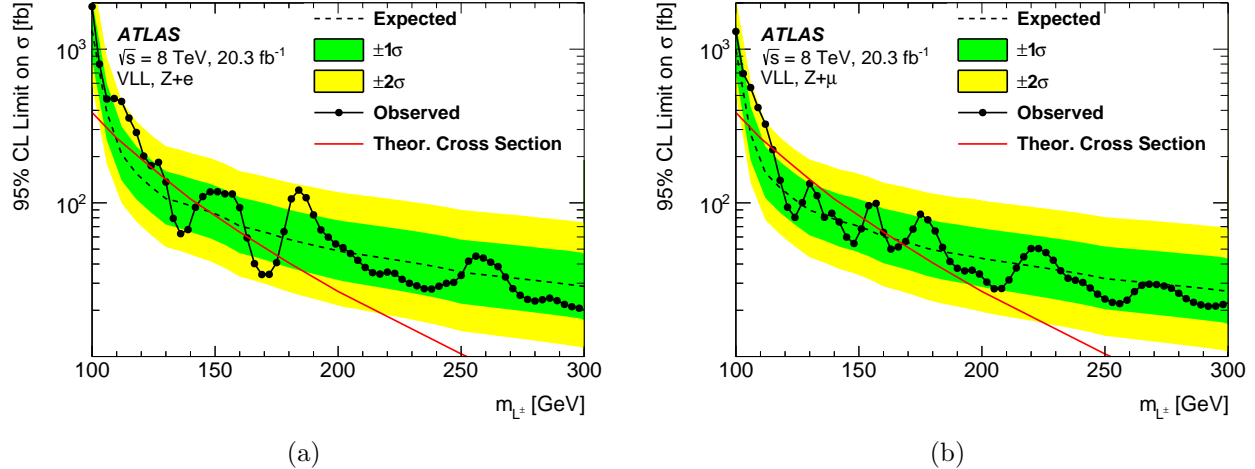


Figure 8.28: 95% CL upper limits on the vector-like lepton cross section. The left (right) plot shows the limits assuming 100% branching fraction to  $e/\nu_e$  ( $\mu/\nu_\mu$ ). The solid line shows the observed limit. The dashed line shows the median expected limit for a background-only hypothesis, with green and yellow bands indicating the expected fluctuations at the  $\pm 1\sigma$  and  $\pm 2\sigma$  levels. The limit is evaluated in 3 GeV intervals.

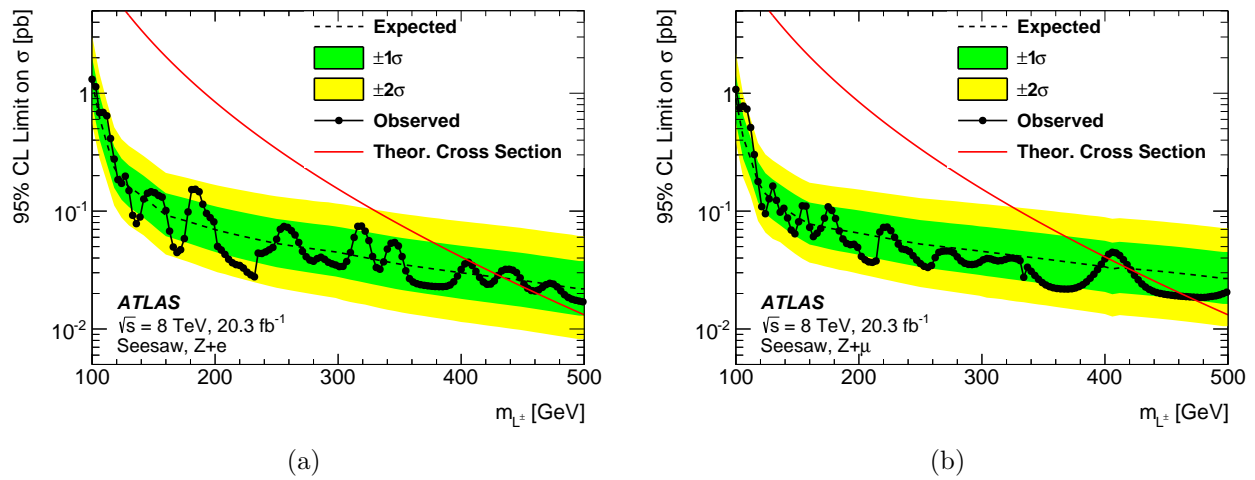


Figure 8.29: 95% CL upper limits on the type III seesaw production cross section. The left (right) plot shows the limits assuming 100% branching fraction to  $e/\nu_e$  ( $\mu/\nu_\mu$ ). The solid line shows the observed limit. The dashed line shows the median expected limit for a background-only hypothesis dataset, with green and yellow bands indicating the expected fluctuations at the  $\pm 1\sigma$  and  $\pm 2\sigma$  levels. The limit is evaluated in 3 GeV intervals.

data sample,  $20.3 \text{ fb}^{-1}$ . The 95% CL upper limits on  $\sigma_{\text{vis}}$ , denoted  $\sigma_{95}^{\text{vis}}$ , are derived from a fit to each flavour channel with  $f_V = 1$ , i.e. using only the peak component of the signal. The results for the two flavour channels, derived from the inclusive event selection without dividing the events into the three categories, are shown in figure 8.30.

The limits on  $\sigma_{\text{vis}}$  can be used to test specific models after taking into account the model's acceptance with respect to a fiducial volume,  $\mathcal{A}$ , and reconstruction and selection efficiency of events within the fiducial volume,  $\epsilon_{\text{fid}}$ . The 95% CL upper limit on the cross section for the model is given by:

$$\sigma_{95} = \frac{\sigma_{95}^{\text{vis}}}{\mathcal{A} \times \epsilon_{\text{fid}}}. \quad (8.19)$$

The acceptance  $\mathcal{A}$  is defined as the probability for generated signal events to lie within a fiducial volume defined by the kinematics of the generated leptons. The leptons are considered at *particle level*, i.e. after parton shower and hadronization and with lifetimes longer than  $10^{-11} \text{ s}$ , and are *dressed*, including the contributions from radiated photons within a cone of  $\Delta R = 0.1$ . The fiducial volume requires that events contain an  $L^\pm$  decaying to a prompt electron or muon and a  $Z$  boson that then decays to electrons or muons. The three leptons from the  $L^\pm$  decay are required to have  $p_T > 15 \text{ GeV}$  and lie within  $|\eta| < 2.5$ , with at least one lepton satisfying  $p_T > 26 \text{ GeV}$ . Two of the leptons must form a same-flavour opposite-sign pair with a mass within 10 GeV of  $m_Z$ , and the  $Z$  boson and the off- $Z$  lepton must be separated by  $\Delta R < 3$ . The events are divided into flavour channels according to the flavour of the off- $Z$  lepton. For the VLL and type III seesaw models used in this analysis, the acceptance of events containing an  $L^\pm \rightarrow Z(\ell\ell)\ell$  decay to fall within the fiducial volume is in the range 60%–65% for most of the mass range, decreasing at higher masses due to the cut on the  $\Delta R$  between the  $Z$  boson and the off- $Z$  lepton. The acceptance decreases at low masses due to the lepton  $p_T$  requirement, reaching 30%–35% at  $m_{L^\pm} = 100 \text{ GeV}$ .

For type III seesaw and VLL events within the fiducial volume,  $\epsilon_{\text{fid}}$  ranges from 20% to 49% if the other heavy lepton decays to a neutrino and a  $W$ ,  $Z$ , or  $H$  boson. If the other heavy lepton decays to an electron or a muon, the efficiency is 10%–20% lower, due to the increased probability of incorrectly selecting the off- $Z$  lepton. The event selection efficiencies for the type III seesaw model in scenarios where the second heavy lepton decays to a  $W$  boson are shown in figure 8.31 as a function of  $m_{L^\pm}$ ; the efficiencies for scenarios where the second heavy lepton decays to a  $Z$  or  $H$  boson and for the vector-like leptons model are consistent with these efficiencies within the statistical uncertainties.

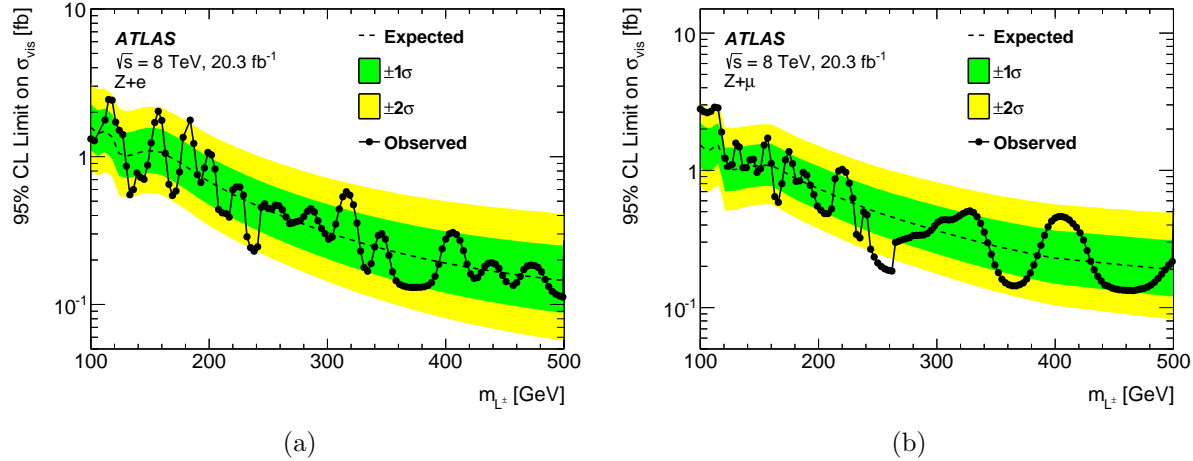


Figure 8.30: Upper limits at 95% CL on  $\sigma_{\text{vis}}$  for the  $Z + e$  (left) and  $Z + \mu$  (right) flavour channels, derived without dividing events into the three categories. The limits are evaluated in 3 GeV intervals.

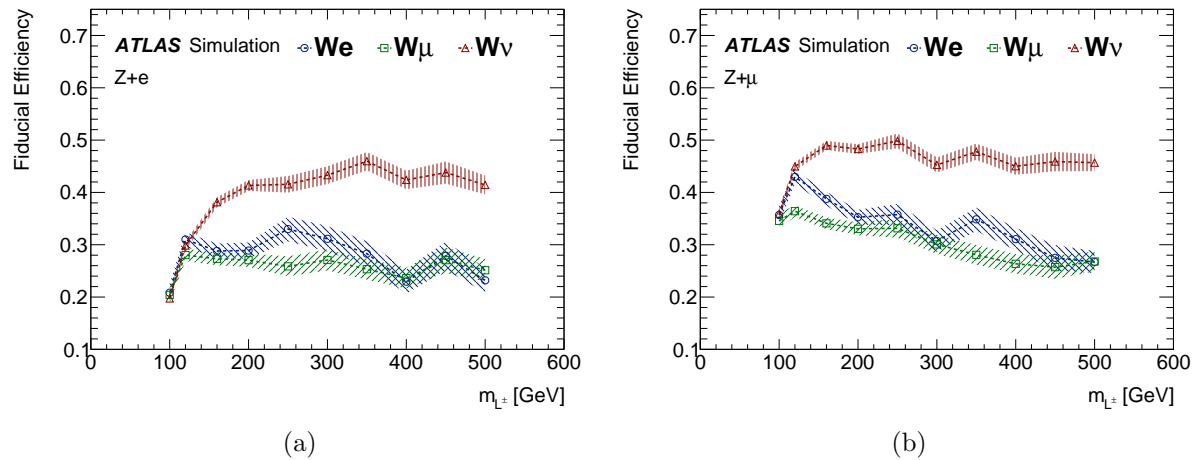


Figure 8.31: Efficiencies for reconstructing and correctly identifying the  $L^\pm \rightarrow Z(\ell\ell)L^\pm$  decay in events within the fiducial volume for the type III seesaw model. The left (right) plot shows the efficiencies for events containing a  $L^\pm \rightarrow Z(\ell\ell)e$  ( $L^\pm \rightarrow Z(\ell\ell)\mu$ ) decay. The decay of the second heavy lepton is specified in the legend. The shaded bands show the statistical uncertainty.

# Bibliography

- [1] J. .-.E. Augustin et al., *Discovery of a Narrow Resonance in  $e^+e^-$  Annihilation*, Phys. Rev. Lett. **33** (1974) p. 1406,  
URL: <http://link.aps.org/doi/10.1103/PhysRevLett.33.1406>.
- [2] J. J. Aubert et al., *Experimental Observation of a Heavy Particle J*, Phys. Rev. Lett. **33** (1974) p. 1404,  
URL: <http://link.aps.org/doi/10.1103/PhysRevLett.33.1404>.
- [3] S. W. Herb et al., *Observation of a Dimuon Resonance at 9.5 GeV in 400-GeV Proton-Nucleus Collisions*, Phys. Rev. Lett. **39** (1977) p. 252.
- [4] UA1 Collaboration, G. Arnison et al., *Experimental observation of lepton pairs of invariant mass around 95 GeV/c<sup>2</sup> at the CERN SPS collider*, Physics Letters B **126** (1983) p. 398,  
URL: <http://www.sciencedirect.com/science/article/pii/0370269383901880>.
- [5] The ATLAS Collaboration, *Observation of a new particle in the search for the Standard Model Higgs boson with the ATLAS detector at the LHC*, English, Physics Letters B **716.1** (Sept. 2012) pp. 1–29,  
URL: <http://dx.doi.org/10.1016/j.physletb.2012.08.020>.
- [6] The CMS Collaboration, *Observation of a new boson at a mass of 125 GeV with the CMS experiment at the LHC*, English, Physics Letters B **716.1** (Sept. 2012) pp. 30–61,  
URL: <http://dx.doi.org/10.1016/j.physletb.2012.08.021>.
- [7] The ATLAS Collaboration, *Search for high-mass dilepton resonances in pp collisions at  $\sqrt{s} = 8$  TeV with the ATLAS detector*, English, arXiv.org 5 (May 2014) p. 052005, arXiv: 1405.4123 [hep-ex],  
URL: <http://link.aps.org/doi/10.1103/PhysRevD.90.052005>.
- [8] The CMS Collaboration, *Search for physics beyond the standard model in dilepton mass spectra in proton-proton collisions at  $\sqrt{s} = 8$  TeV*, English, Journal of High Energy Physics **2015.4** (Apr. 2015) pp. 25–49,  
URL: [http://link.springer.com/10.1007/JHEP04\(2015\)025](http://link.springer.com/10.1007/JHEP04(2015)025).

- [9] *Search for anomalous production of prompt same-sign lepton pairs and pair-produced doubly charged Higgs bosons with  $\sqrt{s} = 8$  TeV pp collisions using the ATLAS detector*, English, **2015**.3 (Mar. 2015) pp. 41–48,  
URL: [http://link.springer.com/article/10.1007/JHEP03\(2015\)041](http://link.springer.com/article/10.1007/JHEP03(2015)041).
- [10] U. Bellgardt et al., *Search for the Decay  $\mu^+ \rightarrow e^+e^+e^-$* , Nucl.Phys. **B299** (1988) p. 1.
- [11] LHCb Collaboration, *Searches for violation of lepton flavour and baryon number in tau lepton decays at LHCb*, Phys.Lett. **B724** (2013) pp. 36–45,  
arXiv: 1304.4518 [hep-ex].
- [12] C. Biggio and F. Bonnet, *Implementation of the type III seesaw model in FeynRules/MadGraph and prospects for discovery with early LHC data*, arXiv.org (July 2011), arXiv: 1107.3463, URL: <http://arxiv.org/abs/1107.3463>.
- [13] S. P. Martin, *Extra vector-like matter and the lightest Higgs scalar boson mass in low-energy supersymmetry*, arXiv.org (Oct. 2009), arXiv: 0910.2732 [hep-ph],  
URL: <http://arxiv.org/abs/0910.2732>.
- [14] A. Abada et al.,  *$\mu\rightarrow e\gamma$  and  $\tau\rightarrow l\gamma$  decays in the fermion triplet seesaw model*, English, arXiv.org 3 (Mar. 2008) p. 033007, arXiv: 0803.0481 [hep-ph],  
URL: <http://link.aps.org/doi/10.1103/PhysRevD.78.033007>.
- [15] A. Abada et al., *Low energy effects of neutrino masses*, arXiv.org 12 (July 2007) pp. 061–061, arXiv: 0707.4058v3 [hep-ph],  
URL: <http://stacks.iop.org/1126-6708/2007/i=12/a=061?key=crossref.ce48ac8dec87628e866116bc62a5d955>.
- [16] F. del Aguila, J. de Blas, and M. Perez-Victoria, *Effects of new leptons in Electroweak Precision Data*, English, arXiv.org 1 (Mar. 2008) p. 013010, arXiv: 0803.4008 [hep-ph],  
URL: <http://link.aps.org/doi/10.1103/PhysRevD.78.013010>.
- [17] W. Altmannshofer, M. Bauer, and M. Carena, *Exotic leptons: Higgs, flavor and collider phenomenology*, English, Journal of High Energy Physics **2014**.1 (Jan. 2014) pp. 60–39,  
arXiv: 1308.1987 [hep-ph],  
URL: [http://link.springer.com/10.1007/JHEP01\(2014\)060](http://link.springer.com/10.1007/JHEP01(2014)060).
- [18] J. Alwall et al., *The automated computation of tree-level and next-to-leading order differential cross sections, and their matching to parton shower simulations*, JHEP **1407** (2014) p. 079, arXiv: 1405.0301 [hep-ph].
- [19] P. M. Nadolsky et al., *Implications of CTEQ global analysis for collider observables*, Phys. Rev. **D78** (2008) p. 013004, arXiv: 0802.0007 [hep-ph].
- [20] ATLAS Collaboration, *ATLAS Run 1 Pythia8 tunes*, ATL-PHYS-PUB-2014-021 (Nov. 2014),  
URL: <https://cds.cern.ch/record/1966419/>.

- [21] T. Sjöstrand, S. Mrenna, and P. Skands,  
*A brief introduction to PYTHIA 8.1*, English,  
Computer Physics Communications **178**.11 (June 2008) pp. 852–867,  
arXiv: 0710.3820 [hep-ph],  
URL: <http://linkinghub.elsevier.com/retrieve/pii/S0010465508000441>.
- [22] P. Meade and M. Reece, *BRIDGE: Branching ratio inquiry / decay generated events* (2007), arXiv: hep-ph/0703031 [hep-ph].
- [23] K. Olive et al., *Review of Particle Physics*, Chin.Phys. **C38** (2014) p. 090001.
- [24] G. Cowan et al., *Asymptotic formulae for likelihood-based tests of new physics*, Eur. Phys. J. C **71**, 1554 (Feb. 2011) p. 1554, arXiv: 1007.1727 [physics.data-an].
- [25] A. L. Read, *Presentation of search results: The CL(s) technique*, J.Phys. **G28** (2002) pp. 2693–2704.

# Chapter 9

## Conclusion

# Chapter 10

## Appendix

### 10.1 Electron Fake Factors

#### 10.1.1 Photon Conversion Reweighting

Backgrounds due to  $Z + \gamma$ , where the  $Z$  boson decays leptonically and the photon converts asymmetrically in the detector and is reconstructed as a single electron, are estimated with SHERPA. The rate of photons being reconstructed as electrons is observed to be overestimated in Monte Carlo, especially for denominator electrons. The net effect of this mismodeling is a *deficit* in the background prediction, due to its larger effect on the subtraction of prompt contamination than on the prompt background estimation itself. Scale factors are derived to account for the mismodeling of the conversion rate.

The principle of the method is the same as that used to estimate the electron “charge flip” mismeasurement rate. Charge flips and conversions occur through similar processes: charge flips occur through “trident” processes in which an electron emits a photon, which then converts asymmetrically and is reconstructed as an electron of the wrong charge. The method uses a  $Z$ -enriched region to estimate the conversion rate in bins of  $p_T$  and  $|\eta|$ ; for more details, see [1]. The scale factors are shown in table 10.1; the scale factor is applied to each  $Z + \gamma$  event based on the classification of the reconstructed lepton closest to the truth photon (within  $\Delta R < 0.2$ ). A 30% systematic uncertainty is assigned on the scale factors, mostly due to variations in the scale factors obtained from different Monte Carlo generators.

	$ \eta  < 2.2$	$2.2 <  \eta  < 2.37$	$2.37 <  \eta  < 2.47$
Numerators	1.02	0.95	0.95
Denominators	0.82	0.66	0.40

Table 10.1: Data-to-MC scale factors for photon conversions.

### Systematic From Heavy Flavor Fraction

As described above in section 6.2.2, the electron fake factors address fake electrons from two sources, semileptonic heavy flavor decays and misidentified light hadrons. Based on Monte Carlo studies, the truth fake factors for the two sources are numerically quite different, with heavy flavor fake factors generally several times larger than the light flavor counterpart. Since the combined fake factor is a weighted average of the truth heavy and light flavor fake factors, the fake factors may be measured inaccurately if there is a difference in the heavy flavor fraction between the control region and the signal regions.

The size of this effect is estimated using the MC@NLO  $t\bar{t}$  sample. Two quantities are extracted from the Monte Carlo: (a) the truth fake factors for fake electrons arising from heavy or light flavor jets,  $f_{H,L}$ , and (b) the  $d_0$  significance distributions for heavy and light flavor fakes. The truth fake factors are taken to be universal parameters, in particular independent of the composition of sample, and are shown in figure 10.1.

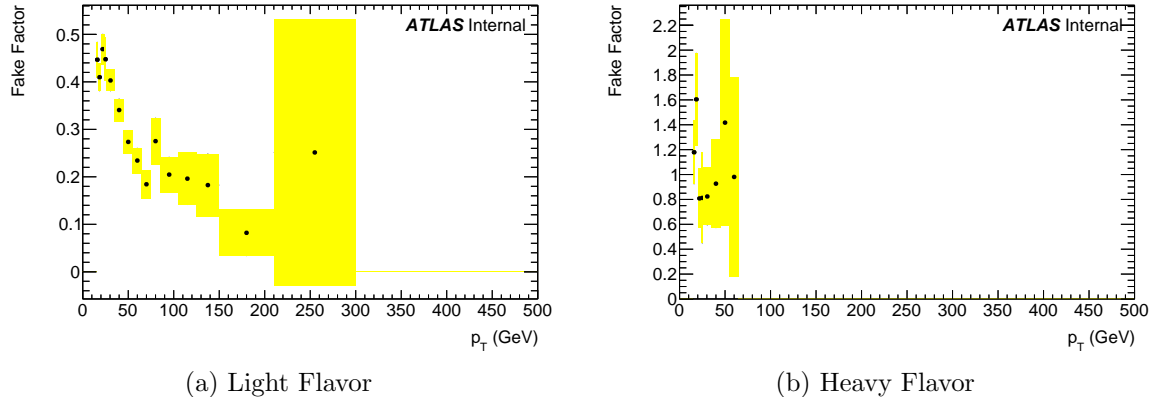


Figure 10.1: MC fake factors for fakes from heavy and light flavor jets, from MC@NLO  $t\bar{t}$  Monte Carlo.

The fake factors in the control and signal regions can be expressed in terms of the truth heavy/light fake factors,  $f_{H,L}$ , and the fraction of denominators from heavy flavor,  $\rho^{HF}$ , by separating the numerators into heavy and light flavor truth origin:

$$f_c = \frac{N_N^{HF} + N_N^{LF}}{N_D} \quad (10.1)$$

$$= \frac{f_H \rho_c^{HF} N_D + f_L (1 - \rho_c^{HF}) N_D}{N_D} = f_H \rho_c^{HF} + f_L (1 - \rho_c^{HF}) \quad (10.2)$$

$$f_s = \frac{f_H \rho_s^{HF} N_D + f_L (1 - \rho_s^{HF}) N_D}{N_D} = f_H \rho_s^{HF} + f_L (1 - \rho_s^{HF}). \quad (10.3)$$

The bias in fake factor is then given by the difference,

$$f_c - f_s = (f_H - f_L) \times (\rho_c^{HF} - \rho_s^{HF}) \quad (10.4)$$

The heavy flavor fraction in the denominator region are extracted using the truth  $d_0$  significance distributions of heavy and light flavor fakes. In particular, in the MC sample, let  $\rho_{HF}^{\text{high}}$  be the fraction of truth heavy flavor denominator objects that satisfy  $\frac{d_0}{\sigma_{d_0}} > 3$ , and similarly for light flavor. Then, in the data samples, the number of denominator objects with high  $d_0$  significance is:

$$N_{D,c}^{\text{high}} = N_{D,c} \left( \rho_c^{HF} \rho_{HF}^{\text{high}} + \rho_c^{LF} \rho_{LF}^{\text{high}} \right) \quad (10.5)$$

$$\rho_{D,c}^{\text{high}} = \left( \rho_c^{HF} \rho_{HF}^{\text{high}} + (1 - \rho_c^{HF}) \rho_{LF}^{\text{high}} \right) \quad (10.6)$$

Solving for  $\rho_c^{HF}$ ,

$$\rho_c^{HF} = \frac{\rho_{D,c}^{\text{high}} - \rho_{LF}^{\text{high}}}{\rho_{HF}^{\text{high}} - \rho_{LF}^{\text{high}}} \quad (10.7)$$

The truth high- $d_0$  significance fractions for truth heavy and light flavor denominator objects are taken from the  $t\bar{t}$  MC to be  $\rho_{LF}^{\text{high}} = 0.696$  and  $\rho_{HF}^{\text{high}} = 0.015$ .

With these quantities, equation 10.4 gives the shift in fake factor value between the control and signal regions. The heavy flavor fractions extracted from the control and some signal regions are shown in table 10.2. Figure 10.2 shows the percent variation in fake factor for a number of signal regions as a function of transverse momentum. The maximum deviation of 20% is taken as a flat systematic uncertainty on the fake factors.

## 10.2 Trilepton Resonance Search

### 10.2.1 $\Delta R(Z, \ell_3)$ Cut Optimization

The value of the cut on the separation between the  $Z$  candidate and the third lepton,  $\Delta R(Z, \ell_3)$ , is chosen based on a study of the expected sensitivity of the analysis at different values of the cut. The expected sensitivity is determined using a simple cut-and-count framework using narrow mass windows, rather than the fit-based framework. The half-width of the mass windows is taken from a linear fit to the full-width half-maxima of the signal peaks as determined from the signal fits (section 10.2.2). The expected 95% CL exclusion on the signal cross section is then determined from the number of signal and background events inside the mass window predicted from Monte Carlo simulation, using the  $\text{CL}_s$  method (section ??) implemented in the `mclimits` framework [2].

The expected exclusions for cut values of  $\Delta R < 2.0, 2.25, 2.5, 2.75, 3.0, 3.14, 3.5$ , and 4.0 are shown in figure 10.3. The same cut is applied to all signal categories, as no significant

Region	Heavy Flavor Fraction
Control	$0.031 \pm 0.006$
onZ / $e\mu$ / All	$-0.001 \pm 0.001$
onZ / $e\mu$ / Weak	$-0.003 \pm 0.001$
onZ / $e\mu$ / Strong	$0.021 \pm 0.007$
onZ / $e\mu$ / High MET	$-0.008 \pm 0.011$
onZ / $e\mu$ / Low MET	$-0.001 \pm 0.001$
offZ / $e\mu$ / All	$-0.004 \pm 0.003$
offZ / $e\mu$ / Weak	$-0.019 \pm 0.025$
offZ / $e\mu$ / Strong	$0.039 \pm 0.019$
offZ / $e\mu$ / High MET	$0.003 \pm 0.003$
offZ / $e\mu$ / Low MET	$-0.006 \pm 0.003$
offZ / $e\mu$ / High $m_T^W$	$0.026 \pm 0.020$

Table 10.2: Denominator object heavy flavor fractions in the control and signal regions, extracted using the fraction of events with  $3 < \frac{d_0}{\sigma_{d_0}} < 10$ .

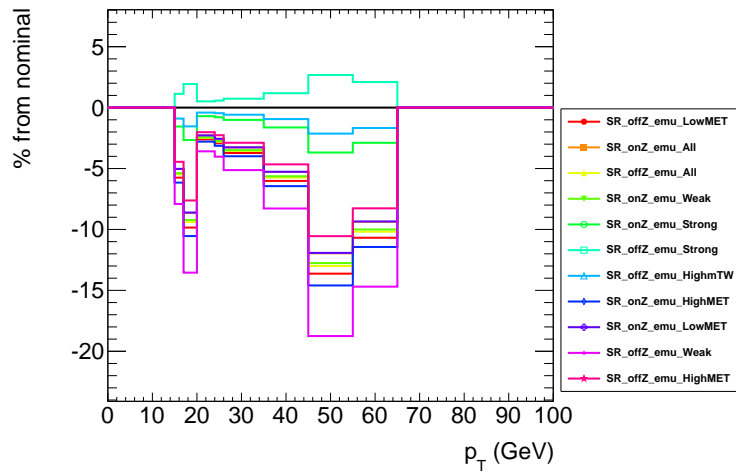


Figure 10.2: Percent deviation in fake factor between the control and signal regions due to variable heavy flavor fractions.

gain is observed by optimizing each cut individually. Smaller values of the cut ( $\Delta R(Z, \ell_3) \lesssim 2.0$ ) perform similarly to more stringent cuts at low signal mass hypotheses, but perform worse at higher mass hypotheses. Cuts above  $\Delta R(Z, \ell_3) \lesssim 3.0$  perform approximately equally. For simplicity, a flat cut value  $\Delta R(Z, \ell_3) < 3.0$  is chosen, independent of the mass hypothesis.

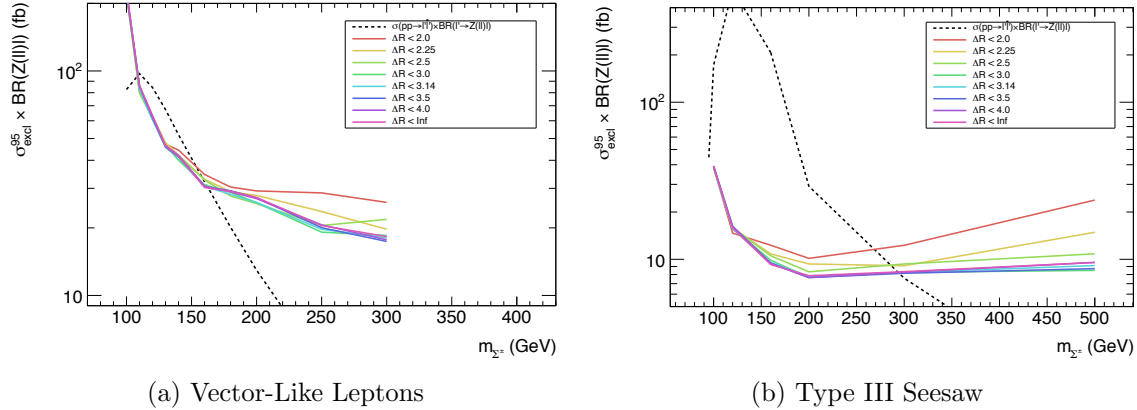


Figure 10.3: Expected upper limits on the heavy lepton production cross section times branching ratio to final states with least one  $Z(\ell\ell) + \ell$  decay for different cuts on the maximum value of  $\Delta R(Z, \ell_3)$ .

### 10.2.2 Signal Fit Details

Tables 10.3-10.6 show the results of fitting the Voigtian plus Landau function to each signal point for the type III seesaw and vector-like leptons models. The fits are performed in the inclusive category in  $Z + e$  and  $Z + \mu$  flavor channels.

### 10.2.3 Additional Kinematic Distributions

This section shows the  $m_{3\ell}$ ,  $\Delta R(Z, \ell_3)$ ,  $m_T^W$ , and  $E_T^{\text{miss}}$  distributions in each of the signal regions (the primary distributions are shown in section 8.6).

Table 10.3: Fit parameters for the type III seesaw model in the  $Z + e$  flavor channel and inclusive category.  $m_V$ ,  $\Gamma_V$ , and  $\sigma_V$  represent the mean, Lorentzian width, and Gaussian width of the Voigt function, and  $m_L$  and  $\sigma_L$  represent the mean and width of the Landau function. Note that the absence of the intrinsic width of the  $Z$  boson in the simulation leads to smaller values than expected for the width of the Voigtian peak for masses below  $\sim 250$  GeV.

Mass [GeV]	$m_V$ [GeV]	$\Gamma_V$ [GeV]	$\sigma_V$ [GeV]	$m_L$ [GeV]	$\sigma_L$ [GeV]	Ratio
100	$8.7222 \pm 0.015$	$0.131 \pm 0.04$	$0.32 \pm 0.03$	$36.1 \pm 0.7$	$10.9 \pm 0.355118$	0.34
120	$28.5035 \pm 0.024$	$0.594 \pm 0.12$	$0.72 \pm 0.06$	$34.1 \pm 0.8$	$10.2 \pm 0.391391$	0.59
160	$68.3224 \pm 0.037$	$1.34 \pm 0.15$	$1.13 \pm 0.08$	$45.9 \pm 0.7$	$15.3 \pm 0.392333$	0.57
200	$108.294 \pm 0.052$	$1.86 \pm 0.20$	$1.59 \pm 0.10$	$59.1 \pm 1.1$	$21.3 \pm 0.568737$	0.58
250	$158.039 \pm 0.090$	$3.08 \pm 0.37$	$1.48 \pm 0.26$	$75.6 \pm 2.1$	$27.6 \pm 1.10452$	0.59
300	$207.856 \pm 0.129$	$2.96 \pm 0.45$	$2.75 \pm 0.23$	$92.3 \pm 2.6$	$35.7 \pm 1.39974$	0.55
350	$257.775 \pm 0.169$	$4.52 \pm 0.63$	$3.21 \pm 0.33$	$106.8 \pm 3.4$	$41.6 \pm 1.85383$	0.57
400	$308.066 \pm 0.198$	$6.84 \pm 0.77$	$2.77 \pm 0.48$	$129.7 \pm 4.2$	$51.3 \pm 2.34715$	0.55
450	$357.463 \pm 0.277$	$7.37 \pm 1.05$	$3.91 \pm 0.61$	$142.1 \pm 5.3$	$58.3 \pm 3.06396$	0.54
500	$407.731 \pm 0.262$	$5.39 \pm 1.02$	$5.26 \pm 0.53$	$179.9 \pm 6.1$	$71.5 \pm 3.65063$	0.52

Table 10.4: Fit parameters for the type III seesaw model in the  $Z + \mu$  flavor channel and inclusive category.  $m_V$ ,  $\Gamma_V$ , and  $\sigma_V$  represent the mean, Lorentzian width, and Gaussian width of the Voigt function, and  $m_L$  and  $\sigma_L$  represent the mean and width of the Landau function. Note that the absence of the intrinsic width of the  $Z$  boson in the simulation leads to smaller values than expected for the width of the Voigtian peak for masses below  $\sim 250$  GeV.

Mass [GeV]	$m_V$ [GeV]	$\Gamma_V$ [GeV]	$\sigma_V$ [GeV]	$m_L$ [GeV]	$\sigma_L$ [GeV]	Ratio
100	$8.78 \pm 0.01$	$0.1 \pm 0.0$	$0.176 \pm 0.01$	$35.6 \pm 0.5$	$10.6 \pm 0.3$	0.45
120	$28.71 \pm 0.01$	$0.28 \pm 0.057$	$0.62 \pm 0.02$	$31.2 \pm 0.5$	$8.7 \pm 0.2$	0.60
160	$68.56 \pm 0.03$	$1.86 \pm 0.14$	$1.18 \pm 0.08$	$44.7 \pm 0.6$	$15.3 \pm 0.3$	0.60
200	$108.3 \pm 0.05$	$3.10 \pm 0.25$	$1.99 \pm 0.13$	$56.6 \pm 0.9$	$19.4 \pm 0.5$	0.61
250	$158.1 \pm 0.1$	$4.36 \pm 0.61$	$3.64 \pm 0.31$	$73.6 \pm 1.9$	$27.0 \pm 1.0$	0.61
300	$207.7 \pm 0.1$	$8.17 \pm 0.84$	$3.87 \pm 0.46$	$86.2 \pm 2.4$	$32.3 \pm 1.3$	0.61
350	$258.3 \pm 0.2$	$10.04 \pm 1.44$	$6.15 \pm 0.75$	$103.1 \pm 3.2$	$40.2 \pm 1.7$	0.59
400	$307.2 \pm 0.3$	$13.09 \pm 1.69$	$6.39 \pm 0.98$	$120.9 \pm 4.2$	$50.2 \pm 2.3$	0.58
450	$357.4 \pm 0.5$	$18.08 \pm 3.05$	$8.86 \pm 1.64$	$137.7 \pm 5.9$	$57.9 \pm 3.4$	0.56
500	$407.6 \pm 0.5$	$14.20 \pm 3.10$	$12.2 \pm 1.44$	$166.7 \pm 6.1$	$67.9 \pm 3.6$	0.53

Table 10.5: Fit parameters for the VLL model in the  $Z + e$  flavor channel and inclusive category.  $m_V$ ,  $\Gamma_V$ , and  $\sigma_V$  represent the mean, Lorentzian width, and Gaussian width of the Voigt function, and  $m_L$  and  $\sigma_L$  represent the mean and width of the Landau function.

Mass [GeV]	$m_V$ [GeV]	$\Gamma_V$ [GeV]	$\sigma_V$ [GeV]	$m_L$ [GeV]	$\sigma_L$ [GeV]	Ratio
100	$10.77 \pm 0.18$	$0.1 \pm 0.1$	$2.5 \pm 0.2$	$34.3 \pm 1.5$	$12.12 \pm 0.47$	0.37
110	$18.54 \pm 0.04$	$1.9 \pm 0.2$	$1.0 \pm 0.1$	$34.1 \pm 1.8$	$10.08 \pm 0.51$	0.69
120	$28.25 \pm 0.04$	$2.7 \pm 0.4$	$0.7 \pm 0.2$	$35.8 \pm 3.0$	$10.95 \pm 1.02$	0.75
130	$38.18 \pm 0.04$	$2.2 \pm 0.2$	$1.2 \pm 0.1$	$31.0 \pm 0.6$	$9.40 \pm 0.32$	0.71
140	$48.07 \pm 0.04$	$2.2 \pm 0.2$	$1.5 \pm 0.1$	$33.4 \pm 0.6$	$10.29 \pm 0.28$	0.69
160	$68.00 \pm 0.04$	$3.0 \pm 0.2$	$1.4 \pm 0.1$	$37.0 \pm 0.7$	$11.52 \pm 0.32$	0.70
180	$87.97 \pm 0.05$	$3.2 \pm 0.2$	$1.6 \pm 0.1$	$43.8 \pm 0.7$	$14.05 \pm 0.35$	0.67
200	$107.89 \pm 0.05$	$3.0 \pm 0.2$	$2.0 \pm 0.1$	$49.7 \pm 0.8$	$16.38 \pm 0.39$	0.65
250	$157.75 \pm 0.06$	$3.2 \pm 0.2$	$2.6 \pm 0.2$	$66.2 \pm 0.9$	$22.76 \pm 0.47$	0.59
300	$207.57 \pm 0.07$	$3.4 \pm 0.3$	$3.3 \pm 0.2$	$83.9 \pm 1.1$	$29.64 \pm 0.58$	0.57
400	$307.53 \pm 0.09$	$4.2 \pm 0.3$	$4.4 \pm 0.2$	$118.9 \pm 1.7$	$46.42 \pm 0.93$	0.53

Table 10.6: Fit parameters for the VLL model in the  $Z + \mu$  flavor channel and inclusive category.  $m_V$ ,  $\Gamma_V$ , and  $\sigma_V$  represent the mean, Lorentzian width, and Gaussian width of the Voigt function, and  $m_L$  and  $\sigma_L$  represent the mean and width of the Landau function.

Mass [GeV]	$m_V$ [GeV]	$\Gamma_V$ [GeV]	$\sigma_V$ [GeV]	$m_L$ [GeV]	$\sigma_L$ [GeV]	Ratio
100	$10.9 \pm 0.13$	$0.1 \pm 0.05$	$2.85 \pm 0.10$	$35.63 \pm 1.21$	$11.98 \pm 0.40$	0.44
110	$18.7 \pm 0.03$	$2.13 \pm 0.16$	$0.73 \pm 0.11$	$32.88 \pm 1.55$	$9.47 \pm 0.46$	0.74
120	$28.5 \pm 0.03$	$2.26 \pm 0.19$	$0.78 \pm 0.11$	$30.72 \pm 1.17$	$9.44 \pm 0.59$	0.75
130	$38.4 \pm 0.03$	$2.23 \pm 0.16$	$1.07 \pm 0.09$	$29.40 \pm 0.48$	$8.83 \pm 0.26$	0.73
140	$48.5 \pm 0.03$	$2.38 \pm 0.16$	$1.26 \pm 0.09$	$30.57 \pm 0.50$	$9.31 \pm 0.25$	0.73
160	$68.5 \pm 0.05$	$2.71 \pm 0.19$	$1.74 \pm 0.10$	$33.97 \pm 0.55$	$10.45 \pm 0.27$	0.71
180	$88.3 \pm 0.05$	$2.73 \pm 0.21$	$2.19 \pm 0.11$	$40.06 \pm 0.62$	$12.76 \pm 0.30$	0.68
200	$108.4 \pm 0.1$	$3.34 \pm 0.26$	$2.81 \pm 0.14$	$45.44 \pm 0.65$	$14.28 \pm 0.32$	0.66
250	$158.2 \pm 0.1$	$4.45 \pm 0.34$	$3.89 \pm 0.17$	$61.10 \pm 0.85$	$20.71 \pm 0.42$	0.62
300	$208.0 \pm 0.1$	$6.21 \pm 0.48$	$5.26 \pm 0.25$	$76.50 \pm 1.01$	$26.62 \pm 0.51$	0.58
400	$307.9 \pm 0.2$	$9.12 \pm 0.84$	$8.63 \pm 0.40$	$114.84 \pm 1.60$	$42.99 \pm 0.85$	0.53

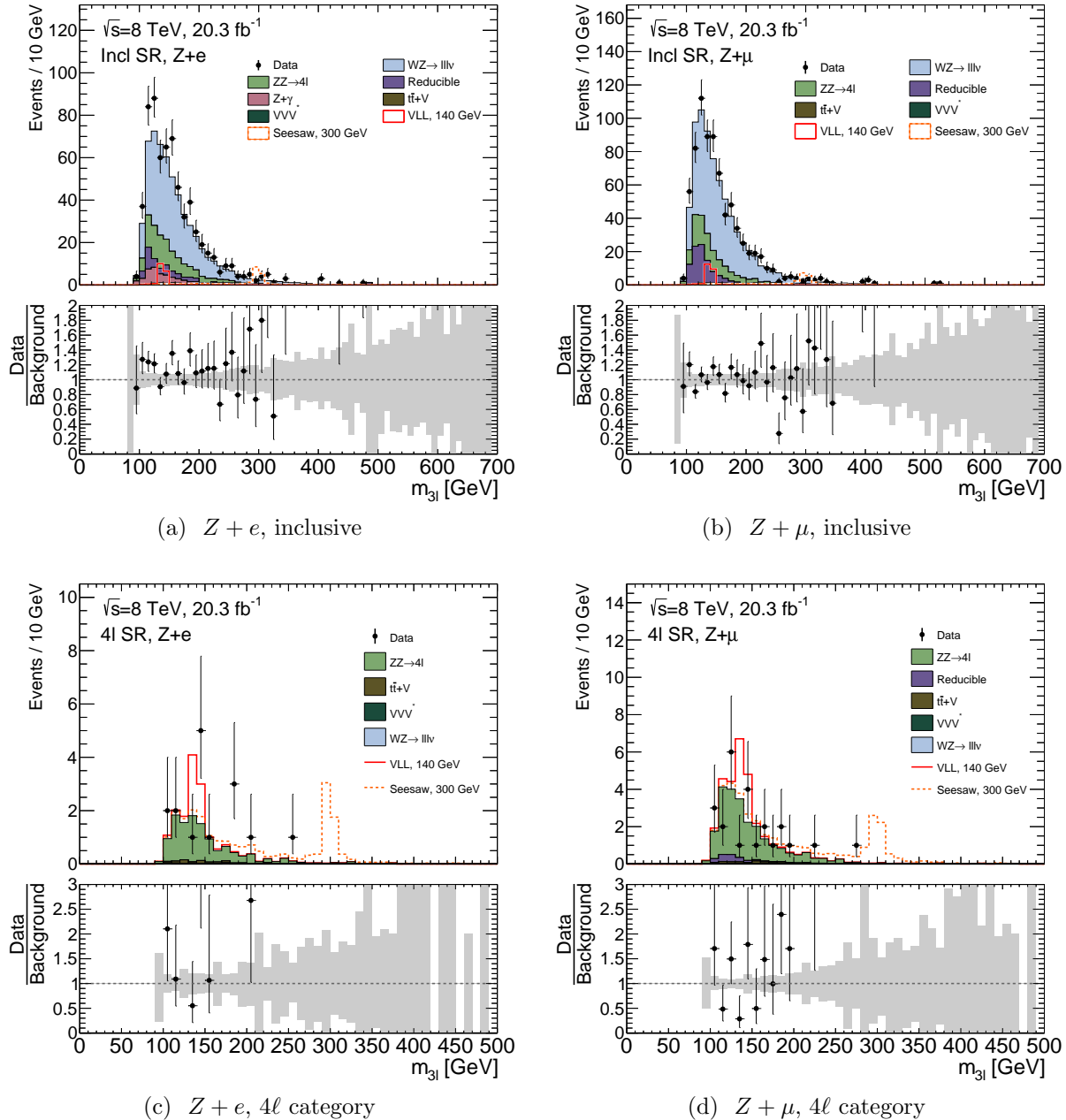


Figure 10.4:  $m_{3\ell}$  distributions for  $Z + e$  and  $Z + \mu$  candidates, for the inclusive and  $4\ell$  signal regions (linear scale).

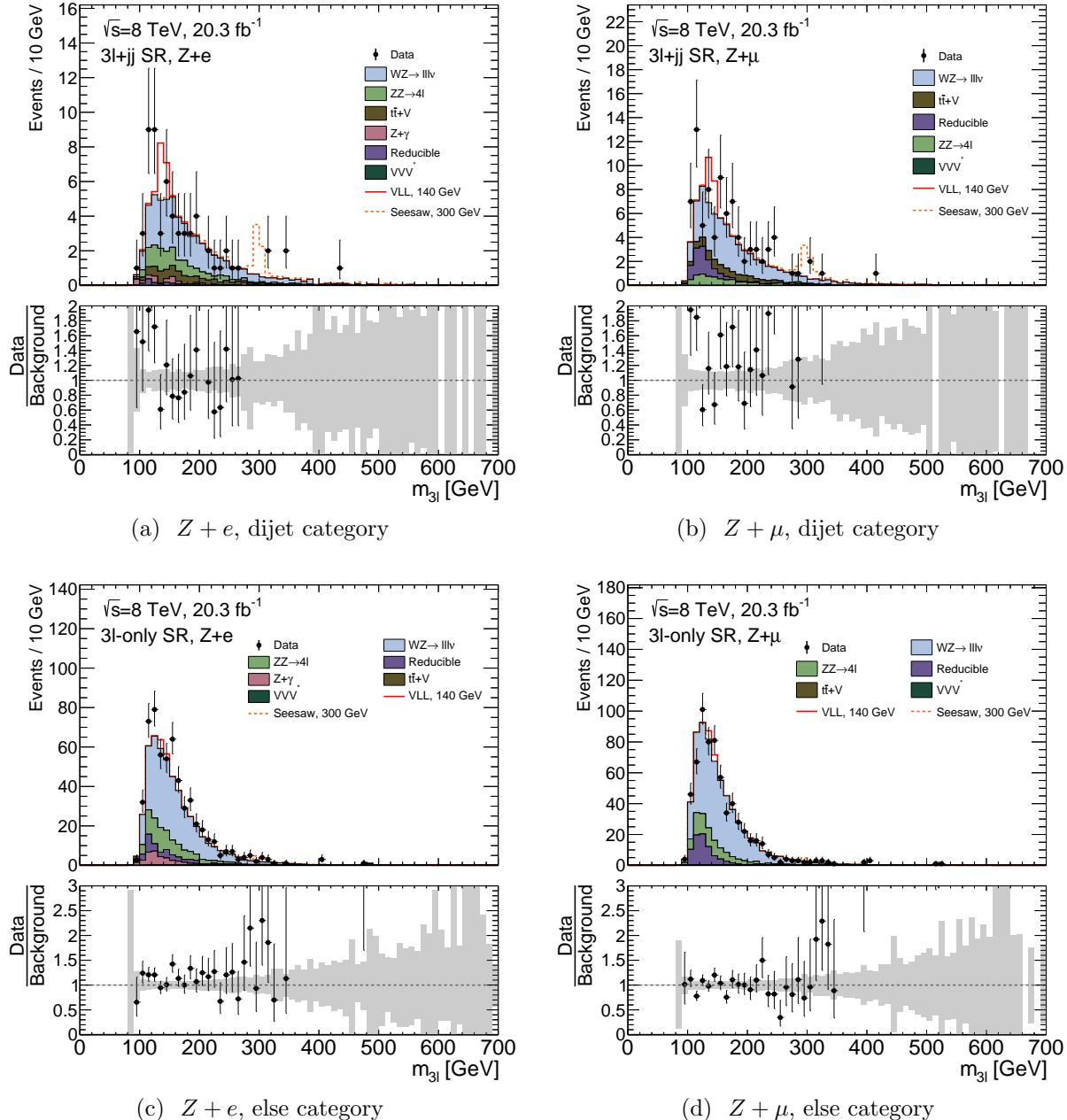


Figure 10.5:  $m_{3\ell}$  distributions for  $Z + e$  and  $Z + \mu$  candidates, for the  $3\ell + jj$  and  $3\ell$ -only signal regions (linear scale).

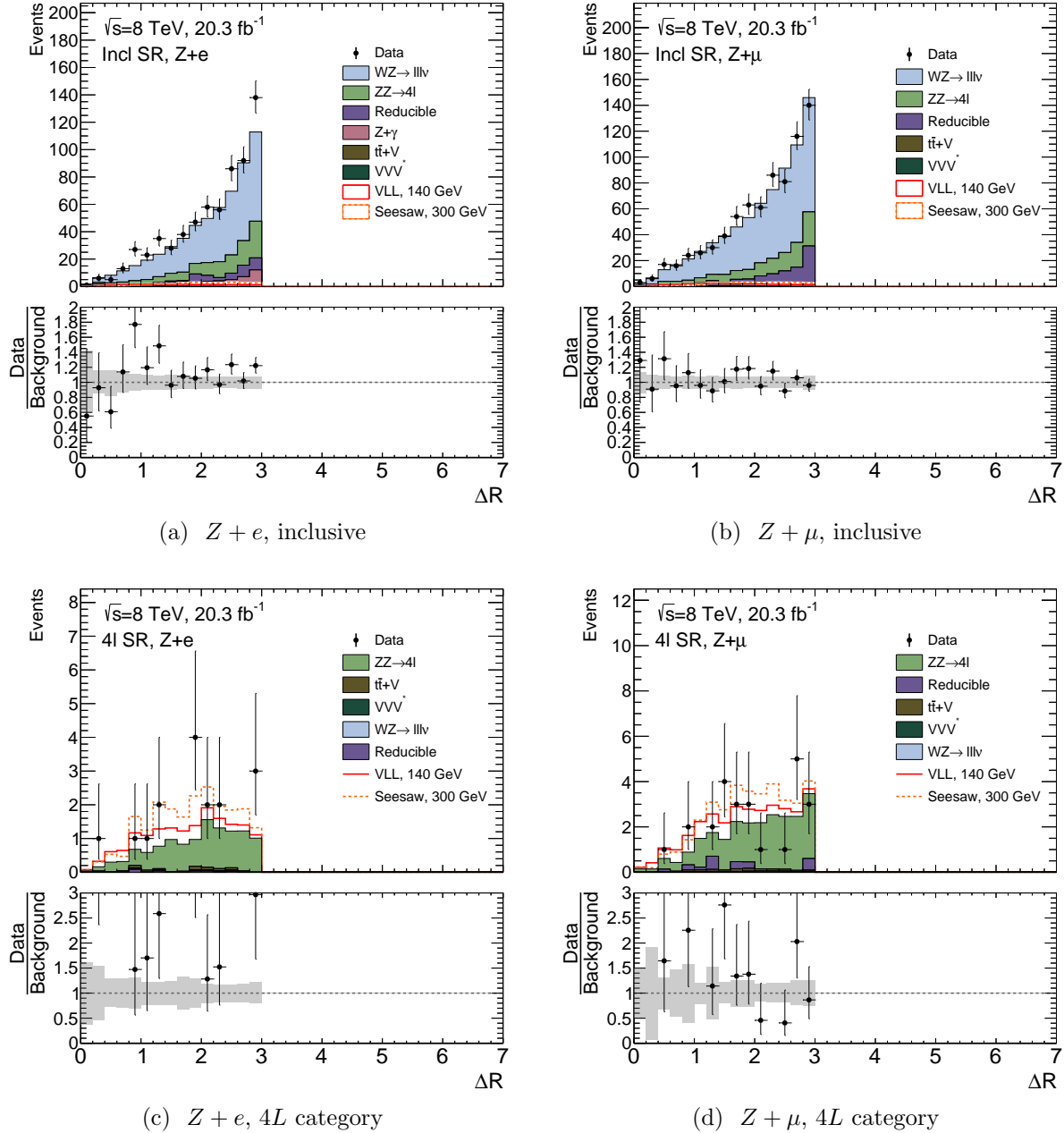


Figure 10.6:  $\Delta R(Z, \ell_3)$  distributions for  $Z + e$  and  $Z + \mu$  candidates, for the inclusive and  $4\ell$  signal regions (linear scale).

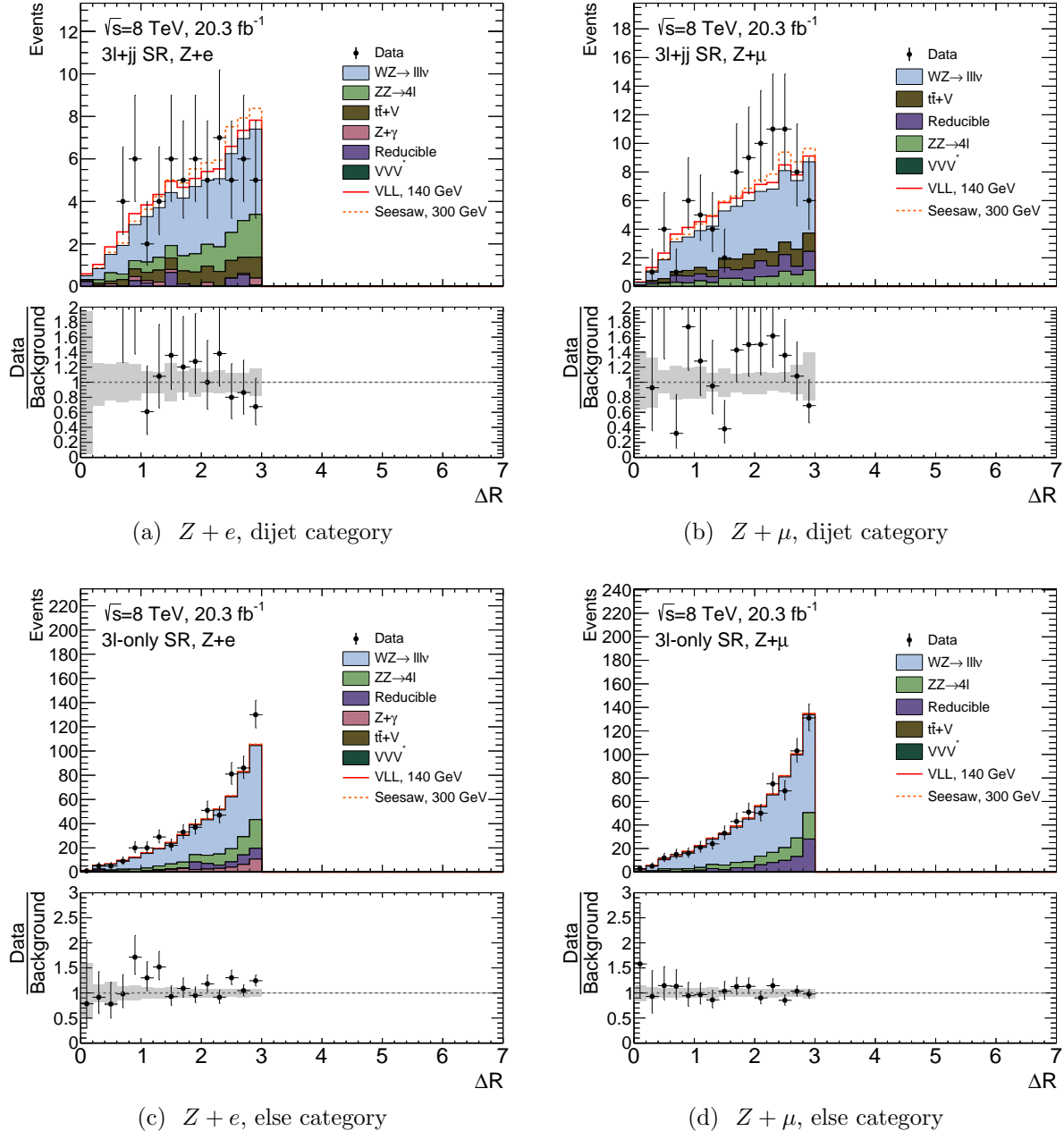


Figure 10.7:  $\Delta R(Z, \ell_3)$  distributions for  $Z + e$  and  $Z + \mu$  candidates, for the  $3\ell + jj$  and  $3\ell$ -only signal regions (linear scale).

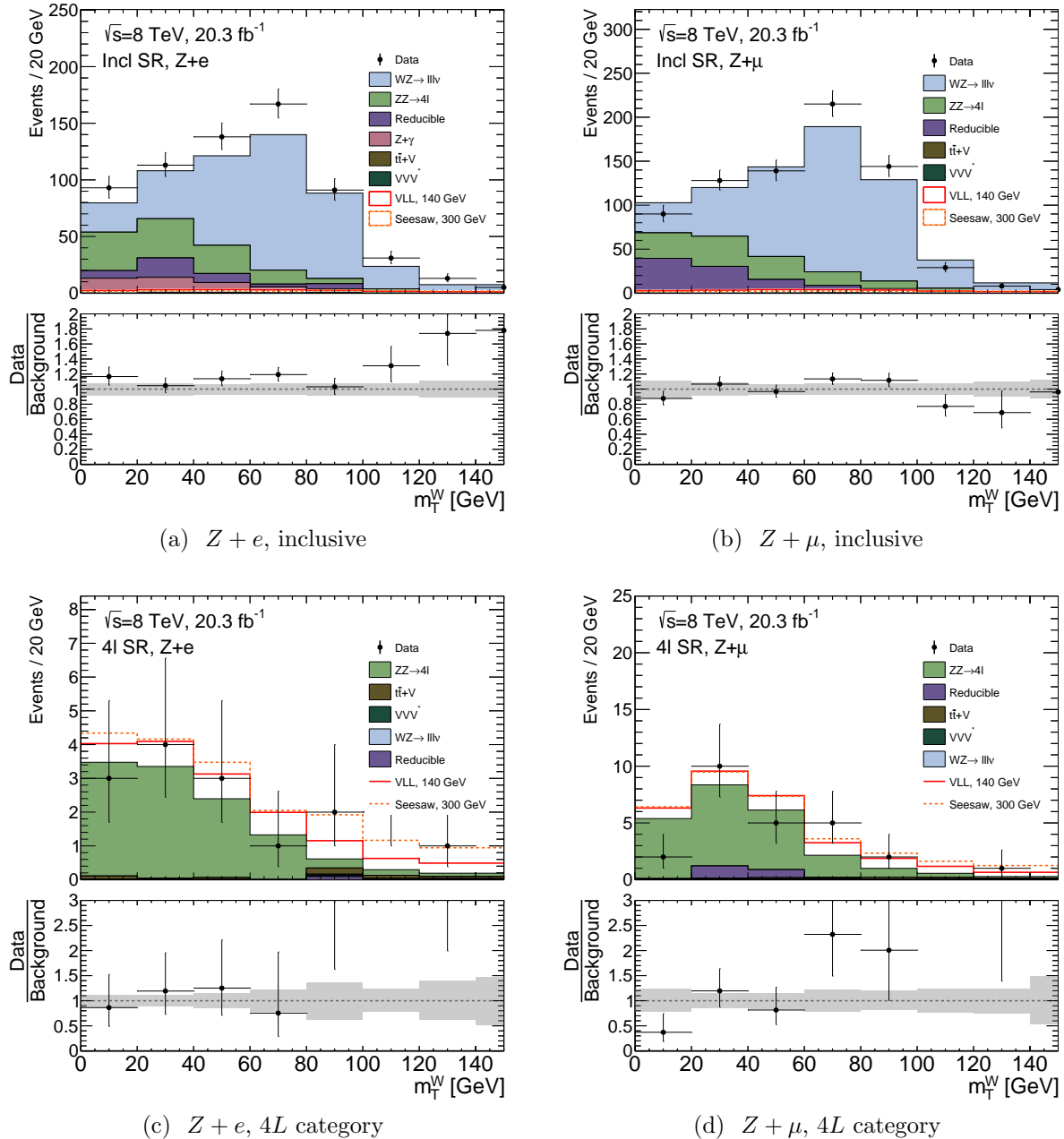


Figure 10.8: Transverse mass of the missing energy and bachelor lepton ( $m_T^W$ ) for  $Z + e$  and  $Z + \mu$  candidates, for the inclusive and  $4\ell$  signal regions.

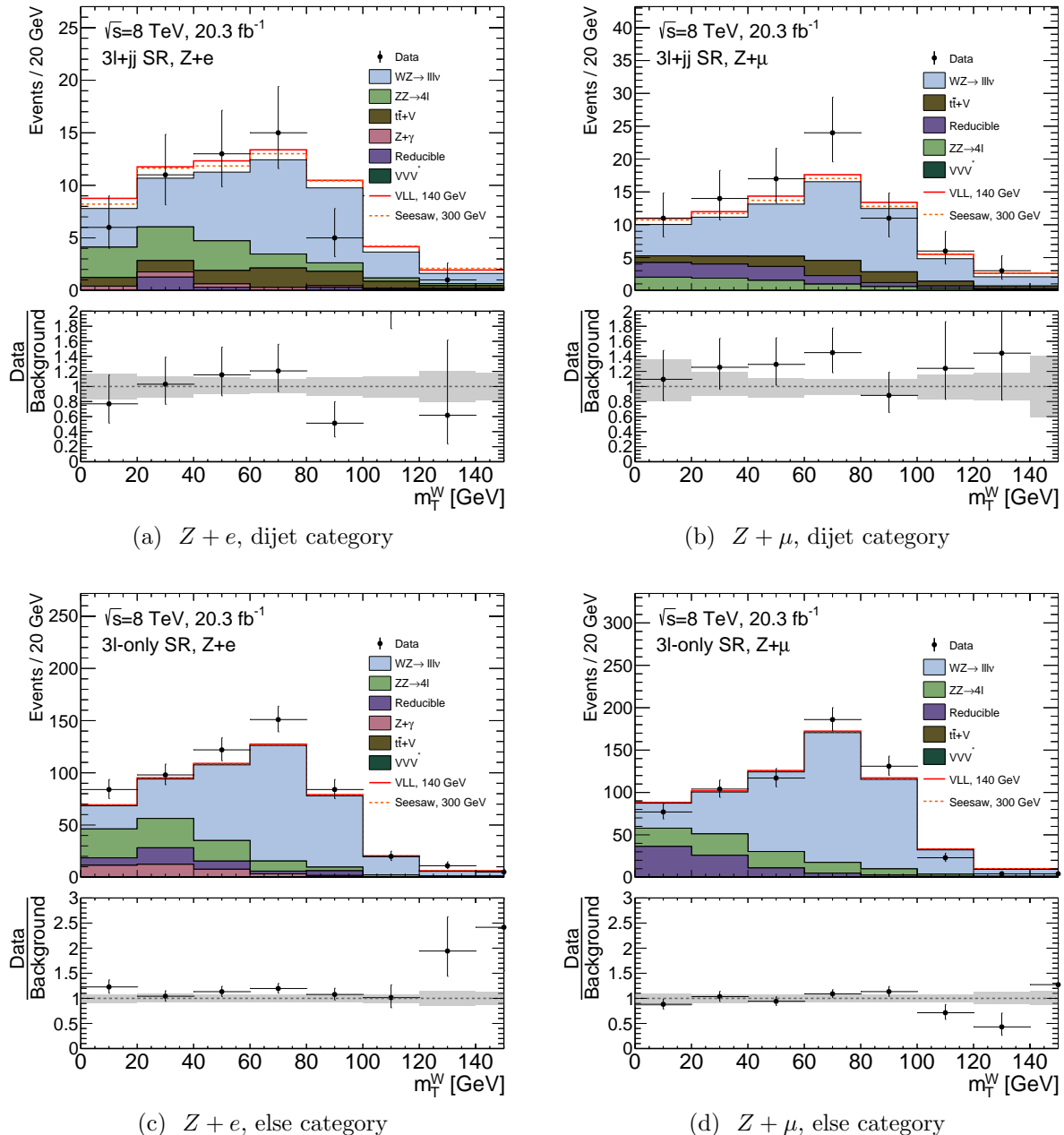


Figure 10.9: Transverse mass of the missing energy and bachelor lepton ( $m_T^W$ ) for  $Z + e$  and  $Z + \mu$  candidates, for the  $3\ell + jj$  and  $3\ell$ -only signal regions.

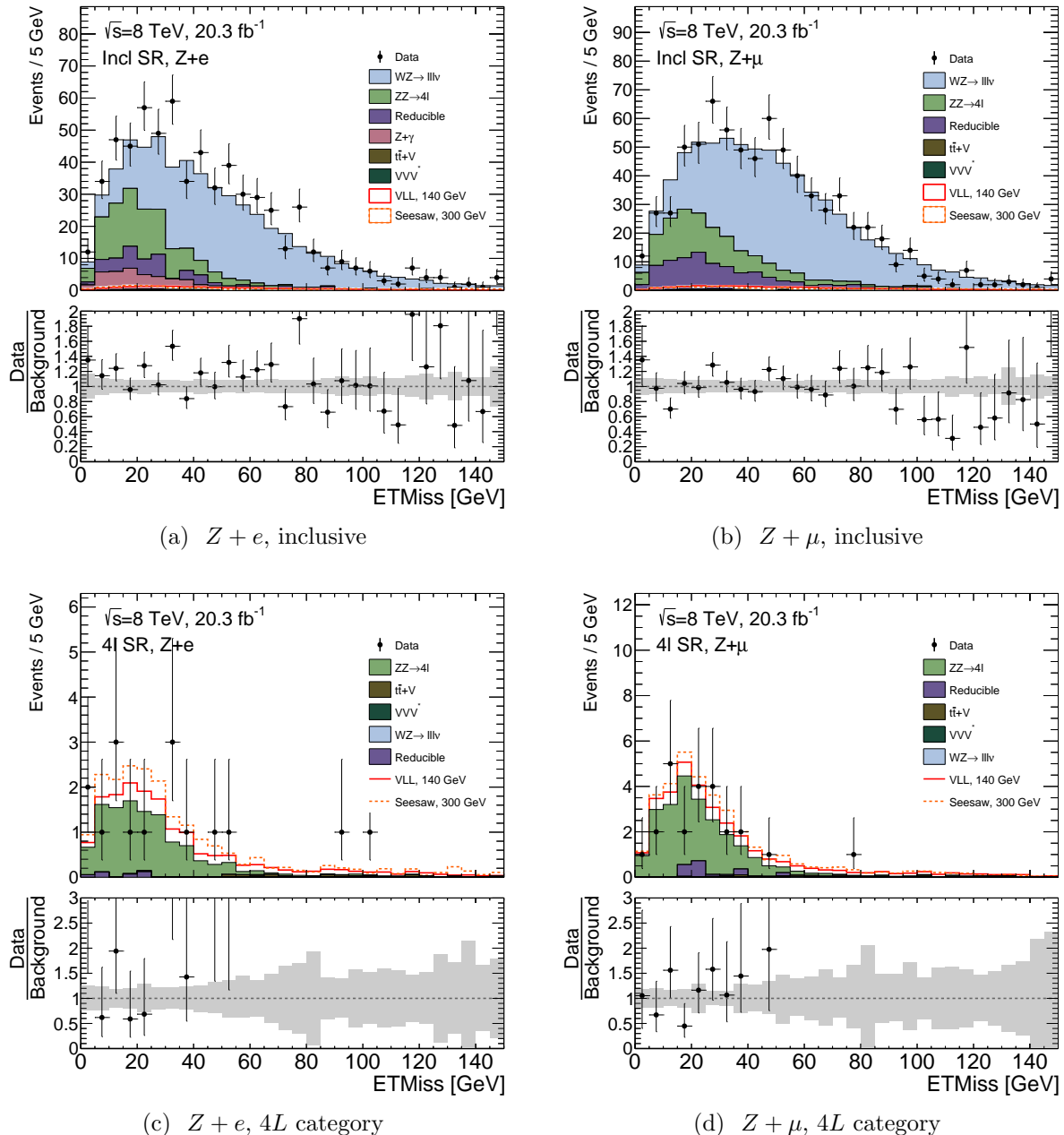


Figure 10.10: Missing energy ( $E_T^{\text{miss}}$ ) for  $Z + e$  and  $Z + \mu$  candidates, for the inclusive and  $4\ell$  signal regions.

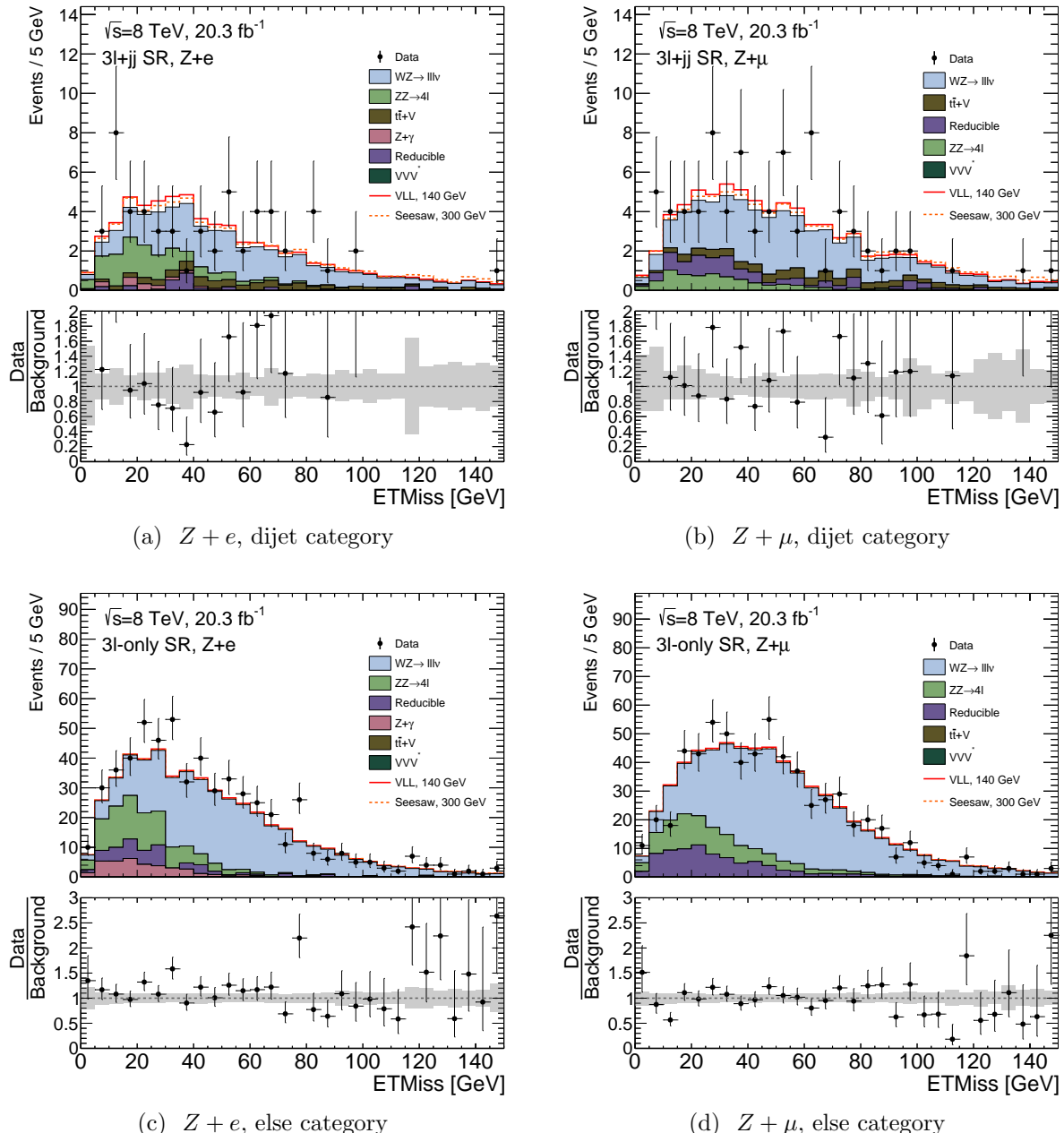


Figure 10.11: Missing energy ( $E_T^{\text{miss}}$ ) for  $Z + e$  and  $Z + \mu$  candidates, for the  $3\ell + jj$  and  $3\ell$ -only signal regions.